Thermal-fluid performance modelling of a transcritical carbon dioxide heat pump cycle

M Botha

orcid.org/0000-0002-5428-1114

Dissertation accepted in fulfilment of the requirements for the degree *Master of Engineering in Mechanical Engineering* at the North-West University

Supervisor: Prof M Van Eldik

Co-supervisor: Dr PVZ Venter

Graduation: August 2023

Student number: 27243060

ACKNOWLEDGEMENTS

The author of this dissertation is sincerely grateful to all parties involved in making this study possible over the past two years and would like to express a particular thanks to:

- My supervisor, Prof. Martin Van Eldik, for your exceptional leadership, passion, time, effort, and willingness to always be of assistance regardless of your busy schedule.
- My co-supervisor, Dr Philip Venter, for your insight, knowledge, and assistance that guided me through critical stages of the study and for always making time to offer your valuable expertise.
- A great thanks to the North-West University, the NRF and Prof. Martin Van Eldik for the financial support that made it possible for me to pursue this full-time study.
- My four parents: Jan, Karin, Nico, and Tilla. Thank you for your constant support, motivation, all your prayers, and mostly thank you for always believing steadfastly in me.
- My sister, Nicolene, thank you for always reaching out and caring in the ups and downs, as well as for all your prayers.
- My girlfriend, Chené, thank you for all your love, care, prayers, positivity, and belief in me. Thank you for all your emotional and physical support and for unifying with me in the ups and downs.

Superior to all, thank you Lord for the talent and this opportunity You have abundantly blessed me with. Thank You for always being there and for all the strength and courage You have given me. All glory and praise to You alone.

ABSTRACT

The continuous augmentation of environmental laws for refrigerants has forced the HVACR sector to re-consider natural refrigerants, with Carbon Dioxide (R744) being a promising candidate due to its competitive heat transfer properties and negligible environmental impact. When operated in a transcritical heat pump cycle, R744 can heat water to above-conventional temperatures such as 90°C without a severe downgrade in cycle efficiency. Recent literature revealed that 18.8% of the total industrial energy demand in South Africa is integrative with this system when operating at such high water temperatures. Although the system's ability and potential market have been pointed out, actual cycle performance data is limited to low ambient temperatures only, which is unusual for South Africa. Thus, the need exists to predict the cycle performance at the mentioned water outlet temperatures over a range of high ambient temperatures, typically beyond 25°C.

In this study, a thorough literature study was carried out to evaluate the component types, methods and correlations typically used to numerically model the cycle in question. The relevant theory that governs the thermo-physical behaviour of each component was compiled and integrated into a simulation model. The verification revealed that the component models were able to predict their reference data within an absolute maximum deviation of 3.17%. The individual component model validations (relative to experimental data) and the full cycle simulations (relative to literature data) proved the model to deliver satisfactory accurate and tangible results for the purpose of this study.

After sizing the system to criteria that provide a sufficient capacity to satisfy all intended operating conditions, various simulations followed. At a water outlet temperature of 90°C, subject to an ambient temperature rise from 25°C to 40°C, the best-recorded COP value enhanced from 3.02 to 3.37 (+11.6%), whilst the heating capacity rose from 32.7 kW to 41.1 kW (+25.7%). This was accompanied by a moderate rise in optimal discharge pressure. Other parameters such as the heat transfer rates, mass flow rates, and power consumption were also studied. Normalised to the most appropriate literature, the noted efficiencies were found lower than Yamaguchi *et al*. (2011), yet, higher than Wang *et al*. (2013a). It was concluded that the high ambient temperatures did not result in significantly higher efficiencies than those of literature, which is linked to lower ambient temperatures, yet, at higher humidity. Hence, the important influence of ambient humidity was also considered. At an ambient temperature of 40°C, a rise in relative humidity from 30% to 60% led to a COP_H improvement from 3.37 to 3.77 (+11.9%). At such high ambient conditions, it was also revealed that the evaporation temperature needs to be maintained at a low enough value (in this case 16.4°C) for the R744 discharge temperatures to still be satisfactory for the application of such high water temperatures. Supplementary, at the conditions of interest, it was found that an increase in water inlet temperature heavily degrades the cycle efficiency.

KEYWORDS

Carbon dioxide (R744)

Transcritical heat pump cycle

Thermal-fluid modelling

High water heating temperatures

High ambient temperatures

Coefficient of performance (COP)

LIST OF ABBREVIATIONS

CFC	Chlorofluorocarbon
CHTC	Convection Heat Transfer Coefficient
COP	Coefficient of Performance
CV	Control Volume
DB	Dry-bulb
DOS	Degree of Superheat
EES	Engineering Equation Solver
GWP	Global Warming Potential
HFCF	Hydro-Chlorofluorocarbon
HFO	Hydrofluoro-Olefin
HFS	Hydrofluorocarbon
HVACR	Heating, Ventilation, Air Conditioning, and Refrigeration
IHX	Internal Heat Exchanger
LMTD	Logarithmic Mean Temperature Difference
ODP	Ozone Depletion Potential
ODP	Optimal Discharge Pressure
PID	Proportional Integral Derivative
PR	Pressure Ratio
RH	Relative Humidity of Air
SCFD	Systems-Computational-Fluid-Dynamics
WB	Wet-bulb

NOMENCLATURE

A	$Surface\ area$	$[m^2]$
A_{ff}	$Free\ flow\ area$	$[m^2]$
A_f	$Fin\ surface\ area$	$[m^2]$
A_t	$Tube\ outside\ surface\ area$	$[m^2]$
$A_{frontal}$	$Evaporator\ frontal\ area$	$[m^2]$
$A_{air,o}$	$Total\ surface\ area\ of\ air\ (A_f + A_t)$	$[m^2]$
B	$Body\ forces\ acting\ on\ the\ control\ surface$	$[N]$
COP_H	$Heating\ coefficient\ of\ performance$	[-]
COP_L	$Cooling\ coefficient\ of\ performance$	[-]
C_p	$Specific\ heat\ at\ constant\ pressure$	$[J/kg.K]$
D_c	$Evaporator\ collar\ diameter\ (D\_o + 2\delta_f)$	$[m]$
D_i	$Tube\ inside\ diameter$	$[m]$
D_o	$Tube\ outside\ diameter$	$[m]$
D_{eq}	$Equivalent\ diameter$	$[m]$
D_H	$Hydraulic\ diameter$	$[m]$
f	$Friction\ factor$	[-]
F_p	$Fin\ pitch$	$[m]$
Fr	$Froude\ number$	[-]
G	$Mass\ flux$	$[kg/m^2]$
g	$Gravitational\ constant$	$[m/s^2]$
H	$Height$	$[m]$
h	$Static\ enthalpy$	$[J/kg]$
h_0	$Total\ enthalpy$	$[J/kg]$
h_c	$Convection\ heat\ transfer\ coefficient$	$[W/m^2.K]$
h_{lv}	$Latent\ heat\ of\ vaporisation$	$[J/kg]$
h_m	$Mass\ transfer\ coefficient$	$[kg/(m^2.s)]$
h_v	$Enthalpy\ of\ the\ vapour\ carried\ by\ the\ air$	$[J/kg]$
j	$Colburn - j\ factor\ for\ heat\ transfer$	[-]

k	*Thermal conductivity*	$[W/(m.K)]$
L	*Length*	$[m]$
Le	*Lewis number*	[-]
m	*Function used in the Schmidt* (1949) *approximation*	[-]
M	*Molecular weight*	$[kg/kmol]$
$\dot{m}$	*Mass flow*	$[kg/s]$
N	*Number of tube rows*	[-]
Nu	*Nusselt number*	[-]
P	*Static pressure*	$[Pa]$
P_{crit}	*Critical pressure*	$[Pa]$
P_0	*Total pressure*	$[Pa]$
P_l	*Longitudinal tube pitch*	$[m]$
P_t	*Transversal tube pitch*	$[m]$
Pr	*Prandtl number*	[-]
q	*Heat flux*	$[W/m^2]$
$\dot{Q}$	*Heat transfer rate*	$[W]$
$\dot{Q}_L$	*Heat absorbed by R744 (Cooling capacity)*	$[W]$
$\dot{Q}_H$	*Heat absorbed by R744 (Heating capacity)*	$[W]$
R_f	*Fouling factor*	$[m^2s/W]$
r_o	*Tube outer radius*	$[m]$
Re	*Reynolds number*	[-]
RH	*Relative humidity*	[%]
T	*Static temperature*	$[°C]$
T_0	*Total temperature*	$[K]$
u	*Internal energy*	$[J/kg]$
UA	*Overall thermal resistance*	$[W/K]$
V	*Velocity*	$[m/s]$
V_m	*Mean velocity of the vapour phase*	$[m/s]$
~~V~~	*Volume*	$[m^3]$
$\dot{W}$	*Work performed*	$[W]$

We	$Webber\ number$	[-]
x	$Vapour\ quality$	[-]
z	$Elevation$	$[m]$

Greek

α	$Evaporator\ ratio: Surface\ area\ over\ volume$	[-]
Δ	$Delta\ (Difference)$	[Various units]
ε	$Void\ fraction$	[-]
η	$Surface\ efficiency$	[-]
ω	$Humidity\ ratio$	$[kg_{water}/kg_{air}]$
ϕ	$Function\ used\ in\ the\ Schmidt\ (1949)\ approximation$	[-]
ρ	$Density$	$[kg/m\text{^}3]$
θ	$Angle$	$[rad]$
μ	$Dynamic\ viscosity$	$[kg/(m \cdot s)]$
σ	$Surface\ tension$ / $Evaporator\ ratio: Free\ flow\ area\ over\ frontal\ area$	$[N/m]$ / [-]
τ	$Shear\ forces\ acting\ on\ the\ CV\ surface$	$[N]$
δ	$Thickness$	$[m]$

Subscripts

a	Air
A	$Annular$
avg	$Average$
c	$Cold\ fluid$
C	$Compressor\ /\ Cooling$
cb	$Convective\ boiling$
dis	$Discharge$
D	$Dryout$
Dc	$Evaluated\ at\ collar\ diameter$
$D\&H$	$Dang\ and\ Hihara$
de	$Dryout\ completion$
di	$Dryout\ inception$

e	$Outlet\ /\ evaporator$
f	Fin
h	$Hot\ fluid$
H	$Homogeneous\ /\ Heating$
i	$Inlet\ /\ Inner$
I	$Intermittent$
IA	$Intermittent - Annular\ transition$
inc	$Increment$
L	$Latent\ /\ Liquid$
Lv	$Liquid - vapour$
$L0$	$Evaluating\ the\ total\ lv\ as\ liquid\ flow$
M	$Mist$
nb	$Nucleate\ boiling$
o	$Outer\ /\ overall$
r	$Refrigerant\ (R744)$
s	$Sensible$
sh	$Superheat$
suc	$Suction$
t	$Tube$
T	$Total$
tp	$Two - phase\ mixture$
v	$Vapour$
w	$Water\ /\ water\ condensate\ film$
Y	$Correction\ factor$

TABLE OF CONTENTS

ABSTRACT ..... **III**

KEYWORDS ..... **IV**

LIST OF ABBREVIATIONS ..... **V**

NOMENCLATURE ..... **VI**

1. CHAPTER 1: INTRODUCTION **1**

1.1 Background **1**

1.2 Problem statement **4**

1.3 Objectives **4**

1.4 Research methodology **4**

2. CHAPTER 2: LITERATURE REVIEW **6**

2.1 Performance of air-to-water transcritical R744 heat pump cycles **6**

2.1.1 Initial investigation conducted on transcritical R744 heat pump cycles 6

2.1.2 Influence of operating conditions on cycle performance 7

2.1.3 Performance of air-to-water transcritical R744 heat pump cycles at above conventional water outlet temperatures and relatively high ambient temperatures 14

2.1.4 Summary 17

2.2 Numerical modelling of a transcritical R744 heat pump cycle **18**

2.2.1 Systems modelling level 19

2.2.2 Detailed modelling level 22

2.2.3 Summary 31

2.3 Conclusion **32**

3. CHAPTER 3: THEORETICAL STUDY **34**

3.1 Conservation laws 34
3.1.1 Conservation of mass 34
3.1.2 Conservation of energy 35
3.1.3 Conservation of momentum 36
3.1.4 Application of conservation laws 37
3.2 Compressor theory 41
3.3 Gas cooler theory 42
3.3.1 Heat transfer 42
3.3.2 Pressure drop 43
3.3.3 Free flow and surface areas 44
3.3.4 Heat exchanger analysis and thermal resistance 45
3.4 Evaporator theory 46
3.4.1 Refrigerant side 46
3.4.2 Airside 47
3.4.3 Free flow and surface areas 49
3.4.4 Heat exchanger analysis 50
3.5 Combined heat pump cycle 50
3.6 Conclusion 51

4. CHAPTER 4: MODEL IMPLEMENTATION 52
4.1 Cycle overview 52
4.2 Overview of the modelling approach 54
4.3 Component models 54
4.3.1 Compressor 55
4.3.2 Gas cooler 56
4.3.3 Expansion valve 60
4.3.4 Evaporator 60

4.4 Integrated heat pump cycle model 68

4.5 Conclusion 68

5. CHAPTER 5: MODEL VERIFICATION AND VALIDATION 69

5.1 Reciprocating compressor model 70

5.2 Water-source tube-in-tube gas cooler model 73

5.2.1 Verification: Comparison to Flownex simulation 74

5.2.2 Validation: Comparison to experimental data of Harris (2014) 74

5.3 Air-source wavy-finned tube evaporator model 76

5.3.1 Overall heat transfer rate 78

5.3.2 R744 side temperature 79

5.3.3 Airside temperature and moisture 82

5.3.4 Summary 85

5.4 Heat exchanger pressure drops: Brief verification check 86

5.5 Conclusion 88

6. CHAPTER 6: COMPONENT DESIGNS 89

6.1 Design conditions 89

6.2 Compressor selection 90

6.3 Heat exchanger designs 92

6.3.1 Evaluation of the considered parameters 93

6.3.2 Conclusion of heat exchanger designs 96

6.4 Conclusion 97

7. CHAPTER 7: SIMULATION RESULTS 99

7.1 Effect of ambient temperature at fixed water mass flow rates 100

7.2 Effect of ambient temperature at a fixed water outlet temperature 103

7.2.1 Resulting COP_H and ODP 104

7.2.2 Comparison to the most applicable literature as identified in Section 2.1.3 105

7.2.3 Resulting heat transfer rates, power consumption, and mass flow rates 109

7.3 Additional investigation: The influence of higher ambient humidity and water inlet temperatures 114

7.3.1 Higher ambient relative humidity 115

7.3.2 Higher water inlet temperature 118

7.4 Conclusion 121

8. CHAPTER 8: CONCLUSION AND RECOMMENDATIONS 125

8.1 Conclusion 125

8.2 Future recommendations 127

9. BIBLIOGRAPHY 129

APPENDIX A 137

APPENDIX B 138

APPENDIX C 150

APPENDIX D 162

APPENDIX E 176

APPENDIX F 179

LIST OF TABLES

Table 1-1: Basic properties of common natural and Freon refrigerants (Nawaz, *et al.* 2018, Rony*, et al*. 2019)..... 3

Table 2-1: Review of previously reported cycle performance at operating conditions most relevant to high water outlet temperatures and/or high ambient temperatures (Varying values are subject to the ambient temperature)..... 15

Table 2-2: Review of previous correlation approaches to the compressor modelling. 23

Table 2-3: Review of previous approaches to the gas cooler modelling in air-to-water transcritical R744 heat pump cycles. 25

Table 2-4: Average relative error of different Nusselt correlations relative to the experimental values under in-tube cooling conditions of R744 at relatively higher Reynolds number ranges (Harris, 2014). 26

Table 2-5: Review of previous approaches to the evaporator modelling (in sequence of ascending date). 28

Table 4-1: Required inputs for compressor model. 55

Table 4-2: Coefficient values of the compressor characteristic equations. 56

Table 4-3: Required inputs for tube-in-tube gas cooler model: Heat exchanger properties. 57

Table 4-4: Required inputs for gas cooler model: Boundary conditions of fluids. 58

Table 4-5: Required inputs for evaporator model: Heat exchanger properties. 64

Table 4-6: Required inputs for evaporator model: Boundary conditions of fluids. 64

Table 5-1: Generated operating conditions for the compressor model verification. 71

Table 5-2: Physical heat exchanger inputs for the gas cooler model verification and validation. Adapted from Harris (2014). 73

Table 5-3: Operating conditions for the gas cooler model verification and validation (Harris, 2014). 74

Table 5-4: Physical heat exchanger inputs for the evaporator model verification and validation, adapted from Strydom (2013)..... 77

Table 5-5: Operating conditions for the evaporator model verification. 77

Table 5-6: Expansion valve pressure ratios recorded by Strydom (2013) and simulated mean two-phase heat flux for the considered evaporator conditions. 82

Table 5-7: Summary of evaporator model verification and validation results (differences). 86

Table 5-8: Verification check of simulated pressure drops at condition one of the gas cooler and evaporator, respectively. 87

Table 6-1: Design conditions (worst possible combination) according to which the heat pump system is sized. 90

Table 6-2: Resulting design outputs of the heat pump system. 97

Table 7-1: Standard operating conditions (standard simulation inputs) at which the system performance is to be evaluated (per condition of interest). 100

Table 7-2: Summary of the resulting ODP range and best-recorded COP at a 90°C water outlet temperature and 25-40°C ambient temperature range..... 105

Table 7-3: COP_H summary at coinciding WB ambient temperature ranges of the three considered sources. 108

Table 7-4: Parametric summary of the cycle performance when heating water to 90°C over an ambient temperature range of 25-40°C. 114

Table 7-5: Summary of change in evaporation temperature approach for higher ambient relative humidity values at an ambient temperature of 40°C and water outlet temperature of 90°C. 116

LIST OF FIGURES

Figure 2-1: An early transcritical R744 heat pump cycle alongside its accompanying T-s diagram (Neksa, *et al.,* 1998). 7

Figure 2-2: Effect of discharge pressure on the heating COP at 25°C ambient temperatures over a range of water outlet temperatures (Wang, *et al.,* 2013a). 8

Figure 2-3: P-h plot of R744 with an increase in R744 discharge pressure 9

Figure 2-4: Effect of water inlet temperature on the cycle COP_H at two respective water mass flow rates (Lin, *et al*., 2013) 10

Figure 2-5: Influence of ambient temperature on (a) heating COP and (b) ODP over a range of water outlet temperatures (Wang *et al.* 2013a) 11

Figure 2-6: Effect of ambient temperature on evaporating temperature when heating water to 60°C (Wang, *et al.,* 2013a). 13

Figure 2-7: Recorded pressure values of an air-to-water transcritical R744 heat pump as a function of ambient temperature (Yamaguchi, *et al*., 2011). 13

Figure 2-8: Influence of ambient temperatures on the system heat transfer rates and power consumption (Yamaguchi, *et al*., 2011). 16

Figure 3-1: Schematic illustration of a finite control volume (Rousseau, 2013). 34

Figure 4-1: Schematic illustration of the air-to-water R744 transcritical heat pump cycle, adapted from (Lin, *et al.,* 2013). 52

Figure 4-2: Typical transcritical R744 heat pump T-s diagram, adapted from (Uren, *et al.,* 2020). 53

Figure 4-3: Tube-in-tube gas cooler model overview (Kim, *et al.,* 2005). 57

Figure 4-4: Schematic of the gas cooler's simulation model. 59

Figure 4-5: Schematic frontal view of a typical finned-tube evaporator with omitted fins, adapted from Strydom (2013). 61

Figure 4-6: Schematic view of a single evaporator coil circuit with attention to the inlet, outlet and tube path (Strydom, 2013). 61

Figure 4-7: Two-dimensional overview of the single evaporator coil circuit with discretised sections. Adapted from Strydom (2013). 62

Figure 4-8: Detailed schematic of an evaporator circuit increment. Adapted from Ding *et al.* (2011). 62

Figure 4-9: Schematic of the interconnection between incremental air properties (Strydom, 2013). 63

Figure 4-10: Schematic of the evaporator's simulation model. 67

Figure 5-1: Comparison of the compressor simulation and Bitzer-software results: a) Mass flow rate, b) Temperature difference, and c) Compressor work rate. 72

Figure 5-2: Results comparison of the gas cooler simulation, Flownex simulation, and Harris (2014) experimental data: a) R744 temperature difference, b) Water temperature difference, and c) Gas cooler heat transfer rate. 75

Figure 5-3: Heat transfer rate comparison of the evaporator model simulation, EVAP-COND simulation, and Strydom (2013) experimental data. 78

Figure 5-4: R744 temperature comparison of the evaporator model simulation, EVAP-COND simulation, and Strydom (2013) experimental data. 79

Figure 5-5: Airside comparison of the evaporator model simulation, EVAP-COND simulation, and Strydom (2013) experimental data: a) Air outlet temperature, b) Sensible heat transfer rate, c) Latent heat transfer rate..... 83

Figure 5-6: Comparison of the total overall (a) and latent (b) heat transfer rates for the three increased RH conditions. 85

Figure 6-1: Most applicable compressor identified at the design condition (Bitzer, 2022). 91

Figure 6-2: Compressor options at the design conditions over a range of discharge pressures: a) Mass flow rate, and b) Discharge temperature. 92

Figure 6-3: Cycle parameters at the design conditions over the discharge pressure range: a) Gas cooler length, b) Gas cooler overall heat transfer coefficient (average), c) Evaporator length, d) Power consumption and cooling capacity, e) Cycle COP_H, f) Heat exchanger pressure drops. 94

Figure 6-4: Resulting cycle T-s diagrams at the design conditions over the range of R744 discharge pressures. 95

Figure 7-1: Resulting water outlet temperatures at fixed water mass flow rates over a range of ambient temperatures. 101

Figure 7-2: Resulting cycle COP_H at fixed water mass flow rates over a range of ambient temperatures. 101

Figure 7-3: Cycle COP_H at a 90°C water discharge temperature resulting under various ambient temperatures over a range of discharge pressures. 104

Figure 7-4: Exponential forecast of Wang et al. (2013)'s cycle COP at 90°C water outlet temperature. 106

Figure 7-5: System COP_H comparison for operating at a 90°C water outlet temperature over a wide WB ambient temperature range. *Approximation used (as explained at the start of this sub-section). 107

Figure 7-6: Heat and power transfer at a 90°C water discharge temperature resulting at various ambient temperatures over a range of discharge pressures: Heating capacity, cooling capacity, and power consumption. 109

Figure 7-7: Resulting T-s diagrams at the minimum and maximum R744 discharge pressures at a 40°C ambient temperature. 110

Figure 7-8: Resulting R744 mass flow rates at a 90°C water discharge temperature resulting at various ambient temperatures over a range of discharge pressures. 111

Figure 7-9: Resulting P-h diagram at the minimum and maximum ambient temperatures at a 14 MPa R744 discharge pressure. 113

Figure 7-10: Resulting cycle parameters at a 90°C water discharge temperature, 40°C ambient temperature, and range of air relative humidity with the constant 8°C evaporation temperature approach used: a) R744 Discharge temperature, b) Cycle heating COP, and c) Heating capacity. 116

Figure 7-11: Resulting cycle parameters at a 90°C water discharge temperature, 40°C ambient temperature, and range of air relative humidity adapted to a fixed evaporation temperature of 16.4°C: a) R744 Discharge temperature, b) Cycle heating COP, c) Heating capacity, and d) Power consumption. 117

Figure 7-12: Resulting cycle parameters at a 90°C water discharge temperature over a range of water inlet temperature: a) COP_H, b) Power consumption, c) Heating capacity, d) R744 mass flow rate, and e) Water mass flow rate. ... 119

Figure 7-13: Resulting T-s diagrams at the minimum and maximum water inlet temperatures at a 12.0 MPa R744 discharge pressure. 120

1. CHAPTER 1: INTRODUCTION

1.1 Background

In modern times, global warming is a problem faced by countries worldwide, especially industrialising countries. Engineering sectors of heating, ventilation, air conditioning and refrigeration (HVACR) have been forced by legislation to govern the usage of refrigerants in vapour-compression cycles. Worldwide treaties such as the Montreal- and Kyoto protocol have enforced refrigerant regulations on ozone depletion and greenhouse gas emissions (Harris, 2014). The most common indexes used to quantify the environmental harmfulness of a refrigerant are the Ozone Depletion Potential (ODP) and Global Warming Potential (GWP). The former measures the ability of refrigerants to diminish the stratospheric ozone relative to an equal mass of R11 refrigerant, whereas the latter measures the heat-trapping effect of a gas over a fixed period in the atmosphere (usually 100 years), relative to an equal mass of carbon dioxide (Calm & Didion, 1998).

Thus far, extensive research has gone into technology with the potential to improve the environmental friendliness and energy efficiency of the HVACR sector. A recent area where potential has been identified for both these aspects is the application of heat pumps in the industrial industry. In particular, for the heating of water or process fluids to high temperatures (beyond 60°C), which are typically required within this industry (IEA, 2014). According to the World Energy Outlook report of 2021, the industrial sector is accountable for almost 40% of the current global energy consumption (IEA, 2021).

Although heat pumps may be viable for heating fluids in the industrial sector, few refrigerants exist with the ability to do so efficiently as well as an environmental-friendly essence. During the early use of industrial heat pumps in the 1970s and 1980s, the chlorofluorocarbon (CFC) refrigerant R114 was typically applied. This came as a result of its high critical temperature and low pressure, which are beneficial for the application. However, this refrigerant is part of the chlorofluorocarbon (CFC) group, which is among the hydro-chlorofluorocarbons (HCFC) group of synthetic refrigerants, banned today (Wolf, *et al.*, 2012)

The latest generation of synthetic refrigerants developed up to date, namely hydrofluoro-olefins (HFOs), entails both a zero ODP and low GWP rating. The properties of a typical HFO refrigerant, namely R1234ze, are illustrated in Table 1-1 relative to other common refrigerants. The mentioned R1234ze has the theoretical ability to provide heat sink temperatures of 105-125°C, making it applicable for high-temperature industrial applications. Although, this is only possible when the heat sink enters the system at temperatures beyond 60°C (Bamigbetan, *et al.,* 2018).

Moreover, despite the newer generations of synthetic refrigerants that have been developed thus far, history has proven that unforeseen environmental consequences came forward and that the greatest proportion of synthetic refrigerants remains flammable and or toxic. Thus, it can be reasoned that natural refrigerants should be the focus of the future (Bamigbetan, *et al*., 2017).

One such natural refrigerant, namely carbon dioxide (R744), was re-introduced in 1994 as a competitive vapour-compression cycle option when operated as a transcritical cycle, i.e., both sub-critical and supercritical. Unlike conventional heat pump cycles, a gas cooler is incorporated in place of the condenser. This cycle takes advantage of a large temperature glide on the heat sink in the gas cooler, which makes it beneficial for high-temperature heating applications (Bamigbetan, *et al.,* 2017). Ever since its re-introduction, R744 has been proven to be viable for high-temperature heat pump applications by researchers such as Neksa *et al*. (1998) and more. A study conducted by White *et al.* (2002) investigated the potential of R744 to heat water to above-conventional temperatures, i.e., above 65°C. A prototype water-to-water heat pump was constructed, after which experimental results were recorded at water outlet temperatures of up to 90°C. The authors concluded that a relatively small degradation in heating capacity and system efficiency was observed at such temperatures.

Apart from R744's ability to heat water to above-conventional temperatures, it includes many advantages over Freon refrigerants, as is evident in Table 1-1. Notably, R744 has relatively superior eco-friendliness considering its zero ODP and GWP of one. Considering R744's refrigeration capacity, it can also be regarded as a relatively good choice for heat transfer applications. Additionally, R744 is one of a few recognised natural refrigerants that is both non-flammable and non-toxic. However, R744 also has disadvantages such as a) its low critical temperature, which results in less effective heat transfer to ambient conditions lower than its critical temperature, and b) its particularly high operating pressures, which require expensive and specialised components (Kaiser & Van Eldik, 2019). Even so, this natural refrigerant has evolved into the leading refrigerant choice for a multitude of refrigeration and heat pump applications (Cao *et al.,* 2020).

A recent study by Kaiser (2021) investigated the potential of integrating transcritical R744 heat pumps into the South African industrial sector for the heating of water/process fluids with temperature requirements up to 100°C. Hence, the author indicated a potential heat demand of 219.5 PJ, which corresponds to 18.8% of the total industrial energy demand in South Africa. This potential integration will also reduce the environmental impact of coal and electricity, which are the country's primary sources of process heat generation.

Although literature has revealed the system's ability and potential market for R744 heat pumps to supply water in the proximity of 90°C, its performance data is limited under such conditions. This is especially the case when the system is operated at ambient conditions exceeding 25°C – which are typical conditions found in South Africa. It has been found from literature that most studies of R744 heat pumps include water outlet temperatures of roughly 65°C and ambient temperatures ranging from -15°C to 25°C. Only three studies could be identified that reported on the cycle performance at water outlet temperatures of 90°C or higher (Cao, *et al.,* 2020; Yamaguchi, *et al.,* 2011; Ye, *et al.,* 2020). Note that this included air-to-water R744 heat pumps only and that the highest ambient temperature investigated by these studies was that of Yamaguchi *et al*. (2011) at 28°C.

Table 1-1: Basic properties of common natural and Freon refrigerants (Nawaz, *et al.* 2018, Rony, *et al*. 2019).

PROPERTIES	R12 (CFC)	R22 (HCFC)	R134A (HFC)	R1234ZE (HFO)	R744 (NATURAL)	R717 (NATURAL)
ODP	0.9	0.05	0	0	0	0
GWP	8100	1700	1300	4	1	0
FLAMMABILITY	Non	Non	Non	Low	Non	Low
TOXICITY	Non	Non	Non	Low	Non	High
CRITICAL PRESSURE [MPA]	4.06	4.97	4.07	3.63	7.38	112.8
CRITICAL TEMPERATURE [°C]	100.9	96.0	101.1	109.4	31.3	132.3
REFRIGERATION CAPACITY* [KJ/M^3]	2734	4356	2868	2725	22545	4382

** Volumetric refrigeration capacity at 0°C.*

Since 2010, various research on R744 heat pumps has been conducted within the North-West University (NWU). This included the accuracy evaluation and development of heat transfer correlations for the cooling and heating of R744. Furthermore, numerical models of the cycle's compressor and heat exchangers have been established.

The integration of the above-mentioned studies may allow for research to be performed on the cycle as a whole. Sian and Wang (2017) reported that although experimental studies add practicality and useful data to the understanding of transcritical R744 cycles, they require hefty financial and time resources. In contrast, modern and more cost-effective research techniques such as numerical simulations have evolved into a robust alternative to continue investigating this technology.

In summary, considering that a potential market exists for transcritical R744 heat pumps to supply water for industrial processes with temperature requirements below 100°C, an investigation of this technology's performance at South African ambient temperatures may be beneficial to the field of knowledge.

1.2 Problem statement

Despite the ability of transcritical R744 heat pumps to supply water at high temperatures, performance data thereof remains limited to low ambient temperatures. Recent literature indicated the potential of integrating this system in the industrial sector of South Africa, a country known for its typical hot weather conditions. Thus, the need exists to simulate the system's performance when supplying water in the proximity of 90°C at ambient temperatures beyond 25°C (dry-bulb).

1.3 Objectives

The objectives of this study include:

- Research literature on the performance of R744 heat pump systems. Focus on operating conditions that include high water outlet temperatures such as 90°C as well as ambient temperatures exceeding 25°C. Furthermore, review literature available on the typically used component types, methods, and theory previously used to develop numerical models of air-to-water transcritical R744 heat pump cycles. Include previous studies conducted within the NWU regarding the cycle and its components.
- Based on the above findings of literature, develop a detailed numerical model to predict the performance of a transcritical R744 heat pump system. Subsequently, verify and validate the model by comparing simulation results to results available from credible and independent sources.
- Use the developed model to size the system in such way that it will be able to satisfy all intended operating conditions to be simulated. Hence, generate data on the system's performance by simulating the cycle performance at high water outlet and ambient temperatures.

1.4 Research methodology

The study will be introduced by conducting a thorough literature study of the existing performance data of transcritical R744 heat pumps, especially when operating at the desired conditions of this study. In addition, the numerical modelling strategies applied by previous researchers to model such systems will be analysed. These findings will serve as a rationale for the numerical model development and include the component types, correlations, assumptions, and modelling methods.

Based on the findings of the literature review, the relevant theory of a transcritical R744 heat pump cycle and its subcomponents will be reviewed. This includes the conservation laws, compressor theory, heat and mass transfer theory, thermo-physical correlations, as well as heat exchanger analysis as applicable to the respective subcomponents of the cycle.

Subsequently, the theory will be integrated into a systems-computational-fluid-dynamics (SCFD) model. The model will be coded in a simulation software package, namely Engineering Equation Solver (EES). The mentioned simulation software consists of built-in thermodynamic property functions as well as a numerical solver with iterative solving abilities. The model will then be verified by comparing the simulation results of the model to results available from credible and independent sources such as published experimental data and other simulation software.

For the literature study, theory review, and model development, references will often be made to former studies published in the NWU regarding R744 heat pump cycles. These studies will aid as valuable contributions to the current study.

Using the developed model, the system will be concisely designed to allow for the simulation of all intended operating conditions. Hence, results will be thoroughly evaluated by simulating the desired operating conditions.

2. CHAPTER 2: LITERATURE REVIEW

In this chapter, a review follows of previous investigations on transcritical R744 heat pump cycles with focus on the ambient temperature's influence on the system efficiency. For this reason, only air-to-water transcritical R744 heat pump cycles will be considered. The literature study is grouped into the following two sections:

1. Performance of the system: The effect of various operating conditions on the system performance will be discussed with emphasis on the ambient temperature and water outlet temperatures. Literature that covers the cycle performance at conditions closest to the current interest will also be highlighted.
2. Numerical modelling of the cycle: This section will focus on the approaches and correlations used by previous researchers to develop numerical models of the cycle. This includes the modelling on both a systems and component level. Focus will also be placed on the specific component types and configurations previously used. This will serve as a foundation to appropriately select the component types and configurations to be later used in the numerical model of this study.

2.1 Performance of air-to-water transcritical R744 heat pump cycles

Historical studies have been conducted on the performance of air-to-water transcritical R744 heat pump cycles. For background, this section will briefly review one of the earlier studies performed by Neksa *et al.* (1998) on the system. Subsequently, literature regarding the influence of relevant operating conditions will be reviewed. Ultimately, an analysis is carried out of the performance data available at the desired conditions of this study, i.e., water outlet temperatures in the region of 90°C and ambient temperatures beyond 25°C.

Note that where the considered sources included information about the ambient wet-bulb (WB) temperature or moisture content to derive so, the air temperature will be indicated in terms of both dry-bulb (DB) and WB. Where this is not the case, no indication will be given and the air temperatures should be solely interpreted as DB.

2.1.1 Initial investigation conducted on transcritical R744 heat pump cycles

Neksa *et al.* (1998) conducted one of the earliest experimental studies on a transcritical R744 heat pump cycle. Nevertheless, this air-to-water prototype provided a 50 kW heating capacity and heated water from 8°C to 60°C. At an ambient temperature of 5°C and evaporation temperature

of 0°C, the authors recorded a cycle heating coefficient of performance (COP_H) of 4.3. The authors pointed out that for any operating condition, a maximum system efficiency exists at a specific discharge pressure known as the optimal discharge pressure (ODP). In other words, more than one R744 discharge pressure can satisfy the operating condition, yet, at different system efficiencies. At the aforementioned condition, the ODP was found to be roughly 9.3 MPa. The accompanying cycle layout and T-s diagram are portrayed in Figure 2-1.

In addition, Neksa *et al.* (1998) investigated the cycle behaviour when heating water to above-conventional temperatures (above 60°C) by increasing the R744 discharge pressure. Whilst doing so, the evaporation temperature and water inlet temperature were held constant at 0°C and 8°C, respectively. A moderate degradation from 4.3 to 3.6 in COP_H was indicated when the water outlet temperature was raised from 60°C to 80°C. Compared to electrical and gas systems, it was concluded that transcritical R744 heat pumps are effective systems for water heating and provide a further advantage, which is their ability to heat water to higher temperatures such as 90°C without operational difficulties.

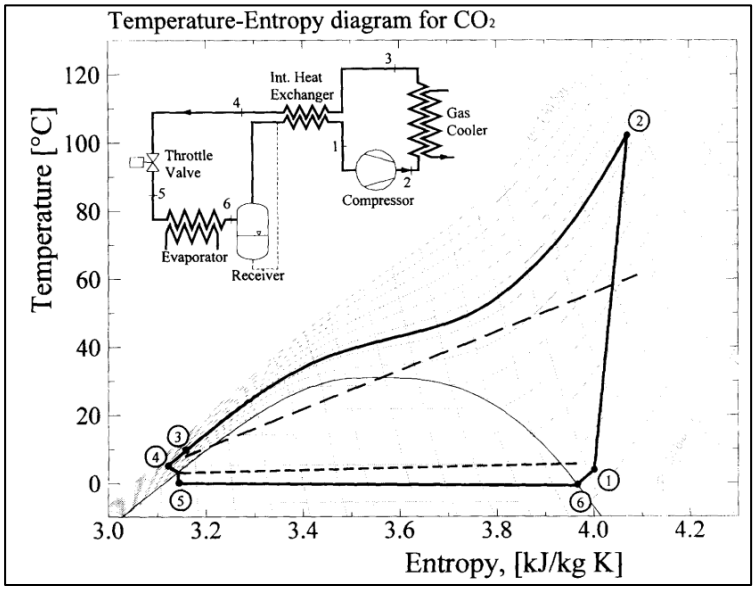

Figure 2-1: An early transcritical R744 heat pump cycle alongside its accompanying T-s diagram (Neksa, *et al.*, 1998).

2.1.2 Influence of operating conditions on cycle performance

The performance of vapour compression cycles is affected by their operating conditions. Literature regarding the main influences of relevant operating parameters on the performance of transcritical R744 heat pumps will now be considered. These parameters include:

- R744 discharge pressure

- Water inlet temperature
- Water outlet temperature
- Ambient temperature and evaporation temperature

2.1.2.1 R744 Discharge Pressure

Wang *et al.* (2013a) analysed the efficiency of the considered cycle subject to the discharge pressure. Figure 2-2 illustrates the recorded cycle COP_H values as a function of the discharge pressure over a range of water outlet temperatures. A higher water outlet temperature was reached when the discharge pressure increased. Analogous to Neksa *et al.* (1998), it was revealed that the discharge pressure has a non-monotonical influence on the cycle efficiency. At the instance of a 25°C DB (20°C WB) ambient temperature and water outlet temperature of 65°C, a 9.8 MPa discharge pressure resulted in a cycle COP_H of 3.8.

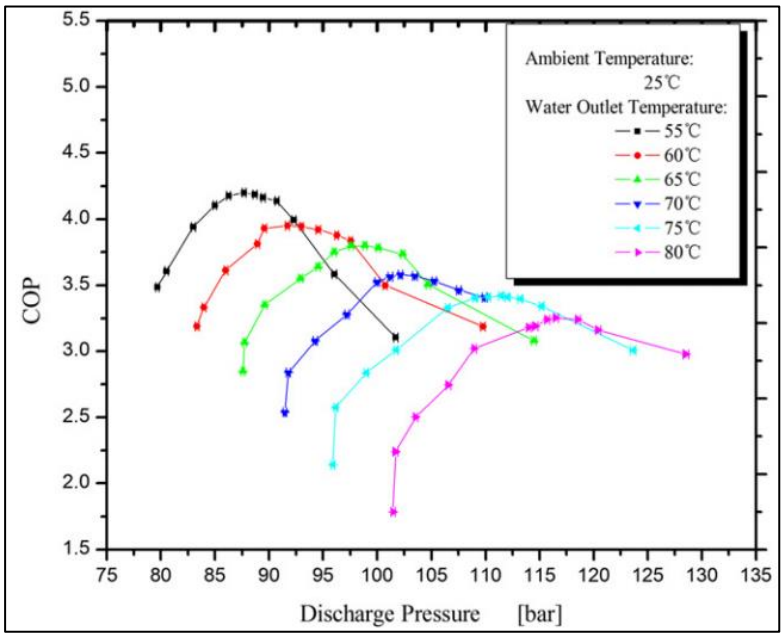

Figure 2-2: Effect of discharge pressure on the heating COP at 25°C ambient temperatures over a range of water outlet temperatures (Wang, *et al.*, 2013a).

Note that the interdependence between the ODP and COP_H may primarily be attributed to the unique thermophysical properties of R744, especially around the pseudocritical region. When considering the P-h plot of R744, as shown in Figure 2-3, it can be seen that the isotherms are relatively flat close to the critical point. As the discharge pressure increases, the R744 gas cooler outlet temperatures and evaporating pressure decrease correspondingly. Therefore, both the heating capacity and required compressor power increase. However, as the supercritical region near the critical region and beyond are reached, the unique thermophysical properties of R744

are enhanced. At this point, the increase in heat capacities for the corresponding decrease in R744 gas cooler outlet temperatures and increase in discharge enthalpy are greater than the increase in required compressor power. Hence, the cycle COP_H increases (Wang, *et al*., 2013a). Yet, with a further increase, the R744 discharge reaches the ODP at which the cycle efficiency realises a maximum value. From Figure 2-2, it can be seen that the ODP is unique for each given water outlet temperature. As the discharge pressure increases beyond this point, the rise in heat capacity for the corresponding decrease in R744 gas cooler outlet temperatures and rise in discharge enthalpy is no longer greater than the increase in required compressor power. Consequently, the cycle's COP_H starts to decrease (Wang, *et al.,* 2013a).

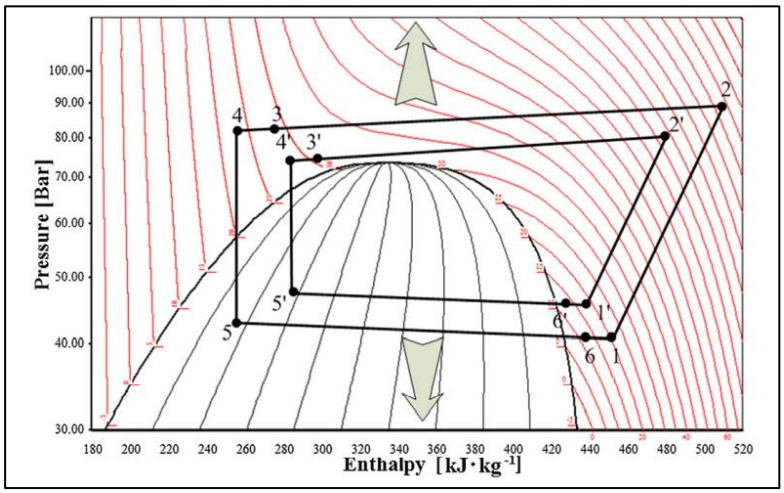

Figure 2-3: P-h plot of R744 with an increase in R744 discharge pressure

Supplementary studies investigating the effect of discharge pressure and ODP on system performance include: (Cao, *et al.,* 2020; Kauf, 1999; Wang, *et al.,* 2012a; Wang, *et al.,* 2013b; Yang, *et al.,* 2016; Yang, *et al.,* 2019).

2.1.2.2 Water inlet temperature

Lin *et al*. (2013) reported that for a constant water mass flow rate, a rise in water inlet temperature leads to a considerable decrease in system COP_H and heating capacity. From Figure 2-4, it can be seen for a water mass flow rate of 0.08 kg/s that the COP_H downgraded from around 3.7 to 3.1 subject to a water inlet temperature increase from 5°C to 30°C. It can also be seen that the greater water mass flow rate of 0.20 kg/s resulted in overall higher cycle efficiency. Nevertheless, subject to an increase in this parameter, the authors further revealed that the R744 discharge pressure

rose, whilst the compressor power slightly increased and the heating capacity decreased. These results were recorded at a 27°C DB (20°C WB) ambient temperature.

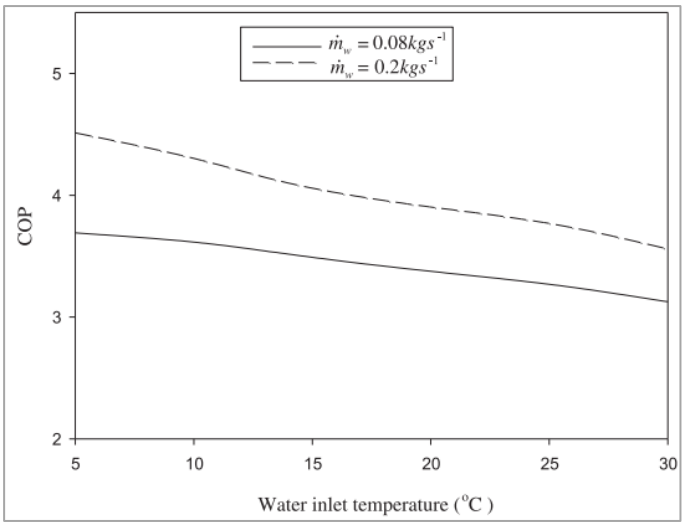

Figure 2-4: Effect of water inlet temperature on the cycle COP_H at two respective water mass flow rates (Lin, *et al*., 2013).

This negative trend in COP_H with an increase in water inlet temperature is similar to the findings of Cao *et al*. (2020), where a decrease in COP_H from 3.0 to 2.2 was realised when the water inlet temperature rose from 10°C to 40°C. Considering that the R744 gas cooler outlet temperature is restricted by the water inlet temperature, it rises accordingly and reduces the enthalpy difference between the R744 inlet and outlet states (this decrease is also intensified by the R744 transcritical nature). As a result, the gas cooler capacity deteriorates (Fronk & Garimella, 2011). This is the principle reason for the change in cycle COP_H (Dai & Qin, 2022). Furthermore, due to the higher R744 gas cooler outlet temperature, to improve the heat transfer temperature difference between the R744 and water, the R744 discharge pressure and thus R744 discharge temperature is increased (Song, *et al.,* 2019). As the R744 discharge pressure rises, the pressure ratio increases. Consequently, the compressor volumetric and isentropic efficiencies degrade and lead to an increase in compressor power consumption (Fronk & Garimella, 2011).

Additional studies investigating the influence of water inlet temperature on system performance include: (Laipradit, *et al*., 2008, Yamaguchi, *et al.*, 2011, Yokoyama, *et al.,* 2007, Wang*, et al.,* 2020, Lin *et al*., 2013).

2.1.2.3 Water outlet temperature

The study by Wang *et al*. (2013a) also investigated the effect of water outlet temperature on the system performance at a fixed water inlet temperature of 12°C. Figure 2-5a portrays the reported

experimental influence of the water outlet temperature on the cycle efficiency and discharge pressure over a range of ambient temperatures. A general downward trend in cycle COP_H was revealed due to a rise in water outlet temperature. At an ambient temperature of 25°C DB (20°C WB), a decrease in cycle COP_H from roughly 4.1 to 3.3 (-19.5%) was recorded as the water outlet temperature rose from 55°C to 80°C (+45.5%).

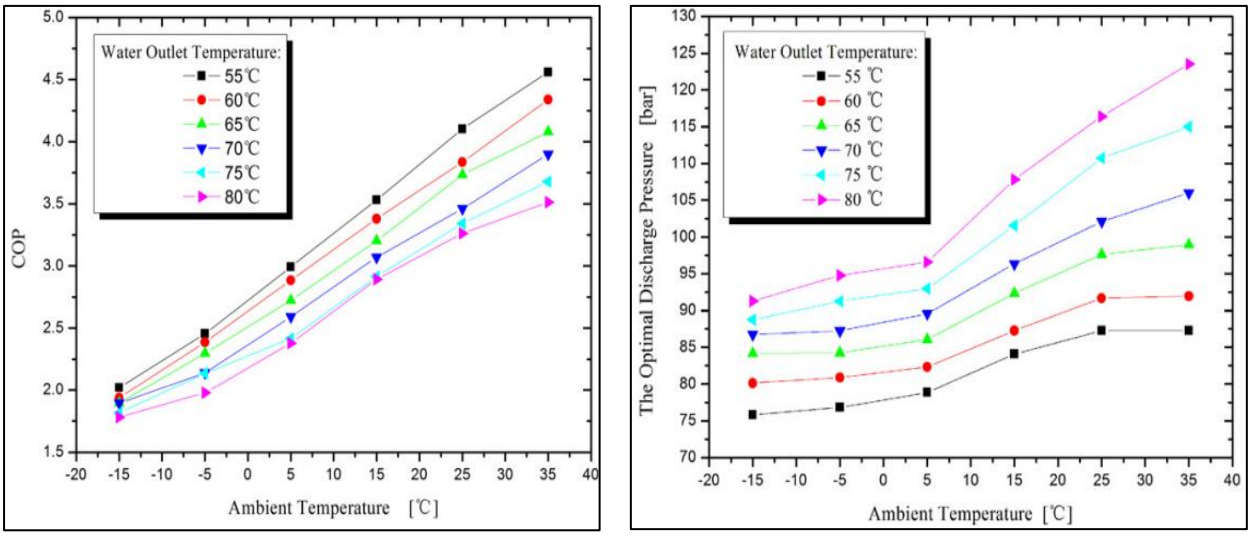

a) COP_H b) ODP

Figure 2-5: Influence of ambient temperature on (a) heating COP and (b) ODP over a range of water outlet temperatures (Wang *et al.* 2013a).

The authors accredited this downgrade in cycle efficiency to the higher R744 discharge pressures that are required to deliver the greater water outlet temperatures. For the same variation in conditions, Figure 2-5b demonstrates that the ODP rose from around 8.8 MPa to 11.7 MPa. As a result of the increased discharge pressures, despite the increase in heating capacity, higher compressor power is required, which leads to the observed degrading in cycle COP_H.

Although literature contains several investigations conducted on air-to-water transcritical R744 heat pump cycles, few could be found that explicitly analysed the cycle performance subject to the water outlet temperature. Nevertheless, similar findings were reported by Neksa *et al*. (1998) and Ye *et al*. (2020).

2.1.2.4 Ambient temperature and evaporation temperature

Saikawa and Koyama (2016) examined the influence of ambient temperature on the cycle COP_H. An improvement from roughly 3.2 to 3.8 was recorded when the ambient temperature rose from 4.6°C to 22.5°C, whilst the heating capacity increased from 4.0 kW to 5.5 kW. The influence of ambient temperature on the system behaviour was also included by Wang *et al.* (2013a). At respective water inlet and outlet temperatures of 12°C and 60°C, the COP_H advanced from 1.9 to

4.3 due to an ambient temperature increase from -15°C to 35°C DB (-16.4°C to 25°C WB), as shown in Figure 2-5a.

Note from Figure 2-5b that the ODP also increased with a rise in ambient temperature. For the same variation in conditions, a rise in ODP from around 8.0 MPa to 9.2 MPa was recorded. The authors stated that for a fixed water inlet and outlet temperature, R744 discharge temperature is the influential factor for the heat transfer that occurs in the gas cooler. Due to the varying thermophysical properties of R744 near the pseudocritical region, the resulting heat transfer in the gas cooler is influenced. With an increase in pressure and temperature, the specific heat and Prandtl number decrease. Since the evaporation temperature rises with ambient temperature, the pressure ratio decreases, which leads to a reduced discharge temperature. Since this affects the heat transfer, a higher temperature difference than that is required in the gas cooler to yield the best heat transfer. As a result, the discharge temperature needs to be increased, which implies a higher ODP (Wang, *et al*., 2013a).

It was further reported by Wang *et al.* (2013a) that the evaporation temperature is a function of the ambient temperature and that the difference between these two variables remains approximately constant within the evaporator. Likewise, Qi *et al.* (2013) also stated that the evaporation temperature is a function of the ambient temperature and that these two variables trend in the same direction. Nevertheless, respective to the amount of literature available subject to the ambient temperature, little information could be found regarding the difference in fluid temperatures within the evaporator. Despite the statement of Qi *et al.* (2013), no numerical data thereof was reported by these authors. The rest of this subsection will focus on literature that could be found on the relationship between these two parameters.

For a water outlet temperature of 60°C, Wang *et al.* (2013a) revealed an approximately linear rise in evaporation temperature due to an increase in ambient temperature, as depicted in Figure 2-6. Over a DB ambient temperature range of 15°C to 35°C DB (11°C to 25°C WB), the evaporation temperature rose from -1°C to 13°C. Over this range, the temperature difference between the WB air temperature and evaporation temperature was approximately 12°C. The authors further stated that in an actual plant, the evaporation temperature is slightly affected by the discharge pressure. As a result, the experimentally recorded evaporation temperatures were implemented into the author's numerical model by use of interpolation functions.

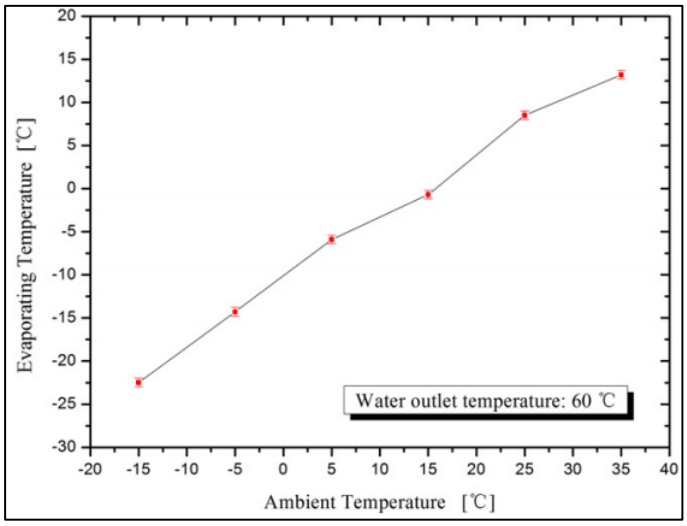

Figure 2-6: Effect of ambient temperature on evaporating temperature when heating water to 60°C (Wang, *et al.*, 2013a).

Yamaguchi *et al*. (2011) reported the compressor suction pressure subject to the ambient temperature, as portrayed by the lower line in Figure 2-7. For the current argument, the pressure loss difference between the suction pressure and evaporation pressure is neglected. From the figure, it can be seen that the evaporation pressure linearly increased from approximately 3.9 MPa (≈4.3°C evaporation temperature) to 5.0 MPa (≈14.3°C evaporation temperature) when the ambient temperature rose from 13°C to 28°C. These results were reported at an inlet water temperature of 20°C. No information on the air's relative humidity (RH) was included.

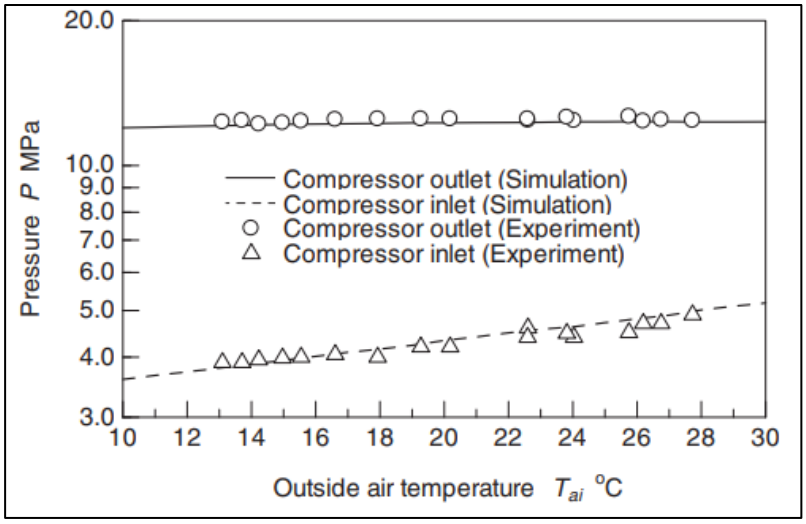

Figure 2-7: Recorded pressure values of an air-to-water transcritical R744 heat pump as a function of ambient temperature (Yamaguchi, *et al*., 2011).

Ye *et al*. (2020) incorporated a constant temperature difference within their numerical model used to investigate the cycle performance subject to a varying ambient temperature and water inlet temperature. Unlike Wang *et al.* (2013a) and Yamaguchi *et al*. (2011), as far as reported, the authors did not have experimental results to verify or calibrate their evaporation temperatures. Nevertheless, an approximation approach of 10°C between the evaporator fluids was used at operating conditions that include ambient temperatures between -10°C and 20°C, water outlet temperatures of 60°C to 90°C, and water inlet temperatures with a range of 15-45°C.

Supplementary studies that involved the individual influence of ambient temperature or evaporation temperature on the system performance include: (Cao, *et al.,* 2020, Laipradit, *et al.,* 2008, Neksa, *et al.,* 1998, Qi, *et al.,* 2013, Wang, *et al*., 2012a, White, *et al*., 2002, Yamaguchi, *et al.,* 2011, Yang, *et al.,* 2016, Wang, *et al.,* 2020, Lin, *et al.,* 2013).

2.1.3 Performance of air-to-water transcritical R744 heat pump cycles at above conventional water outlet temperatures and relatively high ambient temperatures

As mentioned in Chapter 1, limited literature could be found on the cycle performance at conditions including water outlet temperatures in the region of 90°C, as well as ambient temperatures beyond 25°C. Yet, in an attempt to gain an underlying understanding of the cycle performance at these conditions, literature pertaining to operating conditions closest thereto will be evaluated. In this way, a perspective is gained of the typical values and trends that can be expected of the cycle behaviour when operated at the desired conditions of this study. Note that only one of the below studies included information on the WB ambient temperatures (or relative humidity to derive so).

Table 2-1 outlines the cycle behaviour data from four different studies that involved operating conditions closest to the desired values of the current investigation. These correspond to the three air-to-water R744 heat pump studies that entail water outlet temperatures of 90°C, as were also pointed out in Chapter 1. As will be justified below, the study of Wang et al. (2013a) is also included. Note that the values reported in the table are subject to the indicated ambient temperature. Also, only the most relevant data of the respective studies are listed in the table. In other words, only data relating to the highest recorded ambient temperature and water outlet temperatures.

From the table, it is seen that despite Wang *et al.* (2013a) investigating a water outlet temperature as high as 80°C. Over an ambient temperature range of 15 – 35°C DB (11 – 25°C WB), the authors reported an improvement in system COP_H from 2.85 to 3.50, whilst the accompanying

ODP increased from 11.7 MPa to 12.3 MPa. These results were recorded at a water inlet temperature of 12°C and are also shown in Figure 2-5.

Table 2-1: Review of previously reported cycle performance at operating conditions most relevant to high water outlet temperatures and/or high ambient temperatures (Varying values are subject to the ambient temperature).

STUDY / PARAMETER	Wang *et al.* (2013A)	Yamaguchi *et al.* (2011)	Ye *et al.* (2020)	Cao *et al.* (2020)
Water outlet temperature [°C]	80	90	90	90
Ambient temperature [°C]	25 – 35 DB / 11 – 25 WB	13 – 28*	(-10) – 20*	2*
Evaporation temperature [°C]	Unspecified	4.3 – 14.3	(-20) - 10	Unspecified
ODP [MPa]	11.7 – 12.3	± 12.5	10.2 – 12.7	11.89
Water inlet temperature [°C]	12	20	15	10
COP_H [-]	2.85 – 3.50	3.2 – 3.6	Unspecified	2.75
Heating capacity [kW]	Unspecified	22 – 27	Unspecified	55.8
Compressor power [kW]	Unspecified	6.5 – 5.5	Unspecified	20.3
R744 mass flow rate [kg/s]	Unspecified	0.085 - 0.128	Unspecified	Unspecified
Water mass flow rate [kg/s]	Unspecified	0.075 – 0.092	Unspecified	0.167

*No information of the WB temperature was included (or of the air humidity to derive so).

Of all the studies listed in the table, Yamaguchi *et al.* (2011) included the most cycle performance data subject to their investigated ambient temperature. As mentioned before, this is also the study with the highest reported ambient temperature for an outlet water temperature of 90°C. At a water inlet temperature of 20°C, an improvement in cycle COP_H from 3.2 to 3.6 was experienced as the ambient temperature rose from 13°C to 28°C. As portrayed in Figure 2-7, the ODP remained fairly constant at around 12.5 MPa, whilst the evaporation temperature increased from around 4.3°C to 14.3°C (as earlier derived from the suction pressure). The authors did not justify the unchanged ODP. The recorded R744 mass flow rate increased from 0.085 kg/s to 0.128 kg/s, compared to the less significant water mass flow rate that rose from 0.075 kg/s to 0.092 kg/s. Moreover, Figure 2-8 illustrates that the heating capacity rose from roughly 22 kW to 27 kW, whilst the power consumption decreased from approximately 6.5 kW to 5.5 kW.

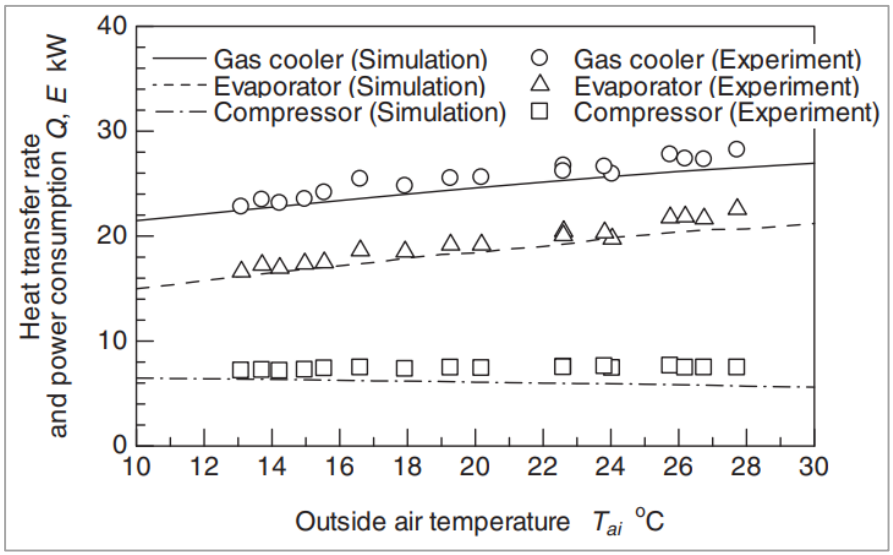

Figure 2-8: Influence of ambient temperatures on the system heat transfer rates and power consumption (Yamaguchi, *et al*., 2011).

Despite for ambient temperatures below 25°C, other studies that also included a water outlet temperature of 90°C are Ye *et al.* (2020) and Cao *et al.* (2020). Over an ambient temperature range of -10°C to 20°C, the former recorded a rise in ODP from 10.2 MPa to 12.7 MPa (+24.5%) at a water inlet temperature of 15°C. The latter only included a single condition at which the ambient and water inlet temperatures were 2°C and 10°C, respectively. In this case, an ODP of 11.98 MPa, COP_H of 2.75, and a water mass flow rate of 0.167 kg/s were recorded. In addition, the heating capacity and power consumption were indicated as 55.8 kW and 20.3 kW, respectively.

Aside from the effect of ambient temperature at such high water temperatures, the influence of an internal heat exchanger (IHX) was also included by Ye *et al.* (2020) and Cao *et al.* (2020). Both studies pointed out that the addition of an IHX reduces the required R744 discharge pressure, which improves the system efficiency. With the addition of an IHX, the former indicated that the above-mentioned ODP range lowered from 10.2-12.7 MPa to 9.6-12.3 MPa. The latter indicated that the ODP reduced from 11.89 MPa to 11.25 MPa, which resulted in a COP_H enhancement from 2.75 to 2.91 (+5.8%). However, note than conditions included by the latter as well as Kim *et al.* (2005) also reported a reduction in heating capacity due to the addition of an IHX due to the higher suction temperature and thus R744 mass flow rate.

Furthermore, the influence of water inlet temperature was additionally considered by Yamaguchi *et al.* (2011) and Ye *et al.* (2020). Similar trends to those in the previous section were reported. At a constant ambient temperature of 16°C, when the water inlet temperature varied from 10°C to 40°C, the former indicated that the cycle COP_H downgraded from roughly 3.5 to 2.6, whilst the

heating capacity decreased from approximately 24.5 kW to 21.0 kW. Also, the R744 mass flow rate marginally rose from around 0.091 kg/s to 0.096 kg/s, whilst the compressor power consumption slightly rose from 6.0 kW to 7.0 kW. The latter reported that although the ODP increases due to higher water inlet temperatures, the effect that ambient temperature has on the ODP lessens. At a water inlet temperature of 40°C instead of 10°C, the above-mentioned ODP range of the latter rose from 11.1 MPa to 13.3 MPa (+19.8%), rather than from 10.2 to 12.7 (+24.5%).

Based on the above, an overview of the cycle performance has now been gained at operating conditions closest to the interest of this study. This is especially the case for Wang *et al.* (2013a) and Yamaguchi *et al.* (2011), which will later (Chapter 7) be brought into perspective with the findings of the current study.

2.1.4 Summary

The first part of this literature study considered the historical performance information of air-to-water R744 transcritical heat pumps. The section was introduced by briefly reviewing the early study of Neksa *et al.* (1998), which pointed out that the best cycle efficiency can be achieved by operating the system at its corresponding ODP. Also, the system is capable of heating water to above-conventional temperatures such as 90°C without a severe downgrade in efficiency and operational difficulties.

Subsequently, literature on the effect of various operating conditions on the cycle behaviour was studied. Not all studies indicated whether their reported ambient temperatures are DB or WB and neither included information of the air RH to derive so. Nevertheless, analogous to Neksa *et al.* (1998), it was noted that higher water outlet temperatures can be achieved as a result of increased R744 discharge pressures and moderately downgraded system efficiency. An increase in R744 discharge pressure leads to an improvement in system efficiency up until the ODP is reached, after which a reduction occurs with a further increase in R744 discharge pressure. The relationship between the ODP and maximum cycle efficiency was also described and attributed to the unique transcritical nature of R744. Furthermore, subject to an increase in water inlet temperature, it was reported that the system COP_H and heating capacity heavily decreases, whilst the compressor power slightly increases. In addition, due to an increase in water mass flow rate, an improvement in the cycle efficiency was indicated. The influence of ambient and evaporation temperatures was also considered. It was reported that the latter is a relatively linear function of the former and that the concurrent increase of these two parameters leads to an improvement in

system efficiency. As will be discussed in the second part of this chapter, some researchers used experimental data to relate these two variables, whereas others used an approximation approach.

The final part of this section focussed on system performance literature that involved water outlet temperatures as high as 90°C and/or ambient temperatures exceeding 25°C. Of the considered studies, Yamaguchi *et al.* (2011) and Wang *et al.* (2013a) included operating conditions closest to the interest of this study. The former involved a water outlet temperature of 90°C, yet at ambient temperatures of only up to 28°C, whereas the latter included ambient temperatures of up to 35°C, although, at a maximum water outlet temperature of only 80°C. Furthermore, also at a 90°C water outlet temperature, the influence of water inlet temperature and the addition of an IHX on the cycle behaviour were considered. It was reported than an IHX improves the system efficiency, yet, tends to have a negative impact on the heating capacity. Note that these findings will be brought into perspective in Chapter 7 when evaluating the results of the present investigation.

In conclusion of the first part of the literature review, the performance and underlying influences of an air-sourced transcritical R744 heat pump system have been examined. As a result, perspective has been gained on the aforementioned. The second part of the literature review will specifically focus on the numerical models used by previous researchers to predict the performance of the technology in question.

2.2 Numerical modelling of a transcritical R744 heat pump cycle

In this section, the typically used component types, modelling approaches and correlations used in previous studies will be reviewed. As mentioned at the beginning of this chapter, this will serve as an appropriate guideline for the decisions to be made regarding the aforementioned aspects in the numerical model of this study. Note that the current study focuses only on air-to-water transcritical R744 heat pumps used for water heating. Eight prior studies that entailed the numerical modelling of the cycle have been identified from literature and are listed below:

- Kim *et al.* (2005)
- Laipradit *et al.* (2008)
- Yamaguchi *et al.* (2011)
- Lin *et al.* (2013)
- Wang *et al.* (2013a)
- Sian and Wang (2017)
- Ye *et al*. (2020)
- He *et al.* (2020a)

The models employed in the above-listed studies will be reviewed on a systems modelling level. Thereafter, a detailed review follows of the specific correlations and methods used on a component modelling level.

2.2.1 Systems modelling level

In all eight of the above-listed studies, the following common assumptions or approaches were included in the numerical model:

- The model will be simulated in steady-state only.
- Heat losses to the environment are negligible within the heat exchangers.
- Changes in kinetic and potential energy are negligible (All studies except Yamaguchi *et al.* (2011), which accounted for changes in kinetic energy).
- The connecting pipelines between the cycle components have a negligible pressure drop (All studies except Laipradit *et al.* (2008)).
- The finite volume method is used to evaluate the heat exchangers.
- Apart from heat transfer through convection, conduction through the lateral heat exchanger walls is also accounted for (except Kim *et al.* (2005) and Laipradit *et al.* (2008)).

2.2.1.1 Study by Kim et al. (2005)

The cycle model of Kim et al. (2005) consisted of a semi-hermetic compressor, counterflow tube-in-tube gas cooler and -evaporator, expansion valve, and counterflow tube-in-tube IHX.

The following assumptions or approaches were further reported:

- A finite volume method was used to model the heat exchangers
- For each finite volume, the log mean temperature difference (LMTD) method was used to perform the heat balance calculations.
- A constant degree of superheat (DOS) of 5°C was assumed.

2.2.1.2 Study by Laipradit *et al.* (2008)

The cycle model of Laipradit et al. (2008) consisted of a reciprocating compressor, counterflow tube-in-tube gas cooler, smooth finned-tube evaporator, and expansion valve.

The following assumptions and approaches were further reported:

- The evaporator is divided into three zones, namely superheated R744 with dry air, two-phase R744 boiling with dry air, and two-phase R744 boiling with wet air.
- The enthalpy-based method proposed by Threlkeld (1962) is used to calculate the heat balance in the evaporator. Note that this method accounts for the effect of moist air as well as fin efficiency.
- The heat balance in the gas cooler is calculated with the aid of the effectiveness-NTU method.
- Both frictional pressure loss and acceleration pressure loss are accounted for in the R744's two-phase boiling zone.
- Pressure drops in the connecting pipes are accounted for as determined by the Darcy-Weisbach (1942) equation.

2.2.1.3 Study by Yamaguchi *et al.* (2011)

The cycle model of Yamaguchi *et al*. (2011) consisted of a reciprocating compressor, helically coiled counter-flow tube-in-tube gas cooler, smooth finned-tube evaporator, expansion valve, and counterflow twin-tube IHX.

The following assumptions and approaches were further included:

- Water flow in the gas cooler is assumed to have a flow pattern that is identical to fully developed laminar flow.
- Pressure loss in the gas cooler and IHX's high-pressure side consists of losses caused by friction- and deceleration loss, whilst pressure loss in the evaporator and IHX's low-pressure side consists of the losses caused by friction and momentum.
- Fin efficiency is accounted for in the heat transfer of the evaporator.

2.2.1.4 Study by Lin *et al.* (2013)

The cycle model of Lin *et al.* (2013) consisted of a semi-hermetic compressor, counterflow tube-in-tube gas cooler, smooth finned-tube evaporator, and capillary tube (expansion device).

The following assumptions and approaches were further stated:

- The enthalpy-based method suggested by Threlkeld (1962) is used to calculate the heat balance in the evaporator.
- In the capillary tube pressure drop calculation, both single- and two-phase conditions are accounted for.

2.2.1.5 Study by Wang *et al.* (2013a)

The cycle model of Wang *et al.* (2013a) consisted of a semi-hermetic compressor, helically coiled counter-flow tube-in-tube gas cooler, wavy finned-tube evaporator, expansion valve, and counterflow tube-in-tube IHX.

The following assumptions and approaches were also reported:

- The water flow regime in the gas cooler is assumed to be turbulent flow.
- Threlkeld (1962)'s enthalpy-based method is utilised to calculate the heat balance in the evaporator.
- In the capillary tube pressure drop calculation, both single- and two-phase conditions are accounted for.
- Because there are two rows in the evaporator, at the airside, for every infinitesimal length of the tube, the air outlet parameters of the first row are assumed equal to those at the inlet of the second row.
- On the evaporator's airside, two rows of tubes are encountered where the R744 flows through. For every segment of the tube, the outlet conditions of the first row are substituted as the inlet conditions for the second row.
- The evaporation temperatures are based on experimental data and are incorporated into the model with linear interpolation functions.

2.2.1.6 Study by Sian and Wang (2017)

The cycle model of Sian and Wang (2017) consisted of a semi-hermetic compressor, counter-flow plated gas cooler, smooth finned-tube evaporator, expansion valve, and counter-flow plated IHX.

The following assumptions and approaches were reported within the model of Sian and Wang (2017):

- The enthalpy-based method from Threlkeld (1962) is used to calculate the heat balance in the evaporator.
- The maximum R744 flow rate for the expansion valve is defined as a function of the orifice size as well as the pressure drop over the valve.

2.2.1.7 Study by Ye *et al.* (2020)

The cycle model of Ye *et al.* (2020) consisted of a reciprocating compressor, counter-flow plated gas cooler, wavy finned-tube evaporator, and expansion valve.

The following approaches and assumptions were further pointed out:

- An approximation approach of 10°C is used between the evaporation temperature and ambient temperature.
- The minimum pinch points within the heat exchangers are set to 4°C.
- The finite volume approach is employed to evaluate the heat exchangers.

2.2.1.8 Study by He *et al.* (2020a)

The cycle model of He *et al.* (2020a) consisted of a reciprocating compressor, counter-flow plated gas cooler, wavy finned-tube evaporator, and expansion valve.

The following approaches and assumptions were pointed out in the model of He *et al.* (2020a).

- Homogeneous flow in the two-phase boiling region is assumed.
- Threlkeld (1962)'s enthalpy-based method is used to calculate the evaporator heat balance.
- The finite volume approach is employed to evaluate the heat exchangers.
- The heat transfer in the evaporator is divided between the two-phase R744 region and superheated R744 region.

2.2.2 Detailed modelling level

In this section, a detailed review of the correlations and types of correlations used to model the individual components of the cycle, follows.

2.2.2.1 Modelling of the compressor

A concise overview follows on the compressor modelling of the eight air-to-water transcritical R744 heat pump cycles identified in this literature review. Although the compressor modelling of water-source systems is also relevant, it was decided to limit the investigation to air-to-water systems for conciseness. In addition, a discussion follows on a recently published universal method used to characterise the operation of an R744 compressor.

Table 2-2 lists the different correlational approaches used by the identified studies to evaluate compressor performance. It is clear that the reciprocating type of compressor was used in each of the listed studies. A volumetric, mechanical, and isentropic efficiency was commonly included, opposite to the adiabatic efficiency. Note that all these correlations have been empirically developed, i.e., their polynomials were calibrated by the experimental data of the respective compressors (Wang, *et al.,* 2013a). Except for the compressor correlations of Kim *et al.* (2005) and Laipradit *et al.* (2008) which are computed as a function of both pressure ratio and degree of superheat (DOS), all others are calculated as a function of the pressure ratio only.

Table 2-2: Review of previous correlation approaches to the compressor modelling.

STUDY	COMPRESSOR CONFIGURATION	CORRELATIONS USED			
		Volumetric efficiency	Mechanical efficiency	Isentropic efficiency	Adiabatic efficiency
WANG *ET AL.* (2013A)	Reciprocating	X	X	X	-
SIAN AND WANG (2017)	Reciprocating	X	-	X	-
LIN *ET AL.* (2013)	Reciprocating	X	X	X	-
KIM *ET AL.* (2005)	Reciprocating	X	X	X	-
YAMAGUCHI *ET AL.* (2011)	Reciprocating	X	X	-	X
LAIPRADIT *ET AL.* (2008)	Reciprocating	X	-	X	-
YE ET AL. (2020)	Reciprocating	X	-	X	-

In the recent study by He *et al.* (2020a), a polynomial model was employed to predict the performance of their reciprocating compressor. The mass flow rate and compressor power were directly calculated by the correlation equations as a function of the pressure ratio. Note that the coefficients of the polynomial model were acquired directly from the compressor manufacturer.

Bester (2018) published a novel universal numerical method for developing empirical equations to characterise the performance of a variable speed R744 reciprocating compressor. According to the author, the methodology originated from analytical approaches being too complex and inaccurate, and also from available empirical correlations being non-universal. Moreover, the methodology entails four out of six specific compressor operating parameters to be known for the remaining two parameters to be determined. These six parameters consist of the compressor

operating frequency, refrigerant mass flow rate, suction and discharge temperature, as well as suction and discharge pressure.

Bester (2018) further demonstrated the universal method on a set of experimental data recorded from a relevant reciprocating compressor. In this instance, the two unknown parameters were assigned to the refrigerant mass flow rate and discharge temperature. The developed empirical equations were able to predict the experimental mass flow rate and discharge temperature to within absolute error values of 0.43% and 0.99%, respectively. Furthermore, the author reported that certain statistical decisions were made within the application of the method, which may affect the method's simplicity, accuracy, and applicability to other compressors. A typical example would be to choose the least-squares method instead of the mean value, which may cause the method to be more accurate, yet more complex (Bester, 2018).

Note that the reciprocating compressor utilised by Bester (2018) was also specifically for a transcritical R744 application, and the manufacturer was Bitzer, which is a broadly used compressor producer and industry leader for transcritical R744 applications (Bitzer, 2022, Opalic, *et al.,* 2019).

2.2.2.2 Modelling of the gas cooler

A short overview is given of the correlations used in the gas cooler models of the eight identified studies, followed by a more detailed investigation of the convection heat transfer coefficient (CHTC).

2.2.2.2.1 Gas cooler modelling within air-to-water transcritical R744 heat pump cycles

Table 2-3 lists the various CHTC and pressure drop correlations used in both the R744 and watersides of the gas cooler. Also listed are the gas cooler type and configuration. It can be identified that the tube-in-tube gas cooler, both straight and helical coiled types, are the most popular choices for gas coolers. Note that in all these tube-in-tube gas coolers, a counterflow configuration was used, where the R744 flowed through the inner tube, and the water flowed through the annular tube.

In terms of the reported CHTCs employed on the waterside of the gas coolers, the correlations of Dittus-Boelter (1985) and Gnielinski (1976) were mainly used. Only two of the studies reported waterside friction factors, of which both were the Ito (1959) correlation and intended for helical coiled tube-in-tube gas coolers. Note that the pressure drop was neglected by some of the previous researchers. Where not neglected, for the R744 friction factor, excluding the helical

coiled tube-in-tube gas coolers, the Petrov and Povov (1985) correlation was mainly used. Furthermore, the Dang and Hihara (2004) correlation is noted as the dominant choice of CHTC for R744.

Note that the two predominant friction factor correlations mentioned above, namely Ito (1959) and Petrov and Povov (1985), are modified versions of the Filonenko (1954) friction factor correlation.

Table 2-3: Review of previous approaches to the gas cooler modelling in air-to-water transcritical R744 heat pump cycles.

STUDY	GAS COOLER CONFIGURATION	WATERSIDE CORRELATIONS		SUPERCRITICAL R744-SIDE CORRELATIONS	
		CHTC	Friction factor	CHTC	Friction factor
WANG *ET AL.* (2013A)	Tube-in-tube, counterflow, helical coiled	Dittus-Boelter (1985)	Ito (1959)	Dang and Hihara (2004)	Ito (1959)
YAMAGUCHI *ET AL.* (2011)	Tube-in-tube, counterflow, helical coiled	Not specified	Ito (1959)	Dang and Hihara (2004)	Ito (1959)
LIN *ET AL.* (2013)	Tube-in-tube, counterflow	Gnielinski (1976)	Neglected	Dang and Hihara (2004)	Neglected
KIM *ET AL.* (2005)	Tube-in-tube, counterflow	Gnielinski (1976)	Not specified	Krasnoshchekov *et al.* (1969)	Petrov and Popov (1985)
LAIPRADIT *ET AL.* (2008)	Tube-in-tube, counterflow	Not specified	Not specified	Fang (2001)	Petrov and Popov (1985)
SIAN & WANG (2017)	Brazed-plated	Not specified	Not specified	Martin *et al.* (2010)	Martin *et al.* (2010)
YE ET AL. (2020)	Tube-in-tube, counterflow, helical coiled	Not specified	Not specified	Not specified	Neglected
HE *ET AL.* (2020A)	Brazed-plated	Not specified	Not specified	Dang and Hihara (2004)	Nilpueng and Wongwises (2015)

2.2.2.2.2 Recent studies conducted on the gas cooler correlations of R744

Harris (2014) determined that available Nusselt number correlations that were specifically developed for the in-tube cooling of supercritical R744, are only accurate for fluid conditions with low Reynolds numbers (<300 000) and tubes with smaller diameters (1-7.5 mm). Accordingly, a generic correlation that is applicable to a rather broad range of in-tube supercritical R744, will be delivered. The author investigated these specifically developed Nusselt number correlations for the in-tube cooling of supercritical R744 in a larger 16 mm diameter tube over a broad range of relatively high Reynolds numbers, i.e., 350 000 to 680 000. This range was also described as

representative of a gas cooler being embodied in a full heat pump system. The investigation indicated that the evaluated correlations overpredicted the experimental results with an average relative error between 62% and 458%.

Table 2-4: Average relative error of different Nusselt correlations relative to the experimental values under in-tube cooling conditions of R744 at relatively higher Reynolds number ranges (Harris, 2014).

REYNOLDS NUMBER RANGE	GENERIC CHTC CORRELATIONS		PARTICULARLY DEVELOPED CORRELATIONS FOR SUPERCRITICAL R744 COOLING					
	Dittus & Boelter (1985)	Gnielinski (1976)	Zhao & Jiang (2011)	Son & Park (2006)	Dang & Hihara (2004)	Pitla et al. (2003)	Yoon et al. (2003)	Oh & Son (2010)
350K - 400K	28%	97%	118%	110%	95%	162%	300%	127%
400K - 450K	59%	138%	158%	133%	173%	275%	346%	566%
450K - 500K	24%	42%	56%	46%	75%	139%	139%	1169%
500K - 550K	12%	28%	43%	47%	98%	80%	99%	654%
550K - 600K	11%	24%	44%	56%	37%	63%	91%	554%
600K - 650K	9%	15%	34%	58%	23%	38%	75%	107%
650K - 700K	4%	4%	21%	53%	8%	17%	56%	29%
AVERAGE	**20%**	**45%**	**62%**	**72%**	**73%**	**111%**	**158%**	**458%**

In parallel, Harris (2014) also compared generic Nusselt number correlations such as Dittus & Boelter (1985) and Gnielinski (1976) to the experimental data. As in the case of the above-mentioned particularly developed correlations, an overprediction of the experimental values was recorded. Although, in this case, an average relative error of only 20% and 45% were recorded from the Dittus & Boelter (1985) and Gnielinski (1976) correlations, respectively. Table 2-4 lists the average relative error of each correlation compared to the experimental values over the range of Reynolds numbers. The correlations are sorted from left to right in the sequence of the best-recorded accuracy. The investigation led to the conclusion that the Nusselt number and therefore CHTC of R744 under cooling conditions in larger diameter tubes and relatively higher Reynolds numbers are more accurately predicted by generic correlations. Opposite to the specifically developed Nusselt correlations for R744, the improved accuracy was accredited to the absence of thermo-physical property ratios within the generic correlations (Harris, 2014).

2.2.2.3 Modelling of the expansion device

From reviewing the eight identified studies listed earlier in this section, it was found that seven of the eight studies employed an expansion valve in the modelling of their systems, whereas the other used a capillary tube. It is identified that all the expansion valves were modelled by simply assuming an isenthalpic expansion process, i.e., the fluid enthalpy will remain constant over the

expansion valve (Sian & Wang, 2017). Furthermore, the inlet pressure of the expansion valve was set as the outlet pressure of the gas cooler, and the outlet pressure was set to the inlet pressure of the evaporator. In the study of Laipradit *et al.* (2008), this was also the case, except for including pressure loss in the connection pipes.

The capillary tube reported by Lin *et al.* (2013) was modelled by also assuming an isenthalpic expansion process. The pressure drop over the capillary tube was calculated by accounting for both wall friction and flow acceleration (Agrawal, *et al.,* 2011). A homogeneous two-phase flow approach was used by evaluating the mean two-phase viscosity model proposed by McAdams *et al.* (1942), as well as by evaluating the two-phase friction factor with the Lin *et al.* (1991) correlation.

2.2.2.4 Modelling of the evaporator

A brief overview is given of the correlations used in the evaporator models as reported in the eight identified studies. In addition, a more detailed investigation follows of the correlations and modelling approaches used for R744 evaporator models.

2.2.2.4.1 Evaporator modelling within air-to-water transcritical R744 heat pump systems

Table 2-5 lists the various CHTC and pressure drop correlations used on either side of the evaporator. The correlations on the R744-side include both single-phase and two-phase states. Also listed are the evaporator type and configuration. It can be seen that smooth and wavy finned-tubes are the predominant types, being listed four and three times, respectively. However, the wavy type has been used more frequently in more recent studies. Furthermore, for finned tube evaporators, experimental data of only a wavy-finned type is available to the present author, which can later be used for model validation. Considering these arguments, it is viewed as logical to only consider wavy-finned-tube evaporators further.

On the airside CHTC, it is evident that Li et al. (1997) and Wang et al. (1999) are equally listed in terms of frequency. Even so, Wang *et al.* (1999) involve correlations for both the CHTC and friction factor and can be used for both. It is further seen that the majority of the listed studies neglected the pressure drop, or did not specify whether the pressure drop was considered nor which friction factor was used (if considered).

On the R744-side, it is notable that Gnielinski (1976) is the most used correlation for the single-phase CHTC. From the studies that reported on a correlation used for single-phase friction factor, the correlations of Blasius (1913), Filonenko (1954), and Dang and Hihara (2004) are equally

common. Although, since the Dang and Hihara (2004) correlation is a slightly modified (and more recent) version of the Filonenko (1954) correlation, it can be regarded as the favourable choice of friction factor correlation for the single-phase R744. Similar to the airside, the unspecified or neglection of the pressure drop is commonly seen, which is likely due to its small margin (Mastrullo, *et al*., 2019).

Table 2-5: Review of previous approaches to the evaporator modelling (in sequence of ascending date).

STUDY	EVAPORATOR CONFIGURATION	AIRSIDE CORRELATIONS		SINGLE-PHASE R744 CORRELATIONS		TWO-PHASE R744 CORRELATIONS	
		CHTC	Friction factor	CHTC	Friction factor	CHTC	Friction factor
KIM *ET AL.* (2005)	Tube-in-tube, counterflow	Gnielinski (1976)	Not specified	Gnielinski (1976)	Blasius (1913)	Yoon et al. (2004)	Jung & Radermacher (1989)
LAIPRADIT *ET AL.* (2008)	Finned-tube, smooth fins	Not specified	Not specified	Gnielinski (1976)	Filonenko (1954)	Modified Bennet-Cheng (1980)	Filonenko (1954)
YAMAGUCHI *ET AL.* (2011)	Finned-tube, smooth fins	Seshimo and Fujii (1991)	Seshimo and Fujii (1991)	Dittus-Boelter (1985)	Dang & Hihara (2004)	Cheng et al. (2008a&b)	Cheng et al. (2008a&b)
LIN *ET AL.* (2013)	Finned-tube, smooth fins	Wang et al. (1997)	Neglected	Gnielinski (1976)	Neglected	Hihara and Tanaka (2000)	Neglected
WANG *ET AL.* (2013A)	Finned-tube, wavy fins	Li et al. (1997)	Wang et al. (2000a)	Dittus-Boelter (1985)	Not specified	Cheng et al. (2008a&b)	Cheng et al. (2008a&b)
SIAN & WANG (2017)	Finned-tube, smooth fins	Wang et al. (2000a)	Not specified	Gnielinski (1976)	Not specified	Hihara and Tanaka (2000)	Not specified
YE ET AL. (2020)	Finned-tube, wavy fins	Not specified	Neglected	Not specified	Neglected	Not specified	Neglected
HE *ET AL.* (2020A)	Finned-tube, wavy fins	Wang et al. (1999)	Wang et al. (1999)	Not specified	Not specified	Gungor and Winterton (1986)	Choi et al. (1999)

In terms of the CHTC correlation used for the two-phase state, the correlations of Hihara and Tanaka (2000) and Cheng *et al.* (2008a&b) are equally common. Furthermore, the correlation of Cheng *et al.* (2008a&b) is identified as the mainly used friction factor correlation for the two-phase state of R744.

2.2.2.4.2 Recent studies conducted on the correlations and modelling of an R744 evaporator

A study performed by Strydom (2013) included the development of a numerical model for an R744 finned coil evaporator. Since the present study will also develop such a model to be used in the full heat pump cycle model, the following information as elaborated by the aforementioned publishment is regarded as highly relevant:

c:

- The accuracy of such a thermal-fluid model is highly dependent on the heat transfer and pressure drop correlations. Therefore, with verification and validation, the acceptable margin of deviation should be decided in line with the correlations' accuracies.
- Generic correlations used for R744 flow boiling tend to result in an underprediction of heat transfer and, in contrast, an overprediction of pressure drop. This is due to the unique thermal-fluid characteristics of R744 within its two-phase region. Also, most correlations are developed from experimental data of fluids with lower pressures.
- Correlations specifically developed for either side of the evaporator can only accurately predict data within the operational ranges they were developed from. As mentioned in Section 2.2.2.2, this is also the case for R744 correlations within the gas cooler.
- Per element (as created by the finite volume method), fluid properties are generally determined at the average state, i.e., the mean of the inlet and outlet values. Yet, on account of simulation time and stability, it was argued that the fluid properties should rather be evaluated at the element's inlet, which is also known as an upwind discretisation. As was the case for Strydom (2013), this approach is suitable for adequately sized elements with small variations.

R744-side modelling highlights of Strydom (2013):

- From the eight R744 flow boiling and pressure drop correlations considered, Cheng *et al.* (2008a&b) relatively covers the largest range of operational conditions, i.e. a tube diameter of 0.6 – 10.0mm, mass flux of 50-1500 kg/m^2, heat flux of 1.8 to 46 W/m^2, and saturation temperature ranging from -28°C to 25°C.
- The correlation of Cheng *et al.* (2008a&b) was able to predict 71.4% of their own heat transfer data to within ±30%, and 81.5% of their own pressure drop data to within ±30%. These levels of accuracy were termed as a good agreement.
- As a result, Cheng *et al.* (2008a&b)'s correlation was chosen for the evaporator model's two-phase R744 heat transfer and pressure drop.

- Gnielinski (1976) and Filonenko (1954) correlations were chosen for the single-phase heat transfer and pressure drop, respectively.

Note that even more recently, Mastrullo *et al.* (2019) performed a state-of-the-art review on the heat transfer correlations for R744 flow boiling with and without oil. Of the extensive database of considered correlations, only Fang *et al.* (2017) involved applicable ranges as broad as Cheng *et al.* (2008a&b). Relative to the extensive database considered by the authors, Fang *et al.* (2017) was reported as the most accurate, however, a downside is that its mathematical essence is unsuitable for iterative design purposes (Shah, 2019). Thus, up to date, Cheng *et al.* (2008a&b) is still regarded as the most accurate two-phase R744 correlation to be used in a numerical model for the simulation of broad applications. Even so, this correlation yielded a 51.6% absolute deviation with respect to the extensive database considered by Mastrullo *et al.* (2019).

Airside modelling highlights of Strydom (2013):

- From the five wavy-finned airside heat transfer and friction factor correlations considered, Wang *et al.* (2002a) relatively covers the vastest range of applicable conditions, i.e., a Reynolds number of 300 – 10 000, collar diameter of 7.66 to 16.85 mm, transversal pitch of 21.0 to 38.1 mm, longitudinal pitch of 12.7 to 33.0 mm, fin spacing of 1.21 to 6.43 mm, and also total tube rows from one to six.
- Of the data considered by Wang *et al.* (2002a), their correlation was able to predict 91% of the heat transfer values to within ±15%, and 85% of the pressure drop values to within ±15%. These margins were stated as a good agreement. Moreover, this correlation is a refinement of the Wang *et al.* (1999) correlation (as listed in Table 2-5).
- Accordingly, the Wang *et al.* (2002a) correlation was chosen for the heat transfer and pressure drop.
- The effect of moist air was accounted for. The fin temperatures of finned tube heat exchangers often drop below the dew point of the approaching air, causing dehumidification to take place. In such a case, parallel to the heat transfer, mass transfer also occurs and has a considerable influence on the heat exchanger performance.
- From the reported literature, Pirompugd *et al*. (2007) argued that the common assumption of a 1:1 ratio between moist air's ability to transport heat and mass is incorrect and hence proposed a correlation therefor. Note that this ratio is presented by the Lewis number. Researchers such as Bourbaraa *et al.* (2011) and Wang *et al*. (2000b) have also published similar correlations therefor.

- The nodes and elements model implemented by Oliet *et al*. (2010) accurately simulates the temperature distributions of the evaporator's outer surface. This allows the model to account for surfaces that are both fully and partially wet due to the occurring dehumidification. However, such a model requires hefty computational power and since the heat exchanger will be discretised into smaller elements, the approach of only considering fully wet and dry surface conditions per discretised element is sufficient. This was also the modelling approach used by Potgieter (2013), who developed a similar finned-tube R744 evaporator model.

The evaporator model of Strydom (2013) delivered a sufficient accuracy level since it was able to predict 82% of the experimental data to within ±20%. Moreover, when compared to EVAP-COND, a relevant simulation software package for heat exchangers, 92.6% of the results were predicted to within ±20%.

2.2.3 Summary

The second part of this literature review analysed previous numerical models of the cycle and its subcomponents. A number of eight studies that modelled air-to-water transcritical R744 heat pumps were analysed on a systems and component modelling level. Also considered were recent studies that specifically investigated the accuracy and applicability of R744 heat transfer correlations.

Key assumptions that were pointed out include that the models are simulated in steady-state, the heat exchangers have negligible heat losses to the environment and are modelled using a finite volume method, the connection pipes between the components have a negligible effect on the system performance, and the variations in kinetic and potential energies are insignificant. It was also noted that a moderate part of the considered studies either neglected the heat exchanger pressure drops, or did not specify whether it was accounted for not which correlations were used (if not neglected).

Subject to the compressor, they reciprocating type was undoubtedly reported as the preferred option for transcritical R744 heat pump systems. For this application, Bitzer was pointed out as a well-suited manufacturer choice. The universal method from Bester (2018) that derives a reciprocating compressor's empirical equations was also discussed. For the expansion process, an expansion valve was indicted as the typically used expansion device and in all cases, its expansion process was assumed to be adiabatic. Respective to the evaporator, the assumption of a unity Lewis number was revealed as inaccurate, and the use of a correlation was suggested

to rather define the ratio between the heat and mass transfer of the incoming air. In the case of a discretised evaporator model with an adequate number of elements, the use of an upwind discretisation as well as the assumption of only fully wet/dry surface conditions were indicated as suitable. Furthermore, researchers such as Ye *et al.* (2020) did not have experimental data to base their evaporation temperatures on and made use of an approximation approach between the evaporation temperature and ambient temperature.

Aside from the methods and approaches, the various correlations previously used to model the R744 and secondary-medium sides of the heat exchangers were listed and compared in terms of frequency. Recent studies that evaluated the accuracy and applicability of these correlations were also described. The typically modelled gas cooler was identified as the tube-in-tube type with the R744 and water flowing through the inner and annular tube, respectively. The following correlations were reckoned most applicable for the gas cooler model: Dittus-Boelter (1985) for the R744 CHTC; Dang and Hihara (2004) for the R744 friction factor; and Gnielinski (1976) for the water CHTC.

Subject to the evaporator, the finned-tube type with wavy fins was pointed out as the most appropriate, and the following correlations were deemed most relevant for its modelling: Cheng *et al.* (2008a&b) model for the CHTC and pressure drop of the two-phase R744 region; Gnielinski (1976) and Dang and Hihara (2004) for the CHTC and pressure drop of the superheated R744 zone, respectively; Wang *et al.* (2002a) for the CHTC and friction factor of dry air; and Wang *et al.* (2000a) for the CHTC of wet air.

The author of this study would like to emphasise that the aforementioned R744 CHTCs were chosen not only due to their presence in previous studies, yet, also due to their generic attributes that allow them to be applied over a broad range of operating conditions, unlike the other R744 CHTC correlations reported in literature (Harris, 2014; Strydom, 2013).

2.3 Conclusion

In this chapter, a literature review was carried out on two aspects of the air-to-water transcritical R744 heat pump system. The first part focussed on the historical performance data of the system and a summary thereof can be found in Section 2.1.4. The corresponding findings will be used to set boundary values and inputs for the verification (Chapter 5) and component design (Chapter 6) of the cycle model to be developed in this study. These findings will also be used to compare the results of this study with (Chapter 7). This is especially the case for the findings of Yamaguchi

et al. (2011) and Wang *et al.* (2013a), which included operating conditions closest to that focussed on by this study.

The second part of the literature review considered the typical component types, methods, and correlations used by previous researchers to numerically model the system. A summary hereof is available in Section 2.2.3. Based hereon, the numerical model of this study will be developed. It is concluded that the reciprocating compressor, tube-in-tube gas cooler, expansion valve, and wavy-finned tube evaporator are logical component choices for the present study and will accordingly be used for the rest of this study. Based on the findings particularly relating to the numerical modelling methods and correlations, a theoretical study will be performed in the next chapter that describes the background theory governing the thermophysical behaviour of the system and its subcomponents (Chapter 3). Moreover, the findings specifically relating to the modelling methods and assumptions will later be used to appropriately integrate the compiled theory into a numerical model (Chapter 4).

3. CHAPTER 3: THEORETICAL STUDY

In the previous chapter, literature concerning transcritical R744 heat pump cycle performances, as well as the typical component types and modelling approaches thereof, were discussed. Based on the findings relating to the typical component types and their modelling approaches, this chapter focuses on the required theory to numerically model a transcritical R744 heat pump cycle.

An analysis follows of the conservation equations applied to a control volume (CV), after which it will specifically be applied to the different components of the cycle. Thereafter, a discussion follows on the operational, heat transfer, and correlation theory as relevant to the respective components of the cycle. In the final section of this chapter, the theory relevant to the unified heat pump cycle will be reviewed.

3.1 Conservation laws

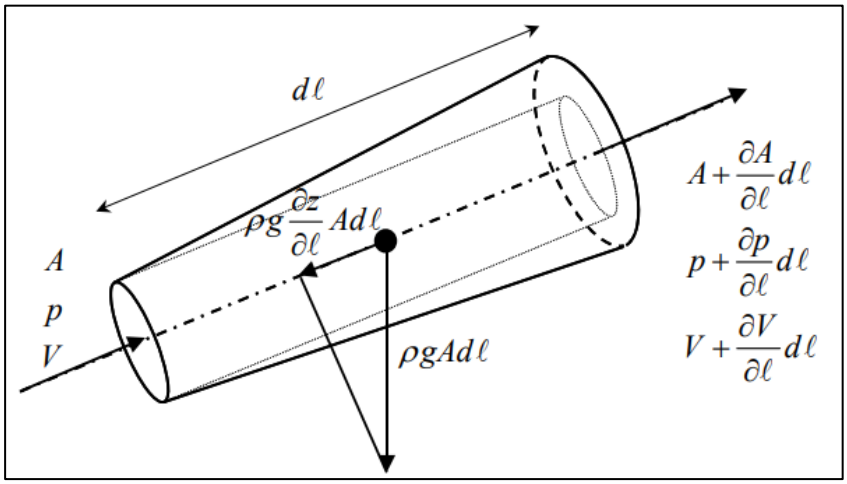

Figure 3-1: Schematic illustration of a finite control volume (Rousseau, 2013).

Conservation laws are known as the conservation of mass, momentum, and energy. These laws serve as foundation for the modelling of all thermal fluid cycles. When applied to a finite control volume (CV), as typically shown in Figure 3-1, the conservation laws outlined by Rousseau (2013). can be defined below. Recall that a CV can be defined as a fictional boundary that encloses a finite volume of physical matter (Cengel & Boles, 2015).

3.1.1 Conservation of mass

When considering a control volume, the conservation of mass law in integral form is given by:

$$\frac{\partial}{\partial t}\left(\iiint \rho d\forall\right) + \oiint \rho \bar{V} \cdot \overline{dA} = 0 \tag{3.1}$$

Where:

- $\forall : Volume\ [m^3]$
- $\rho : Fluid\ density\ [kg/m^3]$
- $V : Fluid\ velocity\ [m/s]$
- $A : Cross\ sectional\ flow\ area\ [m^2]$

The conservation of mass equation applied to a CV can be derived resulting in:

$$\forall \frac{\partial \rho}{\partial t} + \dot{m}_e - \dot{m}_i = 0 \tag{3.2}$$

Where:

- $\dot{m} : Mass\ flow\ [kg/s]$

Note that the subscripts *i* and *e* will be used to denote the inlet and outlet states of a fluid. Where no subscript is specified, the mean state between the inlet and outlet is referred to. For steady-state flow, i.e., $\forall \frac{\partial \rho}{\partial t} = 0$, the conservation of mass equation further simplifies to:

$$\dot{m}_e = \dot{m}_i = \dot{m} \tag{3.3}$$

3.1.2 Conservation of energy

When considering a control volume, the conservation of energy law in integral form is given by:

$$\dot{Q} + \dot{W} = \frac{\partial}{\partial t}\left(\iiint \left(u + \frac{1}{2}V^2 + gz\right)\rho\, d\forall\right) + \oiint \left(h + \frac{1}{2}V^2 + gz\right)\rho \bar{V} \cdot \overline{dA} \tag{3.4}$$

Where:

- $\dot{Q} : Heat\ transfer\ rate\ [W]$
- $\dot{W} : Work\ performed\ [W]$
- $z : Elevation\ [m]$
- $u : Internal\ energy\ [J/kg]$
- $h : Static\ enthalpy\ [J/kg]$
- $g : Gravitational\ constant\ [m/s^2]$

The conservation of energy equation applied to a control volume can be derived to give:

$$\dot{Q} + \dot{W} = \cancel{V}\frac{\partial}{\partial t}(\rho h_0 - p) + \dot{m}_e h_{0e} - \dot{m}_i h_{0i} + \dot{m}_e g z_e + \dot{m}_i g z_i \tag{3.5}$$

Where:

- $h_0 : Total\ enthalpy\ [J/kg]$

Note that the subscript *0* denotes the total stagnation condition of a fluid. However, under the assumption of negligible changes in kinetic energy, the subscript *0* can be omitted for the difference in total enthalpy values. Furthermore, for steady-state flow, i.e., $\cancel{V}\frac{\partial}{\partial t}(\rho h_0 - p) = 0$, and the assumption of negligible elevation differences, i.e., $z_e - z_i = 0$, the conservation of energy equation further simplifies to:

$$\dot{Q} + \dot{W} = \dot{m}_e h_e - \dot{m}_i h_i \tag{3.6}$$

3.1.3 Conservation of momentum

When considering a control volume, the conservation of momentum law in integral form is given by:

$$\oiint \tau \overline{dA} + \iiint \bar{B}\rho d\cancel{V} = \frac{\partial}{\partial t}\left(\iiint \bar{V}\rho d\cancel{V}\right) + \oiint \bar{V}\,(\rho \bar{V} \cdot \overline{dA}) \tag{3.7}$$

Where:

- $B : Body\ forces\ acting\ on\ the\ control\ surface\ [N]$
- $\tau : Shearing\ stress\ [N/m^2]$

When incompressible flow is under consideration, the conservation of momentum equation can be derived to yield:

$$\rho L \frac{\partial V}{\partial t} + (p_{0e} - p_{0i}) + \rho g (z_e - z_i) + \Delta p_{0L} = 0 \tag{3.8}$$

Where:

- $L : Control\ Volume\ Length\ [m]$
- $\Delta p_{0L} : Total\ pressure\ drop\ [m^3]$
- $p_0 : Total\ pressure\ [Pa]$

For steady-state flow, i.e., $V\frac{\partial}{\partial t}(\rho h_0 - p) = 0$, the conservation of momentum equation for incompressible flow can further be simplified to:

$$(p_{0e} - p_{0i}) + \rho g(z_e - z_i) + \Delta p_{0L} = 0 \tag{3.9}$$

When compressible flow is under consideration, the conservation of momentum equation can be derived to:

$$\rho L\frac{\partial V}{\partial t} + \frac{p}{p_0}(p_{0e} - p_{0i}) + \frac{1}{2}\rho V^2\frac{1}{T_0}(T_{0e} - T_{0i}) + \rho g(z_e - z_i) + \Delta p_{0L} = 0 \tag{3.10}$$

Where:

- $T_0 : Total\ temperature\ [K]$

For steady-state flow, i.e., $V\frac{\partial}{\partial t}(\rho h_0 - p) = 0$, the conservation of momentum equation for compressible flow can be simplified to:

$$(p_{0e} - p_{0i}) + \rho g(z_e - z_i) + \Delta p_{0L} = 0 \tag{3.11}$$

Under the assumption of negligible elevation and kinetic differences, Equations (3.9) and (3.11) can further be reduced to:

$$\Delta p_L = p_i - p_e \tag{3.12}$$

Up till this point, the conservation laws applied to a general CV have been discussed. According to the described assumptions, the conservations of mass, energy, and momentum were reduced to their simplest forms and are represented by Equations (3.3), (3.6), and (3.12), respectively. In the subsection to follow, these conservation laws will be applied to the individual components of the heat pump cycle.

3.1.4 Application of conservation laws

When applying the conservation laws as stated in the previous subsections to the individual components of the heat pump cycle, further component-specific assumptions can be made where relevant. This is done to better describe the thermo-physical behaviour of the respective components.

3.1.4.1 Applied to the compressor

In a compression process, mechanical work is added to the fluid. Thus, the temperature and pressure increase. It is generally assumed that this process occurs under isolated conditions with zero heat absorbed or rejected by the fluid (Cengel & Boles, 2015). Accordingly, the conservation of energy stated in Equation (3.6) can further be derived resulting in:

$$\dot{W}_C = \dot{m}(h_e - h_i) \tag{3.13}$$

Where $\dot{W}_C$ represents the total work rate performed by the compressor and is also referred to as the power consumption of the cycle.

Furthermore, the compressor's conservation of mass is represented by Equation (3.3).

3.1.4.2 Applied to the gas cooler

In the gas cooler, heat is rejected by the R744 stream and simultaneously absorbed by the water stream. It is assumed that no work is done onto or by these fluids (Incropera, *et al.,* 2013). As a result, the conservation of energy given by Equation (3.6) can be written as follow:

$$\dot{Q}_H = \dot{m}(h_i - h_e) \tag{3.14}$$

$$\dot{Q}_w = \dot{m}_w\big(h_{e,w} - h_{i,w}\big) = \dot{m}_w c_{p,w}(T_{e,w} - T_{i,w}) \tag{3.15}$$

Where $\dot{Q}_H$ ascribes the rate of heat rejected by the R744 (heating capacity), and $\dot{Q}_w$ the rate of heat absorbed by the water. Identify that the subscript *w* denotes the parameters in terms of the water fluid.

Furthermore, for both fluid streams present in the gas cooler, the conservation of mass and momentum are represented by Equations (3.3) and (3.12), respectively.

3.1.4.3 Applied to the expansion valve

In the expansion process, the fluid is throttled, which results in a local pressure decrease. It is assumed that the expansion process is adiabatic ($\dot{Q} = 0$). Since no work is performed onto or by the fluid during this process, the conservation of energy stated in Equation (3.6) can be simplified to (Yamaguchi *et al.* 2011):

$$h_i = h_e \tag{3.16}$$

In a practical heat pump, the expansion valve opening is adjusted to control parameters such as the pressure drop and refrigerant mass flow rate (Kim, *et al.,* 2005; Sian & Wang, 2017). For simplicity, the mass flow rate and pressure drop are assumed independent of the expansion valve openness. Therefore, the conservation of mass can be given by Equation (3.3).

3.1.4.4 Applied to the evaporator

For fluency purposes of this subsection, the conservation laws applied to the R744 and airside will be discussed independently. This is done due to the added complexity of the moisture entrained in the air.

3.1.4.4.1 Refrigerant side

Analogous to the gas cooler R744-side, the conservation of energy given by Equation (3.6) is written without the work rate term. Yet, in this case, heat is added to the R744. The energy conservation is therefore given by:

$$\dot{Q}_L = \dot{m}(h_e - h_i) \tag{3.17}$$

Where $\dot{Q}_L$ represents the total evaporator heat transfer rate (cooling capacity). Also, similar to the gas cooler R744-side, the conservation of mass and momentum is represented by Equations (3.3) and (3.12), respectively.

3.1.4.4.2 Airside

On the airside of the evaporator, a distinction is made between dry-surface and wet-surface conditions on the evaporator fins. Wet surfaces occur when the fin temperature drops below the dew point temperature of the inflowing moist air. Note that dry and wet surface conditions will be discussed in more detail in Section 4.3.4.

The conservation of mass for dry conditions is represented by Equation (3.3). Nonetheless, moist air contains both air and water, which brings both fluids into consideration with the conservation of mass for wet conditions. Note that water is present in two forms, namely the vapour entrained in the air as well as the condensate film forming on the evaporator surface. The mass conservation of water can be written in integral form as:

$$\frac{\partial}{\partial t}\left(\iiint \rho_w d\forall_w\right) + \oiint \rho_w \bar{V}_w \cdot \overline{dA_w} + \oiint \rho\omega\bar{V} \cdot \overline{dA} = 0 \tag{3.18}$$

In this equation, the first term ascribes the water mass change within the CV. The second term ascribes the net condensate water mass flow rate from the CV, whereas the last term ascribes the net vapour water mass flow rate from the CV. This simplifies to:

$$\dot{m}_{w,e} - \dot{m}_{w,i} + \dot{m}_{a,e}\omega_e - \dot{m}_{a,i}\omega_i = 0 \tag{3.19}$$

Where:

- $\dot{m}_w$: $Condensate\ mass\ flow\ rate\ [kg/s]$
- ω : $Absolute\ humidity\ ratio\ [kg/s]$

Note that the subscripts a and w denote air and water, respectively. Considering the tiny amount of water existent in moist air, as well as the additional complexity it brings to the simulation, the water mass conservation will be neglected. Alternatively, the moist air mass flow rate is assumed identical to that of the dry air and is constant. The effect of the moist air is accounted for by the wet condition correlations, as will be described in Section **Error! Reference source not found.**

The conservation of momentum for the airside can be given by Equation (3.12) and is valid for both dry and wet conditions.

The conservation of energy can be simplified by assuming the moist air as an ideal gas. Therefore, the change in enthalpy of the air can be determined by the difference in DB temperature multiplied by the specific heat capacity (Cengel & Boles, 2015). Also, as in the case of the refrigerant side, zero work is assumed to be performed onto or by the fluid. By considering these two assumptions whilst evaluating Equation (3.6), the following equation results for the conservation of energy under dry conditions:

$$\dot{Q}_{a,s} = \dot{m}_a C_{p,a}\left(T_{a,i} - T_{a,e}\right) \tag{3.20}$$

Where:

- $\dot{Q}_{a,s}$: $Sensible\ heat\ transfer\ rate\ of\ air\ [W]$
- T_a : $Dry-bulb\ temperature\ of\ air\ [°C]$
- $C_{p,a}$: $Specific\ heat\ capacity\ of\ air\ at\ constant\ pressure\ [J/kg.K]$

Under dry conditions, only sensible heat transfer is present. However, for wet conditions, a water condensate film is formed on the evaporator surface and must also be accounted for. The conservation of energy under wet conditions can be written in its integral form:

$$\dot{Q}_{a,wet} + \dot{W} = \frac{\partial}{\partial t}\left(\iiint \left(u_w + \frac{1}{2}V_w^2 + gz_w\right)\rho_w \, d\forall_w\right) + \oiint (h_w + \frac{1}{2}V_w^2 + gz_w)\,\rho_w \bar{V}_w \cdot \overline{dA_w}$$
$$+\frac{\partial}{\partial t}\left(\iiint \left(u_a + \frac{1}{2}V_a^2 + gz_a\right)\rho \, d\forall_a\right) + \oiint (h_a + \frac{1}{2}V_a^2 + gz_a)\,\rho_a \bar{V}_a \cdot \overline{dA_a} \quad (3.21)$$

The first integral term represents the energy change rate ascribed to the condensate film within the CV, whereas the second integral term represents the net energy flow ascribed to the condensate film from the CV. The third integral term represents the energy change rate within the CV, whereas the last integral term represents the net energy flow from the CV. Considering that no work is done onto/by the fluid and that gravitational differences can be neglected, this simplifies the heat transfer under wet conditions to:

$$\dot{Q}_{a,wet} = \dot{m}_{w,i}h_{w,i} - \dot{m}_{w,e}h_{w,e} + \dot{m}_{a,i}h_{a,i} - \dot{m}_{a,e}h_{a,e} \quad (3.22)$$

By rendering the small energy contribution of the condensate film insignificant, the energy conservation further reduces to:

$$\dot{Q}_{a,wet} = \dot{m}_{a,i}h_{a,i} - \dot{m}_{a,e}h_{a,e} \quad (3.23)$$

Note that Equation (3.23) accounts for both sensible- and latent heat transfer of the moist air, and can also be written as:

$$\dot{Q}_{a,wet} = \dot{Q}_{a,s} + \dot{Q}_{a,l} \quad (3.24)$$

With the latent heat transfer rate, $\dot{Q}_{a,l}$, equated by:

$$\dot{Q}_{a,l} = \dot{m}_a h_v(\omega_i - \omega_e) \quad (3.25)$$

Where h_v represents the enthalpy of the vapour carried by the air.

3.2 Compressor theory

The theory that defines the numerical model of the compressor other than the conservation laws is the isentropic efficiency and pressure ratio.

The isentropic efficiency describes the degree of energy degradation in steady-flow equipment. For a compressor, the isentropic efficiency is defined as the ratio of isentropic work rate over actual work rate, i.e. (Borgnakke and Sonntag 2014):

$$\eta_C = \frac{\dot{W}_{C,isentropic}}{\dot{W}_C} \tag{3.26}$$

With the isentropic work rate calculated as follow:

$$\dot{W}_{C,isentropic} = \dot{m}(h_{e,s} - h_i) \tag{3.27}$$

Note that the subscript *s* denotes the isentropic state of the fluid. In other words, the state where the outlet entropy is equal to the inlet entropy, considering that the entropy of an isentropic process remains constant.

The pressure ratio (PR) of a compression process is known as the ratio of the discharge pressure over the suction pressure and can be written as (Borgnakke and Sonntag 2014):

$$PR = \frac{P_{dis}}{P_{suc}} \tag{3.28}$$

3.3 Gas cooler theory

In this section, the heat transfer, pressure drop, and accompanying correlations of the R744 and water streams will be discussed. Thereafter, a review will be given on the relevant free flow and surface areas of the gas cooler. In the final subsection, a discussion follows on the approach used to analyse the heat exchanger, as well as on the thermal resistance present in the gas cooler.

Consistent with the studies reviewed in literature, the R744 and water will flow through the inner and annular tubes of the gas cooler, respectively.

3.3.1 Heat transfer

The local CHTC of a fluid is calculated by the following equation (Incropera *et al.* 2013):

$$h_c = Nu\frac{k}{D_H} \tag{3.29}$$

Where:

- k : $Fluid\ thermal\ conductivity\ [W/(m.K)]$
- D_H : $Hydraulic\ diameter\ [m]$
- Nu : $Nusselt\ number\ [-]$

For the R744-side, the Nusselt number is approached as a constant value for laminar flow and is correlated by the generic Dittus-Boelter equation for turbulent flow (Cengel & Boles, 2015):

$$Nu = \begin{cases} 4.36 & (for\ laminar\ flow: Re < 2300) \\ 0.023 Re^{0.8}\,\mathrm{Pr}^{0.3} & (for\ turbulent\ flow: Re > 2300) \end{cases} \quad (3.30)$$

(3.31)

Where:

- Re : $Reynolds\ number$ $[-]$
- Pr : $Prandtl\ number$ $[-]$

The non-dimensional Reynolds and Prandtl numbers are equated by:

$$\mathrm{Re} = \frac{\rho V D_H}{\mu} \quad (3.32)$$

$$\mathrm{Pr} = \frac{\mu c_p}{k} \quad (3.33)$$

With:

- V : $Fluid\ velocity$ $[m/s]$
- μ : $Fluid\ dynamic\ viscosity$ $[Pa.s]$
- k : $Fluid\ thermal\ conductivity$ $[W/m.K]$

The waterside Nusselt number is computed by the Gnielinski (1976) correlation:

$$Nu_w = \frac{\left(\frac{f_{fil}}{8}\right)(Re - 1000)Pr}{1 + 12.7\left(\frac{f_{fil}}{8}\right)^{0.5}(Pr^{\frac{2}{3}} - 1)} \quad (3.34)$$

Where f_{fil} is determined as follows:

$$f_{fil} = [1{,}82\log(Re) - 1.64]^{-2} \quad (3.35)$$

3.3.2 Pressure drop

The effect of dynamic pressure losses is small and therefore neglected. Accounting for only frictional pressure losses, the pressure drop can be calculated with (Incropera *et al.* 2013):

$$\Delta p_{0L} = \frac{\rho V^2}{2}\frac{fL}{D_H} \tag{3.36}$$

Where L and f represent the tube length and friction factor, respectively.

The friction factor for the in-tube cooling of R744 is given by the Dang and Hihara (2004) equation:

$$f_{D\&H} = \left[1{,}82\log\left(Re_f\right) - 1.64\right]^{-2} \tag{3.37}$$

Furthermore, the friction factor for the waterside is determined with the Darcy-Weisbach (1942) friction factor and can be obtained from the moody chart supplied in Appendix C (Cengel & Boles, 2015).

3.3.3 Free flow and surface areas

The hydraulic diameter of the gas cooler can be determined as follow (Incropera *et al.* 2013):

$$D_H = \begin{cases} D_{i,i} & for\ the\ R744\ side\ (inner\ tube) \\ D_{o,i} - D_{i,o} & for\ the\ water\ side\ (annular\ tube) \end{cases} \tag{3.38}$$

(3.39)

Where:

- $D_{i,i}$: $Inner\ tube\ inside\ diameter\ [m]$
- $D_{i,o}$: $Inner\ tube\ outside\ diameter\ [m]$
- $D_{o,i}$: $Annular\ tube\ inside\ diameter\ [m]$

The free flow area of the R744 and water streams are independent of the tube length and can be determined with (Incropera *et al.* 2013):

$$A_{ff,r} = \frac{\pi}{4}{D_{i,i}}^2 \tag{3.40}$$

And

$$A_{ff,w} = \frac{\pi}{4}({D_{o,i}}^2 - {D_{i,o}}^2) \tag{3.41}$$

Unlike the free flow areas, the surface areas of the two fluid streams are dependent on the tube length and can be equated by:

$$A_r = \pi D_{i,i} L \tag{3.42}$$

And

$$A_w = \pi D_{i,o} L \tag{3.43}$$

3.3.4 Heat exchanger analysis and thermal resistance

When analysing the gas cooler, it is assumed that the outside of the heat exchanger is well isolated and that energy losses to the environment can be neglected. Accordingly, the total heat rejected and absorbed by the two individual heat-exchanging fluids in the gas cooler are deemed equal, i.e.:

$$\dot{Q}_H = \dot{Q}_w \tag{3.44}$$

One method of determining the heat transfer rate of two fluids with temperature fluctuations between the inlet and outlets of a heat exchanger is the logarithmic mean temperature difference (LMTD) method. The LMTD method for counterflow is equated as follows (Incropera *et al.* 2013):

$$\dot{Q}_H = UA \cdot LMTD \tag{3.45}$$

with

$$LMTD = \frac{\left(T_{h,i} - T_{c,o}\right) - \left(T_{h,e} - T_{c,i}\right)}{\ln\left(\frac{T_{h,i} - T_{c,o}}{T_{h,e} - T_{c,i}}\right)} \tag{3.46}$$

Where:

- $T_h : Hot\ fluid\ temperature\ [°C]$
- $T_c : Cold\ fluid\ temperature\ [°C]$

In this case, the hot- and cold fluid refers to the R744 and water, respectively.

The overall heat transfer coefficient (UA) for a tube-in-tube heat exchanger (no fins) can be determined by the total thermal resistance between the two fluid streams, i.e. (Incropera *et al.* 2013):

$$\frac{1}{UA} = \frac{1}{h_c A_r} + \frac{R_f}{A_r} + \frac{\ln\left(\frac{D_{i,o}}{D_{i,i}}\right)}{2\pi k_t} + \frac{1}{h_{c,w} A_w} + \frac{R_{f,w}}{A_w} \tag{3.47}$$

Where:

- R_f : $Fouling\ factor\ on\ the\ refrigerant\ side\ [m^2s/W]$
- $R_{f,w}$: $Fouling\ factor\ on\ the\ water\ side\ [m^2s/W]$
- k_t : $Tube\ conductivity\ [W/(m.K)]$

3.4 Evaporator theory

Similar to the gas cooler theory section, the heat transfer, pressure drop, and accompanying correlations relevant to the evaporator will be discussed. Yet, to aid with the fluency of this section, the theory will individually be discussed for the R744 and airside. Hence, the geometrical parameters and thermal resistance of the evaporator are evaluated, as well as the approach used to analyse the heat exchanger.

Note that for conciseness and fluency purposes of this section, the numerical correlations will only be referred to, with an outline of their fully defined equations available in Appendix C.

3.4.1 Refrigerant side

In the evaporator, the R744 is present as both a two-phase mixture and superheated vapour. Therefore, the CHTC- and pressure drop correlations are analysed independently for single-phase and two-phase conditions.

3.4.1.1 Heat transfer and pressure drop

Note that the R744 heat transfer rate, $\dot{Q}_L$, given in Equation (3.17) can also be calculated respective to the thermal resistance present between the bulk of the R744 stream and the inner tube wall of the evaporator, i.e.:

$$\dot{Q}_L = h_r A_r (T_{t,i} - T_{r,avg}) \tag{3.48}$$

Where:

- h_r : $R744\ convection\ heat\ transfer\ coefficient\ [W/m^2.K]$
- A_r : $Tube\ wall\ inner\ surface\ area\ [m^2]$
- $T_{t,i}$: $Tube\ wall\ inside\ temperature\ [°C]$

3.4.1.1.1 Two-phase region

For two-phase R744 under flow boiling conditions, the set of correlations developed by Cheng *et al.* (2008a&b) is adopted to evaluate both the CHTC and pressure drop. This set of correlations

is based on an empirical study where eight discrete flow patterns were identified. The boundaries where the transition between these flow patterns occurs are defined in terms of critical quality and mass flux values.

As time progressed, various researchers such as Wang *et al.* (2012b) and Wang *et al.* (2013a) have concluded that only four of the eight flow patterns' mass flux values are typically encountered in industrial R744 finned coil evaporators. Therefore, only the following four flow patterns will be applied:

- Intermittent
- Annular
- Dryout
- Mist

The fully outlined set of equations that define the CHTC (h_r from Equation 3.48) and pressure drop (Δp_L from Equation 3.12) for the correlation set of Cheng *et al.* (2008a&b) is outlined by Equations (C.1 – C.38).

3.4.1.1.2 Superheated region

For superheated R744 under heating conditions, the Nusselt number, Nu_{SH}, is approximated by the Gnielinski (1976) correlation given by Equation (3.34). Subsequently, the CHTC for single-phase conditions can be calculated by substituting Nu_{SH} and D_i into Equation (3.29).

Furthermore, the pressure drop of R744 within the superheated region can be computed by substituting the Dang and Hihara (2004) friction factor supplied by Equation (3.37) into Equation (3.36).

3.4.2 Airside

As reported earlier, both dry and wet surface conditions exist for the airside of the evaporator. The corresponding heat transfer and pressure drop theory for the airside now follows.

3.4.2.1 Heat transfer

The sensible heat transfer, $\dot{Q}_{a,s}$, given in Equation (3.20) can also be calculated with respect to the thermal resistance present between the bulk of the air stream and the outer tube wall of the evaporator. For dry air, this can be equated as follow (Strydom 2013):

$$\dot{Q}_{a,s,dry} = h_{c,dry} A_{a,o} \eta_{o,dry} (T_a - T_{t,o}) \tag{3.49}$$

Where $A_{a,o}$ and $T_{t,o}$ represent the total air surface area and tube wall outer temperature, respectively. The dry air CHTC, $h_{c,dry}$, is adopted by the correlation proposed by Wang *et al.* (2002a), which is outlined by Equations (C.39 – C.46). The overall surface efficiency under dry conditions, $\eta_{o,dry}$, is calculated as follow (Incropera *et al.* 2013):

$$\eta_{dry,o} = 1 - \frac{A_f}{A_{a,o}} (1 - \eta_{dry}) \tag{3.50}$$

Where A_f and η_{dry} represent the fin surface area and single dry fin surface efficiency, respectively. The single dry fin surface efficiency is determined using the Schmidt (1949) approach as defined by Equations (C.48 – C.53).

The sensible heat transfer for wet air, $\dot{Q}_{a,s,wet}$, is calculated likewise to $\dot{Q}_{a,s,dry}$:

$$\dot{Q}_{a,s,wet} = h_{c,wet} A_{a,o} \eta_{o,wet} (T_a - T_{tw,o}) \tag{3.51}$$

In this case, the overall wet surface efficiency, $\eta_{o,wet}$, can be calculated with Equation (3.50) by replacing the single dry fin efficiency, η_{dry}, with the single wet fin efficiency, η_{wet}. The single wet fin efficiency, η_{wet}, is also approximated with the Schmidt (1949) approach and is computed by replacing h_{wet} with h_{dry} in Equation (C.49), and hence that calculated value into Equation (C.48).

Moreover, the wet air CHTC is calculated using the correlation proposed by Kuvannarat *et al.* (2006) as defined by Equation (C.47).

Note that the latent heat transfer, $\dot{Q}_{a,l}$, given in Equation (3.25) can also be determined in terms of the mass resistance present between the bulk of the air stream and the outer tube wall of the evaporator. This is represented by the following equation (Strydom 2013):

$$\dot{Q}_{a,l} = h_m A_{a,o} \eta_{o,wet} (\omega_w - \omega)(h_w - h_v) \tag{3.52}$$

With h_w, the condensate film enthalpy at the tube outer wall temperature ($T_{t,o}$). Moreover, ω_w represents the absolute humidity at the condensate film surface. The mass transfer coefficient, h_m, is correlated as a function of $h_{c,wet}$. This correlation is proposed by Pirompugd *et al.* (2007) and is defined by Equations (C.54 – C.55).

3.4.2.2 Pressure drop

The frictional pressure drop for air is calculated from the equation proposed by Waltrich *et al.* (2010):

$$\Delta P_{0L} = \frac{\dot{m}_a^2}{2\rho_a A_{ff,a}}\left[\left(1-\left(\frac{A_{ff,a}}{A_{frontal}}\right)^2\right)\left(\frac{\rho_{a,i}}{\rho_{a,e}}-1\right)+2f_a\frac{A_{a,o}}{A_{ff,a}}\left(\frac{\rho_{a,i}}{\rho_{a,i}+\rho_{a,e}}\right)\right] \tag{3.53}$$

Where:

- $A_{ff,a}$: $Free\ flow\ area\ of\ air\ [m^2]$
- $A_{frontal}$: $Frontal\ area\ of\ evaporator\ [m^2]$

and f_a, the friction factor, which is adopted from the correlation proposed by Wang *et al.* (2002a) as outlined by Equations (C.56 – C.65).

3.4.3 Free flow and surface areas

The hydraulic diameter of the evaporator can be calculated as follow (Wang *et al.* 2002a):

$$D_H = \begin{cases} D_i & for\ the\ R744\ side\ (inner\ tube) \quad (3.54) \\ \dfrac{4A_{ff,a}W_e}{A_{a,o}} & for\ the\ air\ side\ (finned\ side) \quad (3.55) \end{cases}$$

where W_e is the width of the finned coil.

The surface and free flow area of the R744 stream can be calculated as follow (Kays and London 1998):

$$A_{ff,r} = \frac{\pi}{4}{D_i}^2 \tag{3.56}$$

And

$$A_r = \pi D_i L \tag{3.57}$$

With respect to the air stream, the free flow area can be calculated as (Kays and London 1998):

$$A_{ff,a} = A_{frontal}\sigma \tag{3.58}$$

Where σ represents the ratio of the free flow area over the frontal area. The frontal area can be calculated as follow:

$$A_{frontal} = L_e H_e \tag{3.59}$$

Where L_e and H_e ascribe the length and height of the evaporator, respectively.

Also, for the air stream, the total surface area can be calculated as (Kays and London 1998):

$$A_{a,o} = Vol_e \alpha \tag{3.60}$$

Where α ascribes the ratio of surface area over the volume of the evaporator. Furthermore, the volume of the evaporator can be calculated as follow:

$$Vol_e = L_e W_e H_e \tag{3.61}$$

Note that for an increment, the values of $L_e, W_e,$ and H_e are equal to $L_{inc}, P_l,$ and P_t, respectively. Also, note that the values of α and σ are dependent on the specific finned-tube configuration of the evaporator and will be described in Section 4.3.4.

3.4.4 Heat exchanger analysis

The total heat rejected and absorbed by the moist air and refrigerant in the evaporator is considered equal, i.e. (Incropera *et al.* 2013):

$$\dot{Q}_L = \dot{Q}_a \tag{3.62}$$

The tube wall between the R744 and air stream acts as a common medium for the heat transfer taking place. This heat transfer occurs completely as conduction and can be calculated as:

$$\dot{Q} = \frac{2\pi k_t L}{\ln\left(\frac{D_o}{D_i}\right)}(T_{t,o} - T_{t,i}) \tag{3.63}$$

3.5 Combined heat pump cycle

The theory relevant to the complete cycle will now be briefly discussed (Incropera *et al.* 2013).

The first law of thermodynamics applied to any cycle deems that the net change to a CV's total energy is zero, therefore:

$$\dot{W}_C + \dot{Q}_L - \dot{Q}_H = 0 \tag{3.64}$$

When evaluating the efficiency of a vapour-compression cycle, the following performance parameters become relevant:

$$COP_H = \frac{Q_H}{W_C} \tag{3.65}$$

$$COP_C = \frac{Q_L}{W_C} \tag{3.66}$$

Where:

- COP_H : $Heating\ coefficient\ of\ performance$ $[-]$
- COP_C : $Cooling\ coefficient\ of\ performance$ $[-]$

3.6 Conclusion

In this chapter, the theory that defines the heat pump cycle and its subcomponents were described. This content was based on the findings of the literature review and involved the conservation laws and theory of the compressor, heat transfer, pressure drop and correlations. Furthermore, the free flow and surface areas of the heat exchangers were described, as well as the approach used to analyse the heat exchangers. In the next chapter, the described theory will be integrated into a numerical model of the heat pump cycle.

4. CHAPTER 4: MODEL IMPLEMENTATION

The preceding chapter concentrated on the required theory required to develop the numerical model of the transcritical R744 heat pump cycle. In this chapter, the focus is directed on the integration of this theory into a numerical model. Consistent with the previous chapter, the specific component types and modelling approaches are based on the literature review compiled in Chapter 2.

The present chapter will be introduced with a brief overview of the cycle in question. The focus will then be refined to the development of each component's numerical model. Subsequently, the integration of these component models into an integrated cycle model is explained.

4.1 Cycle overview

A schematic flow diagram of the basic heat pump cycle and it's four sub-components namely the compressor, gas cooler, expansion valve and evaporator, is illustrated in Figure 4-1. The numbering configuration and increments used to discretize the heat exchangers are also shown, which will be elaborated on in the next chapter. In Figure 4-2, a typical transcritical heat pump R744 cycle is depicted on a T-s diagram. These two figures will be used in the succeeding paragraph as visual aids to briefly explain the cycle under examination.

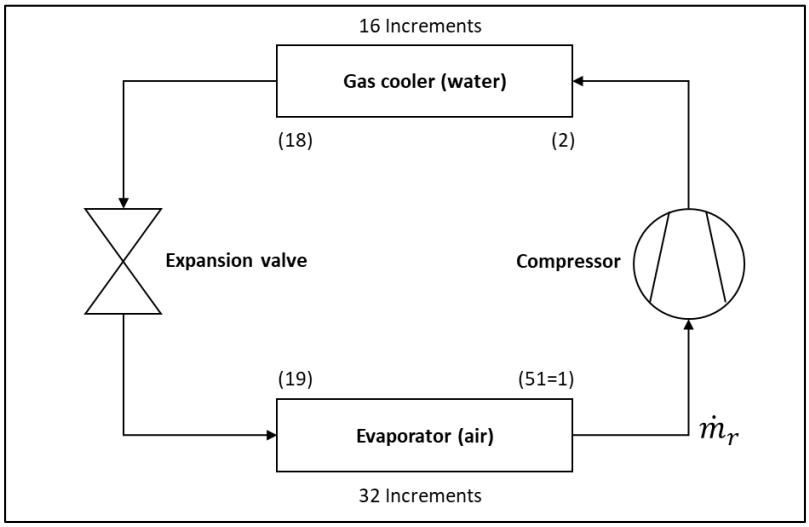

Figure 4-1: Schematic illustration of the air-to-water R744 transcritical heat pump cycle, adapted from (Lin, *et al.*, 2013).

Starting at the denoted cycle point (1) shown in Figure 4-2, R744 at low pressure and superheated vapour state is compressed through a semi-hermetic reciprocating compressor to a higher pressure and temperature – cycle point (2). The R744 exits the compressor in a supercritical

gaseous state and enters the counterflow tube-in-tube gas cooler to be cooled down. Within the gas cooler, the high-temperature R744 is cooled down by rejecting heat to the inflowing cold-water stream – cycle point (18). Simultaneously, the cold water is heated by absorbing the heat from the R744 stream. The exiting R744 from the gas cooler may then be in either a supercritical gaseous or supercritical liquid state. Hence, the R744 is throttled by an expansion valve and consequently experiences a significant pressure and temperature drop – cycle point (19). At this point, the R744 is in a resulting two-phase mixture state and enters the evaporator. Whilst progressing through the finned tube evaporator, the R744 absorbs heat from the inflowing airstream and consequently undergoes heating. The R744 is then heated beyond its saturated gas state into a vapour state – cycle point (51). Simultaneously within the evaporator, the air stream undergoes cooling by rejecting heat to the R744. The superheated R744 then re-enters the compressor to complete the cycle – cycle point (1).

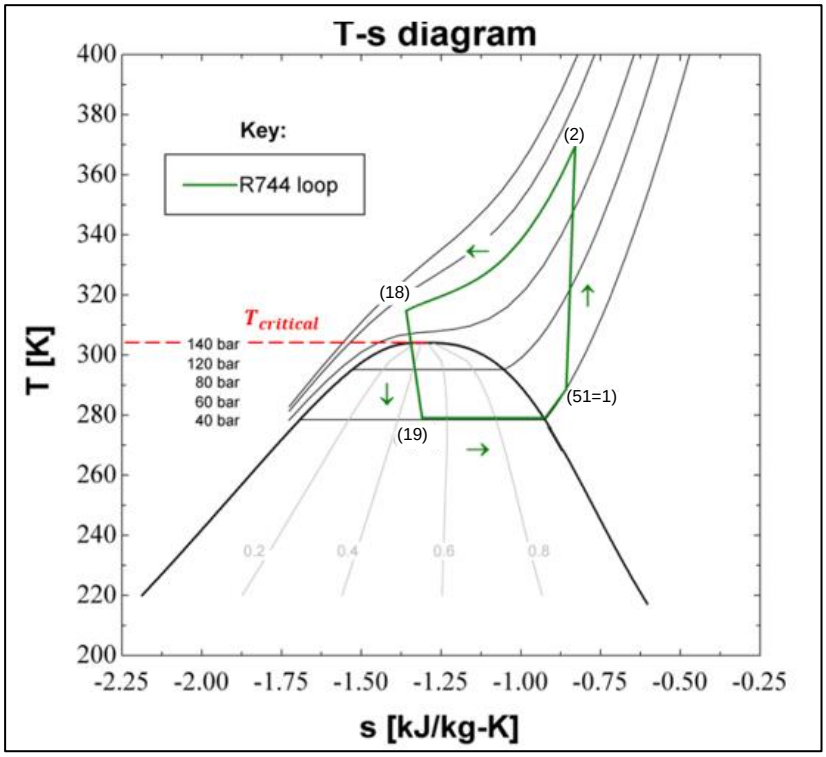

Figure 4-2: Typical transcritical R744 heat pump T-s diagram, adapted from (Uren, *et al.*, 2020).

As highlighted in the literature chapter, the finite volume method is a frequently used method to model heat exchangers. The aforementioned figures also show that the present gas cooler and evaporator will be modelled with 16 and 32 increments, respectively. The rationale of these specific increment quantities follows in Sections 5.2 and 5.3.

Furthermore, as mentioned in literature, an IHX tends to have a negative impact on the heating capacity. Seen that this study focuses on the heating of water, it is decided to exclude an IHX

from the cycle. Also, the simulation software available to the author (more information thereof to follow shortly) has a limited computing capacity and the addition of a third heat exchanger with sufficient increments will worsen the simulation stability and time. As will be stated in Chapter 8, a recommendation for future studies is the use of more powerful simulation software, which will allow the inclusion of more cycle components without the possible compromising of heat exchanger increments and accuracy.

4.2 Overview of the modelling approach

Note that under operational conditions, the cycle's components are interdependent. The implementation of the theory can be divided into two parts, namely:

- Development of a simulation model applicable to each component.
- The integration of the component simulation models to form the integrated simulation of the heat pump cycle.

The former part is used to calculate component-specific parameters, whereas the latter part is used to determine the interdependent behaviour between cycle components. Whenever a cycle with series-connected components is under operation, interdependence is found between cycle components as they interact with and influence their pre- and succeeding cycle components (Incropera, *et al.,* 2013).

The numerical model of this study will be executed on simulation software, namely Engineering Equation Solver (EES). This simulation software is considered applicable due to its built-in thermodynamic and transport property functions as well as its built-in numerical solver, which can perform both simple and iterative calculations (Klein, 2021).

4.3 Component models

In the following sub-sections, the modelling of the heat pump cycle's components will be discussed. When considering inputs for the individual component models, a distinction can be made between fixed and non-fixed inputs. The former mentioned involves heat exchanger geometry and material, whereas the latter mentioned involves boundary conditions of the R744 and secondary fluids, which may vary according to cycle operating conditions and cycle component interdependence.

In the subsections to follow, component-specific assumptions will be stated where relevant. Yet, assumptions that are applicable in general can be summarised as follow:

- All heat transfer-, compression-, and decompression processes occur under steady-state conditions.
- Changes in kinetic- and potential energy are neglected.
- The heat exchangers are well isolated and therefore their associated heat transfer is unaffected by the environment.
- The heat exchangers have constant fluid properties per discretised increment.
- Thermo-physical effects of the non-defined tube paths in the heat exchangers (junctions, return bends, inlet distributor, fin tips, etc.) are neglected.
- Axial conduction within the heat exchangers is assumed insignificant. In other words, thermal conduction alongside the heat exchanger circuit is not considered.

4.3.1 Compressor

As revealed in Section 2.2.2.1, every study considered in the literature review employed reciprocating compressors in their transcritical R744 heat pump cycles. Furthermore, Bitzer was described as an appropriate choice of manufacturer. For the present model, it is thus logical to employ an R744 semi-hermetic reciprocating compressor from Bitzer. As will be justified in Chapter 6, the 4MTE-10K model is specifically regarded as the most suitable option for the present study.

For the present compressor model, the universal method from Bester (2018) is used to develop a set of characterisation equations to predict the R744 discharge temperature, T_2, as well as the R744 mass flow rate, $\dot{m}$. It is assumed that all fluid dynamic property effects are accounted for within the set of characterising equations and that the compressor is operated under a constant frequency of 50 Hz.

Table 4-1: Required inputs for compressor model.

Symbol	Name	Unit
$\boldsymbol{P_1}$ $(\boldsymbol{P_{suc}})$	Suction pressure	$[Pa]$
$\boldsymbol{T_1}$ $(\boldsymbol{T_{suc}})$	Suction temperature	$[°C]$
$\boldsymbol{P_2}$ $(\boldsymbol{P_{dis}})$	Discharge pressure	$[Pa]$

Table 4-1 lists the required inputs of the compressor model, which entails the suction pressure and temperature, as well as the discharge pressure. These inputs are substituted into the set of characterising equations that are given as follows:

$$T_2 = \left[k_{1,1}(P_1) \cdot P_2 + k_{1,0}(P_1)\right] \cdot T_1 + \left[k_{0,1}(P_1) \cdot P_2 + k_{0,0}(P_1)\right] \tag{4.1}$$

$$\dot{m} = \left[k_{1,1}(P_1) \cdot P_2 + k_{1,0}(P_1)\right] \cdot T_1 \; + \left[k_{0,1}(P_1) \cdot P_2 + k_{0,0}(P_1)\right] \tag{4.2}$$

Where the coefficients $k_{m,n}(P_1)$ for $m = 0{,}1$ and $n = 0{,}1$, are functions of P_1. Note that these two similar equations resemble the form of $y = ax + b$. In this view, the subscript m therefore represents a $(if\ m = 0)$ or b $(if\ m = 1)$. Furthermore, a and b also resemble the form of $y = cx + d$ in their respective turns. Similarly, the subscript n represents c $(if\ n = 0)$ or d $(if\ n = 1)$.

These mentioned coefficients are respectively defined for T_2 and $\dot{m}$, as are listed in Table 4-2. Note that the development thereof using Bester (2018)'s method can be found in Appendix D along with the compressor's datasheet (Bitzer, 2022).

Following the implementation of Equations (4.1) and (4.2), the values of T_2 and $\dot{m}$ are known. Since two independent R744 properties are known at cycle points (1) and (2), all other fluid properties can accordingly be determined therefrom. Note that this includes the enthalpy and entropy values, namely $h_1, s_1, h_2,$ and s_2. As a result, the compressor work rate ($\dot{W}_c$), isentropic work rate ($\dot{W}_{c,isentropic}$), as well as isentropic efficiency (η_c), are computed by substituting the calculated outputs into Equations (3.13), (3.27), and (3.26), respectively.

Table 4-2: Coefficient values of the compressor characteristic equations.

Equation	Coefficient	Value
$\boldsymbol{T_2}$	$k_{1,1}(P_1)$	$= (-1.9948e^{-2} \cdot P_1^3) + (3.0424e^{-1} \cdot P_1^2) + (-1.5261e^{0} \cdot P_1) + 2.5922e^{0}$
	$k_{1,0}(P_1)$	$= (2.3950e^{-1} \cdot P_1^3) + (-3.5242e^{0} \cdot P_1^2) + (1.7092e^{1} \cdot P_1) - 2.6687e^{1}$
	$k_{0,1}(P_1)$	$= (1.9083e^{-1} \cdot P_1^3) + (-3.1040e^{0} \cdot P_1^2) + (1.4835e^{1} \cdot P_1) - 1.3189e^{1}$
	$k_{0,0}(P_1)$	$= (-2.7107e^{-0} \cdot P_1^3) + (4.3891e^{1} \cdot P_1^2) + (-2.4061e^{2} \cdot P_1) + 4.2585e^{2}$
$\boldsymbol{\dot{m}}$	$k_{1,1}(P_1)$	$= (5.2808e^{-5} \cdot P_1^3) + (-7.4167e^{-4} \cdot P_1^2) + (3.5035e^{-3} \cdot P_1) - 5.5059e^{-3}$
	$k_{1,0}(P_1)$	$= (-9.1276e^{-4} \cdot P_1^3) + (1.2011e^{-2} \cdot P_1^2) + (-5.3817e^{-2} \cdot P_1) + 7.9997e^{-2}$
	$k_{0,1}(P_1)$	$= (-7.0211e^{-4} \cdot P_1^3) + (9.1382e^{-3} \cdot P_1^2) + (-4.1873e^{-2} \cdot P_1) + 6.0374e^{-2}$
	$k_{0,0}(P_1)$	$= (2.0301e^{-2} \cdot P_1^3) + (-2.4404e^{-1} \cdot P_1^2) + (1.0744e^{0} \cdot P_1) - 1.4629e^{0}$

4.3.2 Gas cooler

In this subsection, an overview of the model and the required inputs is described. Hence, the simulation model and outputs will be discussed with aid of a logic diagram.

4.3.2.1 Model overview and required inputs

A schematic overview of a typical counterflow tube-in-tube heat exchanger is illustrated in Figure 4-3. The R744 flows through the inner tube area, whereas the water flows through the annulus area.

For the modelling of the gas cooler, the finite control volume method is employed. As illustrated in Figure 4-3, the schematic gas cooler is discretised into equal-length sections along the R744 flow direction. These sections will be referred to as increments. Each increment is evaluated as an individual counterflow heat exchanger and the outlet conditions of each increment are considered the inlet conditions of the following increment.

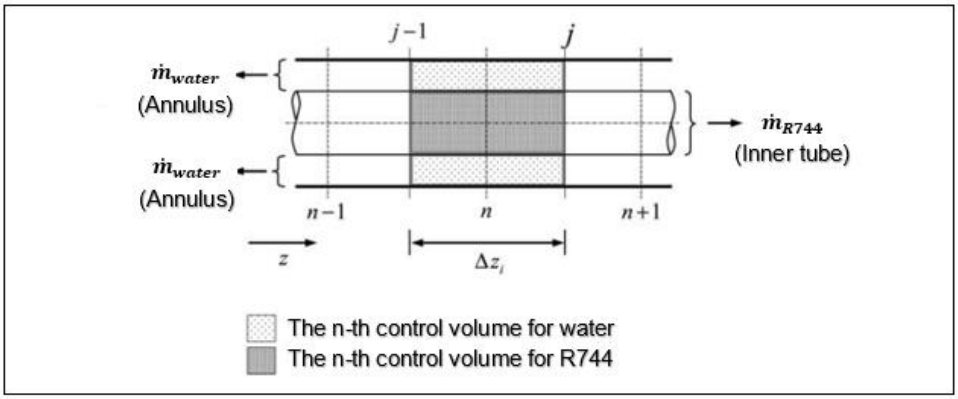

Figure 4-3: Tube-in-tube gas cooler model overview (Kim, *et al.*, 2005).

Table 4-3 groups the fixed inputs required by the gas cooler model, which composes of the physical heat exchanger properties such as the geometry and tube material. Note that the geometry entails the tube diameters, tube length, wall thickness, as well as the number of tubes and increments.

Table 4-3: Required inputs for tube-in-tube gas cooler model: Heat exchanger properties.

Symbol	Name	Unit
$\$GC_{tube}$	Tube material	$[-]$
$N_{t,gc}$	Number of tubes	$[-]$
$D_{i,i}$	Inner tube inside diameter	$[m]$
$D_{i,o}$	Inner tube outside diameter	$[m]$
$D_{o,i}$	Annular tube inside diameter	$[m]$
t_{wall}	Inner tube wall thickness	$[m]$
L_{gc}	Gas cooler tube length	$[-]$
N_{gc}	Number of increments	$[m]$
L_{inc}	Tube length per increment	$[m]$

Table 4-4 lists the variable inputs required by the gas cooler model, which composes of the fluid boundary conditions. From the table, it can be seen that the boundary conditions of both the R744 and water include the input temperature and pressure, as well as the mass flow rate.

Table 4-4: Required inputs for gas cooler model: Boundary conditions of fluids.

Fluid	Symbol	Name	Unit
R744	$\boldsymbol{T_2}$ $(\boldsymbol{T_{r,i}})$	R744 inlet temperature	$[°C]$
	$\boldsymbol{P_2}$ $(\boldsymbol{P_{r,i}})$	R744 inlet pressure	$[Pa]$
	$\boldsymbol{\dot{m}_r}$	R744 mass flow rate	$[kg/s]$
Water	$\boldsymbol{T_{w,i}}$	Water inlet temperature	$[°C]$
	$\boldsymbol{P_{w,i}}$	Water inlet pressure	$[Pa]$
	$\boldsymbol{\dot{m}_w}$	Water mass flow rate	$[kg/s]$

4.3.2.2 Simulation model and outputs

The simulation model employed for the gas cooler model will now be explained with aid of the logic diagram depicted in Figure 4-4. Recognise that the inlet and outlet state of the R744 respectively correspond with points (2) and (18) as denoted in Figure 4-1 and Figure 4-2.

From Figure 4-4, it can be perceived that the parameters listed in Table 4-3 and Table 4-4 are substituted as inputs into the gas cooler model. Pre-calculations are then performed to yield the inlet enthalpies of both R744 and water, which are a function of their corresponding inlet temperature and pressures. The pre-calculations also apply Equations (3.38 - 3.43) to calculate the geometrical parameters such as the hydraulic diameter, free flow area and surface area of the respective fluids.

Thereafter, the incrementing loop is initiated where the outlet properties for each increment are solved iteratively. This entails the initial enthalpy and pressure inputs to be substituted into the first increment, after which respective outlet enthalpy and pressure values are guessed. From this point, the mean incremental enthalpy and pressure values are determined and used to evaluate the incremental fluid properties as a function thereof. Hence, the Nusselt numbers and corresponding CHTCs can be calculated using Equations (3.29 - 3.35). With these values known, the incremental overall thermal resistance is computed with Equations (3.46) and (3.47).

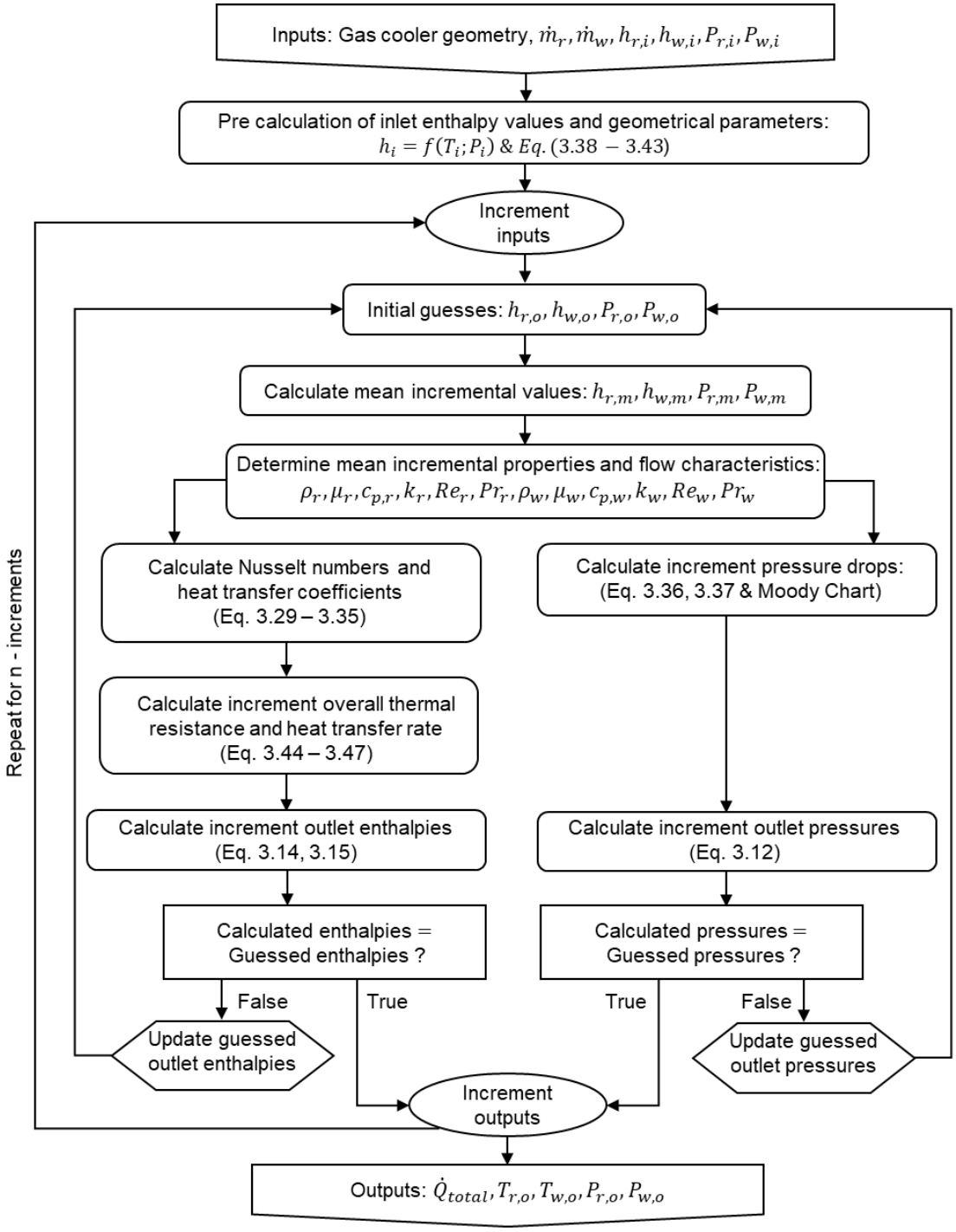

Figure 4-4: Schematic of the gas cooler's simulation model.

Subsequently, the increment's heat transfer rate is determined with Equations (3.44) and (3.45), which allow the respective outlet enthalpies to be calculated. Simultaneously, the increment's pressure drop is calculated with aid of Equation (3.12). This process is repeated iteratively until the guessed outlet enthalpy and pressure values are equal to the calculated outlet enthalpy and pressure values. Since the outlet enthalpy and pressure values of the respective fluids are known at this stage, their outlet temperatures can also be determined.

As indicated in Figure 4-4, this process is repeated for a number of *n* increments. Hence, the outlet temperature and pressure values of the final increment are rendered as the outputs of the gas cooler. Aside from the fluid state outputs, the total heat transfer rate is obtained by summing the heat transfer rates of all the increments.

4.3.3 Expansion valve

As mentioned in Section 3.1.4.3, the expansion process is assumed adiabatic. Also, the mass flow rate and pressure drop are considered independent of the expansion valve openness. For those reasons, the simulation model of the expansion valve can be described as simply setting the inlet enthalpy equal to the outlet enthalpy of the expansion valve. As will be described at the end of this chapter, the effect of connecting pipes between the components is neglected. Thus, the inlet pressure of the expansion valve is set to the outlet pressure of the gas cooler, and the outlet pressure of the expansion valve is designated as the inlet pressure of the evaporator.

4.3.4 Evaporator

The evaporator model will now be described in the following three subsections:

1. Model overview
2. Inputs and assumptions
3. Simulation model and outputs

4.3.4.1 Model overview

A schematic frontal view of a typical finned-tube evaporator to be employed within the heat pump cycle is shown in Figure 4-5. Note that the fins are left out to aid with the visual clarity of the coil circuitry. Also shown are the inlet and outlet of the refrigerant (R744) that flows through the coil circuitry, as well as the inlet and outlet of the air that flows across the coil circuitry. Furthermore, it is notable that the incoming refrigerant splits into several parallel (and identical) circuits before re-joining to exit at the indicated outlet.

When assuming that the incoming refrigerant mass flow rate is uniformly distributed over the number of circuits, it can likewise be assumed that their thermo-physical behaviour is identical. Accordingly, it was decided to model only a single circuit of the finned-tube evaporator and acquire the total finned-tube evaporator values therefrom.

An isometric schematic view focussing on the inlet, outlet and return bends of a single circuit is illustrated in Figure 4-6. Once again, the fins are omitted to emphasise the coil circuitry. It is

evident that one circuit consists of four straight passes connected in series with 180° bends. The R744 flows parallel to the x-direction from the inlet to the outlet of the tube, whilst the air flows perpendicular to the x-direction across the tube. This is known as a crossflow configuration. Also, note that with respect to the y-direction, the R744 widely moves from the back of the circuit to the front. For this reason, a counterflow configuration is encountered with respect to the airflow direction. This combined phenomenon represents a cross-counter flow configuration and is found in practice due to the improved heat transfer from the added counterflow characteristics (Strydom, 2013).

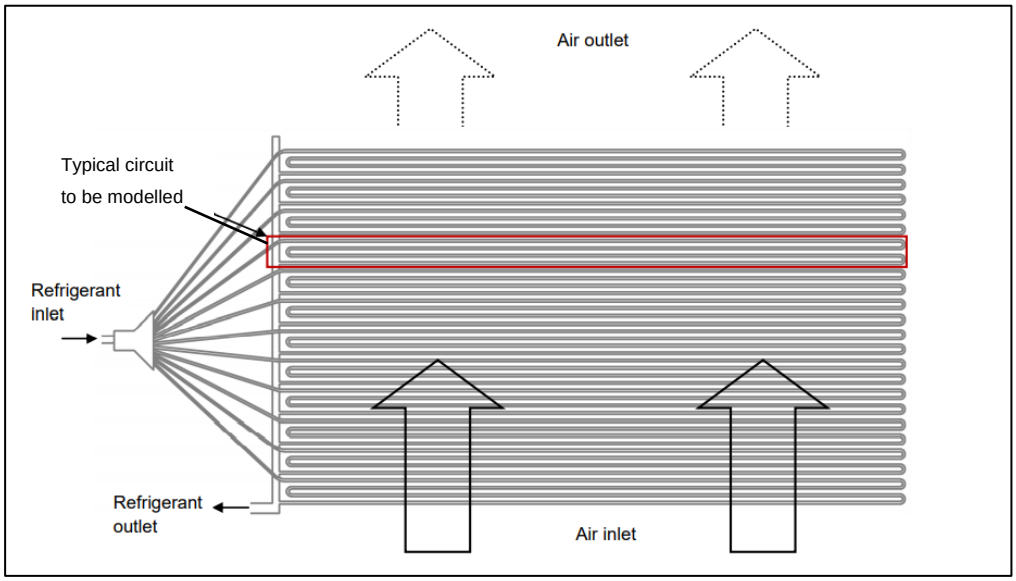

Figure 4-5: Schematic frontal view of a typical finned-tube evaporator with omitted fins, adapted from Strydom (2013).

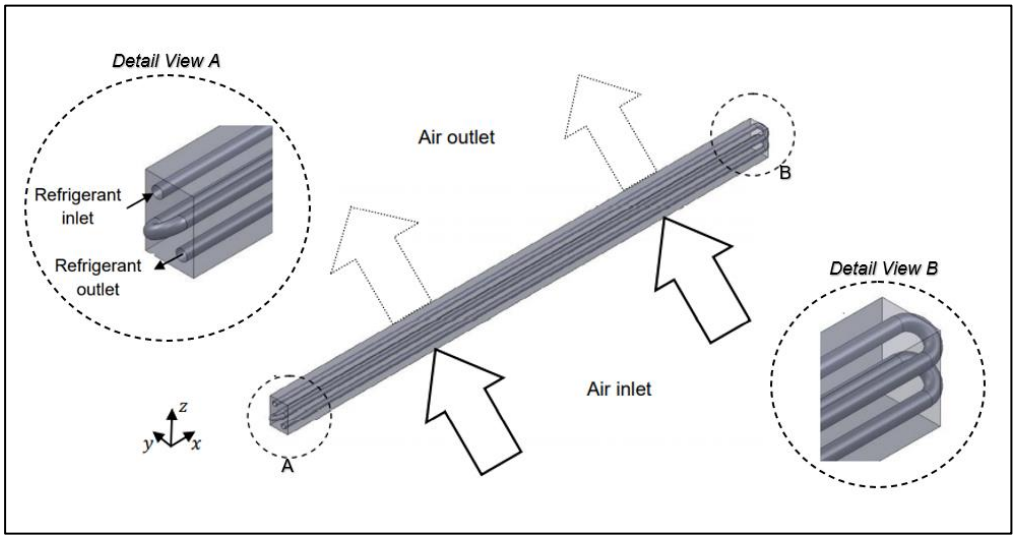

Figure 4-6: Schematic view of a single evaporator coil circuit with attention to the inlet, outlet and tube path (Strydom, 2013).

Consistent with the gas cooler model, the finite control volume method will be used to divide the circuit into equal-length increments along the R744 flow direction. Figure 4-7 portrays a two-dimensional overview of the coil circuit that is divided into 32 equal increments. Since the circuit consists of four passes, the total amount of increments can only be a multiple of four.

Each increment is once again modelled as an individual heat exchanger. However, in this case, a crossflow configuration with respect to the air stream is present, as illustrated in Figure 4-8. Only the R744 outlet conditions from a single increment are equal to the inlet conditions of its succeeding increment.

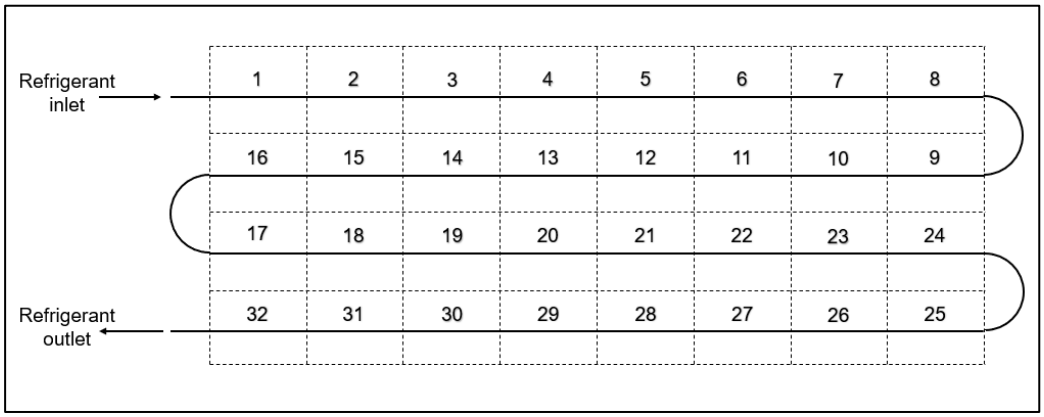

Figure 4-7: Two-dimensional overview of the single evaporator coil circuit with discretised sections. Adapted from Strydom (2013).

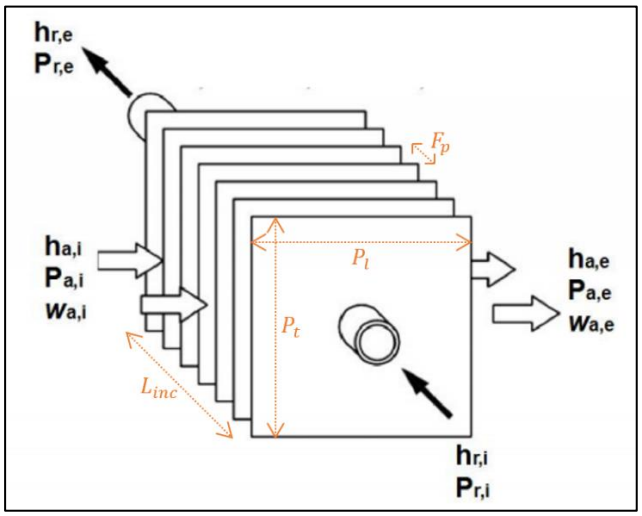

Figure 4-8: Detailed schematic of an evaporator circuit increment. Adapted from Ding *et al.* (2011).

Unlike the R744-side, the interconnection of air properties between increments is not as simple as that of the refrigerant and will now be interpreted with the aid of Figure 4-9. The figure depicts a side view of the circuit in the positive x-axis direction as defined by Figure 4-6. From Figure 4-9, the staggered tube arrangement can be identified. In this figure, a blue cross represents a

refrigerant flow direction going into the page, whereas a blue circle represents a refrigerant flow direction coming out of the page. With respect to the indicated airflow direction, it is clear that the front row tubes (two and four) will receive air at pure ambient conditions, whereas the back row tubes (one and three) will receive air at a mixture of outlet conditions coming from the front row.

It is assumed that the outlet air of the front row increments mixes adiabatically and is in equilibrium. Thus, the inlet conditions of a back row increment are reckoned as the average of the outlet conditions of the two preceding increments situated in the front row. Since the parallel circuits are all assumed to be thermo-physically identical, it is accordingly assumed that the incremental inlet conditions of tube one can also be reckoned from the outlet conditions from the corresponding increments situated in tubes two and four.

Unlike the gas cooler model, the fluid properties for the evaporator model will be evaluated at the inlet state of each increment. This is done as a result of computational capacity and can be justified by the small variations occurring per increment, as well as by the scope of this study.

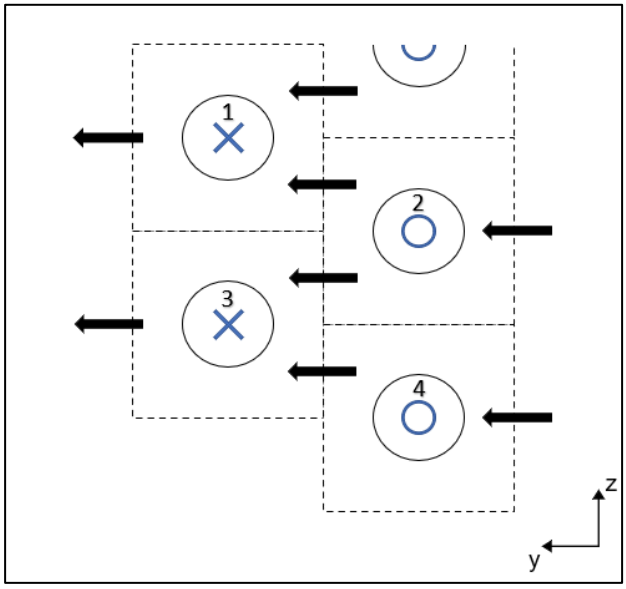

Figure 4-9: Schematic of the interconnection between incremental air properties (Strydom, 2013).

4.3.4.2 Inputs and assumptions

Table 4-5 lists the fixed inputs of the evaporator model, which composes of the physical heat exchanger properties such as the geometry and material of the fins and tubes. Amongst others, the evaporator geometry entails the fin pitch, transversal tube pitch, longitudinal tube pitch, and tube increment length - which are illustrated in Figure 4-8. Table 4-5 further lists the area ratios,

tube diameters, fin thickness, hydraulic diameter of air, as well as the number of tube rows, parallel circuits, and increments into which the evaporator will be discretised.

Table 4-5: Required inputs for evaporator model: Heat exchanger properties.

Symbol	Name	Unit
$\$Evap_{tube}$	Tube material	$[-]$
$\$Evap_{fin}$	Fin material	$[-]$
σ	Ratio of free flow area over frontal area	$[-]$
α	Ratio of air surface area over volume	$[-]$
$A_{fin}/A_{a,o}$	Ratio of fin surface area over total air surface area	$[-]$
D_i	Inner tube diameter	$[m]$
D_o	Outer tube diameter	$[m]$
N_{tr}	Number of tube rows	$[-]$
F_p	Fin pitch	$[m]$
P_t	Transversal tube pitch	$[m]$
P_l	Longitudinal tube pitch	$[m]$
δ_f	Fin thickness	$[m]$
$D_{h,air}$	Hydraulic diameter of air	$[m]$
L_{evap}	Tube length (for a single parallel circuit)	$[m]$
$N_{c,evap}$	Number of parallel circuits	$[-]$
N_{evap}	Number of increments per tube	$[-]$
L_{inc}	Tube length per increment	$[m]$

Error! Not a valid bookmark self-reference. reports the parameter inputs required by the evaporator model, such as the fluid boundary conditions. For the R744-side, this entails the inlet enthalpy and pressure, as well as the mass flow rate. On the airside, the boundary conditions include the inlet temperature, pressure, velocity, and RH. Considering that a two-phase R744 region is present in the evaporator, pressure and temperature will no longer be independent properties throughout the gas cooler. Thus, the boundary conditions on the R744-side are the inlet pressure and enthalpy.

Table 4-6: Required inputs for evaporator model: Boundary conditions of fluids.

Fluid	Symbol	Name	Unit
R744	h_{19} $(h_{r,i})$	Inlet enthalpy	$[J/kg]$
	P_{19} $(P_{r,i})$	Inlet pressure	$[Pa]$
	$\dot{m}_r$	Mass flow rate	$[kg/s]$
Air	$T_{a,i}$	Inlet temperature	$[J/kg]$
	$P_{a,i}$	Inlet pressure	$[Pa]$
	V_a	Inlet air velocity	$[kg/s]$

	RH_i	Inlet RH	[%]

Apart from the general assumptions and those stated in terms of the modelling approach, further assumptions relevant to the evaporator model are listed as follows:

- Constant thermal conductivity for the tube and fin materials.
- The fin base temperature is assumed equal to the outer surface temperature of the tube.
- The fins have a uniform temperature that is equal to the fin base temperature. Therefore, no temperature gradient exists between the base and tip of the fin.
- The air heat transfer surface (both fin and outer tube surface) is considered either fully wet or fully dry per increment - Since the fin temperature is uniform, only fully wet / fully dry conditions can be considered.
- A uniform airflow distribution over the entire frontal area of the evaporator is assumed. Put differently, the front row of parallel evaporator circuits and their respective increments will receive ambient air at the same conditions (temperature, pressure, humidity, velocity).

The assumption of a uniform fin temperature and thus only fully wet or fully dry incremental conditions can be justified as follow. A condition known as partially wet exists when the dewpoint is lower than the fin tip temperature, yet greater than the fin base temperature. In such a condition, only the surface areas below the dew point will induce condensation (Pirompugd, *et al.,* 2007). As mentioned in Section 2.2.2.4, the modelling of a fin temperature distribution requires hefty computational power. Considering that the present model only requires the prediction of total heat transferred between the R744 and air, the modelling approach of fully wet and fully dry conditions per discretised increment is deemed sufficient.

4.3.4.3 Simulation model and outputs

The simulation model employed for the evaporator model will now be explained by way of the logic diagram illustrated in Figure 4-10. Recognise that the inlet and outlet states of the R744 respectively correspond with the cycle points (19) and (51=1) denoted in Figure 4-1 and Figure 4-2.

The evaporator is modelled with an upwind discretisation and thus the fluid properties are evaluated at the inlet of each increment. For this reason, no guessed outlet values are present in the evaporator's simulation model (unlike that of the gas cooler, where such is needed for the fluid properties to be evaluated at the mean increment values). As highlighted in Section 2.2.2.4.2, for increments with small variations, this approach aids with the simulation time and stability (Strydom, 2013). As will be elaborated on in Section 5.3, to ensure this approach is suitable for

the present study, the increment size of this evaporator model will thus be equal to or smaller than that of Strydom (2013).

The logic diagram in Figure 4-10 firstly shows that the inputs from Table 4-5 and **Error! Not a valid bookmark self-reference.** reports the parameter inputs required by the evaporator model, such as the fluid boundary conditions. For the R744-side, this entails the inlet enthalpy and pressure, as well as the mass flow rate. On the airside, the boundary conditions include the inlet temperature, pressure, velocity, and RH. Considering that a two-phase R744 region is present in the evaporator, pressure and temperature will no longer be independent properties throughout the gas cooler. Thus, the boundary conditions on the R744-side are the inlet pressure and enthalpy.

Table 4-6 are substituted as inputs into the evaporator model. From the inputs, the pre-calculations are performed. This entails the geometrical parameters with aid of Equations (3.54 – 3.61), as well as the evaluation of the fluid properties, which are a function of the input boundary conditions. Hence, the pre-calculations are continued to obtain the air CHTCs for dry and wet conditions by using Equations (C.39 – C.47), mass transfer coefficient by using Equations (C.54) and (C.55), and friction factor using Equations (C.56 – C.56). Furthermore, Equations (3.50) and (C.48 – C.53) are applied to calculate the dry and wet fin efficiencies.

Subsequently, the deployment of the incrementing loop follows where the outlet properties for each increment are solved iteratively. The incremental loop starts with two logical operations, of which one is executed to classify the R744 as a single-phase or two-phase fluid. With respect to the R744 state, Equations (C.1 – C.38) are applied to determine the CHTC and pressure drop in the case of a two-phase mixture, whereas Equations (3.34), (3.29), (3.36), and (3.37) are used to calculate those of superheated vapour. Hence, the incremental heat transfer rate is computed with Equation (3.48) followed by the evaluation of the increment outlet enthalpy and pressure, which are reckoned with Equations (3.17) and (3.12), respectively. With the increment outlet enthalpy and pressure known, the corresponding fluid properties can be evaluated as a function thereof.

In parallel, the second logical operation is performed to distinguish between dry and wet conditions present on the evaporator's outside surface. In the case of dry surface conditions, the pre-calculated dry CHTC and fin efficiency are called to calculate the incremental sensible heat transfer with the aid of Equation (3.49). Under wet surface conditions, the wet air heat and mass transfer coefficients are applied in Equations (3.51) and (3.52) to compute the increment sensible and latent heat transfer rate. Thereafter, the outlet temperature, pressure (using the pressure

drop in Equation (3.53)), and humidity of the air can be found by solving Equations (3.20), (3.12), and (3.25), respectively. Accordingly, the increment outlet fluid properties can be evaluated as a function of the known air outlet temperature, pressure, and humidity.

As illustrated in the figure, this process is repeated for a number of *n* increments. Hence, the total heat transfer rates (sensible, latent, and overall) are obtained by summing the heat transfer rates of all the increments. Aside from the total heat transfer rates, the outputs also include the R744 outlet enthalpy and pressure of the evaporator, which are deemed as those of the final increment's outputs. Since the air exits the evaporator at all the increments situated in the back two rows, the outputs are therefore obtained by averaging the outlet temperature, pressure, and RH of each back row increment.

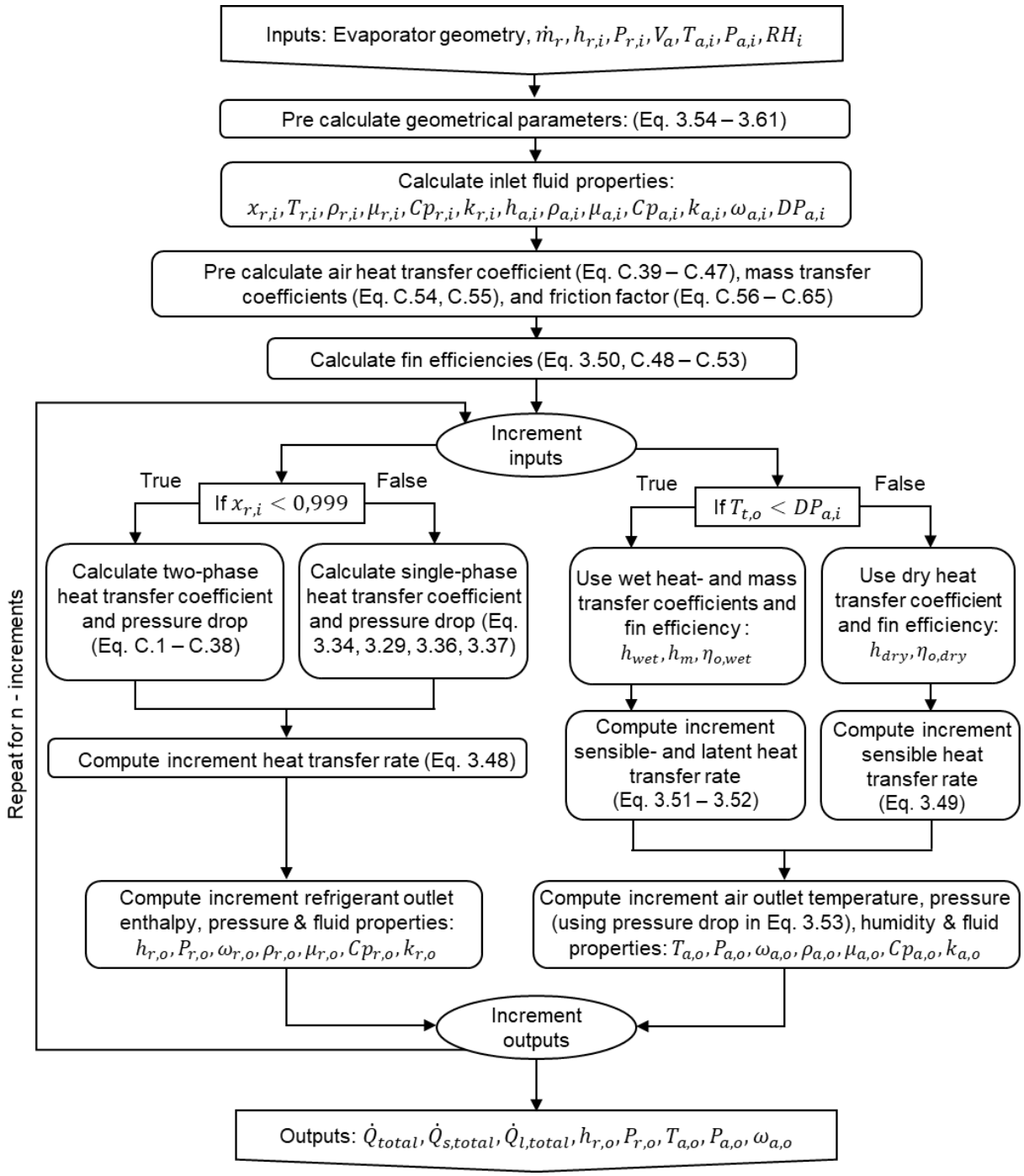

Figure 4-10: Schematic of the evaporator's simulation model.

4.4 Integrated heat pump cycle model

In this sub-section, a brief overview is given of the integration of the individual component models into an integrated heat pump cycle model.

As noted in literature, the effect of connection pipes between the cycle components is generally neglected, which will also be the case for the model of this study. Thus, the outlet conditions of one component are deemed equal to the inlet conditions of the next component. Furthermore, considering that this is a fully theoretical study, similar to Ye *et al*. (2020), an approximation approach will be used to relate the evaporation temperature to the ambient temperature (WB).

As mentioned before, the main purpose of this study is to investigate the performance of the cycle over a wide range of operating conditions. As will be elaborated in Chapter 6, to do so, an adequately designed system is required to ensure that the intended high-temperature water can be achieved over the full range of operating conditions. This will be achieved by sizing the system with a capacity large enough still fulfil the requirements at the worst possible case of operating conditions. As a result, the system's heat exchangers may be oversized when operating at more favourable operating conditions. For this reason, to avoid the simulations yielding unpractical heat transfer, a minimum temperature pinch point of 4°C was included within the heat exchanger models. In other words, should the temperature difference between two fluids drop below 4°C in a heat exchanger, any further heat transfer will be disregarded for that portion(s) of the heat exchanger.

4.5 Conclusion

In this chapter, the models of the individual subcomponents of the cycle as well as the integration thereof into a unified cycle model were described. The included the assumptions made and the modelling approach followed for each component. The respective inputs and outputs of each model were described, as well as where the theory discussed in Chapter 3 fits into the models. Aside from this, the characteristic equations of the compressor were developed by applying the universal method of Bester (2018), as outlined in Appendix D.

As for any study, the numerical model should be verified to confirm its accuracy, as will follow in the next chapter.

5. CHAPTER 5: MODEL VERIFICATION AND VALIDATION

The preceding chapter focussed on the simulation model of the four component models as well as their integration into a heat pump cycle and the simulation model thereof. In this chapter, the focus is directed on the validation and verification of the heat pump cycle model.

Note that verification is the method used to ensure that an analytical model is implemented accurately, whereas validation is the process applied to confirm that the analytical model is representative of the real-world application (Smuts, 2015).

Limited data in literature is available on the performance of transcritical carbon dioxide heat pumps with the same cycle and component configurations as in this study (as justified by the comprehensive literature review). That is i) a transcritical R744 heat pump cycle without an internal heat exchanger, ii) a semi-hermetic reciprocating compressor, iii) a water source tube-in-tube gas cooler, and iv) an air-source finned-tube evaporator with a wavy-fin configuration. Also, a limitation to this study is that the does not have access to such an experimental test-bench. Accordingly, it was decided to verify and validate the model per individual component by comparing the simulated results of the model to results of independent and credible sources.

The component-based validation and verification will be reported on in the following sequence:

1. Semi-hermetic reciprocating compressor.
2. Water-source tube-in-tube gas cooler.
3. Air-source wavy-finned tube evaporator.

For each above-listed component, a description will be given of the reference sources (where data will be gathered from to compare against the simulation results). Per component, five independent conditions will then be discussed and used for the comparison between the simulated and reference results.

Only the most important results will be evaluated in this chapter using a graphical format. A tabular hereof format can be found in appendix E, which also includes the set ups and inputs of the alternative simulation models (from commercial software) used for verification purposes. For the compressor, this will include the mass flow rate, delta temperature, and work rate values. In the case of the heat exchangers, this will include the heat transfer rate and delta temperature values. Furthermore, as shown in the literature review, the heat exchanger pressure drops of the considered system have been neglected in some of the previous studies, which motivates only a concise verification check thereof at the end of this chapter.

5.1 Reciprocating compressor model

As will be revealed in Section 6.2, a specifically sized compressor is selected as the most appropriate choice for the present study. Unfortunately, the author of this study does not have access to such an experimental test bench or direct experimental data. However, the compressor manufacturer, Bitzer, has developed software that accurately predicts their products' performance according to the European Standard EN12900 (Bitzer, 2022). Furthermore, Bester (2018) included a comparison between the accuracy of the Bitzer software relative to the experimental test bench of a similar reciprocating R744 compressor. The software was reportedly able to predict the mass flow rate and discharge temperature values within absolute average errors of 2.89% and 4.82%, respectively. Although the specific compressor model of Bester (2018) slightly differs from that of the present, this further adds credibility to the Bitzer prediction software.

Based on the above discussion, performance data gathered from the Bitzer software are deemed representative of the real-world compressors (in other words, validated). Moreover, since the present study focuses on the whole heat pump cycle's performance, it is deemed acceptable to only verify the compressor model against the aforementioned manufacturer software. Note that a study done by Opalic *et al.* (2019) relating to transcritical R744 cooling applications, made use of the exact same approach, i.e., Bitzer prediction software for their reciprocating R744 compressors.

As described in Section 4.3.1, the compressor input parameters consist of the suction pressure, suction temperature, and discharge pressure. Within the expected operating conditions and manufacturer limits of the compressor, per input parameter, five random values will be generated for the verification conditions of the compressor model. The rationale behind the expected boundaries of these randomly generated parameters is briefly discussed below.

- According to Bitzer (2022), the present compressor's operating conditions are confined to the following limits: Minimum DOS of 5°C; maximum discharge pressure of 14.0 MPa; and maximum discharge temperature of 160°C.
- The ambient temperature range considered by this study is 25-40°C. As will be discussed in Chapter 6, a typical air RH of 30% is considered in this study. This corresponds to a WB temperature range of 13.7-24.4°C.
- Input parameter 1: Suction pressure - For verification purposes, the expected suction pressure is assumed equal to the evaporation temperature's corresponding saturation pressure. In other words, the pressure drop in the evaporator is neglected in this regard. For the 8°C temperature approach between the WB air temperature and evaporation

temperature, an evaporation temperature from 5.7°C to 16.4°C is expected. Thus, the expected suction pressure will range between 4.04 MPa (5.7°C saturation pressure of R744) and 5.26 MPa (16.4°C saturation pressure of R744).

- Input parameter 2: Suction temperature - Considering the minimum 5°C DOS specified by the compressor manufacturer, the lower limit of the expected suction temperature range is set to 10.7°C. In addition, since the minimum pinch point in the evaporator model may not be lesser than 4°C, the upper limit of the expected suction temperature range is assigned as 36.0°C. Thus, the expected suction temperature range was decided on as ≈11-36°C.
- Input parameter 3: Discharge pressure - As indicated in the literature study, the expected discharge pressure for a transcritical R744 heat pump that heats water to 90°, ranges around 12.0 - 13.0 MPa. It was decided to expand the expected discharge pressure range to 1.0 MPa above and below this range, i.e., 11.0 – 14.0 MPa.

The randomly generated verification conditions are listed in Table 5-1. The evaporation temperature column is shown to interpret the suction pressure easier. Note that whenever a generated suction temperature value resulted in a DOS value lower than 5°C, the value was regenerated until satisfying the minimum DOS limit.

Table 5-1: Generated operating conditions for the compressor model verification.

Condition	T_{evap} [°C] (5.7 – 16.4)	Parameter 1: P_{suc} [MPa] ≈ (4.04 – 5.26)	Parameter 2: T_{suc} [°C] (10.7 – 36.0)	Parameter 3: P_{dis} [MPa] (11.0 – 14.0)
1	7.5	4.23	14.8	13.8
2	9.6	4.46	30.3	12.0
3	13.1	4.86	35.7	11.7
4	5.7	4.04	16.1	13.6
5	16.2	5.24	24.6	11.3

The simulated results of the compressor model relative to those of the Bitzer software are illustrated in Figure 5-1. This includes the R744 mass flow rate, delta temperature (difference between the compressor's suction and discharge temperature), and compressor work rate.

Figure 5-1a shows the comparison of the mass flow rates generated by the compressor model and Bitzer software at the verification conditions. The simulation generally overpredicted the mass flow rate, yet within a maximum deviation of 0.62% and average deviation of 0.21%. Figure 5-1b illustrates the comparison of the delta temperature values. The simulation slightly underpredicted

the delta temperature, although within a maximum deviation of -0.29% and average deviation of -0.06%. Figure 5-1c depicts the resulting compressor work rate values. Three values were overpredicted and two underpredicted, yet within limited discrepancies. The average and maximum errors were recorded as -0.06% and -0.68%, respectively.

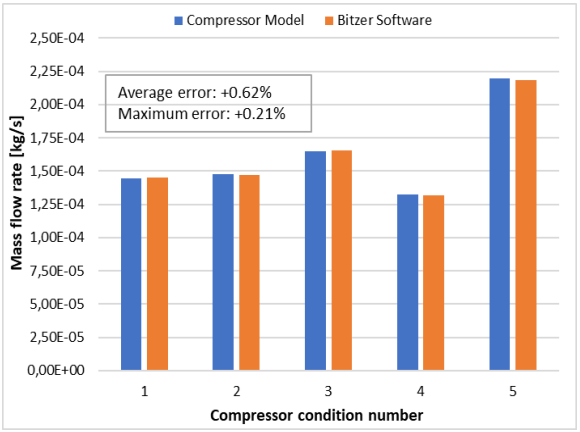

c) Mass flow rate

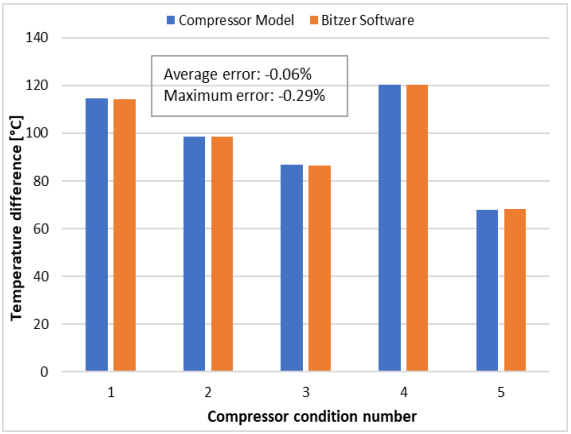

b) Temperature difference

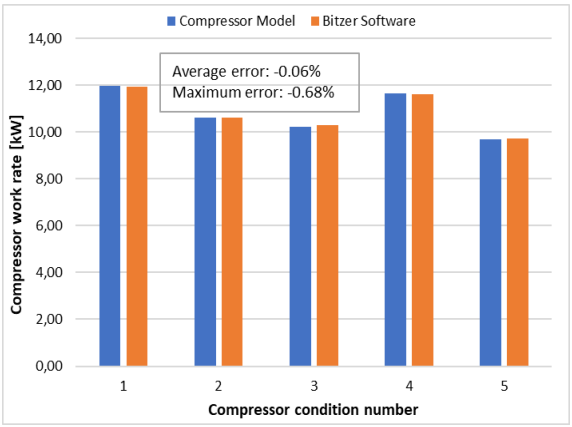

d) Compressor work rate

Figure 5-1: Comparison of the compressor simulation and Bitzer-software results: a) Mass flow rate, b) Temperature difference, and c) Compressor work rate.

The marginal discrepancies recorded in this section can be attributed to mathematical rounding-off errors and the assumptions made within the application of Bester (2018)'s method, such as the polynomial orders used to develop the compressor characteristic correlations (Appendix D).

Seen that the present compressor model predicted the Bitzer-software performance data within very limited discrepancies (<1%), it is concluded as successfully verified. As mentioned before, the values gathered from the Bitzer software are sufficiently representative of real-world data. The compressor model is concluded as sufficiently accurate with tangible results and will be used for the rest of this study.

5.2 Water-source tube-in-tube gas cooler model

For the verification of the gas cooler model, reference will be made to an equivalent Flownex software model. Flownex is a renowned one-dimensional thermo-physical network solver with the capability of simulating a vast range of fluid engineering applications, including heat exchangers. This software is especially suitable for the present verification since it also makes use of the finite volume method and has R744 as a built-in refrigerant option. Furthermore, the same correlations used in the gas cooler model, i.e., Dittus & Boelter (1985) for the R744 side and Gnielinski (1976) for the waterside, are also available in this software (Flownex, 2022).

In parallel, the gas cooler model will be validated relative to experimental results published by Harris (2014). The researcher performed experiments on the R744 tube-in-tube gas cooler test bench at the NWU to analyse the accuracy and applicability of various Nusselt number correlations for the in-tube cooling of R744. Similar to the present study, this test bench also used a counterflow heat exchanger configuration and water as a heat sink.

This verification and validation will be conducted by adapting the physical gas cooler design of the present model and Flownex model to that of Harris (2014)'s test bench. These design specifications are listed in Table 5-2 and include the geometrical parameters, tube material, and flow configuration. Note that Harris (2014) used a number of 12 increments to model a 24.0 m gas cooler, which corresponds to an incremental length of 2.0 m. As will be revealed in Section 6.3, the maximum possible length (in the worst case) of the gas cooler to be used in the desired simulations of this study is 30.32 m. Thus, for the present gas cooler model, a minimum total of 16 increments (rounded up) are used to ensure that the mentioned incremental length will be maintained throughout this study, even for the worst case of the gas cooler design.

Table 5-2: Physical heat exchanger inputs for the gas cooler model verification and validation. Adapted from Harris (2014).

Symbol	Name	Value	Unit
$D_{i,i}$	Inner tube inside diameter	0.016	$[m]$
$D_{i,o}$	Inner tube outside diameter	0.0215	$[m]$
$D_{o,i}$	Outer tube inside diameter	0.026	$[m]$
t_{wall}	Inner tube wall thickness	0.00275	$[m]$
L_{gc}	Gas cooler tube length	24.0	$[m]$
$N_{t,gc}$	Number of tubes	1	$[-]$
$N_{inc,gc}$	Number of increments	16	$[-]$
$\$GC_{config}$	Heat exchanger configuration	'Counterflow'	$[-]$
$\$GC_{tube}$	Tube material	'AISI 304 Stainless Steel'	$[-]$

Similarly, the same operating conditions at which the experimental results of Harris (2014) were gathered, will be used as inputs for the present simulations. Hence, the simulation results of the gas cooler model will be compared to those of the Flownex simulation and Harris (2014)'s experimental data. Table 5-3 lists the inlet pressure, inlet temperature, and mass flow rate of the R744 stream, as well as the corresponding inlet temperature and mass flow rate of the water stream.

Table 5-3: Operating conditions for the gas cooler model verification and validation (Harris, 2014).

Condition	Refrigerant side			Waterside	
	$P_{r,i}\ [MPa]$	$T_{r,i}\ [°C]$	$\dot{m}_r\ [kg/s]$	$T_{w,i}\ [°C]$	$\dot{m}_w\ [kg/s]$
1	9.0	103.5	0.150	23.9	0.181
2	9.5	108.1	0.162	24.2	0.169
3	10.0	115.2	0.165	23.9	0.159
4	10.5	116.8	0.175	24.5	0.129
5	11.0	120.6	0.180	24.5	0.119

The simulation results of the gas cooler model relative to the Flownex simulation and Harris experimental data are portrayed in Figure 5-2. This includes the gas cooler heat transfer rate and delta temperature values of both the R744 and water sides.

5.2.1 Verification: Comparison to Flownex simulation

Relative to the Flownex simulation results, Figure 5-2a to Figure 5-2c show that the two fluid temperature differences and heat transfer rates are almost identical. Of all three considered parameters, the largest inaccuracy was found at the water temperature difference, where a maximum deviation of -0.25% was noted at condition one. Furthermore, the average relative errors for the R744 temperature difference, water temperature difference, and heat transfer rate were recorded as -0.06%, -0.03%, and -0.02%. Seen that the exact same Nusselt correlations are used by the two simulations in question, these close results are expected. The very limited deviations (<1%) may only be due to small inconsistencies such as rounding-off errors in built-in fluid properties. Nevertheless, the gas cooler model is deemed as accurately implemented and thus successfully verified.

5.2.2 Validation: Comparison to experimental data of Harris (2014)

Figure 5-2c show that relative to Harris (2014), the heat transfer rate was generally overpredicted. In this case, the maximum error was +4.50% at condition four, and the average deviation over all the conditions was +3.46%. No explicit relation between the magnitude of this inaccuracy and the

input conditions could be identified, and no experimental uncertainty on the heat transfer rates was reported by the data source.

This overprediction may be caused by correlation inaccuracy. As described in Chapter 2, over the experimental range of Harris (2014), the Dittus & Boelter (1985) Nusselt correlation was reported as the most accurate, yet, with a relative average error of +20%. Accordingly, an overprediction is expected. This inaccuracy may also be due to unaccounted fouling effects in the gas cooler.

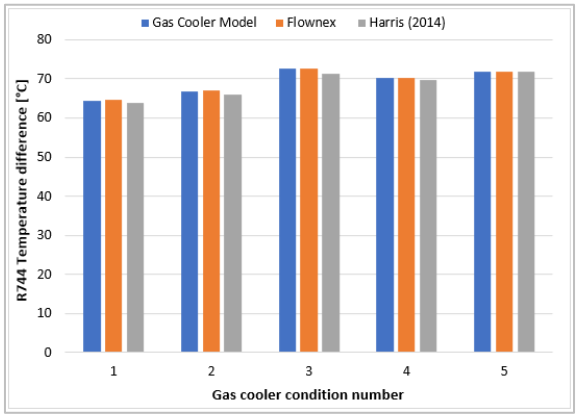

a) R744 temperature-difference

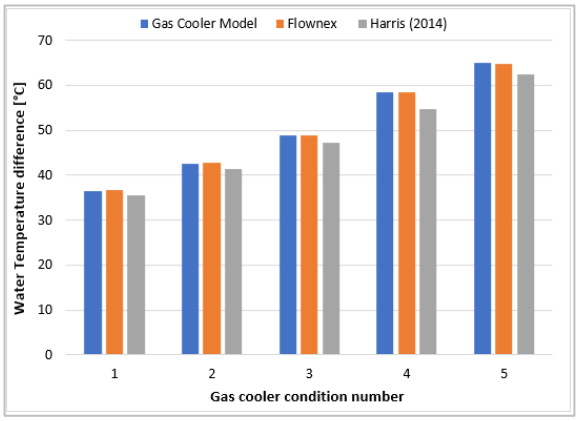

b) Water temperature-difference

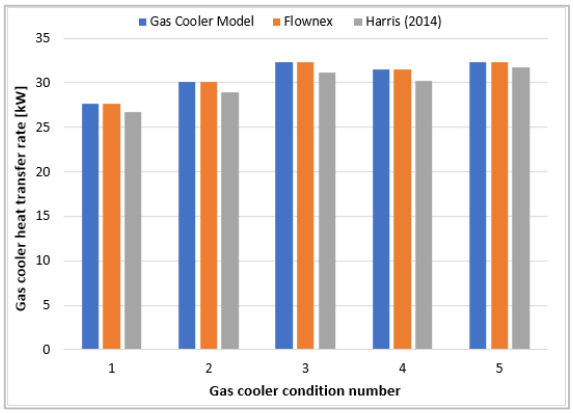

c) Gas cooler heat-transfer rate

Figure 5-2: Results comparison of the gas cooler simulation, Flownex simulation, and Harris (2014) experimental data: a) R744 temperature difference, b) Water temperature difference, and c) Gas cooler heat transfer rate.

Figure 5-2a and Figure 5-2b show that the fluid temperature differences in the gas cooler are also overpredicted. Seen that fluid temperature differences in a heat exchanger are functions of the heat transfer rate, these recorded deviations are argued to be functions of the heat transfer rate's underprediction. Even so, the margin of overprediction differs on the R744 side (relative average of 1.01%) relative to the water side (relative average of 3.92%). This may be accredited to the present model's assumption that thermal losses to the environment are negligible, and also to the

uncertainty of the experimental measurements. No measurement tolerances for any of the discussed outputs were explicitly reported by Harris (2014).

Nevertheless, for the purpose of this study, the above-described deviations relative to the experimental data of Harris (2014) are on an acceptable level. Over all the considered conditions and parameters, the largest individual error was recorded as 4.50%, and the overall relative error was averaged as 2.80%. It is argued that the gas cooler model yields representative data of a real-world application and is thus successfully validated.

5.3 Air-source wavy-finned tube evaporator model

For the verification of the evaporator model, reference will be made to EVAP-COND (NIST 2020), which is a software package developed by NIST that contains simulation models specifically for finned-tube heat exchangers. This software is highly relevant for the present comparison since it also makes use of the finite control volume method and offers R744 as a built-in refrigerant option. Although Flownex also has the aforementioned characteristics, EVAP-COND is preferred in this case since it has specific correlations for the two-phase region. This software also allows for the specifying of assorted refrigerant circuits and includes local parameters for each tube such as temperature, enthalpy, entropy, and mass flow rate (NIST, 2020).

Concurrently, the model will be validated relative to the experimental data of Strydom (2013). The researcher performed experiments on the R744 air-source wavy-finned evaporator at the NWU to study its performance and in parallel, develop and validate an accompanying numerical model.

Similar to the previous section, the verification and validation will be conducted by setting up the present model and EVAP-COND software with the same heat exchanger properties as those of Strydom (2013). These specifications are listed in Table 5-4 and include the geometrical parameters, tube and fin material, and evaporator configuration. Note that Strydom (2013) used 32 increments to model the 4.8 m evaporator circuit, which corresponds to an incremental length of 0.15 m. As will be revealed in Section 6.3, the maximum length (in the worst case) of the evaporator to possibly be used in the actual simulations of this study is 4.15 m. Thus, rounded up to the nearest four, a minimum total of 28 increments are used for the present model to ensure that the aforementioned incremental length will be maintained throughout this study, even for the worst case of the evaporator design. Also note that Strydom (2013) used an upwind discretisation, and that the aforementioned incremental length was thus rendered as sufficient with the inclusion thereof. As mentioned in Section 4.3.4.3, such a discretisation method is applicable for applications with small enough variations. Since the present investigation will later involve a broad

range of ambient temperatures, it is decided to add another four increments, which increases the total number of evaporator increments to 32.

Subsequently, the same set of experimental conditions used by Strydom (2013) will be simulated by both the present evaporator model and the EVAP-COND software. These conditions are outlined in Table 5-5 and entail the R744 evaporation temperature, inlet quality, mass flow rate, as well as the air temperature, relative humidity, and velocity. For each condition, the air pressure is fixed at 85 kPa and the R744 inlet pressure is equal to the corresponding saturation pressure.

Table 5-4: Physical heat exchanger inputs for the evaporator model verification and validation (per parallel circuit), adapted from Strydom (2013).

Symbol	Name	Value	Unit
A_{fin}	Total fin area	2.23914	$[m^2]$
A_{tube}	Total tube area	0.14281	$[m^2]$
$A_{a,o}$	Total outside surface area	2.38195	$[m^2]$
A_{ff}	Total free flow area	0.03245	$[m^2]$
D_i	Inner tube diameter	0.00928	$[m]$
D_o	Outer tube diameter	0.01010	$[m]$
F_p	Fin pitch (excluding fin thickness)	0.0021166	$[m]$
P_t	Transversal tube pitch	0.0254	$[m]$
P_l	Longitudinal tube pitch	0.022	$[m]$
N_{tr}	Number of tube rows	2	$[-]$
θ	Fin wave angle	16	[°]
δ_f	Fin thickness	0.00014	$[m]$
L_{evap}	Tube length	4.8	$[m]$
$N_{inc,evap}$	Number of increments	32	$[-]$
$N_{c,evap}$	Number of parallel circuits	12	$[-]$
$\$Evap_{tube}$	Tube material	'Copper'	$[-]$
$\$Evap_{fin}$	Fin material	'Aluminium'	$[-]$
$\$Evap_{config}$	Evaporator configuration	'Wavy-finned tube'	$[-]$

Table 5-5: Operating conditions for the evaporator model verification.

Condition	Refrigerant side			Airside		
	$T_{r,i}$ [°C]	x_i [−]	$\dot{m}_r$ [kg/s]	$T_{a,i}$ [°C]	RH_i [%]	V_a [m/s]
1	0.3	0.823	0.1435	16.5	34.8	5.25
2	4.8	0.838	0.1705	15.6	35.8	9.71
3	8.9	0.928	0.2204	15.7	35.3	9.61
4	0.0	0.429	0.1662	29.1	30.1	8.95
5	5.0	0.429	0.2039	29.4	30.4	8.94

Considering that the evaporator model is more complex in nature and delivers more outputs than the other models, the verification and validation results will be grouped and discussed as follow:

1. Overall heat transfer rate
2. R744 side temperature
3. Airside temperature and humidity

5.3.1 Overall heat transfer rate

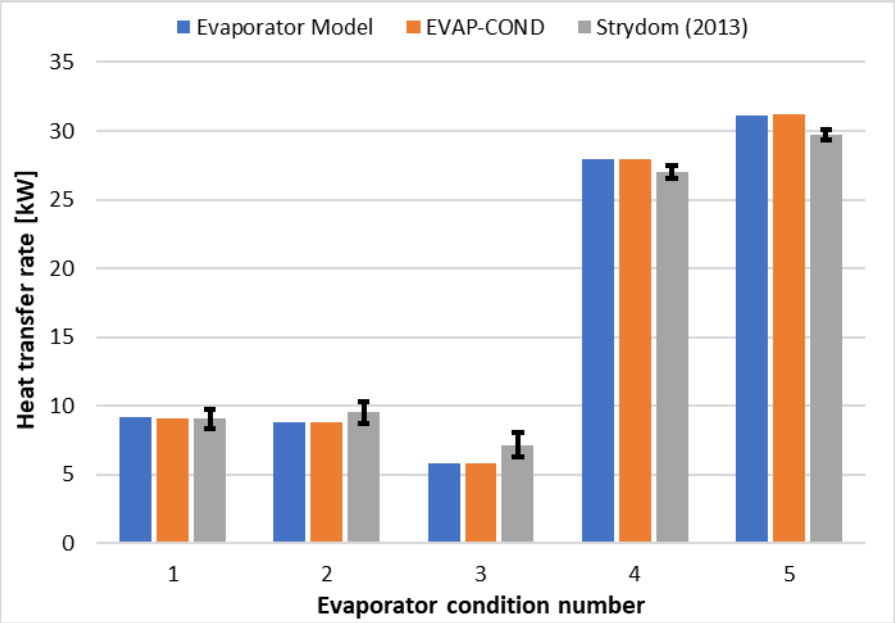

Figure 5-3: Heat transfer rate comparison of the evaporator model simulation, EVAP-COND simulation, and Strydom (2013) experimental data.

5.3.1.1 Verification: Comparison to EVAP-COND simulation

Figure 5-3 illustrates the evaporator heat transfer rates obtained by the present simulation, EVAP-COND, and Strydom (2013). The simulated values are in good agreement with those of EVAP-COND. On average, the heat transfer rate was overpredicted by 0.24%, with the greatest margin being +1.00% at condition one.

This discrepancy is a result of different correlations being used to predict the two-phase heat transfer. EVAP-COND and the present simulation make use of the Thome (2005) and Cheng *et al.* (2008a&b). The latter is regarded as more accurate than the former since it is a refined version thereof and was also developed specifically for R744, unlike the former, which was developed on R22 and R410 data (Cheng, *et al*, 2008a&b; Thome, 2005). In general, literature also reports that an increase in heat transfer rate is linked to an improvement in correlation accuracy (Strydom, 2013).

5.3.1.2 Validation: Comparison to Strydom (2013)'s experimental data

From Figure 5-3 it can be seen condition one and two were predicted within the uncertainty bands of the experimental heat transfer rates. For condition three, an underprediction of 7.64% was recorded, and in contrast, for conditions four and five, an overprediction of 1.93% and 3.56%, respectively. Furthermore, the mean relative error was found as -0.43%.

Neither the present simulation nor EVAP-COND accounts for the effect of compressor oil. As will be elaborated in Section 5.3.2.2, the presence of oil in an evaporator (as was the case for Strydom (2013)) may affect the heat transfer in either a positive or negative manner. Thus, the inaccuracy of this comparison is not due to the simulation (or due to EVAP-COND), but rather due to the influence of oil in the experimental measurements.

In conditions one to three, vapour qualities of 0.823 to 0.928 were present, whereas conditions four and five involved a relatively lower vapour quality of 0.429. For this reason, larger two-phase regions were present at conditions four and five than at conditions one to three. As will also be described in Section 5.3.2.2, due to the oil within the evaporator, it is reasoned that these overpredictions and underpredictions are amongst others, related to greater and smaller two-phase regions, respectively (Strydom, 2013).

5.3.2 R744 side temperature

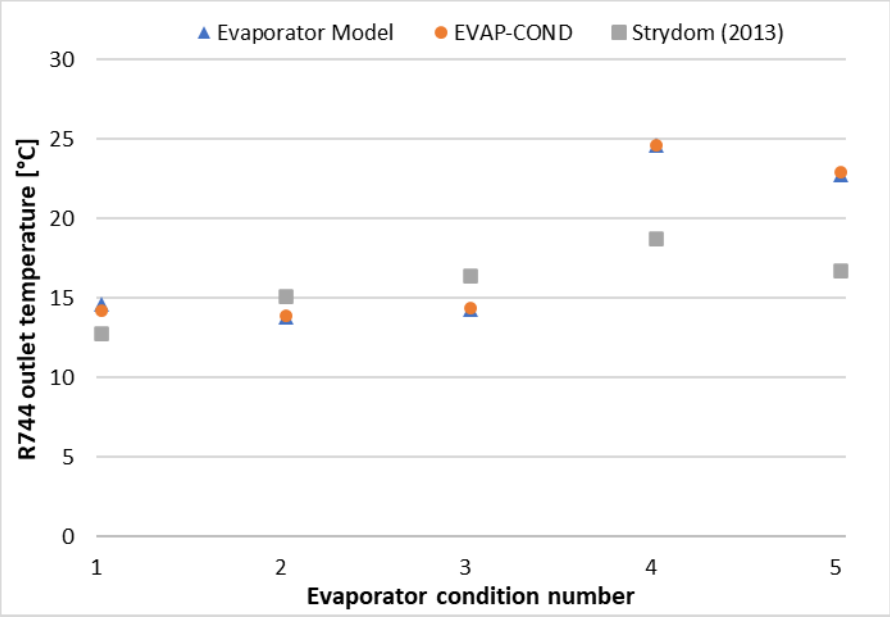

Figure 5-4: R744 temperature comparison of the evaporator model simulation, EVAP-COND simulation, and Strydom (2013) experimental data.

5.3.2.1 Verification: Comparison to EVAP-COND simulation

Figure 5-4 depicts the outlet R744 temperature of the three considered independent sources. Compared to EVAP-COND, the present simulation correlates well, yet with a slight overprediction at condition one, which is expected since this was also the case for the overall heat transfer rate. The average error was +0.19%, and the maximum error +2.68% at condition one.

As mentioned in Section 5.3.1, Cheng *et al.* (2008a&b) is an update of Thome (2005) and also specifically focussed on R744. Since the dryout and mist flow regions (the two-phase regions closest to the saturation point) are predominantly encountered in finned tube evaporators, the greater part of the correlation refinement was based thereon (Strydom, 2013). For these reasons, the present simulation is deemed more accurate as it makes use of Cheng *et al.* (2008a&b). Furthermore, the present model discretised the finned tube evaporator into a total of 32 segments. This allows a finer simulation than EVAP-COND, which is limited to a maximum of 10 increments.

5.3.2.2 Validation: Comparison to Strydom (2013)'s experimental data

Compared to the validation data, Figure 5-4 shows that the R744 temperature is underpredicted for conditions two and three, whereas an overprediction is evident for conditions one, four, and five. In this case, the average deviation was +12.11%, and the maximum deviations were +13.91%, +31.50% and +36.17% at conditions one, four, and five, respectively.

In parallel to the experiments done by Strydom (2013), a similar evaporator model was developed. When compared to his own experimental data, the reported margins of inaccuracy are similar to the above. As mentioned in Chapter 2, the accuracy of a heat exchanger model is highly dependent on those of the incorporated correlations and should be judged appropriately. In the comparison of Strydom (2013), a ±20% margin of error was deemed acceptable, which included the overall heat transfer rate and fluid outlet temperatures. Since the same correlations are used in the present simulation as with Strydom (2013), the ±20% margin is adopted accordingly.

One reason for the observed deviations may be the correlation accuracy of the heat transfer coefficient. Only three of the thirteen data-sets that Cheng *et al*. (2008a&b)'s correlations were developed on, included inner tube diameters greater than 3 *mm*. The nearest to the present application was 10.06 *mm,* being that of Knudsen & Jensen (Strydom, 2013). Even so, as justified in Chapter 2, up to date, Cheng *et al*. (2008a&b) remains the most suitable and accurate two-phase R744 heat transfer correlation for numerical modelling over a broad range of operating conditions.

It is important to note that the experimental compressor used in test bench was reportedly overfilled with oil, and that polyolester (POE) oil type was used. Although termed as large, no numerical quantification of the oil concentration was given by the researcher (Strydom, 2013). The influence hereof on the present comparison will now be discussed.

The under and overprediction of heat transfer due to the effect of oil in the evaporator

The influence of oil in flow boiling may have either a positive or negative effect depending on various operating conditions such as the type of oil, oil concentration, heat and mass flux, tube size, and more. These influenced operating conditions may include a higher bubble point temperature, surface tension, and viscosity. Further included may be lower thermal conductivities and the development of foam (Mastrullo, *et al.,* 2019). Generally, heat transfer coefficients of R744 are negatively influenced by the presence of oil. Only in certain conditions such as lower vapour qualities and lower oil concentrations, marginal increases are found (Wetzel, *et al.,* 2014).

During the performing of Strydom (2013)'s experiments on the heat pump test bench, through the sight glass upstream of the compressor, lubricant foam was reportedly identified at times. Factors that contribute to the formation of such foam are high heat fluxes and oil concentrations. Also, rapid expansions occurring in the expansion valve may incite the formation of POE oil (Strydom, 2013; Wetzel, *et al.,* 2014).

For each of the five considered conditions, Table 5-6 lists the average two-phase heat flux and pressure ratio associated with the expansion process. The former was obtained from the present simulation and the latter from the experimental heat pump data of Strydom (2013). In addition to the high oil concentration, conditions four and five are associated with higher two-phase heat fluxes and more rapid expansion ratios. Thus, the formation of lubricant foam is highly expected in these conditions, which explains the degraded heat transfer coefficient and thus lower R744 temperatures (Strydom, 2013).

Considering their lower two-phase heat fluxes and pressure ratios, the opposite of the above argument is reasoned for condition two and especially condition three, which explains their associated underpredictions in heat transfer coefficients and thus R744 temperature. Furthermore, the effect of this argument is less evident in the conditions of higher inlet qualities since smaller two-phase regions were present, allowing for less/no foaming to take place.

Table 5-6: Expansion valve pressure ratios recorded by Strydom (2013) and simulated mean two-phase heat flux for the considered evaporator conditions.

Condition	Mean two-phase heat flux $[kW/m^2]$	Expansion valve pressure ratio [-]
1	14.0	2.18
2	10.8	1.96
3	6.85	1.69
4	33.1	2.39
5	30.2	2.36

To account for the influence of oil, Strydom (2013) did a supplementary simulation that involved applying a constant degradation factor to the heat transfer coefficient and was calibrated according to the recorded deviations. This is decided not to do for the present model, and the discrepancies seen by the influence of oil are disregarded for the following reasons:

- The oil concentration was specifically high for the experimental data of Strydom (2013) due to the overfilling of the involved compressor. The present evaporator model forms part of a full heat pump cycle model, which is aimed at a more universal purpose.
- Correlations developed for oil-entrained R744 heat transfer coefficients should only be applied to the conditions (including oil type) they were developed on. No correlations are available yet that include the effect of POE oil for macro tubes at evaporation temperatures above 0°C (Mastrullo, *et al.,* 2019).
- As will be stated in Chapter 8, a recommendation for future studies is to define correlations for R744-oil (POE) heat transfer coefficients, or to gather experimental data with an oil type that has such correlations readily available in literature, such as the Polyalkylene glycol (PAG) type.

Up to this point of the evaporator verification and validation, the overall heat transfer rate and R744 outlet temperature have been evaluated. Good agreements have been seen between the present simulation, the experimental data of Strydom (2013) and EVAP-COND. Where this was not the case, in-depth explanations were given to justify that it was not a result of simulation inaccuracy. The next section will consider the airside of the evaporator.

5.3.3 Airside temperature and moisture

5.3.3.1 Validation: Comparison to Strydom (2013)'s experimental data

Figure 5-5a illustrates the recorded outlet temperatures of the three considered sources. Relative to those of Strydom (2013), with the exception of condition three, a slight general overprediction

is present. The average relative deviation was +1.10%, with conditions two and five being predicted within the uncertainty bands, and the largest deviation being +4.41% at condition one.

The differences may be attributed to simulation errors such as correlation inaccuracy and certain assumptions on which the present model was developed. These assumptions include only considering fully wet or fully dry surfaces, neglecting heat transfer to the environment and neglecting the thermo-physical effects of fin tips and return bends.

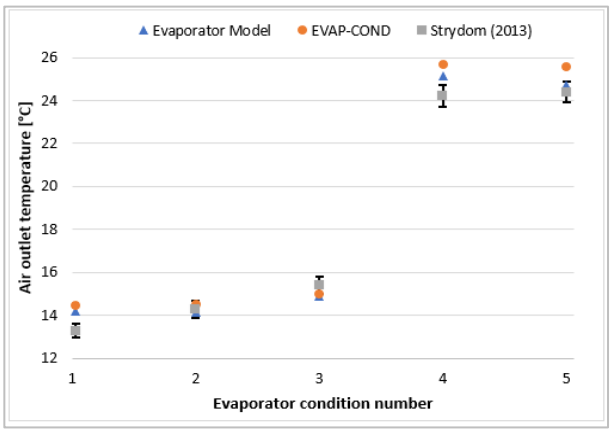

a) DB air outlet temperature

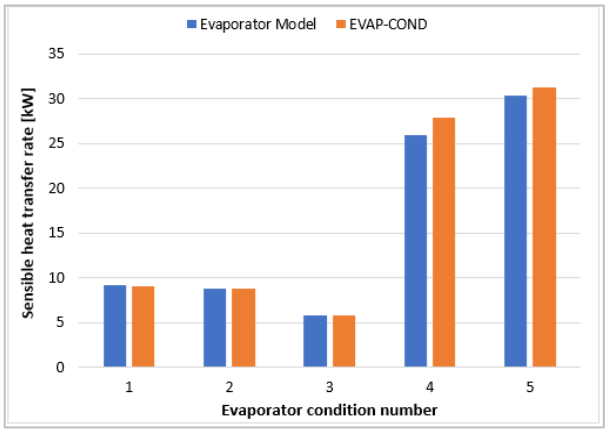

b) Sensible heat transfer rate

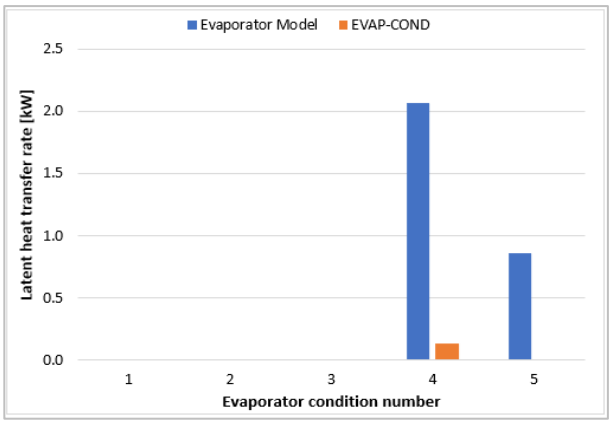

c) Latent heat-transfer rate

Figure 5-5: Airside comparison of the evaporator model simulation, EVAP-COND simulation, and Strydom (2013) experimental data: a) Air outlet temperature, b) Sensible heat transfer rate, c) Latent heat transfer rate.

In parallel, the differences may also be due to measurement uncertainties on the experimental side. Since there is moisture in the air, some of the energy transferred may be of the latent type and thus not in the form of a temperature change. Strydom (2013) reported that condensate wetted the relative humidity sensors during the experiments, which led to negative latent heat transfer measurements. Accordingly, the latent (moisture) aspects of the experimental data are further omitted. Even so, for the purpose of this study, the above-mentioned deviations are on an

acceptable level and still show that the values of the present simulation are representative of tangible results.

5.3.3.2 Verification: Comparison to EVAP-COND simulation

Respective to EVAP-COND, Figure 5-5a shows that the outlet temperature (DB) is generally slightly underpredicted. The mean relative error was -2.19% and the maximum error -3.17% at condition five.

The observed underprediction may be attributed to a combination of calculation differences between the present model and EVAP-COND. For instance, since EVAP-COND does not have wave angle as an input, it is likely that the geometrical calculations slightly differ from those of the present model, leading to an overall correction in total heat transfer rate. As mentioned before, EVAP-COND can only discretize the heat exchanger up to 10 increments, as opposed to the present model at 32 increments. In addition, according to Strydom (2013), the correlation for the heat transfer coefficient employed in the present simulation, Wang *et al.* (2012a), is a refined version of that used by EVAP-COND, Wang, 1999.

Since there is moisture in the air, some of the energy transferred may be of the latent type and thus not in the form of a temperature change. Seen that the total heat transfer rates described in Section 5.3.1 had marginal differences, it can be inferred that the sensible and latent heat transfer rate adds up to the correct amount, although with a deviation in their ratio. Figure 5-5b and Figure 5-5c show a comparison of the predicted sensible and latent heat transfer rate, respectively. The greatest error in sensible heat transfer was -6.98% at condition four, which is also the condition with the highest latent heat transfer rate. As will be discussed in more detail shortly, this difference is due to EVAP-COND using a constant Lewis number, whereas the present simulation is based on a researched correlation (Strydom, 2013).

<u>The ratio of sensible and latent heat transfer</u>

As illustrated in Figure 5-5c, when non-zero latent heat transfer rates were predicted as with conditions four and five, large differences are seen between the present simulation and EVAP-COND. As mentioned, the present simulation uses a correlation rather than a constant value for the Lewis number as is the case for EVAP-COND. Consequently, a difference in mass transfer prediction results. As mentioned in Chapter 2, a Lewis number based on a correlation is theorised as the more accurate approach.

The study by Strydom (2013) revealed similar behaviour when comparing simulation results to EVAP-COND results. The author decided to disregard the latent heat transfer rate comparison in terms of numerical accuracy and rather focus on the accuracy of the trend. Hence, additional simulations at higher inlet RH values were conducted to prospectively obtain higher latent heat transfer rates. For the present study, a similar investigation will be held to compare the findings to those of Strydom (2013). This will be accomplished by re-simulating condition five, except for using higher inlet RH values (40% to 70%).

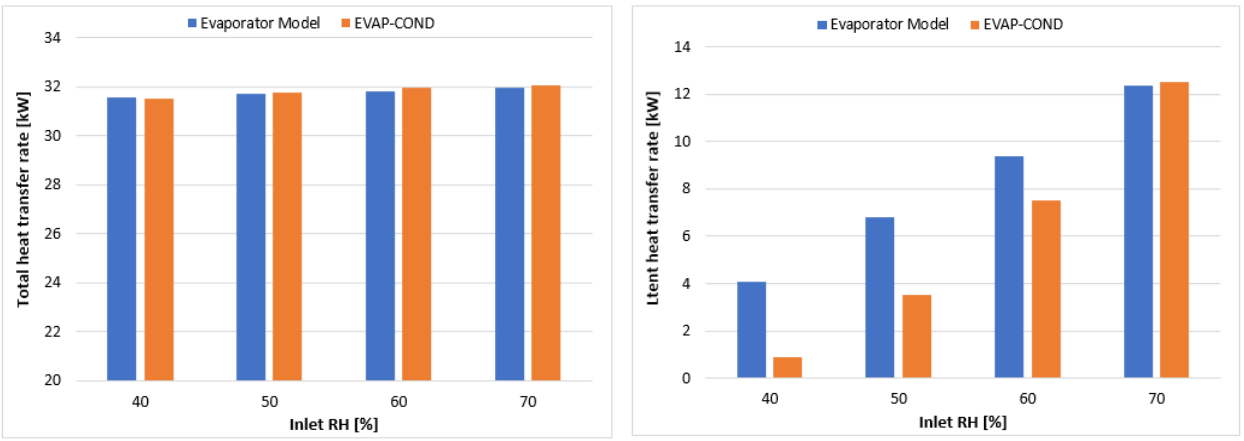

(a) (b)

Figure 5-6: Comparison of the total overall (a) and latent (b) heat transfer rates for the three increased RH conditions.

Hence, between the present simulation and EVAP-COND, Figure 5-6a portrays a good agreement in total heat transfer rate with an average deviation of -0.47%. Over the same conditions, Figure 5-6b shows the latent heat transfer rate. For both the overall and latent heat transfer rate, an increase is reported with a rise in inlet RH. This is the case for both simulations and agrees with the findings of Strydom (2013). As a result, the trend in latent heat transfer rate is sufficiently verified.

5.3.4 Summary

It should again be noted that the accuracy of a numerical heat exchanger model is dependent on its embedded correlations, and that as with Strydom (2013), a ±20% error margin was deemed appropriate. For the verification and validation part of the evaporator model, Table 5-7 summarises the main recorded differences. This excludes the prediction of the two R744 experimental temperatures that had errors greater than 20%. However, as elaborated, this was

mainly due to the influence of oil, which was disregarded due to the rich oil environment of the data source, and also due to the more-universal purpose of the present study.

Aside from the experimental R744 temperature and its oil-related aspects, the largest recorded deviation in terms of validation was -7.64%. The discrepancies relative to validation data were further accredited to correlation inaccuracies, model assumptions, and errors in the experimental measurements. Respective to verification, the largest noted difference was -3.17%, and the observed discrepancies were attributed to simulation inconsistencies such as different correlations, number of increments, geometrical inputs, and assumptions.

Reflecting the exceptional agreement with EVAP-COND, the evaporator model is concluded as satisfactorily verified. Excluding the two above-mentioned R744 temperatures of Strydom (2013) that were appropriately disregarded for the comparison, the evaporator model is reckoned as adequately validated.

Table 5-7: Summary of evaporator model verification and validation results (differences).

Respective to	Parameter	Mean relative error	Maximum error	Predicted to within ±20%
Verification (EVAP-COND)	Overall heat transfer rate	+0.24%	+1.00%	100%
	R744 outlet temperature	+0.19%	+2.68%	100%
	Air outlet temperature[a]	-2.19%	-3.17%	100%
Validation (Strydom (2013) experimental data)	Overall heat transfer rate	-0.43%	-7.64%	100%
	R744 outlet temperature	+12.11%	+36.17%[c]	60%[c]
	Air outlet temperature[b]	+1.10%	+4.41%	100%

*a: The humidity aspect of the outlet air was disregarded in terms of numerical values due to the more accurate approach of a Lewis-number correlation by the present simulation. Even so, the verification was still done on a trend basis.
*b: The humidity aspect of the outlet air was omitted due to the large measurement errors reported by the experimental data source.
*c: With the two data points yielding prediction errors larger than 20% being omitted for the described reasons relating to oil, this value is rather +13.91%.

5.4 Heat exchanger pressure drops: Brief verification check

Although the literature review showed that some of the previously considered studies omitted the heat exchanger pressure drops from their examinations, for the inclusiveness of this numerical

model, it is decided to still account therefor. However, unlike the well-detailed verification and validation performed thus far in the previous sections of this chapter, only a brief verification check will be done for the pressure drops of the heat exchangers.

Table 5-8 shows the resulting pressure drops recorded at condition one of the gas cooler and evaporator (as defined in Sections 5.2 and 5.3), respectively. For the gas cooler, relative to Flownex, the present model overpredicted the pressure drop by 6.92%. For the evaporator model relative to EVAP-COND, the current model underpredicted the pressure drop by 18.46%. The present author could not verify which exact correlation is used by EVAP-COND. However, according to Strydom (2013), the favourable characteristics of R744 and its low pressure drops are not well correlated with the aforementioned software. As is the case for all correlations employed in the current model, the selections of the pressure drop correlations are also strictly based on the literature review and thus viewed as suitable.

Nevertheless, the rightmost column of the table shows the margin of these pressure drops (the maximum of the two compared values) in relation to the high R744 operating pressures. The pressure drops in the gas cooler and evaporator weighed up only 0.22% and 0.06% of their total working pressures, respectively. This agrees with Mastrullo *et al.* (2019)'s claim that the pressure drops are insignificant. Note that for the gas cooler, this statement is only valid for large diameter R744 heat exchanger pipes (as in this case) and may not be the case for smaller diameter R744 pipes or R744 mass flow rates considerably larger than those of this study.

Table 5-8: Verification check of simulated pressure drops at condition one of the gas cooler and evaporator, respectively.

Total pressure drop at gas cooler condition one			
Gas cooler model [MPa]	**Flownex [MPa]**	**Relative error**	**Pressure drop relative to operating pressure**
0.0199	0.0187	+6.92%	0.22%
Total pressure drop at evaporator condition one			
Evaporator model [MPa]	**EVAP-COND [MPa]**	**Relative error**	**Pressure drop relative to operating pressure**
0.00185	0.00227	-18.46%	0.06%

Considering the tiny margins of the pressure drops in perspective of the high operating pressures of R744 heat pump cycles, as well as the purpose of the present study, the brief verification and resulting accuracies seen in this section are on an acceptable level.

5.5 Conclusion

In this chapter, the component models of the transcritical R744 heat pump cycle were successfully verified and validated. This was achieved by comparing the results of the current simulations to those of independent and credible sources. Per component, this was done for five independent conditions.

For the compressor model, discrepancies lower than 1% were noted. This was also the case for the gas cooler model with respect to the Flownex simulation software. Respective to the experimental gas cooler data of Harris (2014), the greatest error was 4.50% and the overall relative error was averaged as 2.80%. A ±20% margin of error was decided for the evaporator model in light of its embedded correlation accuracies. Relative to the EVAP-COND simulation software, this margin was easily satisfied with a maximum recorded error of -3.17%. Relative to the experimental evaporator data of Strydom (2013), except for the R744 temperature measurements, the acceptable margin of error was maintained with a maximum recorded deviation of -7.64%. The aforementioned exception was appropriately motivated by the oil-related conditions of the data source (thus not the inaccuracy of the simulation or EVAP-COND) and the more-universal purpose of the current study.

In addition, a brief validation check was also performed on the R744 pressure drops of the heat exchanger models. For the broader purpose of the current investigation, the briefness of this secondary examination as well as the revealed accuracies were deemed satisfactory in view of the high R744 operating pressures.

As will be stated in Chapter 8, a recommendation for future studies is the procurement of a relevant test bench to allow for a full-cycle validation of the transcritical R744 heat pump system at the conditions of this study.

The prediction model of the cycle, which includes all the theory compiled in Chapter 3 and the modelling approaches described in Chapter 4, is now regarded as sufficiently accurate and tangible and will be used for the rest of the investigation for full-cycle simulations.

6. CHAPTER 6: COMPONENT DESIGNS

The previous chapter illustrated the accuracy of the established numerical model for the transcritical R744 heat pump cycle. In this chapter, as in a real-world application, the system will be designed to best suit the intended application, which is operating at above-conventional water outlet temperatures over a range of high ambient conditions. After the design is finished, in the chapter to follow, the performance of the appropriately sized heat pump system will be simulated for the aforementioned conditions.

The design of the heat pump system entails the sizing of its subcomponents and will be accomplished with aid of the developed cycle model. The author would like to emphasize that the core focus of this study is the system's performance over a range of operating conditions. Therefore, the sole purpose of the design is to provide an appropriately sized system with sufficient capacity to operate at all intended conditions of the investigation. Note that only a graphical representation of the results is given in this chapter, with the tabulated results available in

appendix a.

6.1 Design conditions

As mentioned in Section 4.4, an over-design criterion is used to ensure that the system can supply the desired output conditions even for the worst-case of operating conditions that will be considered. This least favourable combination of conditions will thus be referred to as the design conditions and are listed in Table 6-1. In other words, the table outlines the specifications according to which the system should be designed for this particular purpose of this study. A discussion of the involved specifications follows.

Ambient design conditions: The ambient temperature range for the main investigation of this study is 25-40°C. Since an over-design is used, the design ambient temperature is thus set to the lowest value in this range, i.e., 25°C. The air pressure and RH values are set to conditions typically experienced in Potchefstroom, South Africa. Also, a typical air velocity of 3.0 m/s is assigned.

Water design conditions: The water inlet temperature range included in the main investigation of this study is 15-60°C. Similar to the above argument, the design value of this parameter is consequently set to 15°C. Seen that water outlet temperatures in the region of 90°C are intended to be investigated, it is decided to specify 90°C as a design condition. Note that during the main

investigation of this study, the water outlet temperature may still vary around this value, depending on the input operating conditions. As revealed in literature, a water mass flow rate of 0.1 kg/s can typically be expected and is accordingly assigned. Furthermore, to ensure the water does not evaporate in the gas cooler due to the temperature rise and pressure loss, its inlet pressure is set to 250.0 kPa.

R744 design conditions: As mentioned in Chapter 4, an approximation temperature difference will be used to relate the evaporation and WB ambient temperature. For the operating conditions of this study, the numerical value of the approximation approach was decided as 8°C. At a 25°C ambient temperature and RH of 30%, an equivalent WB temperature of 13.7°C is present. Therefore, the evaporation temperature is set to 5.7°C. Furthermore, since this is the worst possible combination of operating conditions under consideration, the minimum compressor DOS of 5°C is also set as a design condition.

Table 6-1: Design conditions (worst possible combination) according to which the heat pump system is sized.

Fluid	Parameter	Symbo	Value	Unit
Air (Ambient)	Inlet air temperature (DB)	$T_{a,i}$	25.0	[°C]
	Inlet air velocity	V_a	3.0	$[m/s]$
	Inlet air RH	RH_i	30.0	[%]
	Inlet air pressure	$P_{a,i}$	85.0	$[kPa]$
Water	Inlet temperature	$T_{w,i}$	15.0	[°C]
	Inlet pressure	$P_{w,i}$	250.0	$[kPa]$
	Outlet temperature	$T_{w,o}$	90.0	[°C]
	Mass flow rate	$\dot{m}_w$	0.1	$[kg/s]$
R744	Evaporation temperature	T_e	5.7	[°C]
	DOS	DOS	5.0	[°C]

According to the design specifications outlined in Table 6-1, the cycle's component designs will now be determined. For the compressor, using the manufacturer's software, the outcome will be selecting the most appropriate model from real-life options. Hence, using the full cycle model (with the confirmed compressor selection), for the heat exchangers, the outcome will be to determine the best suitable geometric sizes.

6.2 Compressor selection

As justified in the literature review, reciprocating compressors are reckoned as the most appropriate type for transcritical R744 applications. Also as motivated, Bitzer sets the benchmark

and offers a range of such compressors for the application of transcritical R744 refrigeration systems. Using Bitzer (2022)'s software, a relevant reciprocating compressor will be identified.

By substituting the water conditions listed in Table 6-1 into Equation (3.15), it is found that the heating capacity at the design condition is equal to approximately 31.39 kW, assuming that $c_{p,w}$ is equal to 4.185 kJ/kg.K.

Provided that an evaporation temperature of 5.7°C and DOS of 5°C are entered into the Bitzer (2022) software, the compressor model yielding the closest (but not less than) value to the above-stated heating capacity is the 4MTE-10K option. Figure 6-1 illustrates the mentioned compressor model yielding a 31.5 kW heating capacity at a discharge pressure of 12.0 MPa.

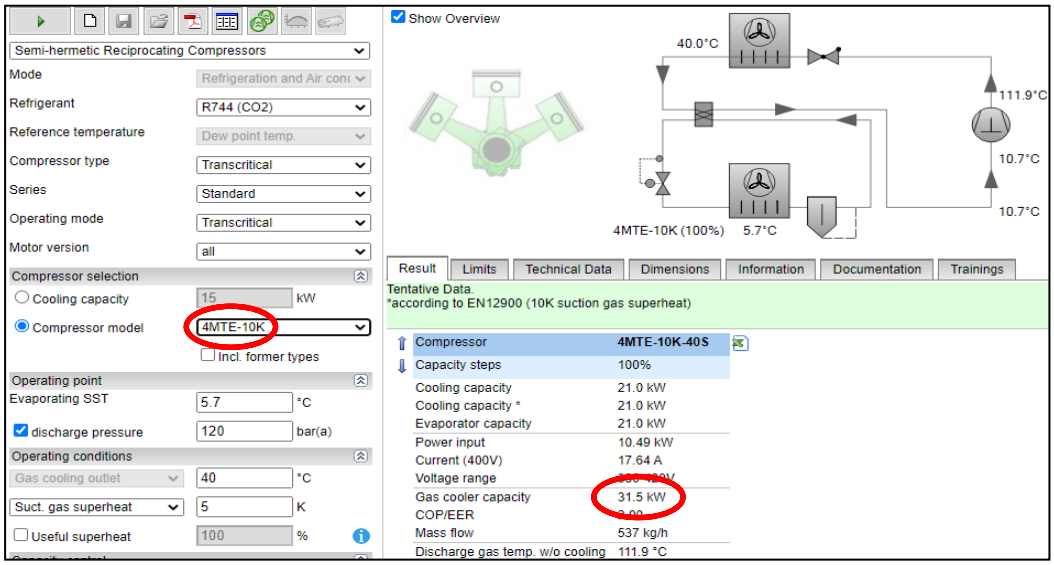

Figure 6-1: Most applicable compressor identified at the design condition (Bitzer, 2022).

Since the temperature and pressure at which the R744 enters the compressor are both known at the design conditions, the discharge pressure is the only remaining variable of the compressor. For the selected compressor, whilst varying the discharge pressure, the resulting mass flow rate and discharge temperature coming from the compressor will be evaluated. This will be done over the typically expected range of discharge pressures, i.e., 11.0 - 14.0 MPa (as described in Section 5.1). Note that 14.0 MPa is also the maximum permissible discharge pressure of the selected compressor.

Figure 6-2a illustrates the resulting R744 mass flow rate. With an increased discharge pressure, the mass flow rate linearly reduces. Over the indicated rise in discharge pressure, the mass flow rate reduced from 0.155 kg/s to 0.138 kg/s. As noted in literature, under the conditions investigated in this study, the R744 mass flow rate is expected to be more significant than that of

the water. Since a water mass flow rate of 0.1 kg/s is present, over the full range of discharge pressures, the present compressor choice is deemed sufficient in terms of yielded R744 mass flow rate, as is evident from the figure.

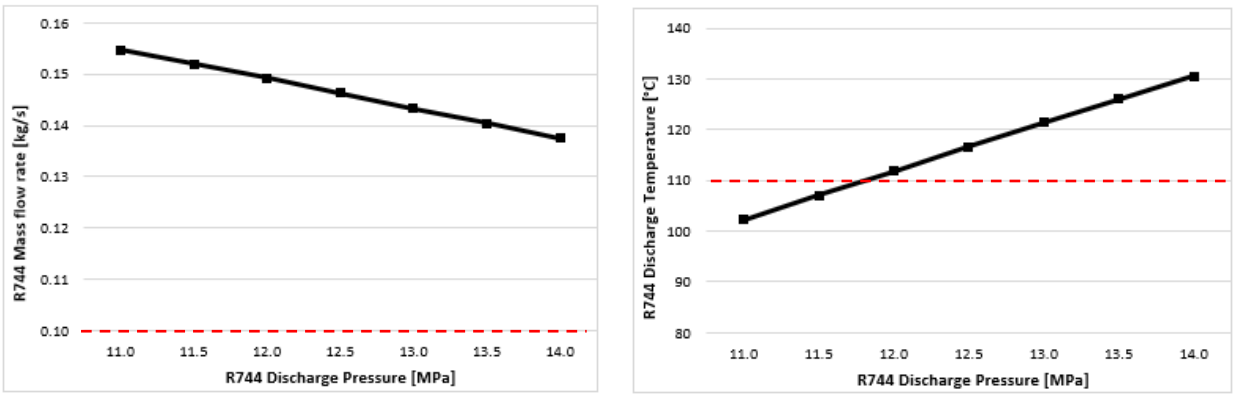

a) R744 Mass flow rate

b) R744 Discharge temperature

Figure 6-2: Compressor options at the design conditions over a range of discharge pressures: a) Mass flow rate, and b) Discharge temperature.

Similarly, the resulting discharge temperatures are demonstrated in Figure 6-2b. A linear rise in discharge temperature is evident with an increase in discharge pressure. At an 11.0 MPa discharge pressure, a discharge temperature close to 102°C resulted. As the discharge pressure rose to 14.0 MPa, the discharge temperature increased to 130°C. Since the water outlet temperature of the gas cooler will be in the order of 90°C, only R744 discharge temperatures beyond 110°C are reckoned applicable. As indicated by the red line in the figure, such discharge temperatures could only be achieved at discharge pressures between 12.0 MPa and 14.0 MPa.

In conclusion, the considered 4MTE-10K model is viewed as an appropriate compressor option considering that a) the Bitzer software predicted it as the option that yields the closest (but not lower than) heating capacity to that of the design specifications, b) it yielded an R744 mass flow rate greater than the design water mass flow rate, which corresponds to literature, and c) for discharge pressures from 12.0 MPa to 14.0 MPa, it produced R744 discharge temperatures above 110°C, which is reckoned high enough for its intended application of heating water in the gas cooler to a design outlet temperature of 90°C.

6.3 Heat exchanger designs

With the compressor selected and its corresponding theoretical equations listed in Section 4.3.1 integrated into the full cycle model, the focus is now directed at the heat exchanger sizes. At this point, all the design conditions listed in Table 6-1 are given as inputs into the full cycle model, with the aim of calculating the heat exchanger geometries as outputs of the full cycle model. As

mentioned in literature, for any operating condition, an ODP exists at which the system yields its maximum efficiency. In other words, an operating condition can be satisfied at more than one R744 discharge pressure, yet with different system efficiencies. Similar to the previous section, the R744 discharge pressure will now also be varied in its appropriate range to evaluate the resulting heat exchanger sizes and system behaviour. For this evaluation, the following parameters are particularly regarded as important:

- Required gas cooler length.
- Overall heat transfer coefficient (U) of the gas cooler.
- Required evaporator length.
- Accompanying power consumption, cooling capacity, and cycle COP_H.

For simplicity, all the physical heat exchanger properties except the lengths are kept constant at the values used for the verification and validation in Chapter 5. Since the focus of this study is to investigate the system performance rather than doing a fully detailed design, this is deemed acceptable, and will also maintain the relevancy of the verified and validated geometries. Thus, excluding the lengths, all the physical properties of the gas cooler and evaporator can be found in Table 5-2 and Table 5-4, respectively.

After discussing the above-listed parameters, an overall conclusion of the heat exchanger designs follows. Since this study focuses on a water heating application, emphasis will be placed on the gas cooler.

6.3.1 Evaluation of the considered parameters

Figure 6-3a demonstrates the required gas cooler length over the range of discharge pressures. With respect to increasing R744 discharge pressure, a decrease in gas cooler length is evident. When the R744 discharge pressure rose from 12.0 MPa to 14.0 MPa, the gas cooler length reduced by 40.0% from 30.32 m to 18.20 m. Similar findings were reported by Wang *et al.* (2013a), who concluded that for the same output conditions, the required R744 discharge pressure reduces as the heat transfer area of the gas cooler increases.

Moreover, the decrease in gas cooler length becomes less significant at lower values. Smaller decreases in gas cooler length are evident at the 13.0-14.0 MPa discharge pressure range (-27.1%) than at the 12.0-13.0 MPa range (-17.7%). In other words, as the gas cooler size increases, the improvement in heat transfer lessens. This observation agrees with the findings of Wang *et al.* (2013b), who accredited it to the sensible heat transfer that remains fairly similar as well as to the constant water inlet temperature that governs the R744 gas cooler outlet

temperature. Also, since the present design criteria involve a fixed heating capacity, this behaviour is also expected.

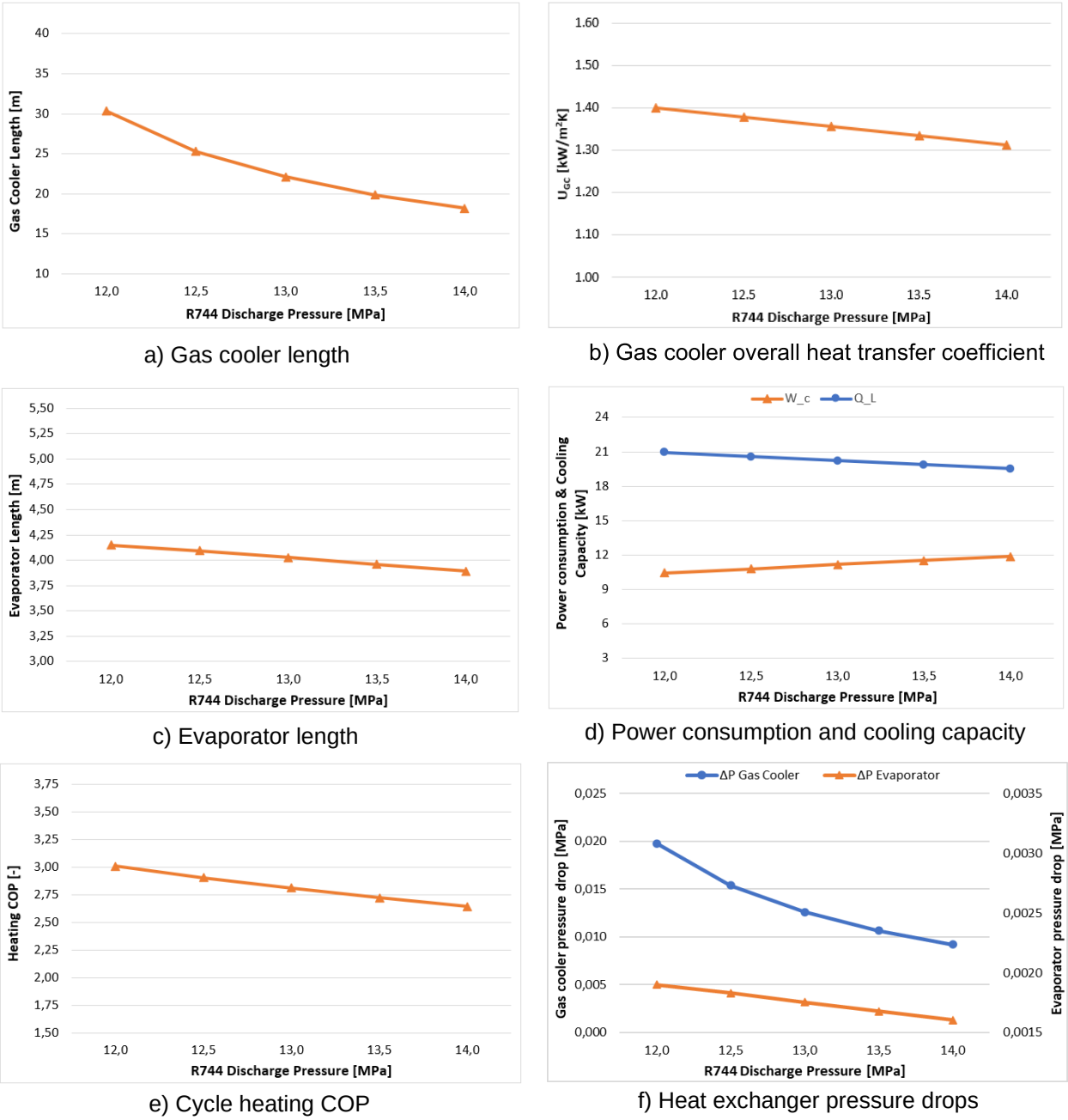

Figure 6-3: Cycle parameters at the design conditions over the discharge pressure range: a) Gas cooler length, b) Gas cooler overall heat transfer coefficient (average), c) Evaporator length, d) Power consumption and cooling capacity, e) Cycle COP_H, f) Heat exchanger pressure drops.

Figure 6-3b illustrates the corresponding average overall heat transfer coefficient of the gas cooler (U_{GC}), which marginally reduced with an increase in R744 discharge pressure. A reduction of 6.2% from 1.40 kW/m^{2}K to 1.31 kW/m^{2}K resulted when the R744 discharge pressure increased from the indicated minimum to maximum value. Considering that the mass flow rate, inlet

temperature, and outlet temperature of the water stream are fixed in this case, it can be inferred that this improvement in the overall heat transfer coefficient of the gas cooler is mainly due to the variation in R744 heat transfer properties near the transcritical region. It is particularly seen that better R744 heat transfer properties are present at lower R744 pressures, i.e., by referring to Figure 6-2, also at lower R744 temperatures and higher R744 mass fluxes. This also agrees with Wang *et al.* (2013b).

Figure 6-3c demonstrates a reduction in evaporator length with a rise in R744 discharge pressure. Over the indicated R744 discharge pressure range, the evaporator length slightly reduced from 4.15 m to 3.89 m (-6.1%). This decrease in evaporator length is caused by an improvement in heat transfer and can be justified as follow. In regions of lower vapour quality, better local R744 heat transfer coefficients are present (Rigola, *et al.,* 2010). However, from the resulting T-s diagrams shown in Figure 6-4, it is evident that the R744 states throughout the evaporator are approximately equivalent, regardless of the associated R744 discharge pressure. Furthermore, as was pointed out in Figure 6-2a, increased R744 discharge pressure leads to a decreased mass flow rate. Thus, it can be inferred that the enhanced heat transfer in the evaporator is a result of a better mass flow ratio between the air and R744 streams.

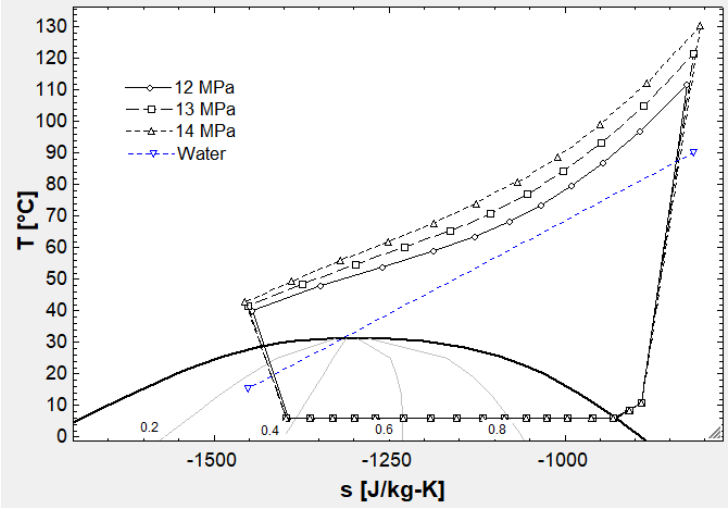

Figure 6-4: Resulting cycle T-s diagrams at the design conditions over the range of R744 discharge pressures.

The resulting compressor power consumption and cooling capacity are depicted in Figure 6-3d. For increasing R744 discharge pressure, the power consumption rises, whereas the cooling capacity lowers. From Equation (3.64), it can be stated that the sum of these two parameters should equal the heating capacity. Considering that a fixed heating capacity is present, the power consumption rises by the same amount which the cooling capacity decreases by. Over the

indicated R744 discharge pressure range, the power consumption rose from 10.44 kW to 11.89 kW (+1.44 kW), whilst the cooling capacity decreased from 20.95 kW to 19.50 kW (-1.45 kW).

The above-mentioned increase in power consumption due to a rise in R744 discharge pressure also explains the downgrade in cycle COP_H that is revealed in Figure 6-3e. This also agrees with the findings of Wang *et al*. (2013a), who reported that the heat transfer areas have a negligible effect on the compressor power. A 12.2% reduction in system efficiency from 3.01 to 2.64 was experienced when the R744 discharge pressure rose from 12.0 MPa to 14.0 MPa.

Figure 6-3f illustrates the corresponding heat exchanger pressure drops, which resemble similar trends to the heat exchanger lengths as expected. Although the pressure drops increase with a decrease in R744 discharge pressure and thus an increase in heat exchanger lengths, as described in Section 5.4, it remains tiny in comparison to the operating R744 pressures. For instance, the maximum pressure drop for the gas cooler was 0.0198 MPa at an inlet operating pressure of 12.00 MPa, whereas that for the evaporator was 0.0019 MPa at an inlet operating pressure of 4.04 MPa.

6.3.2 Conclusion of heat exchanger designs

As has been explained before, the purpose of this chapter is to size the system in such way that it can operate over the entire range of desired operating conditions. Since more than one R744 discharge pressure (and accompanying heat exchanger sizes) exists that satisfies this design criteria, this section aims to identify the most appropriate one.

Although the highest system COP_H is typically desired, from the above discussion, it can be inferred that larger heat exchanger sizes (especially for the gas cooler) are required therefor. For instance, the highest COP_H was 3.01, which is linked to the 12.0 MPa discharge pressure and therefore also to the maximum gas cooler length of 30.32 m, which may be very expensive in a real-life scenario. In contrast, the smallest gas cooler size was 18.20 m, which is linked to the 14.0 MPa discharge pressure and thus also to the lowest COP_H of 2.61. Thus, as was also reported by Zhang *et al.* (2014), a trade-off exists between the installation cost (component sizes) and running cost (system efficiency).

A practical approach for selecting the appropriate design may be to compare the system's installation cost to its running cost over an applicable period and accordingly make the most cost-effective decision. Further practical factors to consider may also be the physically available space for the system, and possible carbon taxes due to the added electricity demand. However, such factors are not part of the present study's scope, which motivates the present author to argue that

since the main examination of this study focuses on the cycle performance, preference is given to efficiency. Consequently, it is decided to fix the heat exchanger sizes to the values associated with the R744 discharge pressure of 12.0 MPa. Although larger pressure drops are associated with longer heat exchangers, it was revealed as insignificant with respect to the high working pressures of R744 in a transcritical cycle. A summary of the design outputs is given in Table 6-2. appendix a also includes a T-s and P-h diagram of the cycle at the final decided design condition.

Table 6-2: Resulting design outputs of the heat pump system.

Parameter	Value	Unit
Heating capacity	31.39	$[kW]$
Power consumption	10.44	$[kW]$
Cooling capacity	20.95	$[kW]$
Cycle COP_H	3.01	$[-]$
R744 Discharge pressure	12.0	$[MPa]$
R744 Discharge temperature	112.1	$[°C]$
R744 Mass flow rate	0.148	$[kg/s]$
Gas cooler length	30.32	$[m]$
Evaporator length (full coil length of one circuit)	4.15	$[m]$

6.4 Conclusion

In this chapter, a discussion was given on the compressor selection and heat exchanger designs to be used in the full-cycle model that will ultimately simulate the desired conditions of this study. This was executed according to the criteria of design conditions, which were defined as the worst possible combination of operating conditions considered by this study. In other words, the system was over-designed to ensure a sufficient system capacity for the whole range of conditions to be examined in the next chapter.

The design conditions were then used to select the most applicable transcritical R744 compressor with aid of the Bitzer (2022) software. After proving to satisfy the required heating capacity, R744 discharge temperature, and R744 mass flow rate, the Bitzer 4MTE-10K compressor model was designated. Hence, with the compressor selected and the design conditions used as inputs into the full-cycle model, the resulting heat exchanger sizes were simulated. For simplification, excluding the lengths, it was decided to keep the other heat exchanger geometries constant to those used in Chapter 5.

Seen that an operating condition (design condition in this case) can be satisfied by more than one R744 discharge pressure, the resulting heat exchanger lengths and considered performance parameters were evaluated over an appropriate R744 discharge pressure range of 12.0 to 14.0

MPa. These considered performance parameters included the overall heat transfer coefficient of the gas cooler, compressor power consumption, cooling capacity, and cycle COP_H. Resultingly, a trade-off between the system installation costs (component sizes) and operational costs (system efficiency) was identified. For the purpose of this study, it was decided to favour the efficiency aspect of the system design and thus choose the design that yields the highest system COP_H (at 3.01). The associated gas cooler and evaporator lengths were found as 30.32 m and 4.15 m, respectively.

As a result, the objective of this chapter has been achieved, i.e., to calculate the most appropriate system design that will allow for the whole range of desired operating conditions to be simulated (in the next chapter).

7. CHAPTER 7: SIMULATION RESULTS

Considering that a numerical model of the transcritical R744 heat pump system has been i) developed on appropriate correlations and modelling approaches, ii) verified and validated, and iii) sufficiently sized for the whole range of intended conditions of this study, the actual investigation of the cycle performance at the desired conditions can now be performed with aid of simulations. Note that the approach of sizing the system to the most appropriate value and evaluating the performance of the sized system is analogous to the eight studies that were reviewed in Section 2.2.1, as well as to an experimental/real world set-up.

In this chapter, the key purpose is to evaluate the system performance at water outlet temperatures around 90°C over an ambient temperature range of 25°C to 40°C. This will be done using both the following approaches:

1. Operating at fixed water mass flow rates (simulation inputs) over the 25 - 40°C ambient temperature range (also simulation inputs), such that water outlet temperatures in the order of 90°C will result (simulation outputs).
2. Operating at a fixed water outlet temperature of 90°C (simulation input) over the 25 - 40°C ambient temperature range (also simulation inputs). In this way, varying water mass flow rates will result (simulation outputs).

In parallel to the above-indicated outputs, further outputs are the cycle performance parameters that will also be evaluated. This will typically include the cycle COP_H, power consumption, heat transfer and mass flow rates.

Following the above, an additional investigation will be done into the cycle performance when operating at higher ambient humidity and water inlet temperatures. Before any of the aforementioned are initiated, it is important to discuss the subordinate operating conditions that also form part of the study.

Standard operating conditions:

Apart from the above-mentioned key operating conditions, certain other operating conditions exist that are not directly examined, although, still form part of the study. These will be referred to as standard operating conditions. On the airside, these include the air (ambient) pressure, humidity, and inlet velocity. On the waterside, this entails the inlet water pressure. Respective to the refrigerant, this includes the evaporation temperature approach. Note that these parameters are listed in Table 7-1, and that their assigned values are consistent with those in Section 6.1 (please

refer back for the rationale of the specific values). Also note that these operating conditions will be held constant throughout the investigation, with the main focus on the above-mentioned main operating conditions.

To avoid confusion, the following statement regarding the R744 discharge pressure is reiterated: As revealed in literature, there exists more than one R744 discharge pressure that can satisfy an operating condition, yet, at different efficiencies. The R744 discharge pressure that yields the highest system COP_H is known as the ODP for that condition. With the investigation focussed on the cycle performance subject to ambient temperature, for each condition, the R744 discharge pressure will thus still be varied from 12.0 MPa to 14.0 MPa in search of the optimal condition. Hence, the R744 discharge pressure varied over the aforementioned range is also viewed as a standard operating condition(s).

Table 7-1: Standard operating conditions (standard simulation inputs) at which the system performance is to be evaluated (per condition of interest).

Fluid	Parameter	Symbol	Value	Unit
Water	Inlet pressure	$P_{w,i}$	250.0	$[kPa]$
	Inlet temperature	$T_{w,i}$	15	$[°C]$
Air (ambient)	Inlet velocity	V_a	3.0	$[m/s]$
	Inlet RH	RH_i	30.0	$[\%]$
	Inlet pressure	$P_{a,i}$	85.0	$[kPa]$
R744	Evaporation temperature approach	$T_{a,i}(WB) - T_e$	8.0	$[°C]$
	Discharge pressure	P_{dis}	12.0 – 14.0	$[MPa]$

Note that the results in this chapter are only presented in a graphical format, with the tabulated results provided in appendix b.

7.1 Effect of ambient temperature at fixed water mass flow rates

In this section, the influence of an ambient temperature (25 – 40°C) on the system performance will be evaluated for fixed water states that enter the gas cooler. These fixed inlet water conditions entail a temperature of 15°C at mass flow rates of 0.09 kg/s, 0.10 kg/s, and 0.11 kg/s, which are expected to yield water outlet temperatures in the order of 90°C.

Since the water mass flow rate and usual R744 discharge pressure are also variables of this section, their influences will firstly be considered to later bring into perspective when evaluating the effect of the ambient temperature (main section topic). Figure 7-1 and Figure 7-2 illustrate the resulting water outlet temperature and system COP_H for the current scenario. Note that due to an

insufficient DOS, the model was unsolvable at an ambient temperature of 25°C and R744 discharge pressures greater than 13.0 MPa.

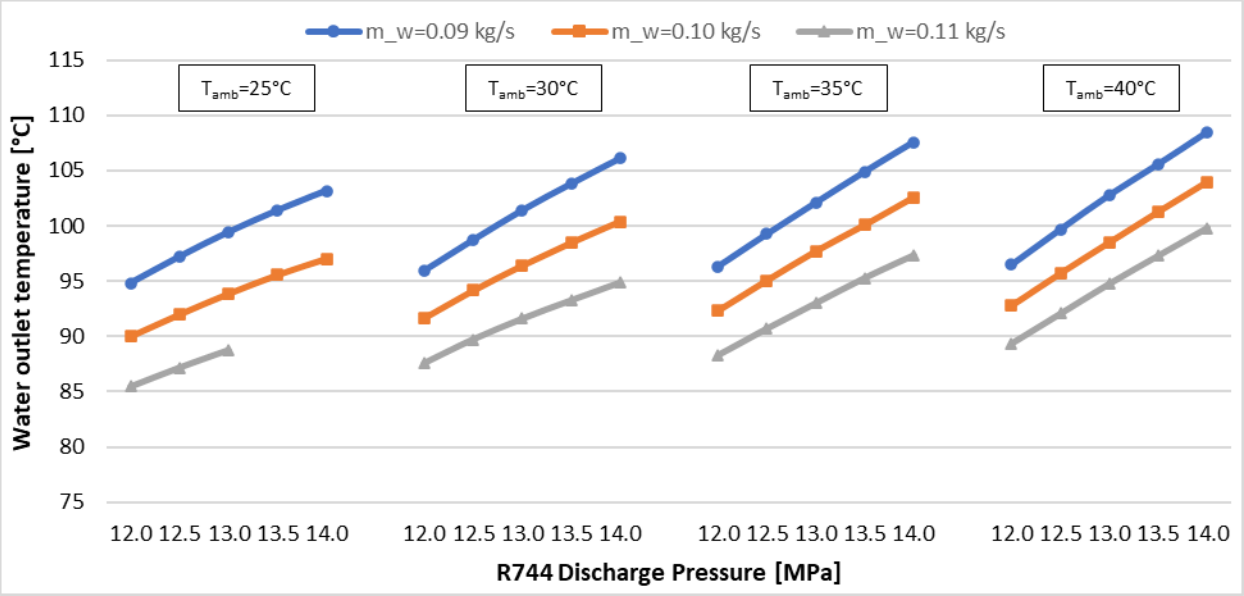

Figure 7-1: Resulting water outlet temperatures at fixed water mass flow rates over a range of ambient temperatures.

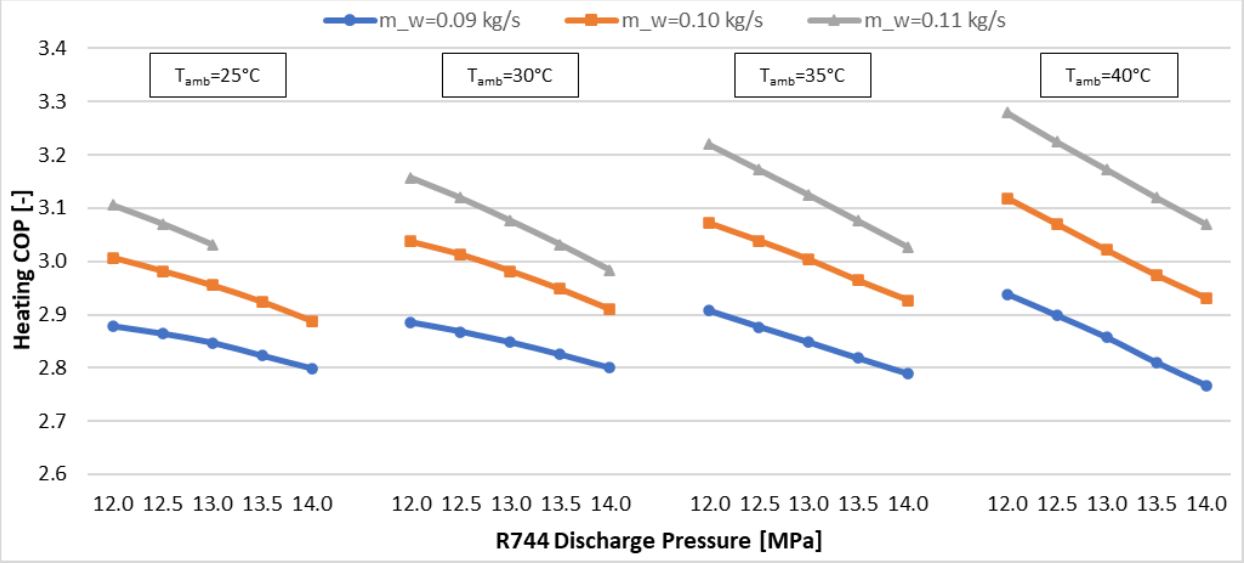

Figure 7-2: Resulting cycle COP_H at fixed water mass flow rates over a range of ambient temperatures.

I. Effect of R744 discharge pressure:

Regardless of the ambient temperature and water mass flow rate, as reported in the literature review, it is seen from Figure 7-1 that an increase in R744 discharge pressure leads to a rise in water outlet temperature. For example, at the 0.10 kg/s mass flow rate and 25°C ambient

temperature, the water outlet temperature rose 7.8% from 90.0°C to 97.0°C when the R744 discharge pressure increased from 12.0 MPa to 14.0 MPa.

Figure 7-2 shows that also irrespective of the other variables, an increase in R744 discharge pressure over the mentioned range leads to a decrease in cycle efficiency. In other words, the efficiencies improve as the R744 discharge pressures lower. For the same condition change example as above, the cycle COP_H reduced by 4.0% from 3.01 to 2.89.

Note that the above statements are only claimed for the considered R744 discharge pressure range of 12.0 to 14.0 MPa, which was chosen for its relevancy to this study's interest in high-water outlet temperatures. It is likely that the COPs will continue to increase with a further decrease in R744 discharge pressure to a point where it reaches its absolute maximum (at the ODP), and then decrease with an even further lowering of R744 discharge pressure. However, the lower water outlet temperatures that will result in such a case are not part of the current scope. In the next section, at a high water outlet temperature of interest, more focus will be placed on the ODP and maximum efficiencies.

II. Effect of water mass flow rate:

Opposite to the effect of increasing R744 discharge pressure, a rise in water mass flow rate leads to a reduction in water outlet temperature and improvement in system efficiency, which agrees with literature. For instance, Figure 7-1 demonstrates that at an ambient temperature of 25°C and R744 discharge pressure of 12.0 MPa, the water outlet temperature lowered from 94.8°C to 85.5°C (-9.8%) as the water mass flow rate increased from 0.09 kg/s to 0.11 kg/s. For the equivalent variation in conditions, Figure 7-2 shows that the cycle COP_H rose from 2.71 to 2.88 (+8.0%).

III. Effect of ambient temperature:

As illustrated by the two mentioned figures, an increase in ambient temperature has a positive influence on both the water outlet temperature and cycle efficiency results. For instance, at a 0.10 kg/s water mass flow rate and 12.0 MPa R744 discharge pressure, as the ambient temperature rose from 25°C to 40°C, the water outlet temperature slightly increased from 90.0°C to 92.8°C (+3.1%), whilst the cycle COP_H marginally enhanced from 3.01 to 3.12 (+3.7%).

It can also be seen that for the same water outlet temperature, the increased ambient temperature allows the system to deliver a greater water mass flow rate. For illustration, at an ambient temperature of 25°C and R744 discharge pressure of 12.0 MPa, the cycle was able to yield 90°C

water at a mass flow rate of about 0.10 kg/s, whereas at an ambient temperature of 40°C, the same condition resulted in a water mass flow rate of 0.108 kg/s. This variation in condition is also linked to a COP_H enhancement from 3.01 to 3.25 (+8.0%). More information regarding the influence of ambient temperature at a constant water output temperature follows in the next section.

Furthermore, Figure 7-1 demonstrates that as the ambient temperature increases, a lower R744 discharge pressure is required to achieve the same water output (both in terms of mass flow rate and temperature). For instance, at an ambient temperature of 25°C, to supply 0.10 kg/s of water at 95°C, a discharge pressure of around 13.4 MPa was required, whereas at an ambient temperature of 40°C, an R744 discharge pressure of only around 13.4 MPa was needed. As can be seen from Figure 7-2, this 7.5% reduction in R744 discharge pressure is linked to a 4.9% improvement in COP_H from 3.08 to 2.93.

Based on the above discussion, for a given R744 discharge pressure, an increase in ambient temperature enables the system to yield the same amount of water at a higher outlet temperature, or a larger mass flow rate at the same outlet temperature. The accompanying cycle efficiency improvement was noted higher for a constant water outlet temperature (+8.0%) than for a constant water mass flow rate (3.7%). Furthermore, also due to a higher ambient temperature, the system was able to supply the same water output (mass flow rate and temperature) at a reduced R744 discharge pressure and improved cycle efficiency.

As seen in this section, an increase in ambient temperature affects the water stream both in terms of mass flow rate and output temperature. In parallel, the R744 discharge pressure also influences these two parameters. In the section to follow, the examination will be narrowed by examining the ambient temperature's effect at the already-best efficiency conditions in terms of R744 discharge pressure (i.e., at the ODPs), in conjunction with a constant (and high) water outlet temperature. This will emphasize the ambient temperature's influence and accordingly address the problem statement, which is to study the system's performance at a high water outlet temperature (such as 90°C) subject to high ambient temperatures.

7.2 Effect of ambient temperature at a fixed water outlet temperature

In the previous section, the effect of ambient temperature on the system performance was considered when operating at fixed water mass flow rates entering the gas cooler at 15°C, which yielded water outlet temperatures around and above 90°C. In this section, it is of interest to do the same, except that the water will now be heated to explicitly 90°C. Firstly, per ambient

temperature, the ODP and corresponding cycle COP_H will be identified and compared to the most appropriate studies identified in literature (Section 2.1.3). Hence, the influence of the ambient temperature on these two parameters will be thoroughly evaluated by considering further cycle performance parameters such as the compressor work rate, heat transfer rates, and mass flow rates.

Note that for both a given water inlet and outlet temperature (simulation inputs), the water mass flow rate will resultingly vary (simulation output). This is also the investigation method that was used by Yamaguchi *et al*. (2011), Wang *et al.* (2013a), and Ye *et al.* (2020). In a practical set-up, this can be achieved by regulating the water's mass flow rate to control its temperature with aid of a control valve and proportional integral derivative (PID) controller (Wang, *et al.,* 2013a).

7.2.1 Resulting COP_H and ODP

Per considered ambient temperature, Figure 7-3 illustrates the resulting COP_H values of the system when operating at a constant 90°C water outlet temperature over the standard range of R744 discharge pressure. Note that due to an insufficient DOS, the simulation was unsolvable at an ambient temperature of 25°C and R744 discharge pressures greater than 13.0 MPa, and at an ambient temperature of 30°C and R744 discharge pressures of 14.0 MPa.

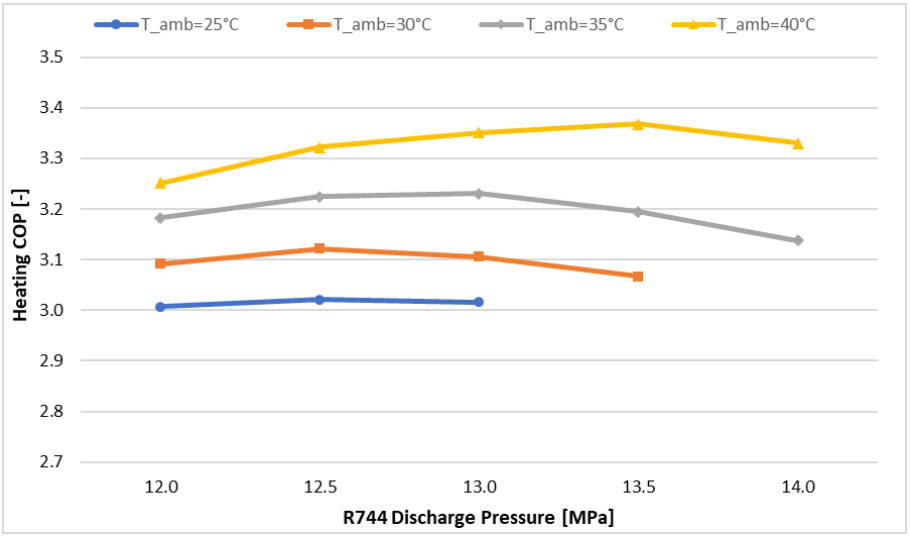

Figure 7-3: Cycle COP_H at a 90°C water discharge temperature resulting under various ambient temperatures over a range of discharge pressures.

Generally, as the ambient temperature increases, the resulting efficiencies are seen to be more sensitive to a variation in R744 discharge pressure variations. The ODP range and best-recorded COP_H values are summarised in Table 7-2. It is evident that the ODP slightly rises with an increase in ambient temperature. At the 25°C, 30°C, and 35°C ambient temperatures, the ODP lied within

the range of 12.5 -13.0 MPa, whereas at the 40°C ambient temperature, the ODP was situated within the 13.0-13.5 MPa range. This also proves that the considered range of R744 discharge pressures (12.0 – 14.0 MPa) is adequate for the present investigation. Furthermore, as the ambient temperature rose from 25°C to 40°C, the highest recorded COP_H value improved by 11.6% from 3.02 to 3.37. These findings are further evaluated in the following sub-section in perspective with literature.

Table 7-2: Summary of the resulting ODP range and best-recorded COP at a 90°C water outlet temperature and 25-40°C ambient temperature range.

Ambient temperature (DB / WB) [°C]	ODP range [MPa]	Best recorded COP_H [-]
25.0 / 13.7	12.5 – 13.0	3.02
30.0 / 17.3	12.5 – 13.0	3.12
35.0 / 20.8	12.5 – 13.0	3.23
40.0 / 24.4	13.0 – 13.5	3.37

Note that the aforementioned ambient temperature range of 25 - 40°C was reported in DB, which at a 30% relative humidity and 85 kPa ambient pressure, corresponds to a WB ambient temperature range of 13.7 – 24.4°C.

7.2.2 Comparison to the most applicable literature as identified in Section 2.1.3

As pointed out in the literature review, the studies of Yamaguchi *et al*. (2011) and Wang *et al.* (2013a) entailed operating conditions closest to those of interest in this study, and will now be brought into perspective with the above findings of the ODP and COP_H. Limitations to this comparison are that the former did not include any information relating to their ambient moisture content, and the latter included water outlet temperatures of only up to 80°C. However, in attempt to counter these limitations, the following rational assumptions will be made:

I. The study by Yamaguchi *et al*. (2011) was published in Tokyo, Japan. It is assumed that their examination occurred at the mean annual relative humidity of this area, i.e., 61.4% (He, *et al.,* 2021). Also, the little elevation of this area above sea level is neglected and standard atmospheric pressure is adopted. Consequently, a relevant WB air temperature range of 9.2 – 22.3°C can be assigned to their reported DB range of 13 – 28°C.
II. Wang *et al.* (2013a)'s recorded results do not include a water outlet temperature of 90°C. However, as depicted in Figure 7-4, their cycle COP_H at such temperature can be approximated by applying an exponential forecast to those at 60°C, 70°C, and 80°C water

outlet temperatures. Note that the *Forecast.Ets* function of Microsoft Excel was used to gather the data points at 90°C, after which it was plotted as shown. The same is done for the ODP values.

With the inclusion of the above-listed normalisations, the three sources in question now have an equivalent water outlet temperature and the data of Yamaguchi *et al*. (2011) and Wang *et al.* (2013a) will now be compared to the current results (as recorded in Section 7.2.1.). All three considered sources now have a water outlet temperature of 90°C to compare at an overlapping WB ambient temperature range of 13.7 to 22.3°C.

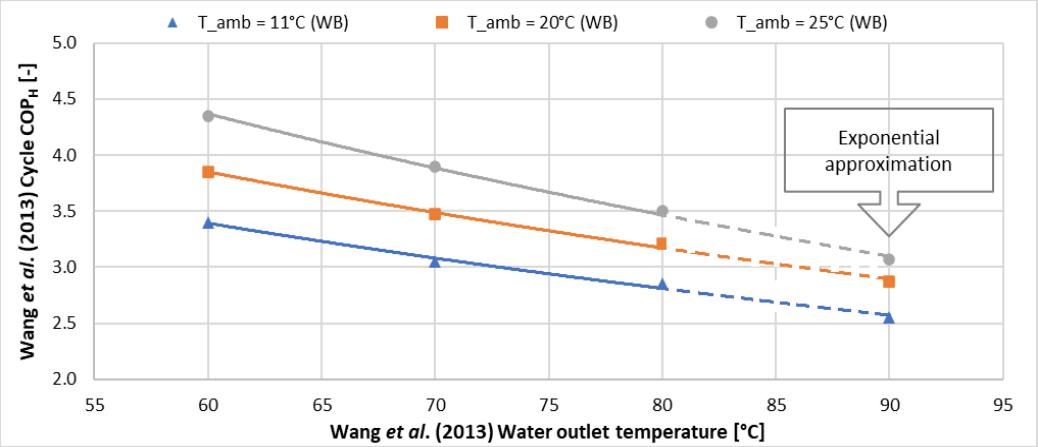

Figure 7-4: Exponential forecast of Wang et al. (2013)'s cycle COP at 90°C water outlet temperature.

7.2.2.1 ODP comparison

Considering that different compressors are used in the present comparison, focus is rather placed on the trend of the ODP (as a function of the ambient temperature). A more in-depth evaluation considering both the trend and quantification follows with the COP_H assessment.

Referring back to Section 7.2.1, the marginally indicated rise in ODP is to a limited extent contradicting to Yamaguchi *et al*. (2011), who reported that the ODP remained relatively constant around 12.5 MPa as the WB ambient temperature varied from 9.2°C to 22.3°C. This was noted at water inlet and outlet temperatures of 20°C to 90°C, respectively. The authors did not justify their finding of unchanged ODP with a variation in ambient temperature. Even so, although uncertainty exists regarding the exact ODP values of the present results, the ranges in which the ODP values were reported did not vary significantly with the rise in ambient temperature. Over the full ambient WB temperature range of 13.7 to 24.4°C, all the ODPs were found within a range of 12.5 - 13.5 MPa.

However, the noted increase in ODP with a rise in ambient temperature agrees with Wang *et al.* (2013a). As mentioned in Section 2.1.3, at a 12°C water inlet temperature and 80°C water outlet temperature, the researchers noted an ODP rise from around 11.7 MPa to 12.3 MPa with a WB ambient temperature increase from 11°C to 25°C. At the same water inlet and outlet temperatures as this study, this increase in ODP with a rise in ambient temperature was also reported by Ye *et al.* (2020).

7.2.2.2 COP_H comparison

As a function of WB ambient temperature, Figure 7-5 illustrates the resulting COP_H of the present simulation relative to two literature-based sources, which values have been rationally approximated. The illustrated COP_H as a function of ambient temperature will firstly be discussed by only considering the coincidence data points, after which a conclusion will follow regarding the question of this study, i.e., the performance of a transcritical R744 heat pump cycle when heating water to a high temperature such as 90°C at high (typically South African) ambient temperatures.

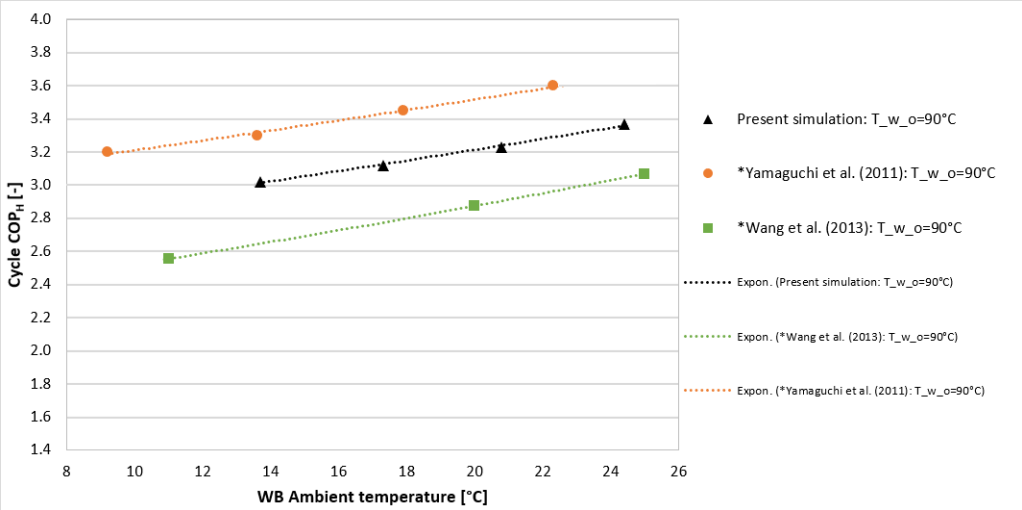

Figure 7-5: System COP_H comparison for operating at a 90°C water outlet temperature over a wide WB ambient temperature range. *Approximation used (as explained at the start of this sub-section).

Coinciding operating conditions

Over the coinciding WB ambient temperature range of 13.7 to 22.3°C, Table 7-3 summarises the resulting COP_H data. Both in terms of trend direction and rate of change, the present simulation yielded COP_H values in proportion to those of Yamaguchi *et al*. (2011) and Wang *et al.* (2013a). Furthermore, the current simulation quantified the COP_H values lower than those of Yamaguchi *et al*. (2011), yet, higher than Wang *et al.* (2013a). Likely reasons for these differences follow below.

Table 7-3: COP_H summary at coinciding WB ambient temperature ranges of the three considered sources.

Source	COP_H at overlapping WB temperature range of 13.7 – 22.3°C		
	Range	Rate of change	Average
Current simulation	3.02 – 3.29	+8.9%	3.16
Yamaguchi *et al*. (2011)	3.30 – 3.60	+9.1%	3.45
Wang *et al.* (2013a)	2.65 – 2.96	+11.9%	2.81

Unlike the present heat pump system, those of the two considered literature-based sources have an IHX, which is known for its positive influence on the system efficiency. As mentioned in Section 2.1.3, Cao et al. (2020) reported a 5.8% increase in system COP_H with the addition of an IHX. This reporting was related to the same water outlet temperature, although to a lower ambient temperature of 2°C. The difference in observed COP_H may also be justified by inconsistencies in the comparison such as the different compressors that operate closer to or further from their best efficiency points, as well as the finer differences in heat exchanger designs used. For instance, the gas cooler of Wang *et al.* (2013a) is made of one large diameter (64 mm OD) tube with twenty smaller diameter (7.9 mm OD) inner tubes, whereas that of Yamaguchi *et al*. (2011) consists of four parallel helically coiled tube-in-tube heat exchangers with smaller diameters (8.0 mm OD inner pipe and 13.5 mm ID outer pipe). That of the present cycle entails a single straight tube-in-tube heat exchanger with larger diameters (21.5 mm OD inner pipe and 26 mm ID outer pipe). Furthermore, seen that Yamaguchi *et al*. (2011) and Wang *et al.* (2013a) had experimental test benches, and they were able to verify the evaporation temperatures used, unlike the current numerical model that uses an approximation approach. This discrepancy may also be motivated by further comparison inconsistencies such as the differences in water inlet temperatures at which these respective systems were designed for and operated at, and the approximation errors linked to the recently described assumptions made for the literature-based data of this comparison.

As will be described in Chapter 8, a recommendation for further studies is to optimise the system with finer design aspects such as the diameter sizing and inclusion of an IHX. Also, the procurement of a test bench will enable the use of more precise evaporation temperatures to eliminate potential errors from the numerical approximation approach used in the current simulation. Nevertheless, the system performance in terms of ODP and efficiency has been proven to correlate with literature and is rendered tangible.

Performance of a transcritical R744 heat pump cycle when heating water to a high temperature such as 90°C at high (typically South African) ambient temperatures.

This sub-section has thus far shown that when the present system operates at a 90°C water outlet temperature, an increase in DB ambient temperature from 25°C to 40°C leads to a cycle COP_H increase from 3.02 to 3.37. This 11.6% improvement therefore proves an obvious advantage for this system to operate at the highest possible ambient temperature. However, when taking the ambient humidity into account, this performance at typically South African ambient temperatures was not found significantly higher than those of Yamaguchi *et al*. (2011) and Wang *et al.* (2013a), who included lower ambient temperatures, yet, at higher humidity. In addition to the ambient temperature, it is concluded that the ambient humidity is an important factor to also consider. In Section 7.3, an additional investigation will follow into the explicit influence of ambient humidity when operating at such high ambient temperatures.

As the cycle performance has now been evaluated in terms of efficiency, the focus will shift to its underlying performance parameters.

7.2.3 Resulting heat transfer rates, power consumption, and mass flow rates

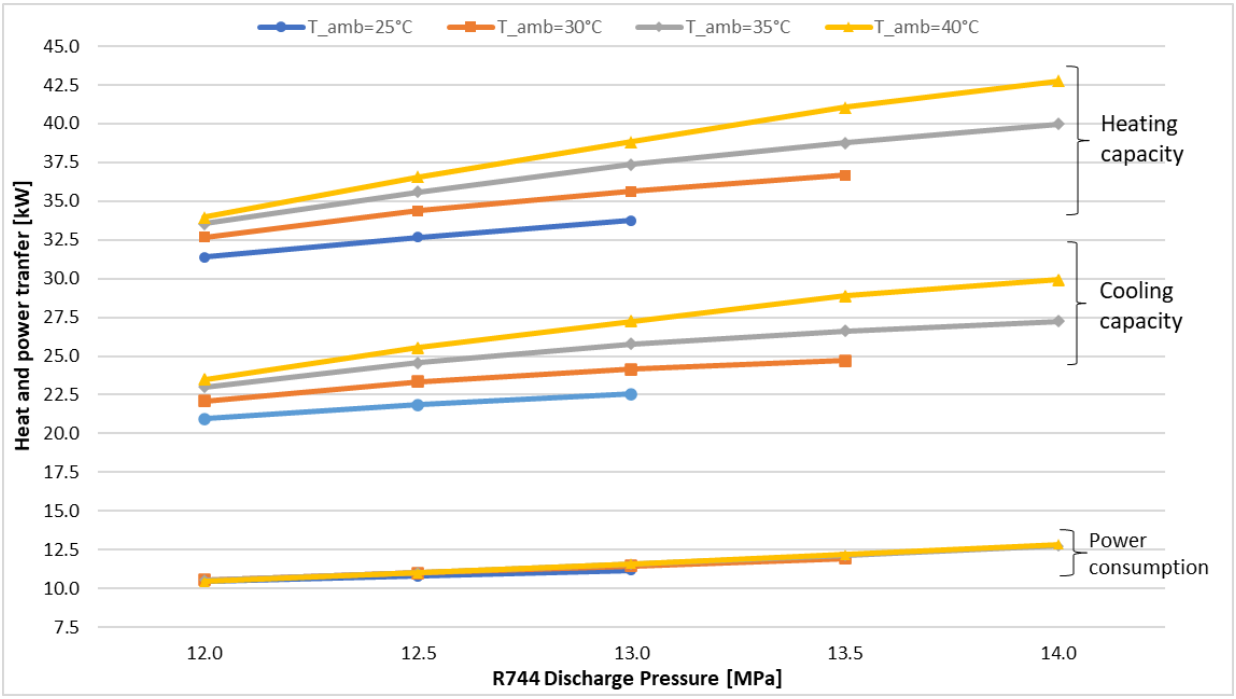

Figure 7-6: Heat and power transfer at a 90°C water discharge temperature resulting at various ambient temperatures over a range of discharge pressures: Heating capacity, cooling capacity, and power consumption.

In light of the previous sub-section, per ambient temperature, the maximum recorded COP_H can also be explained with aid of the accompanying heating transfer rates and power consumption, as shown in Figure 7-6. Respective to increasing R744 discharge pressure, a rise in all three aforementioned parameters is present. As mentioned in literature, at R744 discharge pressures

lower than the ODP, for a given increase in ambient temperature, the rise in heating capacity is larger than that of the power consumption. This leads to the improvement in COP_H values as depicted in Figure 7-3. However, also as shown, at R744 discharge pressures beyond the ODP, the increase in power consumption becomes greater than that of the heating capacity.

In this sub-section, as influenced by the ambient temperature, the variations of the following parameters will now be discussed: a) Heating capacity, b) Cooling capacity, c) Power consumption, and d) Water mass flow rate.

a) Heating capacity:

From Figure 7-6, it is evident that a rise in R744 discharge pressure leads to an increase in heating capacity. For instance, at an ambient temperature of 25°C, the heating capacity rose from 31.4 kW to 33.8 kW (+13.6%) over the shown R744 discharge pressure range. The T-s diagram in Figure 7-7 shows that a higher R744 discharge pressure causes a lower R744 gas cooler outlet temperature, which results in enhanced R744 heat transfer properties in the gas cooler (Sarkar, *et al.,* 2006). The increase in R744 discharge pressure also leads to a higher R744 discharge temperature and thus a greater temperature difference in the gas cooler. From Figure 7-8, it is seen that the R744 mass flow rate is insignificantly affected by the change in R744 discharge pressure, as will be discussed further in this section. Thus, the rise in heating capacity due to an increase in discharge pressure is mainly caused by the improved transcritical R744 heat transfer properties and larger temperature difference in the gas cooler.

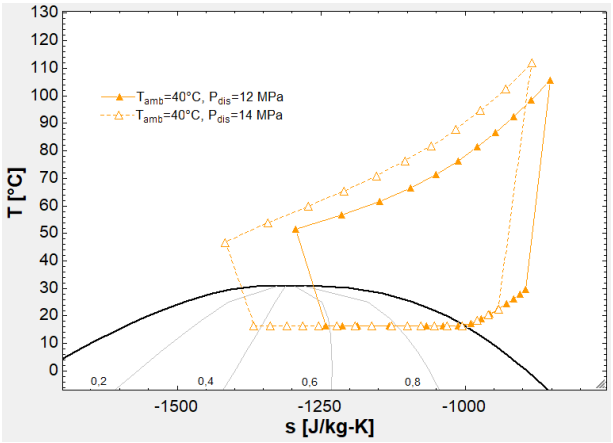

Figure 7-7: Resulting T-s diagrams at the minimum and maximum R744 discharge pressures at a 40°C ambient temperature.

Figure 7-6 further demonstrates that similar to an increase in R744 discharge pressure, a rise in ambient temperature also leads to a higher heating capacity. At 12.0 MPa R744 discharge pressure, this parameter improved from 31.4 kW to 33.9 kW (+8.0%) as the ambient temperature

rose from 25°C to 40°C. Figure 7-8 demonstrates that a rise in ambient temperature causes a higher R744 mass flow rate, which agrees with Yamaguchi *et al*. (2011). As the ambient temperature increased from the indicated minimum to maximum, an average R744 mass flow rate increase of 44.6% resulted. As a result of the increased R744 mass flow rate, the local heat transfer coefficient of the R744 stream rises, which leads to improved heating capacity.

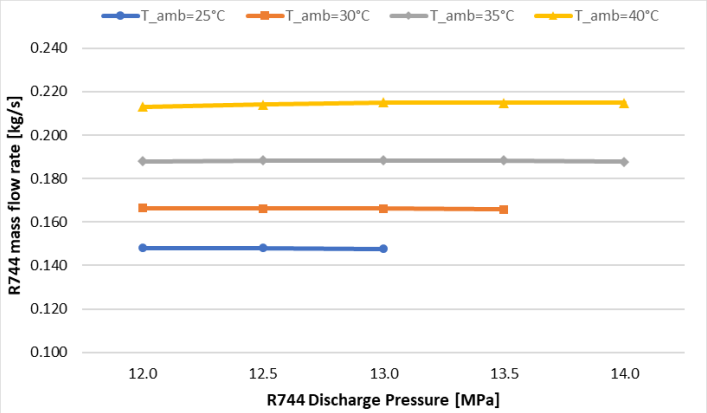

Figure 7-8: Resulting R744 mass flow rates at a 90°C water discharge temperature resulting at various ambient temperatures over a range of discharge pressures.

Note from Figure 7-6 that the positive effect of the ambient temperature on the heating capacity also becomes more significant as the R744 discharge pressure rises (as well as the other way around). This can be justified by the concurrent influence of the increased R744 discharge pressure and ambient temperature as described above. Over the considered ambient temperature range, the heating capacities linked to the best-recorded efficiencies rose by 25.7% from 32.7 kW to 41.1 kW.

It is mentioned once again that as revealed in Section 6.3.1, the pressure drop of the present designed system is insignificant and therefore not explicitly reported upon (although still accounted for in the simulation and still implicitly part of the results). Also as mentioned, this may not be the case for gas coolers with smaller R744 pipe diameters or significantly larger R744 mass flow rates.

b) Cooling capacity:

Figure 7-6 reveals that the cooling capacity rises with both increased ambient temperature and R744 discharge pressure. The former can simply be justified by the additional thermal energy that is rejected by the incoming air in the evaporator, leading to a higher suction temperature and thus R744 mass flow rate. The latter causes the R744 to exit the gas cooler at a reduced temperature, leading to a lower vapour quality at the evaporator inlet. Since a better local R744 heat transfer

coefficient is present at lower vapour qualities, the overall heat transfer in the evaporator increases (Rigola, *et al.,* 2010). As in the case of the heating capacity, this effect also becomes more significant at higher ambient temperatures. As mentioned above, this is due to the higher resulting R744 mass flow rate that further improves the local R744 heat transfer coefficient (in the evaporator as well). Note that at the conditions corresponding to the ODP values, the cooling capacity improved by 32.0% from 21.9 kW to 28.9 kW over the indicated ambient temperature range.

c) Power consumption

As is evident in Figure 7-6, the power consumption rises with an increase in R744 discharge pressure. As mentioned before, for the present numerical model, the evaporation temperature is assumed constant per given ambient temperature. As illustrated in Figure 7-9, for a given ambient temperature, with an increased R744 discharge pressure, a larger pressure ratio needs to be overcome by the compressor. As a result, the enthalpy difference over the compressor increases. Per ambient temperature, from Equation (3.13), it can be inferred that with an unchanged R744 mass flow rate, the increase in compressor power greater is caused by the aforementioned increase in enthalpy difference.

As mentioned above, per ambient temperature, the R744 mass flow rate is insignificantly affected by the R744 discharge pressure. Figure 7-7 depicts that with an increase in R744 discharge pressure, the R744 stream enters the compressor at a lower temperature. With a reduced suction temperature, higher volumetric efficiency and mass flow rate follow (He, *et al.,* 2020b). Although, since the R744 discharge pressure and thus pressure ratio rises, the positive effect on the volumetric efficiency and mass flow rate is countered. Therefore, in this case, the two described influences on the R744 mass flow rate fairly neutralise each other.

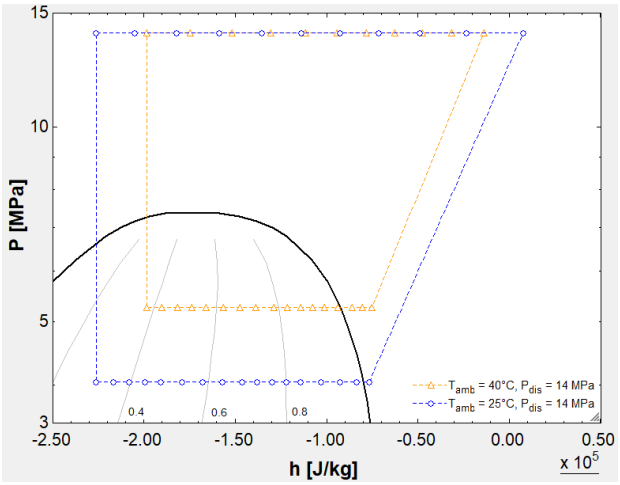

Figure 7-9: Resulting P-h diagram at the minimum and maximum ambient temperatures at a 14 MPa R744 discharge pressure.

As can further be seen in Figure 7-6, a variation in ambient temperature had an insignificant influence on the power consumption. For a given R744 discharge pressure, a rise in ambient temperature will result in a higher evaporation temperature and consequently suction pressure or in other words, a lower pressure ratio. Hence, a smaller enthalpy difference over the compressor results, as is depicted in Figure 7-9. It is known from Equation (3.13) that the power consumption is affected by both the R744 mass flow rate and the difference in specific enthalpy states over the compressor. As it has now been explained that a higher ambient temperature leads to an increase in the former and decrease in the latter, it can be inferred the concurrent effect of these two parameters leads to a counterbalanced power consumption. Nevertheless, as driven by the rise in ODP, the power consumption at the maximum recorded efficiency point increased by 12.9% from 10.8 kW to 12.2 kW as the ambient temperature varied from 25°C to 40°C.

d) Water mass flow rate

Based on the discussions in this section, from Equation (3.15), by assuming a negligible variation in the specific heat of water under the present conditions, it can be inferred that the resulting water mass flow rate is directly proportional to the heating capacity. Hence, as the ambient temperature rose from 25°C to 40°C, the water mass flow rate increased by 25.7% from 0.104 kg/s to 0.131 kg/s. Table 7-4 provides a summary of the discussed parametric variations over the considered ambient temperature range of 25 - 40°C (as linked to the optimal recorded COPs).

Table 7-4: Parametric summary of the cycle performance when heating water to 90°C over an ambient temperature range of 25-40°C.

Performance parameter	Range linked to ambient temperature range of 25-40°C
Best recorded COP_H [-]	3.02 – 3.37 (+11.6%)
ODP range [MPa]	12.5 – 13.5 (+8.0%)
Heating capacity $[kW]$	32.7 – 41.1 (+25.7%)
Cooling capacity $[kW]$	21.9 - 28.9 (+32.0%)
Power consumption $[kW]$	10.8 - 12.2 (+12.9%)
R744 mass flow rate $[kg/s]$	0.148 – 0.214 (+44.6%)
Water mass flow rate $[kg/s]$	0.104 – 0.131 (+25.7%)

In conclusion of this section, the influence of ambient temperature on the performance of a transcritical R744 heat pump system was evaluated at a fixed water outlet temperature of 90°C over an ambient temperature range of 25 – 40°C as typically found in South Africa. Per considered ambient temperature, the corresponding ODP and maximum COP_H were evaluated. As the ambient temperature rose, both these performance parameters increased. A comparison with literature sources that involved the closest operating conditions to the present investigation was performed, and rational assumptions were made to aid with the comparison's consistency. In view of Yamaguchi *et al*. (2011) and Wang *et al.* (2013a), the simulated results were found to be tangible. As the ambient temperature varied over the aforementioned range, a corresponding increase in heating capacity from 32.7 kW to 41.1 kW (+25.8%) and COP_H increase from 3.02 to 3.37 (+11.6%) were noted. In addition to the mentioned parameters, further performance aspects such as the cooling capacity, power consumption, and mass flow rates were thoroughly analysed.

Although at higher ambient temperatures, the noted cycle efficiencies were not notably higher than those of literature, which involved lower ambient temperatures, yet, at higher humidity. Accordingly, the ambient humidity is deemed an important factor to weigh in addition to the ambient temperature. In the next section, a brief investigation follows on the explicit influence of the air relative humidity.

7.3 Additional investigation: The influence of higher ambient humidity and water inlet temperatures

In this section, a concise evaluation follows of the system performance subject to the distinct influences of the ambient relative humidity and water inlet temperature. Note that up to this point, these two parameters were fixed as standard operating conditions, however, in the two subsections to follow, they will be respectively varied.

7.3.1 Higher ambient relative humidity

In Section 7.2, it was revealed that ambient humidity is an important factor to weigh in addition to the ambient temperature's influence on the system performance. In this section, at an ambient temperature of 40°C, the influence of higher relative humidity will be considered from a value of 30% up to 60%, which corresponds to a WB ambient temperature range of 24.4 – 32.3°C. Note that this is an expansion of the WB ambient temperature range in Section 7.2 (13.7 – 24.4°C) and that all other operating conditions are kept the same as in the aforementioned section.

Initial approach:

Figure 7-10 illustrates the R744 discharge temperature, cycle COP_H, and heating capacity of the above-mentioned conditions. Note that the simulation was unsolvable at a relative humidity of 60%, as well as a relative humidity of 50% with R744 discharge pressures lower than 13.0 MPa. This is due to the aforementioned conditions yielding R744 discharge temperatures lower than 94.0°C, which is disregarded since the minimum allowable pinch point of the simulations has been defined as 4°C. These relatively low R744 discharge temperatures are illustrated in Figure 7-10a and as will be explained shortly, are also concluded as the reason for the degradation in system efficiency (Figure 7-10b) and heating capacity (Figure 7-10c). Note that these degradations are in contradiction with literature, which states that an increase in ambient relative humidity has a similar influence on the cycle efficiency than an increase in ambient temperature (Lin, *et al.,* 2013).

Note that as mentioned before, the current simulation makes use of a constant evaporation temperature approach. Since such high WB ambient temperatures are of interest, the evaporation temperatures are resultingly also high, which leads to higher suction pressures and thus lower pressure ratios. With the lower pressure ratios, lower R744 discharge temperatures results. For this reason, it is decided to adapt the evaporation temperature approach for this section (and this section only). Instead of the 8°C lower value than the WB ambient temperature, the evaporation temperature will be limited to that of the 30% relative humidity condition. Hence, it is expected that the pressure ratios will be high enough to supply sufficient R744 discharge temperatures and thus gas cooler pinch points. This change in approach for the current conditions is summarised in Table 7-5. Note that in a practical setup, this can be achieved by setting a lower downstream limit for the expansion valve.

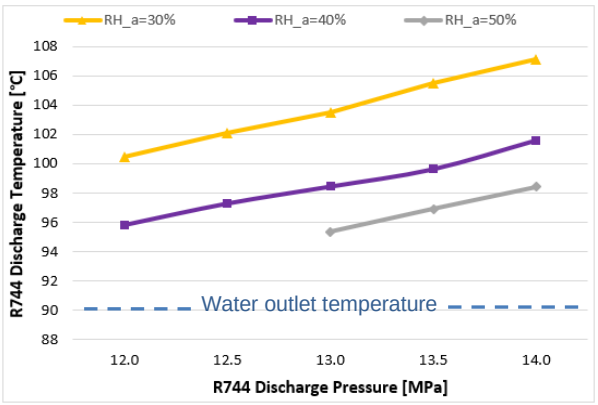

a) R744 discharge temperature

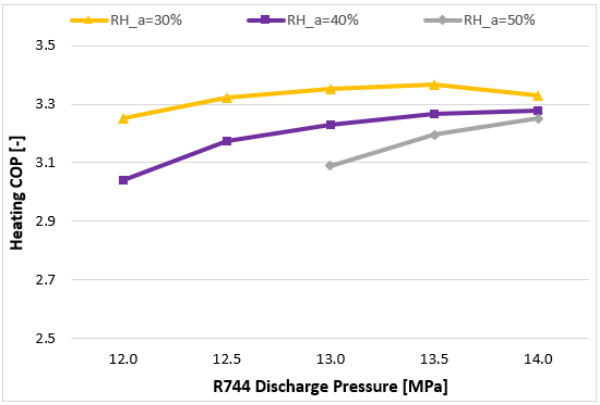

b) Heating COP

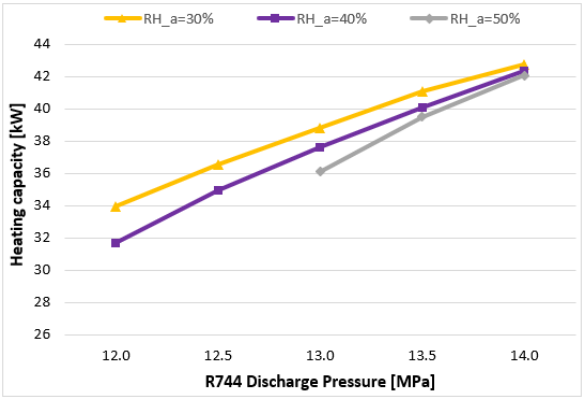

c) Heating capacity

Figure 7-10: Resulting cycle parameters at a 90°C water discharge temperature, 40°C ambient temperature, and range of air relative humidity with the constant 8°C evaporation temperature approach used: a) R744 Discharge temperature, b) Cycle heating COP, and c) Heating capacity.

Table 7-5: Summary of change in evaporation temperature approach for higher ambient relative humidity values at an ambient temperature of 40°C and water outlet temperature of 90°C.

Ambient relative humidity [%]	WB ambient temperature [°C]	Evaporation temperature using constant approach [°C]	Evaporation temperature using adapted approach [°C]
30	24.4	16.4	16.4
40	27.3	19.3	16.4
50	30.0	22.0	16.4
60	32.3	24.3	16.4

Adapted approach:

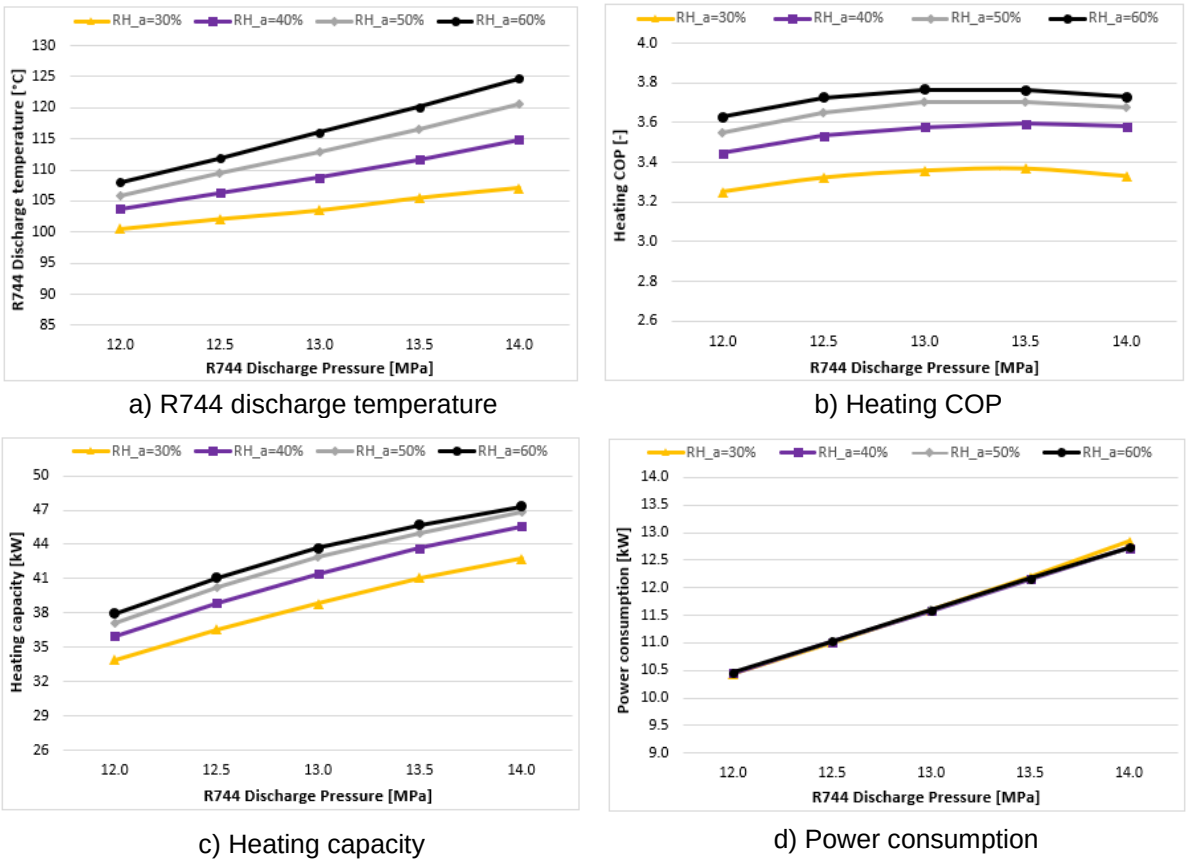

a) R744 discharge temperature

b) Heating COP

c) Heating capacity

d) Power consumption

Figure 7-11: Resulting cycle parameters at a 90°C water discharge temperature, 40°C ambient temperature, and range of air relative humidity adapted to a fixed evaporation temperature of 16.4°C: a) R744 Discharge temperature, b) Cycle heating COP, c) Heating capacity, and d) Power consumption.

Figure 7-11a shows the R744 discharge temperatures that resulted over a range of relative humidity values by rather using a fixed evaporation temperature of 16.4°C. These values are seen to be higher than those of the initial approach and thus allow for greater pinch points within the gas cooler. This proves that this adapted approach is more suitable for very high ambient conditions such as WB temperatures ranging from 24.4°C to 32.3°C.

From Figure 7-11b, it is evident that cycle COP_H increases with a rise in ambient relative humidity, which aligns with literature (Lin, *et al.,* 2013). As the relative humidity rose from 30% to 60%, the best-recorded COP_H value enhanced from 3.37 to 3.77 (+11.9%). Other than expected, the ODP did not increase due to an increase in relative humidity and may be a result of the adapted approach, which involves a fixed evaporation temperature. Subject to an increase in this parameter, Lin *et al.* (2013) only recorded a marginal increase (roughly negligible) in ODP. Considering the currently assumed evaporation temperature, this noted trend is thus not unreliable.

Similar to the influence of a higher ambient temperature, this parameter contributes to a higher thermal load that is absorbed by the system. Respective to the conditions of best-recorded COP_H, Figure 7-11c depicts an increase in heating capacity from 41.1 kW to 43.7 kW (+6.3%), whilst Figure 7-11d shows that the power consumption was fairly unaffected by a change in relative humidity. These trends are also in line with those subject to an increase in ambient temperature.

7.3.2 Higher water inlet temperature

In water heating systems, the water circulates between the heat pump and a storage vessel until the required temperature is achieved. During an operating cycle, this causes the water inlet temperature to rise. In this section, at an ambient temperature of 25°C and water outlet temperature of 90°C, the cycle performance will be considered at water inlet temperatures ranging from 15°C up to 60°C. Whilst doing so, the standard operating conditions outlined in Table 7-1 still apply. With the influence of R744 discharge pressure on the various performance parameters already evaluated in the previous sections of this chapter, only the effect of the water inlet temperature will be focused on.

Figure 7-12a illustrates that cycle COP_H substantially downgrades due to a rise in water inlet temperature. As the water inlet temperature rose from 15°C to 60°C, the best-recorded cycle efficiency reduced from 3.02 to 1.93 (-36.1%). The margin of decrease also becomes more significant as the water inlet temperature increases. When the water inlet temperature rose from 15°C to 30°C, 30°C to 45°C, and 45°C to 60°C, the maximum cycle COP_H decreased by 8.6%, 14.1%, and 18.6%, respectively. This trend agrees with Yamaguchi *et al*. (2011), who recorded an 11.8% decrease in system efficiency as the water inlet temperature varied from 15°C to 30°C.

Also note from Figure 7-12a that as the water inlet temperature rises, the ODP monotonically increases. In this case, at water inlet temperatures of 45°C and higher, the ODPs were restricted to the maximum permissible value of the present compressor (14.0 MPa). This increase in ODP subject to the higher water inlet temperatures also agrees with Yamaguchi *et al*. (2011) and Ye *et al.* (2020).

Figure 7-12b shows that the power consumption is insignificantly affected by the water inlet temperature, which agrees with Yamaguchi *et al*. (2011). Since the evaporation temperature is assumed constant per ambient temperature, for a given R744 discharge pressure, the only varying parameter is the suction temperature. From Figure 7-12e, per R744 discharge pressure, it can be seen that the suction temperature increases due to a rise in water inlet temperature, as will be described further on in this section. Yet, as mentioned, this effect is insignificant to the compressor work rate.

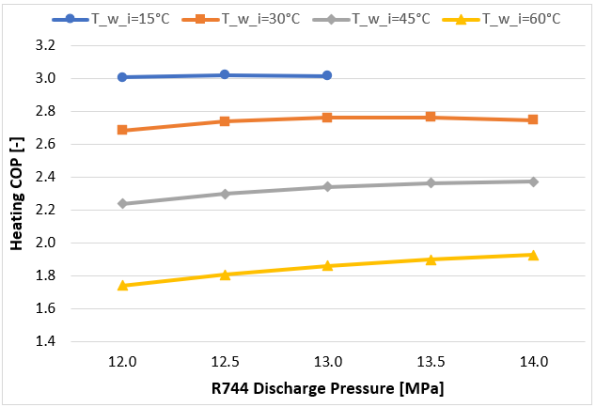

a) Heating COP

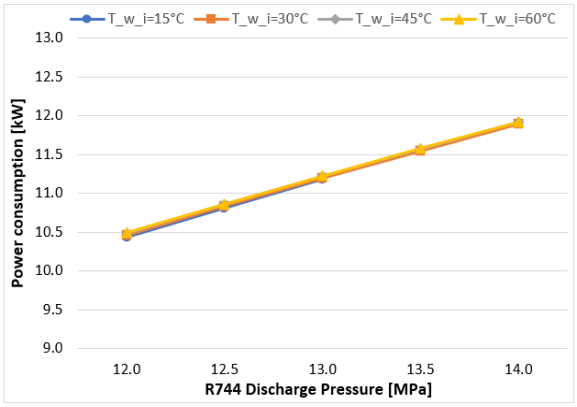

b) Power consumption

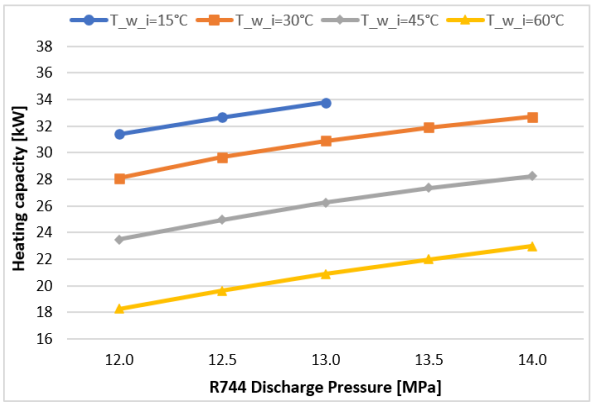

c) Heating capacity

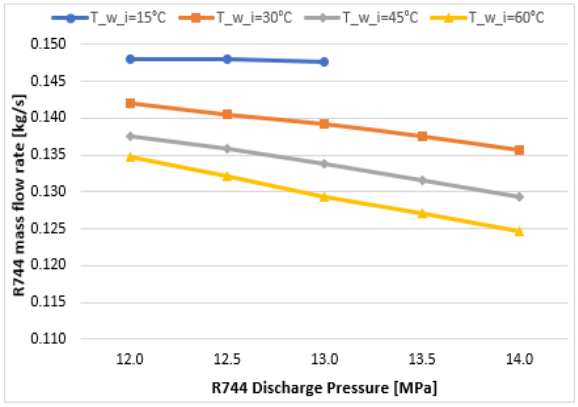

d) R744 mass flow rate

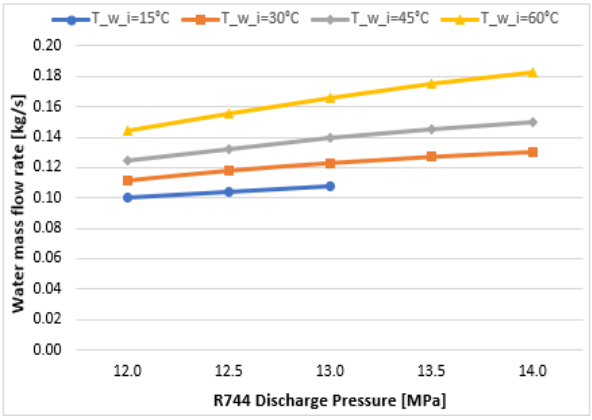

e) Water mass flow rate

Figure 7-12: Resulting cycle parameters at a 90°C water discharge temperature over a range of water inlet temperature: a) COP_H, b) Power consumption, c) Heating capacity, d) R744 mass flow rate, and e) Water mass flow rate.

Figure 7-12c demonstrates that the heating capacity considerably reduces due to a rise in water inlet temperature. At an R744 discharge pressure of 12.0 MPa, the heating capacity reduced from 31.4 kW to 18.1 kW (-42.4%) as the water inlet temperature varied from 15°C to 60°C. As revealed in the literature study, since the R744 gas cooler outlet temperature is restricted by the water inlet temperature, it rises accordingly and reduces the enthalpy difference over the gas cooler as well as the temperature difference between the two fluids. As is evident in Figure 7-13, for a given

R744 discharge pressure, the smaller gas cooler enthalpy difference driven by the higher water inlet temperature leads to a higher suction temperature. As a result, the compressor volumetric efficiency and R744 mass flow rate reduce. Over the considered water inlet temperature range, Figure 7-12d shows that the R744 mass flow rate reduced from 0.148 kg/s to 0.135 kg/s (-8.8%) at an R744 discharge pressure of 12.0 MPa.

In addition, as mentioned above, the R744 gas cooler outlet temperature rises subject to an increase in water inlet temperature. For this to happen, the R744 stream throughout the gas cooler also operates further from the transcritical region and will thus have lower local R744 heat transfer properties (Dai & Qin, 2022; Fronk & Garimella, 2011). This trend is similar to the conventional refrigeration system where an increase in condensing temperature leads to a downgrade in overall efficiency (Lin, *et al.,* 2013).

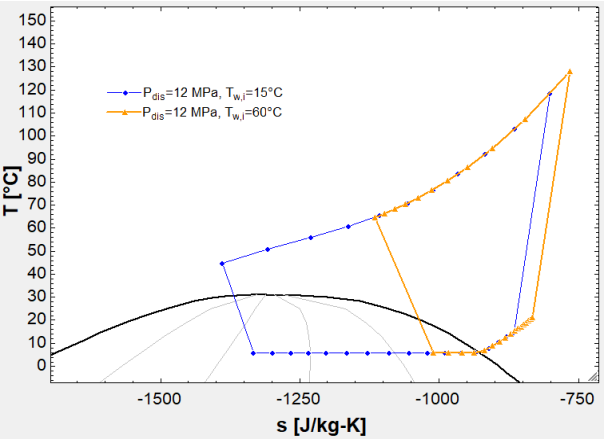

Figure 7-13: Resulting T-s diagrams at the minimum and maximum water inlet temperatures at a 12.0 MPa R744 discharge pressure.

Figure 7-12e indicates the resulting water mass flow rates. Unlike the previous section where the water mass flow rate and heating capacity were proportional, the water mass flow rate increases despite the reduction in heating capacity. At the conditions linked to the optimal recorded cycle efficiencies, the water mass flow rate increased from 0.104 kg/s to 0.183 kg/s (+76.0%) as the water inlet temperature varied from 15°C to 60°C. Despite the losses in system efficiency and heat transfer rates, the power consumption remained relatively unaffected by the change in water inlet temperature. Thus, it can be concluded that for roughly the same amount of power consumption, the cycle can supply larger water mass flow rates at 90°C as the water inlet temperature increases.

Aside from the system efficiency and heating capacity, note from Figure 7-13 that the R744 discharge temperature increases due to the rise in suction temperature, which is driven by the higher water inlet temperature. In this case, the highest recorded R744 discharge temperature

was 148°C at the maximum considered R744 discharge pressure and water inlet temperature. For the present compressor, this is permissible since the compressor's recommended limit is 160°C. However, this parameter should be monitored when operating the system under even higher water inlet temperatures or in the case where the utilised compressor has a lower discharge temperature limit.

7.4 Conclusion

In this chapter, the operating conditions of interest in this study were evaluated with aid of simulations. A set of standard operating conditions was defined and used as constant values for all simulations. Thereafter, the system performance was examined over a variety of operating conditions, of which main findings a summary follows below.

I. Effect of ambient temperature at fixed water mass flow rates:

The cycle efficiency and water outlet temperature were examined at a fixed water inlet temperature of 15°C and three fixed water mass flow rates between 0.09 kg/s and 0.11 kg/s, which resulted in a broad range of outlet temperatures around 90°C. As the R744 discharge pressure increased, the water outlet temperature increased, whilst the system efficiency decreased. An increase in water mass flow rate had the opposite effect. A variation in ambient temperature had the following effect: Respective to a 12.0 MPa R744 discharge pressure and 0.10 kg/s water stream at a 90°C outlet temperature, as the ambient temperature rose from 25°C to 40°C, the system was able to supply (i) the same water mass flow rate at 92.8°C, or (ii) the same water outlet temperature at a mass flow rate of 0.108 kg/s. The corresponding change in cycle efficiency was higher for (ii) at +8.0% than (i) at 3.7%. Furthermore, as the ambient temperature increases, a lower R744 discharge pressure is required to yield the same water output (both in terms of mass flow rate and temperature).

II. Effect of ambient temperature at a fixed water outlet temperature:

In the second section of this chapter, a more detailed evaluation followed where the cycle performance was simulated at a constant water outlet temperature of 90°C and per ambient temperature, considered with respect to the ODP. These findings were then compared to the most applicable literature and appropriate assumptions were made to normalise the comparison. This included extrapolating the cycle performance of Wang et al. (2013a) to a water outlet temperature of 90°C and assuming the humidity conditions of Yamaguchi *et al*. (2011) based on the physical location of their publishment. Subject to an increase in ambient temperature, the ODP was only

compared in terms of trend, whereas the system COP_H was compared with respect to trend, rate of change, and quantification.

It was found that with an increase in ambient temperature, the ODP marginally rose, which differed from Yamaguchi *et al*. (2011), although, agreed with Wang *et al*. (2013a). This also agreed with Ye *et al.* (2020), which is another relevant source identified from literature (Section 2.1.3). At ambient temperatures of 25°C to 35°C, the ODPs were recorded in the range of 12.5 – 13.0 MPa, whereas at ambient temperatures of 40°C, the ODP was noted in a slightly higher range of 13.0-13.5 MPa. Due to an ambient temperature increase from 25°C to 40°C, the best-recorded COP_H value improved by 11.6% from 3.02 to 3.37.

For normalisation purposes, the cycle efficiencies were compared in terms of WB ambient temperature. Over the identified coinciding WB ambient temperature range of 13.7 – 22.3°C, the system COP_H variations of the present simulation, Yamaguchi *et al*. (2011), and Wang *et al*. (2013a) were 3.02 – 3.29 (+8.9%), 3.30 – 3.60 (+9.1%), and 2.65 – 2.96 (+11.9), respectively. In terms of trend direction and rate of change, these results were declared fairly equivalent. In view of quantification, the present simulation's efficiencies were noted as lower than those of Yamaguchi *et al*. (2011), yet, higher than those of Wang *et al*. (2013a). These differences were attributed to the difference in system designs, component designs, and operating conditions such as the water inlet temperatures and utilised evaporation temperatures. Nevertheless, the system performance in terms of ODP and efficiency was proven to agree with literature and was deemed tangible.

It was further concluded that despite the clear efficiency advantage of operating the system at the highest possible ambient temperature, the noted performance at typically South African ambient temperatures was not found to be significantly higher than those of Yamaguchi *et al*. (2011) and Wang *et al*. (2013a) who included lower ambient temperatures, yet, at higher humidity. As a result, in addition to the ambient temperature, the ambient humidity was inferred as a critical parameter to consider. As will follow shortly, the system performance was resultingly also considered at higher ambient conditions in a later stage of this chapter.

Aside from the cycle's efficiency, other parameters such as the heat transfer rates, mass flow rates and power consumption were also analysed. At the conditions corresponding to the best-recorded COP_H values, over the considered ambient temperature range of 25°C to 40°C, the heating capacity rose from 32.7 kW to 41.1 kW (+25.7%), whereas the cooling capacity rose from 21.9 kW to 28.9 kW (+32.0%) and the power consumption from 10.8 kW to 12.2 kW (+12.9%). As described in the mentioned section, these increases were mainly a result of the added ambient

thermal load leading to improved R744 heat transfer abilities (especially near the pseudocritical region in the gas cooler). With the fixed water inlet and outlet temperature, the water mass flow rate is directly proportional to the heating capacity and resultingly rose from 0.104 kg/s to 0.131 kg/s (+25.7%) over the aforementioned conditions.

III. Effect of ambient relative humidity at a fixed water outlet temperature:

After concluding that the standard evaporation temperature approach used by this study is not suitable for very high ambient conditions (WB ambient temperature range of 24.4 - 32.3°C) and water outlet temperature of 90°C, i.e., an adapted approach was used to define the evaporation temperatures. This was reasoned due to the high initial evaporation temperatures that were associated with low pressure ratios, which caused relatively low R744 discharge temperatures. With the low R744 discharge temperatures, insufficient temperature differences were present in the gas cooler and led to a degradation in heating capacity.

The adapted approach limited the evaporation temperature to a maximum of 16.4°C, which was the value yielded from the 30% relative humidity condition. As a result, higher pressure ratios and thus R744 discharge temperatures occurred, which led to better temperature differences throughout the gas cooler. The effect of an increase in relative humidity was revealed to be similar to that of a higher ambient temperature. As the relative humidity varied from 30% to 60%, the best-recorded cycle efficiency improved from 3.37 to 3.77 (+11.9%), whereas the heating capacity rose from 41.1 kW to 43.7 kW (+6.3%). Also similar to ambient temperature, a change in this parameter had an insignificant effect on the power consumption.

IV. Effect of water inlet temperature at a constant ambient temperature:

In supplementary, higher water inlet temperatures were simulated to examine the resulting system behaviour. It was pointed out that as this parameter increases, the system efficiency and heating capacity heavily decrease. At an ambient temperature of 15°C and water outlet temperature of 90°C, the best-recorded COP_H value decreased by 36.1% from 3.02 to 1.93 as the water inlet temperature rose from 15°C to 60°C. It was also found that the ODP rises subject to an increase in water inlet temperature. These trends were revealed to agree with Yamaguchi *et al*. (2011) and Ye *et al.* (2020).

The decrease in system efficiency was described to be mainly caused by a reduction in R744 mass flow rate as well as by downgraded R744 heat transfer properties in both heat exchangers. It was also revealed that the power consumption is fairly unaffected by the water inlet temperature. Furthermore, unlike for a fixed water inlet and outlet temperature, it was found that for the same

power consumption, the system can supply larger water mass flow rates at 90°C as the water inlet temperature increases.

Based on the above, the core outcome of this study was fulfilled, i.e., simulating the performance of a transcritical R744 heat pump system when operating at high water outlet temperatures such as 90°C over a range of high (typically South African) ambient temperatures.

8. CHAPTER 8: CONCLUSION AND RECOMMENDATIONS

8.1 Conclusion

This study aimed to predict the performance of a transcritical R744 heat pump cycle for industrial applications where water in the proximity of 90°C is required. This was subject to a range of relatively high ambient temperatures as typically experienced in South Africa. Thus, the need existed to develop a numerical model of the cycle and hence apply it to simulate the cycle performance when operating under these conditions. This was achieved as follows.

A comprehensive literature study (Chapter 2) was carried out where the first part focussed on the influence of various operating conditions on the cycle performance. Although no data could be found where both the desired high water supply and ambient temperatures were concurrently investigated, perspective was gained on the typical performance at operating conditions closest thereto. Subsequently, the component designs, methods, correlations, and key assumptions previously used to numerically model the cycle were examined, which served as a foundation for the rest of the study and involved decisions regarding the component types and modelling approaches. A review was also carried out on recently published studies within the NWU that evaluated the correlations used to model the subcomponents of the cycle.

Based on the findings of the literature study, the necessary background theory was compiled (Chapter 3). This included the conservation laws, heat transfer theory, and correlations used to define the thermo-physical behaviour of each component. Hence, the theory was integrated into a simulation model for each component (Chapter 4). For the compressor model, empirical equations were derived by applying Bester (2018)'s universal method (Appendix D). A logical breakdown of the functioning of each component model was also described. To ensure satisfactory accuracy and tangibility of the models, verifications and validations were performed by involving credible and independent sources such as widely-adopted alternative simulation software and experimental data available to the present author (Chapter 5). In terms of verification, the compressor model, gas cooler model, and evaporator model could predict their reference data within absolute maximum deviations of <1%, <1%, and 3.17%, respectively. In view of validation, only notable discrepancies were found for the evaporator model. However, after thorough evaluation, this was discarded due to the high oil content of the considered experimental data source, the limitation of available correlations to predict the heat transfer coefficient of POE-type oil-entrained R744, and also considering the much broader application of

the current study. The component models were hence integrated into a system model to perform full cycle simulations, which were later shown to correlate with the most comparable literature.

Subsequently, the developed model was utilised to size the compressor and calculate the heat exchanger sizes using an over-design criterion (Chapter 6). In other words, the system was sized such that it will have sufficient capacity to operate at the full range of operating conditions of interest by this study. The Bitzer 4MTE-10K compressor was chosen, after which the gas cooler and evaporator lengths were calculated as 30.32 m and 4.15 m, respectively. With the present study focused on the cycle performance under the desired operating conditions, and to maintain the relevancy of the verified and validated geometries, the other heat exchanger geometrical parameters were held constant to those used in Chapter 5.

Using the adequately sized system, the cycle performance was simulated at the conditions of interest (Chapter 7). Subject to a constant R744 discharge pressure and an increasing ambient temperature, it was found that the cycle COP_H improves more when supplying the same water outlet temperature at a higher mass flow rate, compared to the opposite. Also, subject to an increasing ambient temperature, the same water output (in terms of both mass flow rate and temperature) can be achieved at a lower R744 discharge pressure.

A more detailed investigation followed on the ambient temperature's influence on the cycle performance when operating at a constant water outlet temperature of 90°C. Since more than one R744 discharge pressure is able to satisfy a given operating condition, yet, at different cycle efficiencies, this parameter was standardly varied to identify the optimal condition (per ambient temperature). As the ambient temperature rose from 25°C to 40°C, the best-recorded COP_H improved by 11.6% from 3.02 to 3.37. This trend direction and rate of change were shown to agree with Yamaguchi *et al*. (2011) and Wang *et al.* (2013a). In terms of quantification, the recorded efficiencies were lower than those of the former, yet, higher than those of the latter. These differences were attributed to the comparison inconsistencies such as system design, component design, and other operating conditions such as water inlet temperature and evaporation temperature. Furthermore, the recorded ODP also rose with an increase in ambient temperature, which contradicts the constant trend of Yamaguchi *et al*. (2011), although, agrees with the increases of Wang *et al.* (2013a) and Ye *et al.* (2020). The influence of the ambient temperature on other cycle performance parameters such as the heat transfer rates, power consumption, and mass flow rates were also examined. Over the considered ambient temperature range, at the conditions linked to the best-recorded COP_H values, the heating capacity and water mass flow rate increased by 25.7% from 32.7 kW to 41.1 kW and from 0.104 kg/s to 0.131 kg/s, respectively.

Furthermore, the influence of higher relative humidity was also considered at an ambient temperature of 40°C. This parameter was varied from 30% to 60%, which is equivalent to a WB ambient temperature range of 24.4 - 32.3°C. For the compressor to still yield appropriate R744 discharge temperatures to enable the gas cooler to heat water to 90°C, it was concluded that the evaporation temperature should be limited to 16.4°C. The influence of a higher relative humidity was revealed to be similar to that of a higher ambient temperature. Over the aforementioned relative humidity range, the best-recorded COP_H value improved from 3.37 to 3.77 (+11.9%), whilst the corresponding heating capacity rose from 41.1 kW to 43.7 kW (+6.3%).

Supplementary, at a constant ambient temperature and water outlet temperature, the cycle behaviour was examined subject to higher water inlet temperatures. With an increase in this parameter from 15°C to 60°C, the best-recorded cycle COP_H considerably downgraded from 3.02 to 1.93 (-36.1%). This as well as the noted increase in ODP agrees with Yamaguchi *et al*. (2011) and Ye et al. (2020). In this case, the ODP was restricted by the maximum permissible value of 14.0 MPa at water inlet temperatures of 45°C and higher.

8.2 Future recommendations

The following recommendations regarding future studies at the NWU may add valuable information to the knowledge field of transcritical R744 heat pump cycles:

- The use of more powerful simulation software: Although EES offers built-in thermodynamic properties and iterative solving capabilities, its computing capacity is limited, which results in modelling limitations and prolonged simulation time.
- Detailed designing of the heat pump system for the present application of heating water for industrial process heating: Using the numerical model of this study, a greater variety of heat exchanger dimensions and the inclusion of an IHX (with the previous recommendation) can be examined to potentially optimise the cycle performance even further. Such an optimisation study may also include determining the exact ODP (up to a decimal value) values over various operating conditions.
- The construction of an experimental test bench: This will allow for experimental data to be gathered, which can also be utilised to further validate the model developed in this study or those of future studies. Moreover, similar to the approach followed by Wang *et al.* (2013a), this will enable the evaporation temperatures used in the numerical model to be based on experimental data, rather than on a constant approximation approach as used in this study.

- The influence of oil entrainment: As operation time progresses, the lubrication in the compressor infiltrates the R744 stream, which affects the heat transfer and overall behaviour of the system. The inclusion of oil-entrained R744 heat transfer coefficients will account for this altered behaviour and can be validated in conjunction with the procurement of an appropriate test bench as mentioned above.

9. BIBLIOGRAPHY

Agrawal N., Bhattacharyya S. & Nanda P. 2011. Flow Characteristics of capillary tube with CO2 transcritical refrigerant using new viscosity models for homogeneous two-phase flow. *International Journal of Low-Carbon Technology,* Issue 6, pp. 243-248.

Bamigbetan O., Eikevek TM., Neksa P., Bantle M. & Schlemminger C. 2018. Theoretical analysis of suitable fluids for high temperature heat pumps up to 125 °C heat delivery. *International Journal of Refrigeration,* Issue 92, pp. 185-195.

Bamigbetan O., Eikevik TM., P N. & Bantle M. 2017. Review of vapour compression heat pumps for high temperature heating using natural working fluids. *International Journal of Refrigeration*, Issue 80, pp. 191-211.

Bester JP. 2018. A methodology for the performance characterisation of a variable speed CO2 compressor, North-West University , Potchefstroom.

Bitzer 2022. *Bitzer Web Software*. [Online] Available at: https://www.bitzer.de/websoftware/Calculate.aspx?cid=1632742379603&mod=HHK.

Bitzer 2022. *Bitzer: Reciprocating Compressors: Semi-hermetic: For transcritical CO_2 application*. [Online] Available at: https://www.bitzer.de/au/en/reciprocating-compressors/ecoline-transcritical/.

Borgnakke C. & Sonntag RE. 2014. *Fundamentals of Thermodynamics*. 8th ed. Wiley, Hoboken.

Bourabaa A., Saighi M. & Belal I. 2011. The influence of the inlet conditions on the air side heat transfer perfroemance of plained finned evaporator. *World Academy of Science, Engineering and Technology*, Issue 59, pp. 28-31.

Calm JM. & Didion DA. 1998. Trade-offs in refrigerant selections: past, present, and future. *Internation Journal of Refrigeration,* 21(4), pp. 308-321.

Cao F., Ye Z. & Wang Y. 2020. Experimental investigation on the influence of internal heat exchanger in a transcritical CO2 heat pump water heater. *Applied Thermal Engineering,* Issue 168, pp. 1-11.

Cengel YA. & Boles MA. 2015. *Thermodynamics: An Engineering Approach*. 8th ed. McGraw-Hill Education, New York.

Cheng L.RG&TJR. 2008b. New prediction methods for CO2 evaporation inside tubes: Part II - An updated general flow boiling heat transfer model based on flow patterns. *International Journal of Heat and Mass Transfer*, Issue 51, pp. 125-135.

Cheng L., Ribatski G., Quiben JM. & Thome JR. 2008a. New prediction methods for CO2 evaporation inside tubes: Part I - a two-phase flow pattern map and a flow pattern based phenomenological model for two-phase flow frictional pressure drops. *International Journal of Heat and Mass Transfer*, Issue 51, pp. 111-124.

Ciccitti A., Lombardi C., Silvestri M., Soldaini G. & Zavattarelli R. 1960. Two-phase cooling experiments-pressure drop, heat transfer and burnout measurements. *Energia Nucleare,* 7(6), pp. 407-425.

Dai C. & Qin X. 2022. Experimental Study on Heating Performance and a Novel Calculation Method of Water Outlet Temperature Based on Air Source Transcritical CO2 Heat Pump System. *Frontiers in Energy Research,* Issue 10, pp. 1-13.

Dang C. & Hihara E. 2004. In-tube cooling heat transfer of supercritical carbon dioxide. Part 2. Comparison of numerical calculation with different turbulence models. *International Journal of Refrigeration,* Issue 27, pp. 748-760.

Ding WK., Fan JF., He YL., Tao WQ., Zheng YX., Gao YF. & Song J. 2011. A general simulation model for performance prediction of plate fin-and-tube heat exchanger with complex circuitry configuration. *Applied Thermal Engineering*, Issue 31, pp. 3106-3116.

Filonenko GK. 1954. Hydraulic resitance in pipelines. *Thermal Engineering*, Issue 4, pp. 40-44.

Flownex. 2022. *Flownex*. [Online] Available at: https://flownex.com/.

Fronk BM. & Garimella S. 2011. Water-coupled carbon dioxide microchannel gas cooler for heat pump water heaters: Part II - Model development and validation. *International Journal of Refrigeration*, Issue 34, pp. 17-28.

Gnielinski V. 1976. New equation for heat and mass transfer in turbulent pipe and channel flow. *Int. Chem. Eng.*, Issue 16, pp. 359-368.

Groeneveld DC. 1973. Post dry-out heat transfer at reactor operating conditions. ANS Topical Meeting on Water Reactor Safety, Salt Lake City.

Harris PM. 2014. Theoretical and experimental analysis of supercritical carbon dioxide cooling, North-West University, Potchefstroom.

He Z., Chin Y., Yu S., Huang J., Zhang CSP., Azarakhsh N. & Sheng J. 2021. The Influence of Average Temperature and Relative Humidity on New Cases of COVID-19: Time-Series Analysis. *JMIR Public Health and Surveillance*, Vol 7.

He YJ., Liang XY., Cheng JH., Shao LL. & Zhang CL. 2020a. Approaching optimum COP by refrigerant charge management in transcritical CO2 heat pump water heater. *International Journal of Refrigeration,* Issue 118, pp. 161-172.

He Z., Li D., Wang X. & Wang T. 2020b. Investigation on the mass flow rate of a refrigerator compressor based on the p-V diagram. *Applied Sciences,* 10(6650), pp. 1-11.

IEA 2014. *HPP -ANNEX 35 -Application of Industrial Heat Pumps Final Report Part 1 and 2*. [Online] Available at: *https://heatpumpingtechnologies.org/publications/application-of-industrial-heat-pumps-part-1/*, [Accessed 19 12 2021.

IEA 2021. World Energy Outlook. 2021. *International Energy Agency, Paris, France*.

Incropera FP., Dewit DP., Bergman TL. & Lavine AS. 2013. *Principles of heat and mass transfer*. 7th ed. Wiley & Sons.

Kaiser WH. 2021. Energy savings potential of CO2 heat pumps in the South African industrial sector, North-West University, Potchefstroom.

Kaiser WH. & Van Eldik M. 2019. Estimating the South African industrial heat demand potential for CO2 heat pumps, School of Mechanical Engineering, North-West University, Potchefstroom.

Kattan N., Thome JR. & Favrat D. 1998. Flow boiling in horizontal tubes. Part 1: Development of a diabatic two- phase flow pattern map. *Journal of Heat and Mass Transfer,* Issue 120, pp. 140-147.

Kauf J. 1999. Determination of the optimum high pressure for transcritical CO2-refrigeration cycles. *International Journal of Thermal Science,* Issue 38, pp. 325-330.

Kays WM. & London AL. 1998. *Compact Heat Exchangers*. 3rd ed. McGraw-Hill, New York.

Kim SG., Kim YJ., Lee G. & Kim MS. 2005. The performance of a transcritical CO2 cycle with an internal heat exchanger for hot water heating. *International Journal of Refrigeration,* Issue 28, pp. 1064-1072.

Klein SA. 2021. *Engineering Equation Solver Version 11.115-3D*. [Online] Available at: www.fchartsoftware.com.

Kuvannarat T., Wang C. & Wongwises S. 2006. Effect of fin thickness on the air-side performance of wavy fin-and-tube heat exchangers under dehumidifying conditions. *International Journal of Heat and Mass Transfer*, pp. 2587-2596.

Laipradit P., Tiansuwan J., Kiatsiriroat T. & Aye L. 2008. Theoretical performance analysis of heat pump water heaters using carbon dioxide as refrigerant. *International Journal of Energy Research,* Issue 32, pp. 356-366.

Lin KH., Kuo CS., Hsieh WD. & Wang CC. 2013. Modeling and simulation of the transcritical CO2 heat pump system. *International Journal of Refrigeration,* Issue 36, pp. 2048-2064.

Mastrullo R., Mauro AW. & Viscito L. 2019. Flow boiling of carbon dioxide: Heat transfer for smooth and enhanced geometries and effect of oil. state of the art review. *International Journal of Refrigeration*, pp. 311-335.

Nawaz K., Shen B., Elatar A., Baxter V. & Abdelaziz O. 2018. Performance optimization of CO2 heat pump water heater. *International Journal of Refrigeration,* Issue 85, pp. 213-228.

Neksa P., Rekstad H., Zakeri GR. & Schiefloe PA. 1998. CO2-heat pump water heater: characteristics, system design and experimental results. *International Journal of Refrigeration,* 21(3), pp. 172-179. [Online].

NIST 2020. *'Evap-cond version 5.0'. Simulation models for Finned-Tube HEat Exchangers with Circuitry Optimisation*. [Online] Available at: https://www.nist.gov/services-resources/software/evap-cond-version-50).

Oliet C., Perez-Segarra CC., Castro J. & Oliva A. 2010. Modelling of fin-and-tube evaporators considering non-uniform in-tube heat transfer. *International Journal of Thermal Sciences*, Issue 49, pp. 692-701.

Opalic SM., Goodwin M., Jiao L., Nielsen HK. & Kohle ML. 2019. Modelling of compressors in an industrial CO2 -Based Operational Cooling System Using ANN for Energy Management

Purposes. *20th International Conference on Engineering Applications of Neural Networks, EANN 2019* Springer Verlag, Hersonissos, pp. 43-54.

Pirompugd W., Wang CC. & Wongwises S. 2007. Finite circular fin method for heat and mass transfer characteristics for plain fin-and-tube heat exchangers under fully and partially wet surface conditions. *International Journal of Heat and Mass Transfer*, Issue 50, pp. 552-565.

Potgieter JHC. 2013. Development and evaluation of an R744 evaporator model, Nort-West University, Potchefstroom.

Qi P-C., He Y-L., Wang X-L. & Meng X-Z. 2013. Experimental investigation of the optimal heat rejection pressure for a transcritical CO2 heat pump water heater. *Applied Thermal Engineering*, Issue 56, pp. 120-125.

Rigola J., Ablanque N., Perez-Segarra CD. & Oliva A. 2010. Numerical simulation and experimental validation of internal heat exchanger influence on CO2 trans-critical cycle performance. *International Journal of Refrigeration,* Issue 33, pp. 664-674.

Rony RU., Yang H., Krishnan S. & Song J. 2019. Recent Advances in Transcritical CO2 (R744) Heat Pump System: A Review. *Energies,* 12(457), pp. 1-35.

Rousseau P. 2013. Thermo-Fluid Systems Modelling I Course Notes. 1st ed., North-West University, Potchefstroom.

Saikawa M. & Koyama S. 2016. Thermodynamic analysis of vapor compression heat pump cycle for tap water heating and development of CO2 heat pump water heater for residential use. *Applied Thermal Engineering*, Issue 106, pp. 1236-1243.

Sarkar J., Bhattacharyya S. & Gopal M.R. 2006. Simulation of a transcritical CO2 heat pump cycle for simultaneous cooling and heating applications. *International Journal of Refrigeration,* Issue 29, pp. 735-743.

Schmidt TE. 1949. Heat Transfer Calculations for extended surfaces. *Journal of the American Society of Refrigerating Engineers,* Issue 57, pp. 351-357.

Shah MM. 2019. Prediction of heat transfer during saturated boiling in helical coils. *Journal of Thermal Science and Engineering Applications*.

Sian RA. & Wang C. 2017. Constraints-free modeling and experimental validation of a transcritical CO2 system for medium and large scale applications. *Applied Thermal Engineering,* Issue 124, pp. 136-151.

Smuts SB. 2015. An energy-based representation of a counter flow single phase heat exchanger, North-West University, Potchefstroom.

Song Y., Wang H. & Cao F. 2019. Investigation of the Impact Factors on the Optimal Intermediate Temperature in a Dual Transcritical CO2 System with a Dedicated Transcritical CO2 Subcooler. *Energies,* 13(2), pp. 309-331.

Strydom 2013. Thermal-fluid simulation of an air-to-CO2 finned coil evaporator, North-West University, Potchefstroom.

Uren KR., Van Schoor G., Van Eldik M. & De Bruin JJA. 2020. An Energy Graph-Based Approach to Fault Diagnosis of a Transcritical CO2 Heat Pump. *Energies,* 13(1783), pp. 1-34.

Waltrich M., Hermes CJL., Goncalves JM. & Melo C. 2010. A first-principles simulation model for the thermo-hydraulic performance of fan supplied tube-fin heat exchangers. *Applied Thermal Engineering,* 30(14), pp. 2011-2018.

Wang CC., Chi KY. & Chang CJ. 2000a. Heat transfer and friction characteristics of plain fin-and-tube heat exchangers, part II: Correlation. *International Journal of Heat and Mass Transfer,* 43(2000), pp. 2693-2700.

Wang CC., Hafner A., Kui C. & Hsieh W. 2012b. An overview of the effect of lubricant on the heat transfer performance on conventional refrigerants and natural refrigerant R-744. *Renewable and Sustainable Energy Reviews,* 16(7), pp. 5071-5086.

Wang S., He Y., Tuo H., Cao F. & Xing Z. 2013b. Effect of heat transfer area and refrigerant mass flux in a gas cooler on heating performance of air-source transcritical CO2 heat pump water heating system. *Energy and Buildings,* Issue 67, pp. 1-10.

Wang CC., Hsieh YJ. & Lin YT. 1997. Performance of plate finned tube heat exchangers under dehumidifying conditions. *ASME J. Heat Transfer,* Issue *119*, pp. 109-117.

Wang C., Hwang Y. & Lin Y. 2002a. Emperical correlations for heat transfer and flow friction characteristics of herringbone wavy fin-and-tube heat exchangers. *International Journal of Refrigeration,* Issue 25, pp. 673-680.

Wang CC., Lin YT. & Lee CJ. 2000b. An airside correlation for plain fin-and-tube heat exchanger in wet conditions. *International Journal of Heat and Mass Transfer,* 43(2000), pp. 1869-1872.

Wang H., Liu H. & Tian J. 2012a. Performance Analysis of Transcritical CO2 Sewage Source Heat Pump by Visual Basic Program, Springer-Verlag Berlin, Heidelberg.

Wang Z., Li G., Wang F., Liu Z. & Wang M. 2020. Performance analysis and operation optimization of air-to-water CO2 heat pump with phase change thermal storage. *Energy & Buildings,* Issue 209, pp. 1-10.

Wang S., Tuo H., Cao F. & Xing Z. 2013a. Experimental investigation on air-source transcritical CO2 heat pump water heater system at a fixed water inlet temperature. *International Journal Of Refrigeration*, Issue 36, pp. 701-716.

Wetzel M., Dietrich B. & Wetzel T. 2014. Influence of oil on heat transfer and pressure drop during flow boiling of CO2 at low temperatures. *Experimental Thermal and Fluid Science*, pp. 202-212.

White FM. 2011. *Fluid Mechanics*. 7th ed. McGraw-Hill, New York.

White SD., Yarall MG., Cleland DJ. & Hedley RA. 2002. Modelling the performance of a transcritical CO2 heat pump for high temperature heating. *International Journal of Refrigeration* Issue 25, pp. 479-486.

Wojtan L., Ursenbacker T. & Thome JR. 2005. Investigation of flow boiling in horizontal tubes: Part II – Development of a new heat transfer model for stratified-wavy, dryout and mist flow regimes. *International Journal of Heat and Mass Transfer,* Issue 48, pp. 2970-2985.

Wolf S., Lambauer J., Blesl M. & Fahl U.VA. 2012. Industrial heat pumps in Germany: Potentials, technological development and market barriers Institute for Energy Economics and the Rational Use of Energy (IER), Stuttgart.

Yamaguchi S., Kato D., Saito K. & Kawai S. 2011. Development and validation of static simulation model for CO2 heat pump. *International Journal of Heat and Mass Transfer*, Issue 54, pp. 1896-1906.

Yang JL., Ma YT. & Zhang JH. 2016. Optimal heat rejection pressure for transcritical CO2 refrigeration cycle with an expander. *International Journal of Green Energy*, Issue 13, pp. 208-212.

Yang LX., Wei XL., Zhao LH., Qin X. & Zhang DW. 2019. Experimental study on the effect of compressor frequency on the performance of transcritical CO2 heat pump system with regenerator. *Applied Thermal Engineering,* Issue 150, pp. 1216-1223.

Ye Z., Wang Y., Song Y., Yin Z. & Cao F. 2020. Optimal discharge pressure in transcritical CO2 heat pump water heater with internal heat exchanger based on pinch point analysis. *International Journal of Refrigeration,* Issue 118, pp. 12-20.

Yokoyama R., Shimizu T., Ito K. & Takemura K. 2007. Influence of ambient temperatures on performance of a CO2 heat pump water heating system. *Energy,* Issue 32, pp. 388-398.

Zhang F., Jiang P. & Zhu YH. 2014. SYSTEM OPTIMIZATION OF CO2 HEAT PUMP WATER HEATER BASED ON ECONOMY. *IIR Gustav Lorentzen Conference on Natural Refrigerants,* Issue 11, pp. 1-7.

APPENDIX A

A-1) Table format of the simulation results at the design conditions (Chapter 6):

Table A-1: Results obtained from simulating the design conditions as described in Chapter 6.

Parameter	Value				
P_{dis} [MPa]	**12.0**	**12.5**	**13.0**	**13.5**	**14.0**
T_{dis} [°C]	112.1	116.8	121.6	126.3	131.0
$\dot{m}_{R744}$ [kg/s]	0.148	0.145	0.142	0.140	0.137
L_{GC} [m]	30.32	25.31	22.11	19.86	18.2
L_{EVAP} [m]	4.15	4.10	4.03	3.96	3.89
Pinch Point GC [°C]	10.4	13.7	16.8	19.7	22.5
$T_{R744,GC,o}$ [°C]	39.8	40.4	41.0	41.6	42.1
U_{GC} [kW/m^{2}K]	1.40	1.38	1.36	1.33	1.31
W_C [kW]	10.44	10.81	11.18	11.54	11.89
Q_L [kW]	20.95	20.58	20.22	19.86	19.50
COP_H [-]	3.01	2.90	2.81	2.72	2.64
R744 ΔP_{GC} [MPa]	0.020	0.015	0.013	0.011	0.009
R744 ΔP_{EVAP} [MPa]	0.002	0.002	0.002	0.002	0.002
Water ΔP_{GC} [kPa]	48.32	40.43	35.37	31.82	29.18

A-2) T-s and P-h diagram of the cycle at the designed condition (Chapter 6):

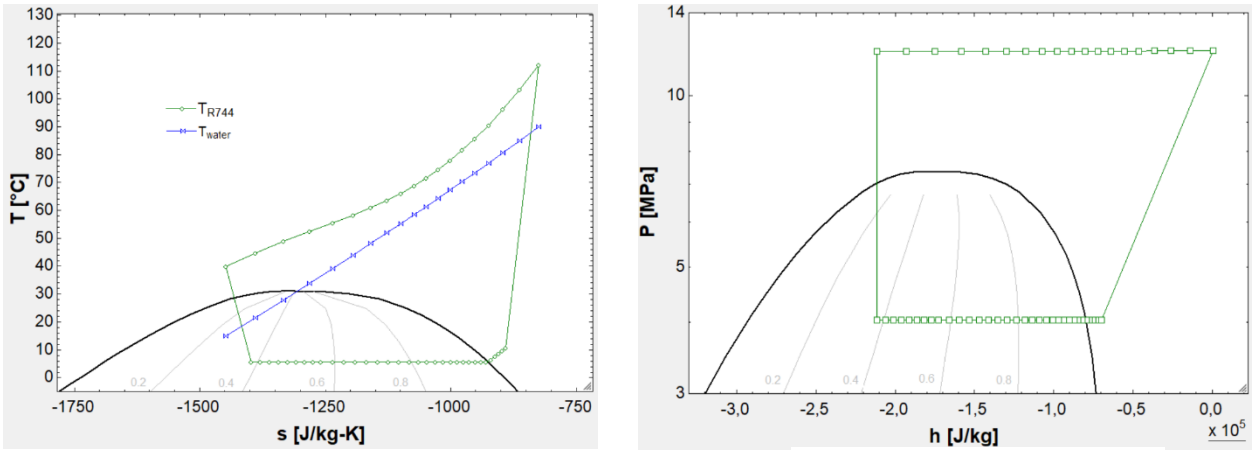

a) T-s diagram b) P-h diagram

Figure A-1: T-s (a) and P-h (b) diagrams of the cycle at the final design condition (R744 discharge pressure of 12.0 MPa).

APPENDIX B

B-1) Section 7.1 - Table format of the simulation results at the different water mass flow rates (0.09-0.11 kg/s) and ambient temperatures (25-40°C):

Table B-1: Results obtained from simulating a fixed water mass flow rate of 0.09 kg/s at an ambient temperature of 25°C.

$T_{water,i}$ = 15°C; $\dot{m}_{water}$ = 0.09 kg/s; T_{amb} = 25°C					
Parameter	**Value**				
P_{dis} [MPa]	**12.0**	**12.5**	**13.0**	**13.5**	**14.0**
COP_H [-]	2.88	2.86	2.85	2.82	2.80
DOS [°C]	7.4	6.6	5.9	5.1	4.3
$\dot{m}_{R744}$ [kg/s]	0.145	0.143	0.141	0.139	0.14
$PinchPoint_{GC}$ [°C]	10.1	10.6	11.2	11.9	12.4
$T_{R744,GC,o}$ [°C]	42.7	41.6	40.2	38.7	37.4
$T_{water,o}$ [°C]	94.8	97.2	99.4	101.4	103.2
X_i [-]	0.43	0.40	0.37	0.34	0.31
$Q_{L,latent}$ [kW]	0.00	0.00	0.00	0.00	0.00
$Q_{L,sensible}$ [kW]	19.63	20.17	20.65	21.03	21.47
$Q_{L,total}$ [kW]	19.63	20.17	20.65	21.03	21.47
Q_H [kW]	30.08	30.99	31.83	32.57	33.34
W_C [kW]	10.45	10.82	11.18	11.54	11.87

Table B-2: Results obtained from simulating a fixed water mass flow rate of 0.09 kg/s at an ambient temperature of 30°C.

$T_{water,i}$ = 15°C; $\dot{m}_{water}$ = 0.09 kg/s; T_{amb} = 30°C					
Parameter	**Value**				
P_{dis} [MPa]	**12.0**	**12.5**	**13.0**	**13.5**	**14.0**
COP_H [-]	2.89	2.87	2.85	2.83	2.80
DOS [°C]	9.0	8.5	8.0	7.5	7.0
$\dot{m}_{R744}$ [kg/s]	0.163	0.161	0.158	0.156	0.154
$PinchPoint_{GC}$ [°C]	9.7	10.2	10.7	11.3	12.0
$T_{R744,GC,o}$ [°C]	46.2	45.6	44.7	43.6	42.3
$T_{water,o}$ [°C]	95.9	98.7	101.4	103.8	106.1
X_i [-]	0.48	0.45	0.42	0.39	0.36
$Q_{L,latent}$ [kW]	0.00	0.00	0.00	0.00	0.00
$Q_{L,sensible}$ [kW]	19.93	20.56	21.13	21.64	22.09
$Q_{L,total}$ [kW]	19.93	20.56	21.13	21.64	22.09
Q_H [kW]	30.50	31.56	32.56	33.49	34.36
W_C [kW]	10.57	11.00	11.43	11.86	12.27

Table B-3: Results obtained from simulating a fixed water mass flow rate of 0.09 kg/s at an ambient temperature of 35°C.

$T_{water,i}$ = 15°C; $\dot{m}_{water}$ = 0.09 kg/s; T_{amb} = 35°C					
Parameter	**Value**				
P_{dis} [MPa]	**12.0**	**12.5**	**13.0**	**13.5**	**14.0**
COP_H [-]	2.91	2.88	2.85	2.82	2.79
DOS [°C]	10.7	10.1	9.6	9.1	8.7
$\dot{m}_{R744}$ [kg/s]	0.184	0.181	0.179	0.177	0.174
$PinchPoint_{GC}$ [°C]	9.0	9.4	9.9	10.5	11.0
$T_{R744,GC,o}$ [°C]	49.3	49.3	49.0	48.4	47.5
$T_{water,o}$ [°C]	96.3	99.3	102.1	104.9	107.6
X_i [-]	0.54	0.51	0.48	0.45	0.42
$Q_{L,latent}$ [kW]	0.00	0.00	0.00	0.02	0.06
$Q_{L,sensible}$ [kW]	20.11	20.72	21.32	21.85	22.33
$Q_{L,total}$ [kW]	20.11	20.72	21.32	21.87	22.40
Q_H [kW]	30.65	31.76	32.86	33.90	34.92
W_C [kW]	10.54	11.04	11.53	12.03	12.52

Table B-4: Results obtained from simulating a fixed water mass flow rate of 0.09 kg/s at an ambient temperature of 40°C.

$T_{water,i}$ = 15°C; $\dot{m}_{water}$ = 0.09 kg/s; T_{amb} = 40°C					
Parameter	**Value**				
P_{dis} [MPa]	**12.0**	**12.5**	**13.0**	**13.5**	**14.0**
COP_H [-]	2.94	2.90	2.86	2.81	2.77
DOS [°C]	12.6	12.1	11.7	11.0	10.7
$\dot{m}_{R744}$ [kg/s]	0.206	0.203	0.201	0.199	0.197
$PinchPoint_{GC}$ [°C]	7.8	8.3	8.8	9.2	9.8
$T_{R744,GC,o}$ [°C]	51.9	52.3	52.5	52.5	52.1
$T_{water,o}$ [°C]	96.5	99.7	102.8	105.6	108.5
X_i [-]	0.60	0.57	0.54	0.51	0.48
$Q_{L,latent}$ [kW]	0.19	0.28	0.35	0.36	0.41
$Q_{L,sensible}$ [kW]	20.07	20.63	21.17	21.64	22.16
$Q_{L,total}$ [kW]	20.26	20.91	21.52	22.00	22.56
Q_H [kW]	30.71	31.93	33.11	34.16	35.29
W_C [kW]	10.45	11.02	11.59	12.16	12.72

Table B-5: Results obtained from simulating a fixed water mass flow rate of 0.10 kg/s at an ambient temperature of 25°C.

$T_{water,i}$ = 15°C; $\dot{m}_{water}$ = 0.10 kg/s; T_{amb} = 25°C					
Parameter	**Value**				
P_{dis} [MPa]	**12.0**	**12.5**	**13.0**	**13.5**	**14.0**
COP_H [-]	3.01	2.98	2.96	2.92	2.89
DOS [°C]	5.0	3.9	3.0	2.2	1.3
$\dot{m}_{R744}$ [kg/s]	0.148	0.147	0.145	0.143	0.141
$PinchPoint_{GC}$ [°C]	10.4	11.0	11.7	12.4	13.3
$T_{R744,GC,o}$ [°C]	39.7	38.4	36.9	35.2	33.6
$T_{water,o}$ [°C]	90.0	92.0	93.9	95.6	97.0
X_i [-]	0.38	0.35	0.32	0.29	0.27
$Q_{L,latent}$ [kW]	0.00	0.00	0.00	0.00	0.00
$Q_{L,sensible}$ [kW]	20.96	21.42	21.84	22.20	22.46
$Q_{L,total}$ [kW]	20.96	21.42	21.84	22.20	22.46
Q_H [kW]	31.40	32.23	33.02	33.73	34.35
W_C [kW]	10.44	10.81	11.17	11.54	11.90

Table B-6: Results obtained from simulating a fixed water mass flow rate of 0.10 kg/s at an ambient temperature of 30°C.

$T_{water,i}$ = 15°C; $\dot{m}_{water}$ = 0.10 kg/s; T_{amb} = 30°C					
Parameter	**Value**				
P_{dis} [MPa]	**12.0**	**12.5**	**13.0**	**13.5**	**14.0**
COP_H [-]	3.04	3.01	2.98	2.95	2.91
DOS [°C]	7.3	6.7	5.9	5.2	4.4
$\dot{m}_{R744}$ [kg/s]	0.165	0.163	0.161	0.159	0.157
$PinchPoint_{GC}$ [°C]	10.0	10.6	11.2	11.8	12.5
$T_{R744,GC,o}$ [°C]	43.5	42.5	41.4	40.0	38.6
$T_{water,o}$ [°C]	91.7	94.2	96.4	98.5	100.4
X_i [-]	0.43	0.39	0.36	0.33	0.30
$Q_{L,latent}$ [kW]	0.00	0.00	0.00	0.00	0.00
$Q_{L,sensible}$ [kW]	21.52	22.14	22.66	23.10	23.47
$Q_{L,total}$ [kW]	21.52	22.14	22.66	23.10	23.47
Q_H [kW]	32.09	33.14	34.09	34.96	35.75
W_C [kW]	10.57	11.00	11.43	11.86	12.28

Table B-7: Results obtained from simulating a fixed water mass flow rate of 0.10 kg/s at an ambient temperature of 35°C.

$T_{water,i}$ = 15°C; $\dot{m}_{water}$ = 0.10 kg/s; T_{amb} = 35°C					
Parameter	**Value**				
P_{dis} [MPa]	**12.0**	**12.5**	**13.0**	**13.5**	**14.0**
COP_H [-]	3.07	3.04	3.00	2.96	2.93
DOS [°C]	9.0	8.4	7.9	7.2	6.9
$\dot{m}_{R744}$ [kg/s]	0.187	0.184	0.182	0.180	0.177
$PinchPoint_{GC}$ [°C]	9.4	9.9	10.4	11.0	11.7
$T_{R744,GC,o}$ [°C]	47.0	46.6	45.9	45.0	43.9
$T_{water,o}$ [°C]	92.3	95.1	97.7	100.1	102.6
X_i [-]	0.48	0.45	0.42	0.39	0.36
$Q_{L,latent}$ [kW]	0.00	0.02	0.07	0.12	0.19
$Q_{L,sensible}$ [kW]	21.84	22.47	23.03	23.51	23.99
$Q_{L,total}$ [kW]	21.84	22.49	23.11	23.63	24.18
Q_H [kW]	32.37	33.53	34.64	35.66	36.70
W_C [kW]	10.54	11.03	11.53	12.03	12.53

Table B-8: Results obtained from simulating a fixed water mass flow rate of 0.10 kg/s at an ambient temperature of 40°C.

$T_{water,i}$ = 15°C; $\dot{m}_{water}$ = 0.10 kg/s; T_{amb} = 40°C					
Parameter	**Value**				
P_{dis} [MPa]	**12.0**	**12.5**	**13.0**	**13.5**	**14.0**
COP_H [-]	3.12	3.07	3.02	2.97	2.93
DOS [°C]	11.0	10.4	9.8	9.3	9.0
$\dot{m}_{R744}$ [kg/s]	0.210	0.208	0.206	0.204	0.201
$PinchPoint_{GC}$ [°C]	8.4	8.9	9.4	9.9	10.5
$T_{R744,GC,o}$ [°C]	49.9	50.0	49.9	49.5	48.9
$T_{water,o}$ [°C]	92.8	95.7	98.5	101.3	104.0
X_i [-]	0.54	0.51	0.48	0.45	0.42
$Q_{L,latent}$ [kW]	0.38	0.40	0.49	0.60	0.79
$Q_{L,sensible}$ [kW]	21.76	22.39	22.92	23.38	23.78
$Q_{L,total}$ [kW]	22.13	22.79	23.40	23.99	24.57
Q_H [kW]	32.58	33.80	34.98	36.14	37.29
W_C [kW]	10.45	11.01	11.58	12.15	12.72

Table B-9: Results obtained from simulating a fixed water mass flow rate of 0.11 kg/s at an ambient temperature of 25°C.

$T_{water,i}$ = 15°C; $\dot{m}_{water}$ = 0.11 kg/s; T_{amb} = 25°C					
Parameter	**Value**				
P_{dis} [MPa]	**12.0**	**12.5**	**13.0**	**13.5**	**14.0**
COP_H [-]	3.11	3.07	3.03	DOS<=0	DOS<=0
DOS [°C]	2.3	1.1	0.1	DOS<=0	DOS<=0
$\dot{m}_{R744}$ [kg/s]	0.152	0.150	0.149	DOS<=0	DOS<=0
$PinchPoint_{GC}$ [°C]	10.6	11.3	12.2	DOS<=0	DOS<=0
$T_{R744,GC,o}$ [°C]	37.1	35.5	33.9	DOS<=0	DOS<=0
$T_{water,o}$ [°C]	85.5	87.2	88.8	DOS<=0	DOS<=0
X_i [-]	0.34	0.31	0.28	DOS<=0	DOS<=0
$Q_{L,latent}$ [kW]	0.00	0.00	0.00	DOS<=0	DOS<=0
$Q_{L,sensible}$ [kW]	21.99	22.41	22.76	DOS<=0	DOS<=0
$Q_{L,total}$ [kW]	21.99	22.41	22.76	DOS<=0	DOS<=0
Q_H [kW]	32.43	33.23	33.96	DOS<=0	DOS<=0
W_C [kW]	10.44	10.82	11.20	DOS<=0	DOS<=0

Table B-10: Results obtained from simulating a fixed water mass flow rate of 0.11 kg/s at an ambient temperature of 30°C.

$T_{water,i}$ = 15°C; $\dot{m}_{water}$ = 0.11 kg/s; T_{amb} = 30°C					
Parameter	**Value**				
P_{dis} [MPa]	**12.0**	**12.5**	**13.0**	**13.5**	**14.0**
COP_H [-]	3.16	3.13	3.08	3.03	2.98
DOS [°C]	5.3	4.4	3.4	2.3	1.5
$\dot{m}_{R744}$ [kg/s]	0.168	0.166	0.165	0.163	0.161
$PinchPoint_{GC}$ [°C]	10.3	10.9	11.6	12.3	13.1
$T_{R744,GC,o}$ [°C]	40.9	39.7	38.4	37.0	35.4
$T_{water,o}$ [°C]	87.6	89.7	91.6	93.3	94.9
X_i [-]	0.38	0.35	0.32	0.29	0.26
$Q_{L,latent}$ [kW]	0.00	0.00	0.00	0.00	0.00
$Q_{L,sensible}$ [kW]	22.85	23.40	23.82	24.14	24.45
$Q_{L,total}$ [kW]	22.85	23.40	23.82	24.14	24.45
Q_H [kW]	33.42	34.41	35.27	36.04	36.79
W_C [kW]	10.57	11.01	11.45	11.90	12.34

Table B-11: Results obtained from simulating a fixed water mass flow rate of 0.11 kg/s at an ambient temperature of 35°C.

$T_{water,i}$ = 15°C; $\dot{m}_{water}$ = 0.11 kg/s; T_{amb} = 35°C					
Parameter	**Value**				
P_{dis} [MPa]	**12.0**	**12.5**	**13.0**	**13.5**	**14.0**
COP_H [-]	3.22	3.17	3.13	3.07	3.03
DOS [°C]	7.2	6.4	5.7	5.0	4.4
$\dot{m}_{R744}$ [kg/s]	0.192	0.190	0.188	0.185	0.183
$PinchPoint_{GC}$ [°C]	9.5	10.1	10.7	11.4	12.1
$T_{R744,GC,o}$ [°C]	44.4	43.7	42.8	41.8	40.6
$T_{water,o}$ [°C]	88.3	90.7	93.0	95.3	97.3
X_i [-]	0.44	0.40	0.37	0.34	0.31
$Q_{L,latent}$ [kW]	0.27	0.35	0.47	0.46	0.50
$Q_{L,sensible}$ [kW]	23.00	23.53	23.96	24.49	24.89
$Q_{L,total}$ [kW]	23.27	23.88	24.43	24.95	25.39
Q_H [kW]	33.74	34.86	35.92	36.98	37.93
W_C [kW]	10.48	10.98	11.49	12.03	12.54

Table B-12: Results obtained from simulating a fixed water mass flow rate of 0.11 kg/s at an ambient temperature of 40°C.

$T_{water,i}$ = 15°C; $\dot{m}_{water}$ = 0.11 kg/s; T_{amb} = 40°C					
Parameter	**Value**				
P_{dis} [MPa]	**12.0**	**12.5**	**13.0**	**13.5**	**14.0**
COP_H [-]	3.28	3.23	3.17	3.12	3.07
DOS [°C]	9.4	8.8	8.3	7.8	7.4
$\dot{m}_{R744}$ [kg/s]	0.214	0.212	0.210	0.207	0.205
$PinchPoint_{GC}$ [°C]	8.9	9.3	9.9	10.5	11.1
$T_{R744,GC,o}$ [°C]	47.9	47.8	47.3	46.7	45.8
$T_{water,o}$ [°C]	89.4	92.1	94.8	97.3	99.8
X_i [-]	0.49	0.46	0.42	0.39	0.36
$Q_{L,latent}$ [kW]	0.47	0.61	0.82	0.92	1.01
$Q_{L,sensible}$ [kW]	23.33	23.87	24.34	24.84	25.34
$Q_{L,total}$ [kW]	23.80	24.48	25.16	25.76	26.35
Q_H [kW]	34.24	35.49	36.74	37.92	39.08
W_C [kW]	10.44	11.00	11.58	12.15	12.73

B-2) Section 7.2 - Table format of the simulation results at the fixed water outlet temperature of 90°C over a 25-40°C range of ambient temperatures:

Table B-13: Results obtained from simulating a fixed water outlet temperature of 90°C at an ambient temperature of 25°C.

$T_{water,i}$ = 15°C; $T_{water,o}$ = 90°C; T_{amb} = 25°C					
Parameter	**Value**				
P_{dis} [MPa]	**12.0**	**12.5**	**13.0**	**13.5**	**14.0**
COP_H [-]	3.01	3.02	3.02	DOS<=0	DOS<=0
DOS [°C]	5.01	2.77	0.81	DOS<=0	DOS<=0
$\dot{m}_{R744}$ [kg/s]	0.148	0.148	0.148	DOS<=0	DOS<=0
$PinchPoint_{GC}$ [°C]	0.100	0.104	0.108	DOS<=0	DOS<=0
$T_{R744,GC,o}$ [°C]	10.36	11.11	12.02	DOS<=0	DOS<=0
$\dot{m}_{water}$ [kg/s]	39.74	37.21	34.58	DOS<=0	DOS<=0
X_i [-]	90.00	90.00	90.00	DOS<=0	DOS<=0
$Q_{L,latent}$ [kW]	0.38	0.33	0.29	DOS<=0	DOS<=0
$Q_{L,sensible}$ [kW]	0.00	0.00	0.00	DOS<=0	DOS<=0
$Q_{L,total}$ [kW]	20.96	21.85	22.56	DOS<=0	DOS<=0
Q_H [kW]	20.96	21.85	22.56	DOS<=0	DOS<=0
W_C [kW]	31.40	32.66	33.75	DOS<=0	DOS<=0

Table B-14: Results obtained from simulating a fixed water outlet temperature of 90°C at an ambient temperature of 30°C.

$T_{water,i}$ = 15°C; $T_{water,o}$ = 90°C; T_{amb} = 30°C					
Parameter	**Value**				
P_{dis} [MPa]	**12.0**	**12.5**	**13.0**	**13.5**	**14.0**
COP_H [-]	3.09	3.12	3.11	3.07	DOS<=0
DOS [°C]	6.60	4.62	2.43	0.46	DOS<=0
$\dot{m}_{R744}$ [kg/s]	0.166	0.166	0.166	0.166	DOS<=0
$PinchPoint_{GC}$ [°C]	0.104	0.110	0.114	0.117	DOS<=0
$T_{R744,GC,o}$ [°C]	10.13	10.90	11.71	12.62	DOS<=0
$\dot{m}_{water}$ [kg/s]	42.43	39.86	37.42	34.97	DOS<=0
X_i [-]	90.00	90.00	90.00	90.00	DOS<=0
$Q_{L,latent}$ [kW]	0.41	0.35	0.30	0.26	DOS<=0
$Q_{L,sensible}$ [kW]	0.00	0.00	0.00	0.00	DOS<=0
$Q_{L,total}$ [kW]	22.11	23.36	24.15	24.72	DOS<=0
Q_H [kW]	22.11	23.36	24.15	24.72	DOS<=0
W_C [kW]	32.67	34.36	35.62	36.68	DOS<=0

Table B-15: Results obtained from simulating a fixed water outlet temperature of 90°C at an ambient temperature of 35°C.

$T_{water,i}$ = 15°C; $T_{water,o}$ = 90°C; T_{amb} = 35°C					
Parameter	**Value**				
P_{dis} [MPa]	**12.0**	**12.5**	**13.0**	**13.5**	**14.0**
COP_H [-]	3.18	3.22	3.23	3.20	3.14
DOS [°C]	8.19	6.22	4.31	2.37	0.67
$\dot{m}_{R744}$ [kg/s]	0.188	0.188	0.188	0.188	0.188
$PinchPoint_{GC}$ [°C]	0.107	0.113	0.119	0.124	0.127
$T_{R744,GC,o}$ [°C]	9.68	10.41	11.21	12.06	13.04
$\dot{m}_{water}$ [kg/s]	45.36	43.10	40.60	38.19	35.76
X_i [-]	90.00	90.00	90.00	90.00	90.00
$Q_{L,latent}$ [kW]	0.44	0.38	0.32	0.27	0.23
$Q_{L,sensible}$ [kW]	0.03	0.16	0.30	0.41	0.51
$Q_{L,total}$ [kW]	22.97	24.40	25.50	26.21	26.72
Q_H [kW]	23.00	24.56	25.79	26.62	27.23
W_C [kW]	33.53	35.60	37.36	38.75	39.97

Table B-16: Results obtained from simulating a fixed water outlet temperature of 90°C at an ambient temperature of 40°C.

$T_{water,i}$ = 15°C ; $T_{water,o}$ = 90°C; T_{amb} = 40°C					
Parameter	**Value**				
P_{dis} [MPa]	**12.0**	**12.5**	**13.0**	**13.5**	**14.0**
COP_H [-]	3.25	3.32	3.35	3.37	3.33
DOS [°C]	9.74	7.92	6.13	4.73	3.19
$\dot{m}_{R744}$ [kg/s]	0.213	0.214	0.215	0.215	0.215
$PinchPoint_{GC}$ [°C]	0.108	0.116	0.124	0.131	0.136
$T_{R744,GC,o}$ [°C]	8.81	9.64	10.48	11.56	12.57
$\dot{m}_{water}$ [kg/s]	48.27	46.33	44.05	41.27	38.79
X_i [-]	90.00	90.00	90.00	90.00	90.00
$Q_{L,latent}$ [kW]	0.50	0.42	0.36	0.29	0.24
$Q_{L,sensible}$ [kW]	0.40	0.86	1.06	1.41	1.74
$Q_{L,total}$ [kW]	23.10	24.69	26.19	27.47	28.19
Q_H [kW]	23.50	25.55	27.24	28.88	29.92
W_C [kW]	33.94	36.55	38.83	41.07	42.76

B-3.1) Section 7.3.1 - Table format of the simulation results at a fixed ambient temperature of 40°C over a 30-60 % relative humidity ambient range:

Table B-17: Results obtained from simulating a fixed ambient temperature of 40°C and ambient relative humidity of 30%.

$T_{water,o}$ = 90°C; T_{amb} = 25°C; $T_{water,i}$ = 15°C; RH = 30%					
Parameter	**Value**				
P_{dis} [MPa]	**12.0**	**12.5**	**13.0**	**13.5**	**14.0**
COP_H [-]	3.25	3.32	3.36	3.37	3.33
DOS [°C]	9.7	7.9	6.1	4.7	3.2
$\dot{m}_{R744}$ [kg/s]	0.213	0.214	0.215	0.215	0.215
$PinchPoint_{GC}$ [°C]	8.8	9.6	10.5	11.6	12.6
$T_{R744,GC,o}$ [°C]	48.3	46.3	44.1	41.3	38.8
$\dot{m}_{water}$ [kg/s]	0.108	0.116	0.124	0.131	0.136
X_i [-]	0.50	0.42	0.36	0.29	0.24
$Q_{L,latent}$ [kW]	0.40	0.86	1.06	1.41	1.74
$Q_{L,sensible}$ [kW]	23.10	24.69	26.19	27.47	28.19
$Q_{L,total}$ [kW]	23.50	25.55	27.24	28.88	29.92
Q_H [kW]	33.94	36.55	38.83	41.07	42.76
W_C [kW]	10.44	11.00	11.59	12.20	12.84
T_{suc} [°C]	15.4	13.6	11.8	10.4	8.9
T_{dis} [°C]	100.5	102.1	103.5	105.5	107.1

Table B-18: Results obtained from simulating a fixed ambient temperature of 40°C and ambient relative humidity of 40%.

$T_{water,o}$ = 90°C; T_{amb} = 25°C; $T_{water,i}$ = 15°C; RH = 40%					
Parameter	**Value**				
P_{dis} [MPa]	**12.0**	**12.5**	**13.0**	**13.5**	**14.0**
COP_H [-]	3.45	3.53	3.58	3.60	3.58
DOS [°C]	11.9	10.6	9.4	8.5	7.8
$\dot{m}_{R744}$ [kg/s]	0.207	0.207	0.207	0.205	0.204
$PinchPoint_{GC}$ [°C]	9.9	10.9	12.0	13.3	14.6
$T_{R744,GC,o}$ [°C]	46.3	43.7	40.8	37.7	34.8
$\dot{m}_{water}$ [kg/s]	0.115	0.124	0.132	0.139	0.145
X_i [-]	0.45	0.36	0.29	0.23	0.17
$Q_{L,latent}$ [kW]	4.93	5.84	6.69	7.50	8.23
$Q_{L,sensible}$ [kW]	20.64	22.06	23.17	24.03	24.61
$Q_{L,total}$ [kW]	25.58	27.90	29.86	31.53	32.84
Q_H [kW]	36.03	38.91	41.44	43.68	45.57
W_C [kW]	10.45	11.01	11.58	12.15	12.72
T_{suc} [°C]	17.6	16.3	15.1	14.2	13.5
T_{dis} [°C]	103.8	106.3	108.8	111.7	114.9

Table B-19: Results obtained from simulating a fixed ambient temperature of 40°C and ambient relative humidity of 50%.

$T_{water,o}$ = 90°C; T_{amb} = 25°C; $T_{water,i}$ = 15°C; RH = 50%					
Parameter	**Value**				
P_{dis} [MPa]	**12.0**	**12.5**	**13.0**	**13.5**	**14.0**
COP_H [-]	3.55	3.65	3.70	3.70	3.68
DOS [°C]	13.3	12.6	12.1	11.4	11.3
$\dot{m}_{R744}$ [kg/s]	0.204	0.202	0.200	0.198	0.195
$PinchPoint_{GC}$ [°C]	10.4	11.6	12.9	14.2	15.7
$T_{R744,GC,o}$ [°C]	45.1	42.0	38.6	35.4	32.4
$\dot{m}_{water}$ [kg/s]	0.118	0.128	0.137	0.143	0.149
X_i [-]	0.42	0.33	0.25	0.19	0.14
$Q_{L,latent}$ [kW]	8.37	9.85	11.18	12.17	13.02
$Q_{L,sensible}$ [kW]	18.26	19.34	20.12	20.68	21.06
$Q_{L,total}$ [kW]	26.63	29.19	31.30	32.85	34.08
Q_H [kW]	37.09	40.21	42.89	45.01	46.80
W_C [kW]	10.46	11.02	11.59	12.16	12.72
T_{suc} [°C]	19.0	18.3	17.8	17.1	17.0
T_{dis} [°C]	105.9	109.4	113.0	116.5	120.7

Table B-20: Results obtained from simulating a fixed ambient temperature of 40°C and ambient relative humidity of 60%.

$T_{water,o}$ = 90°C; T_{amb} = 25°C; $T_{water,i}$ = 15°C; RH = 60%					
Parameter	**Value**				
P_{dis} [MPa]	**12.0**	**12.5**	**13.0**	**13.5**	**14.0**
COP_H [-]	3.63	3.73	3.767	3.762	3.73
DOS [°C]	14.7	14.3	14.0	13.6	13.7
$\dot{m}_{R744}$ [kg/s]	0.200	0.198	0.195	0.193	0.190
$PinchPoint_{GC}$ [°C]	10.8	12.0	13.4	14.8	16.3
$T_{R744,GC,o}$ [°C]	44.1	40.7	37.2	33.9	31.0
$\dot{m}_{water}$ [kg/s]	0.121	0.131	0.139	0.146	0.151
X_i [-]	0.39	0.30	0.23	0.17	0.12
$Q_{L,latent}$ [kW]	11.77	13.52	14.92	15.92	16.70
$Q_{L,sensible}$ [kW]	15.73	16.54	17.16	17.63	17.93
$Q_{L,total}$ [kW]	27.50	30.06	32.08	33.54	34.62
Q_H [kW]	37.96	41.08	43.67	45.71	47.35
W_C [kW]	10.46	11.03	11.60	12.16	12.73
T_{suc} [°C]	20.4	20.0	19.7	19.3	19.4
T_{dis} [°C]	108.0	111.9	116.1	120.1	124.7

B-3.2) Section 7.3.2 - Table format of the simulation results at a fixed ambient temperature of 25°C over a 15-60°C range of water inlet temperatures:

Table B-21: Results obtained from simulating a fixed ambient temperature of 25°C and water inlet temperature of 15°C.

$T_{water,o}$ = 90°C; T_{amb} = 25°C; $T_{water,i}$ = 15°C					
Parameter	**Value**				
P_{dis} [MPa]	**12.0**	**12.5**	**13.0**	**13.5**	**14.0**
COP_H [-]	3.01	3.02	3.02	DOS<=0	DOS<=0
DOS [°C]	5.0	2.8	0.8	DOS<=0	DOS<=0
$\dot{m}_{R744}$ [kg/s]	0.148	0.148	0.148	DOS<=0	DOS<=0
$PinchPoint_{GC}$ [°C]	10.4	11.1	12.0	DOS<=0	DOS<=0
$T_{R744,GC,o}$ [°C]	39.7	37.2	34.6	DOS<=0	DOS<=0
$\dot{m}_{water}$ [kg/s]	0.100	0.104	0.108	DOS<=0	DOS<=0
X_i [-]	0.38	0.33	0.29	DOS<=0	DOS<=0
$Q_{L,latent}$ [kW]	0.00	0.00	0.00	DOS<=0	DOS<=0
$Q_{L,sensible}$ [kW]	20.96	21.85	22.56	DOS<=0	DOS<=0
$Q_{L,total}$ [kW]	20.96	21.85	22.56	DOS<=0	DOS<=0
Q_H [kW]	31.40	32.66	33.75	DOS<=0	DOS<=0
W_C [kW]	10.44	10.81	11.19	DOS<=0	DOS<=0
T_{suc} [°C]	10.7	8.5	6.5	DOS<=0	DOS<=0

Table B-22: Results obtained from simulating a fixed ambient temperature of 25°C and water inlet temperature of 30°C.

$T_{water,o}$ = 90°C; T_{amb} = 25°C; $T_{water,i}$ = 30°C					
Parameter	**Value**				
P_{dis} [MPa]	**12.0**	**12.5**	**13.0**	**13.5**	**14.0**
COP_H [-]	2.68	2.74	2.76	2.76	2.75
DOS [°C]	9.6	8.6	7.5	6.6	5.9
$\dot{m}_{R744}$ [kg/s]	0.142	0.141	0.139	0.138	0.136
$PinchPoint_{GC}$ [°C]	9.4	10.2	11.0	11.0	9.3
$T_{R744,GC,o}$ [°C]	46.5	44.5	42.6	40.6	38.9
$\dot{m}_{water}$ [kg/s]	0.112	0.118	0.123	0.127	0.130
X_i [-]	0.50	0.45	0.40	0.36	0.33
$Q_{L,latent}$ [kW]	0.00	0.00	0.00	0.00	0.00
$Q_{L,sensible}$ [kW]	17.61	18.83	19.70	20.35	20.78
$Q_{L,total}$ [kW]	17.61	18.83	19.70	20.35	20.78
Q_H [kW]	28.07	29.66	30.89	31.89	32.67
W_C [kW]	10.47	10.83	11.19	11.54	11.89
T_{suc} [°C]	15.3	14.3	13.2	12.3	11.6

Table B-23: Results obtained from simulating a fixed ambient temperature of 25°C and water inlet temperature of 45°C.

$T_{water,o}$ = 90°C; T_{amb} = 25°C; $T_{water,i}$ = 45°C					
Parameter	**Value**				
P_{dis} [MPa]	**12.0**	**12.5**	**13.0**	**13.5**	**14.0**
COP_H [-]	2.24	2.30	2.34	2.37	2.37
DOS [°C]	13.1	12.3	11.7	11.3	11.0
$\dot{m}_{R744}$ [kg/s]	0.138	0.136	0.134	0.132	0.129
$PinchPoint_{GC}$ [°C]	7.1	7.5	7.5	6.6	5.7
$T_{R744,GC,o}$ [°C]	54.0	53.4	52.5	51.5	50.5
$\dot{m}_{water}$ [kg/s]	0.125	0.132	0.139	0.145	0.150
X_i [-]	0.67	0.62	0.57	0.53	0.50
$Q_{L,latent}$ [kW]	0.00	0.00	0.00	0.00	0.00
$Q_{L,sensible}$ [kW]	12.98	14.09	15.04	15.79	16.33
$Q_{L,total}$ [kW]	12.98	14.09	15.04	15.79	16.33
Q_H [kW]	23.47	24.94	26.25	27.36	28.24
W_C [kW]	10.48	10.85	11.22	11.57	11.91
T_{suc} [°C]	18.8	18.0	17.4	17.0	16.7

Table B-24: Results obtained from simulating a fixed ambient temperature of 25°C and water inlet temperature of 60°C.

$T_{water,o}$ = 90°C; T_{amb} = 25°C; $T_{water,i}$ = 60°C					
Parameter	**Value**				
P_{dis} [MPa]	**12.0**	**12.5**	**13.0**	**13.5**	**14.0**
COP_H [-]	1.73	1.80	1.86	1.90	1.93
DOS [°C]	15.3	15.3	15.3	15.0	14.7
$\dot{m}_{R744}$ [kg/s]	0.135	0.132	0.129	0.127	0.125
$PinchPoint_{GC}$ [°C]	3.0	2.9	2.8	2.7	2.4
$T_{R744,GC,o}$ [°C]	62.9	62.9	62.7	62.6	62.3
$\dot{m}_{water}$ [kg/s]	0.144	0.156	0.166	0.175	0.183
X_i [-]	0.86	0.82	0.78	0.74	0.71
$Q_{L,latent}$ [kW]	0.00	0.00	0.00	0.00	0.00
$Q_{L,sensible}$ [kW]	7.65	8.70	9.63	10.41	11.04
$Q_{L,total}$ [kW]	7.65	8.70	9.63	10.41	11.04
Q_H [kW]	18.14	19.56	20.86	21.98	22.95
W_C [kW]	10.49	10.86	11.23	11.58	11.92
T_{suc} [°C]	21.0	21.0	21.0	20.7	20.4

APPENDIX C

C-1) Moody Chart diagram (White 2011)

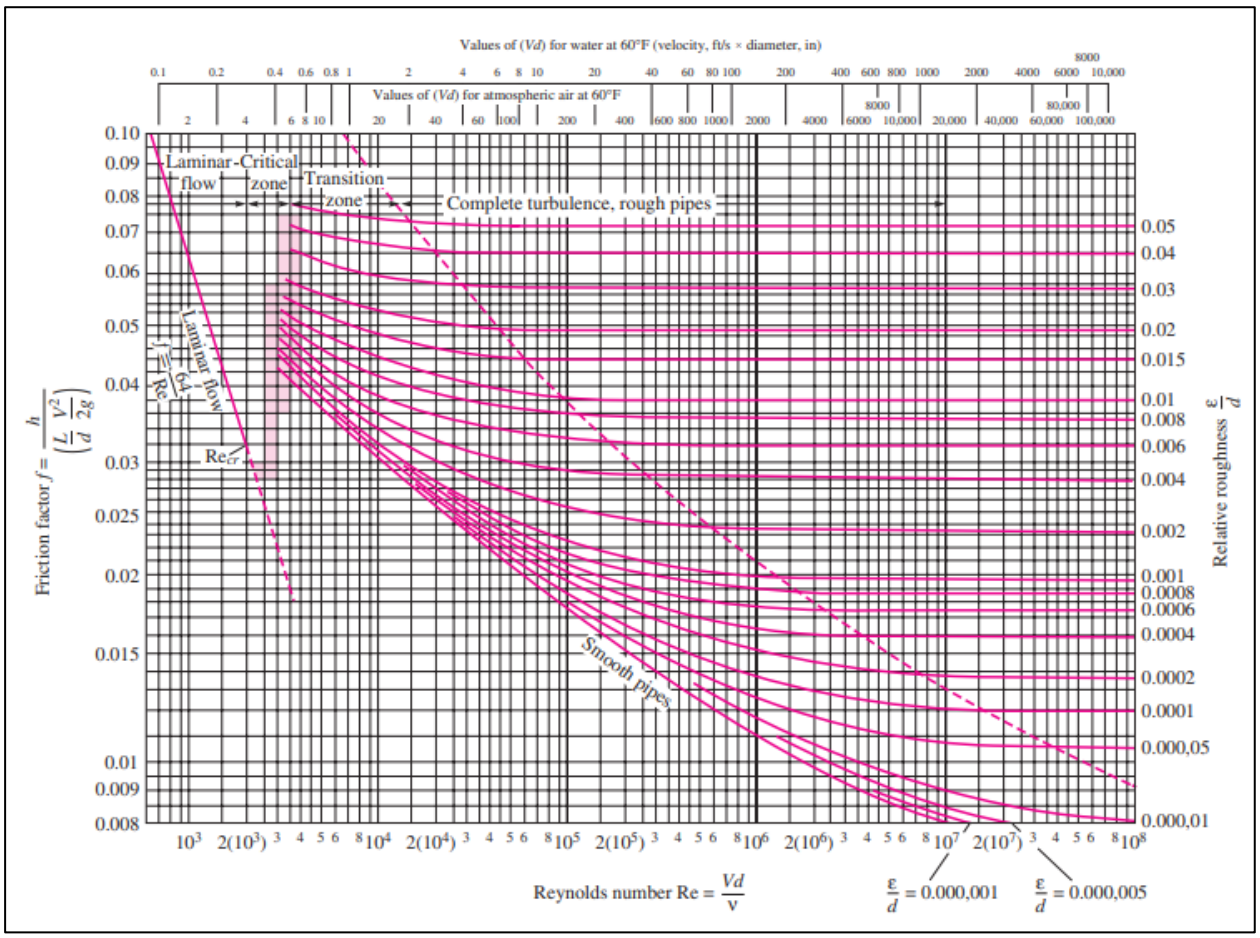

Figure C-1: Moody chart diagram (White 2011).

C-2) Evaporator model correlations

C-2.1) Two-phase R744 correlation set of Cheng et al. (2008a&b)

Before outlining the correlations from Cheng *et al.* (2008a&b) based on the four listed flow patterns in Section 3.4.1.1.1, the boundary values that characterise them will be discussed.

The critical quality value that defines the transition between the intermittent and annular flow patterns is calculated with:

$$x_{IA} = \left(1.8^{1/0.875}\left(\frac{\rho_v}{\rho_l}\right)^{-1/1.75}\left(\frac{\mu_v}{\mu_l}\right)^{-1/7} + 1\right)^{-1} \quad \text{(C.1)}$$

Where:

- $\mu : Dynamic\ viscosity\ [kg/(m.s)]$

Note that the subscript $'l'$ and $'v'$ denote the saturated liquid and -vapour state of the R744, respectively.

For transition between the annular and dryout flow pattern, the critical quality value, also known as the dryout inception quality, is determined with:

$$x_{di} = 0.58 \exp\left(0.52 - 0.236 {We_v}^{0.17} {Fr_{v,Mori}}^{0.17} \left(\frac{\rho_v}{\rho_l}\right)^{0.25} \left(\frac{q}{q_{crit}}\right)^{0.27}\right) \quad \text{(C.2)}$$

Where We_v and $Fr_{v,Mori}$ represent the vapour Weber number and Froude number, respectively. These two numbers are equated as follows:

$$We_v = \frac{G^2 D_i}{\rho_v \sigma} \quad \text{(C.3)}$$

$$Fr_{v,Mori} = \frac{G^2}{\rho_v(\rho_l - \rho_v) g D_i} \quad \text{(C.4)}$$

Where:

- $D_i : Inner\ tube\ diameter\ [m^2]$
- $G : Mass\ flux\ [kg/m^2]$
- $\sigma : Surface\ tension\ [N/m]$
- $g : Gravitational\ constant\ [m/s^2]$

And q_{crit}, the critical heat flux, which is calculated with:

$$q_{crit} = 0.131 {\rho_v}^{0.5} h_{lv} [g\sigma(\rho_l - \rho_v)]^{0.25}$$

Where:

- $h_{lv} : Latent\ heat\ of\ vaporisation\ [m^2]$
- $q : Heat\ flux\ [W/m^2]$

The succeeding transition vapour quality between the dryout and mist flow pattern is also known as the dryout completion quality and is equated as follows:

$$x_{de} = 0.61 \exp\left(0.57 - 0.502 {We_v}^{0.16} {Fr_{v,Mori}}^{0.15} \left(\frac{\rho_v}{\rho_l}\right)^{-0.09} \left(\frac{q}{q_{crit}}\right)^{0.72}\right) \quad \text{(C.5)}$$

Intermittent flow pattern

The intermittent flow pattern is present when $x \leq x_{I-A}$, where x is the vapour quality of the R744 under investigation.

Heat transfer coefficient – Intermittent flow pattern:

The generic Kattan-Thome-Favrat equation published by (Kattan *et al.* 1998) is employed to determine the local two-phase flow boiling CHTC:

$$h_r = \frac{\theta_{dry} h_v + \left(2\pi - \theta_{dry}\right) h_{wet}}{2\pi} \quad \text{(C.6)}$$

Where θ_{dry} ascribes the angle of the dry perimeter. Nonetheless, for the four flow patterns under consideration, $\theta_{dry} = 0$.

The vapour phase CHTC, h_v, is calculated with the Dittus-Boelter equation (Incropera *et al.* 2013):

$$h_v = \frac{0.023 {Re_v}^{0.8} {Pr_v}^{0.4} k_v}{D_i} \quad \text{(C.7)}$$

Where Re_v and Pr_v represent the vapour phase Reynolds and Prandtl number, respectively. These two values are calculated as follows:

$$Pr_v = \frac{Cp_v \mu_v}{k_v} \quad \text{(C.8)}$$

$$Re_v = \frac{GxD_i}{mu_v \varepsilon} \quad \text{(C.9)}$$

and ε, the void fraction that is equated by:

$$\varepsilon = \frac{x}{\rho_v}\left[\left(1 + 0.12(1-x)\right)\left(\frac{x}{\rho_v} + \frac{1-x}{\rho_l}\right) + \frac{1.18(1-x)[g\sigma(\rho_l - \rho_v)]^{0.25}}{G {\rho_l}^{0.5}}\right]^{-1} \quad \text{(C.10)}$$

In terms of the wetted perimeter where liquid phase R744 is encountered, the CHTC is calculated in terms of both nucleate and convective boiling, i.e.:

$$h_{wet} = [(S \cdot h_{nb})^3 + (h_{cb})^3]^{1/3} \tag{C.11}$$

Where S represents a suppression factor to account for the thinning of the liquid film as the R744 condensates and is set to unity for this flow pattern.

The nucleate boiling CHTC, h_{nb}, is determined using the modified Cooper equation:

$$h_{nb} = 131 \left(\frac{P}{P_{crit}}\right)^{-0.0063} \left(-log_{10}(\frac{P}{P_{crit}})\right)^{-0.55} M^{-0.5} q^{0.58} \tag{C.12}$$

Where M represents the molecular weight.

The convective CHTC is computed as follows:

$$h_{cb} = 0.0133 {Re_\delta}^{0.69} {Pr_l}^{0.4} \frac{k_l}{\delta_r} \tag{C.13}$$

Where Re_δ represents the Reynolds number of the liquid film and is calculated by:

$$Re_\delta = \frac{4G(1-x)\delta_r}{\mu_l(1-\varepsilon)} \tag{C.14}$$

And δ_r, the liquid film thickness, which is calculated with:

$$\delta_r = \frac{D_{eq}}{2} - \sqrt{\left(\frac{D_{eq}}{2}\right)^2 - \frac{2A_l}{2\pi - \theta_{dry}}} \tag{C.15}$$

Where:

- D_{eq} : $Equivalent\ tube\ inner\ diameter\ [m]$
- A_l : $Liquid\ phase\ cross-sectional\ area\ [m^2]$

If $D_i > 7.53mm$, then $D_{eq} = D_i$, else $D_{eq} = 7.53mm$. The cross-sectional area reserved by the liquid phase, A_l, is computed with:

$$A_l = A_{ff,r}(1-\varepsilon) \tag{C.16}$$

Also, Pr_l ascribes the Prandtl number of the liquid film and is evaluated by:

$$Pr_l = \frac{Cp_l \mu_l}{k_l} \tag{C.17}$$

<u>Pressure drop: Intermittent flow pattern:</u>

The pressure drop present within the intermittent flow region can be determined with:

$$\Delta P_I = \Delta P_{LO}\left(1 - \frac{\varepsilon}{\varepsilon_{IA}}\right) + \Delta P_A\left(\frac{\varepsilon}{\varepsilon_{IA}}\right) \tag{C.18}$$

Where ΔP_{LO} is calculated as the single-phase frictional pressure drop with liquid phase properties, i.e.:

$$\Delta P = 4 f_{LO}\left(\frac{L}{D_i}\right)\left(\frac{G^2}{2\rho_l}\right) \tag{C.19}$$

Where f_{LO} ascribes the Blasius friction factor and is determined with:

$$f_{LO} = \frac{0.079}{{Re_{LO}}^{0.25}} \tag{C.20}$$

With the Reynolds number, Re_{LO}, calculated as:

$$Re_{LO} = \frac{G D_i}{\mu_l} \tag{C.21}$$

Also, ΔP_A is the pressure drop for the annular flow pattern, which is defined by Equation (C.23) to follow.

Annular flow pattern

The annular flow pattern is present when $x_{IA} < x \leq x_{di}$.

Heat transfer coefficient – Annular flow pattern:

Equation (C.11) is employed to determine the two-phase local CHTC. Yet, in this case, the suppression factor is not set to unity and is equated by:

$$S = 1 - 1.14\left(\frac{D_{eq}}{0.00753}\right)^2\left(1 - \frac{\delta_r}{\delta_{r,IA}}\right)^{2.2} \tag{C.22}$$

Where D_{eq} and δ_r are calculated likewise to the intermittent flow pattern, although $\delta_{r,IA}$ is evaluated at the annular transition quality x_{IA}.

Pressure drop – Annular flow pattern:

The pressure drop is defined by:

$$\Delta P_A = 4 f_A \left(\frac{L}{D_i}\right)\left(\frac{\rho_v {V_{avg,v}}^2}{2}\right) \tag{C.23}$$

With the average vapour velocity equated by:

$$V_{avg.v} = \frac{Gx}{\rho_v \varepsilon} \tag{C.24}$$

And the annular friction factor approached by the following correlation:

$$f_A = 3.128 {Re_v}^{-0.454} {We_l}^{-0.0308} \tag{C.25}$$

Where Re_v is computed by Equation (C.9), and the liquid phase Weber number by:

$$We_l = \frac{\rho_l {V_{avg,l}}^2 D_i}{\sigma} \tag{C.26}$$

With the average liquid velocity determined as follows:

$$V_{avg,l} = \frac{G(1-x)}{\rho_l(1-\varepsilon)} \tag{C.27}$$

Dryout flow pattern

The dryout flow pattern is present under the condition: $x_{di} < x < x_{de}$.

Heat transfer coefficient – Dryout flow pattern:

The linear interpolation approach from Wojtan *et al.* (2005) is employed for the CHTC encountered within the dryout region:

$$h_D = (h_{tp})_{x_{di}} - \frac{x - x_{di}}{x_{de} - x_{di}}\left[(h_{tp})_{x_{di}} - (h_M)_{x_{de}}\right] \tag{C.28}$$

Where $(h_M)_{x_{de}}$ ascribes the mist CHTC given by Equation (C.30), evaluated at the dryout completion quality x_{de}. In the case of an undefined condition, x_{de} is set equal to 0.999.

Pressure drop – Dryout flow pattern:

Analogous to the CHTC, the pressure drop is also evaluated by linear interpolation:

$$\Delta P_D = (\Delta P_A)_{x_{di}} - \frac{x - x_{di}}{x_{de} - x_{di}}\left[(\Delta P_A)_{x_{di}} - (\Delta P_M)_{x_{de}}\right] \tag{C.29}$$

Where $(\Delta P_M)_{x_{de}}$ ascribes the mist frictional pressure drop given by Equation (C.33), evaluated at the dryout completion quality x_{de}. Once again, x_{de}, is set equal to 0.999 in case of an undefined condition.

Mist flow pattern

The mist flow pattern is present under the condition: $x \geq x_{de}$.

Heat transfer coefficient – Mist flow pattern:

The modified correlation from Groeneveld (1973) is adopted to evaluate the CHTC:

$$h_M = 2\ x\ 10^{-8} {Re_H}^{1.97} {Pr_v}^{1.06} Y^{-1.83} \left(\frac{k_v}{D_i}\right) \tag{C.30}$$

With the homogeneous Reynolds number computed as:

$$Re_H = \frac{G D_{eq}}{\mu_v} [x + \frac{\rho_v}{\rho_l}(1-x)] \tag{C.31}$$

and the correctional factor defined as:

$$Y = 1 - 0.1 \left[\left(\frac{\rho_l}{\rho_v} - 1\right)(1-x)\right]^{0.4} \tag{C.32}$$

Pressure drop – Mist flow pattern:

The present frictional pressure drop is equated by:

$$\Delta P_M = 4 f_M \left(\frac{L_{inc}}{D_i}\right)\left(\frac{G^2}{2\rho_H}\right) \tag{C.33}$$

Where the homogeneous density is determined with:

$$\rho_H = \rho_l(1-\varepsilon_H) + \rho_v \varepsilon_H \tag{C.34}$$

The homogenous void fraction is computed by:

$$\varepsilon_H = \left[1 + \frac{1-x}{x}\left(\frac{\rho_v}{\rho_l}\right)\right]^{-1} \tag{C.35}$$

Also, the mist friction factor is approached by the following correlation:

$$f_M = \frac{91.2}{Re_M{}^{0.832}} \tag{C.36}$$

Where the Reynolds number is calculated as:

$$Re_M = \frac{GD_i}{\mu_H} \tag{C.37}$$

With the homogenous dynamic viscosity calculated with the equation proposed by Cicciti *et al.* (1960):

$$\mu_H = \mu_l(1-x) + \mu_v x \tag{C.38}$$

C-2.2) Correlation for airside convection heat transfer coefficient

The CHTC for dry conditions, $h_{c,dry}$, is calculated from the equation (Kays and London 1998):

$$Nu_a = \frac{h_{c,dry}D_c}{k_a} = j_{dry}Re_{Dc}Pr_a{}^{1/3} \tag{C.39}$$

Where:

- $D_c : Collar\ diameter\ [m]$
- $j_{dry} : Colburn - j\ factor\ for\ heat\ transfer\ [-]$
- $Re_{Dc} : Renylods\ number\ evaluated\ at\ the\ collar\ diameter\ [-]$

The correlation from Wang *et al.* (2002a) is adopted to evaluate j_{dry}:

For $300 < Re_{Dc} < 1000$:

$$j_{dry} = 0.882Re_{Dc}{}^{J1}\left(\frac{D_c}{D_h}\right)^{J2}\left(\frac{F_p}{P_t}\right)^{J3}\left(\frac{F_p}{D_c}\right)^{-1.58}(\tanh\theta)^{-0.2} \tag{C.40}$$

With

$$J1 = 0.0045 - 0.491Re_{Dc}{}^{-0.0316-0.0171\ln(N\tan\theta)}\left(\frac{P_l}{P_t}\right)^{-0.109\ln(N\tan\theta)}\left(\frac{D_c}{D_h}\right)^{0.542+0.0471N} \cdot \left(\frac{F_p}{D_c}\right)^{0.984}\left(\frac{F_p}{P_t}\right)^{-0.349} \tag{C.41}$$

$$J2 = -2.72 + 6.84\ tan\theta \tag{C.42}$$

$$J3 = 2.66 \tan\theta \tag{C.43}$$

For $1000 \leq Re_{Dc} < 10000$:

$$j_{dry} = 0.0646 {Re_{Dc}}^{J1} \left(\frac{D_c}{D_h}\right)^{J2} \left(\frac{F_p}{P_t}\right)^{-1.03} \left(\frac{P_l}{D_c}\right)^{0.432} (\tanh\theta)^{-0.692} N^{-0.737} \tag{C.44}$$

With

$$J1 = -0.0545 - 0.0538 \tan\theta - 0.302 N^{-0.24} \left(\frac{F_p}{P_l}\right)^{-1.3} \left(\frac{P_l}{P_t}\right)^{0.379} \left(\frac{P_l}{D_h}\right)^{-1.35} (\tan\theta)^{-0.256} \tag{C.45}$$

$$J2 = -1.29 \left(\frac{P_l}{P_t}\right)^{1.77 - 9.43\tan\theta} \left(\frac{D_c}{D_h}\right)^{0.229 - 1.43\tan\theta} N^{-0.166 - 1.08\tan\theta} \left(\frac{F_p}{P_t}\right)^{-0.174 \ln(0.5N)} \tag{C.46}$$

Where:

- $P_t : Transversal\ tube\ pitch\ [m]$
- $P_l : Longitudinal\ tube\ pitch\ [m]$
- $F_p : Fin\ pitch\ [m]$
- $N : Number\ of\ tube\ rows\ [-]$
- $\theta : Fin\ corrugation\ angle\ [°]$
- $D_h : Hydraulic\ diameter\ of\ air\ stream\ [m]$

Analogous to dry conditions, the CHTC under wet conditions can be determined by respectively substituting j_{wet} with j_{dry}, as well as $h_{c.wet}$ with $h_{c.dry}$ in Equation (C.39). In this case, j_{wet} is correlated by Kuvannarat *et al.* (2006):

$$j_{wet} = 0.213262 {Re_{Dc}}^{-0.51507} N^{0.09891} \left(\frac{A_{air,o}}{A_t}\right)^{0.600543} \left(\frac{\delta_f}{P_l}\right)^{0.072448} \tag{C.47}$$

Where:

- $\delta_f : Fin\ thickness\ [m]$
- $A_t : Tube\ surface\ area\ [m^2]$

C-2.3) Fin efficiency correlation

The single fin efficiency under dry conditions can be approximated by the Schmidt (1949) approach:

$$\eta_{dry} = \frac{\tanh\left(m_{dry} r_o \phi\right)}{m_{dry} r_o \phi} \tag{C.48}$$

with

$$m_{dry} = \sqrt{\frac{2h_{dry}}{k_f \delta_f}} \tag{C.49}$$

and

$$\phi = \left(\frac{R_{eq}}{r_o} - 1\right)\left(1 + 0.35 \ln\left(\frac{R_{eq}}{r_o}\right)\right) \tag{C.50}$$

with

$$\frac{R_{eq}}{r_o} = 1.27 \frac{X_M}{r_o} \left(\frac{X_L}{X_M} - 0.3\right)^{0.5} \tag{C.51}$$

including

$$X_M = \frac{P_t}{2} \tag{C.52}$$

And

$$X_L = \frac{\sqrt{{X_M}^2 + {P_l}^2}}{2} \tag{C.53}$$

Where:

- k_f : $Fin\ thermal\ conductivity\ [W/(m.K)]$
- r_o : $Tube\ outer\ radius\ [m]$
- A_f : $Fin\ surface\ area\ [m^2]$

C-2.3) Correlation for mass transfer coefficient

The mass transfer coefficient, h_m, is computed as a function of the Lewis number, Le, which indicates the fluid's heat transport ability over its mass transport ability:

For $300 < Re_{Dc} < 5500$:

$$Le = \frac{h_{c,wet}}{h_m C_{p,a}} \tag{C.54}$$

The Lewis number can be calculated from the correlation published by Pirompugd *et al.* (2007) and is simplified to the following form (Strydom 2013):

$$\begin{aligned} \mathrm{Le} = 2.28(\mathrm{N})^{0.2393} \left(\frac{F_p}{D_c}\right)^{0.0239N+0.4332} \left(\frac{A_{air,o}}{A_t}\right)^{0.0321N+0.0747} \\ \cdot Re_{Dc}{}^{-0.01833N+0.194\left(\frac{F_p}{D_c}\right)-0.0026\left(\frac{P_l}{D_c}\right)-0.03012\left(\frac{P_t}{D_c}\right)+0.0418} \end{aligned} \tag{C.55}$$

C-2.4) Correlation for airside friction factor

The airside friction factor, f_a, is computed with the correlation of Wang *et al.* (2002a):

For $300 < Re_{Dc} < 1000$:

$$f_a = 4.37 Re_{Dc}{}^{F1} \left(\frac{F_p}{D_h}\right)^{F2} \left(\frac{P_l}{P_t}\right)^{F3} \left(\frac{D_c}{D_h}\right)^{0.2054} N^{F4} \tag{C.56}$$

With:

$$\begin{aligned} F1 = -0.574 - 0.137(\ln(Re_{Dc}) \\ - 5.26)^{0.245} \left(\frac{P_t}{D_c}\right)^{-0.765} \left(\frac{D_c}{D_h}\right)^{-0.243} \left(\frac{F_p}{D_h}\right)^{-0.474} \tan(\theta)^{-0.217} N^{0.035} \end{aligned} \tag{C.57}$$

$$F2 = -3.05 \tan\theta \tag{C.58}$$

$$F3 = -0.192N \tag{C.59}$$

$$F4 = -0.646\, tan\, \theta \tag{C.60}$$

For $1000 < Re_{Dc} < 10000$:

$$f_a = 0.228 Re_{Dc}{}^{F1} (tan\, \theta)^{F2} \left(\frac{F_p}{P_l}\right)^{F3} \left(\frac{P_l}{D_c}\right)^{F4} \left(\frac{D_c}{D_h}\right)^{0.383} \left(\frac{P_l}{P_t}\right)^{-0.247} \tag{C.61}$$

With:

$$F1 = -0.141 \left(\frac{F_p}{P_l}\right)^{0.0512} \left(\frac{P_l}{P_t}\right)^{0.35} \left(\frac{P_t}{D_h}\right)^{0.449 \tan\theta} (tan\, \theta)^{-0.472} N^{-0.049+0.237 \tan\theta} \tag{C.62}$$

$$F2 = -0.562(\ln(Re_{Dc})^{-0.0923}\, N^{0.013} \quad \text{(C.63)}$$

$$F3 = 0.302 {Re_{Dc}}^{0.03} \left(\frac{P_t}{D_c}\right)^{0.026} \quad \text{(C.64)}$$

$$F4 = -0.306 + 3.63\, tan\, \theta \quad \text{(C.65)}$$

APPENDIX D

D-1) Bitzer 4MTE-10K compressor map and datasheet

Selection: Semi-hermetic Reciprocating Compressors

Input Values

Compressor model	4MTE-10K
Mode	Refrigeration and Air conditioning
Refrigerant	R744
Reference temperature	Dew point temp.
Evaporating SST	12,80 °C
High pressure	140,0 bar(a)
Gas cooling outlet	25,0 °C
Suct. gas superheat	5,00 K
Operating mode	Transcritical
Power supply	400V-3-50Hz
Capacity control	100%
Useful superheat	100%

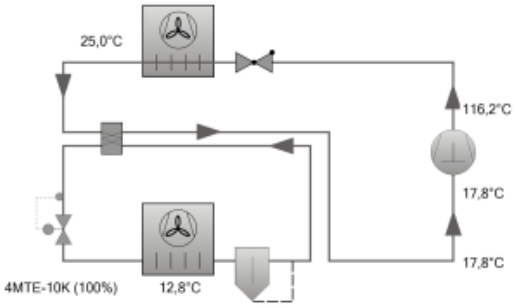

Result

Compressor	**4MTE-10K-40S**
Capacity steps	100%
Cooling capacity	33,6 kW
Cooling capacity *	33,1 kW
Evaporator capacity	33,6 kW
Power input	12,49 kW
Current (400V)	20,7 A
Voltage range	380-420V
Gas cooler capacity	46,1 kW
COP/EER	2,69
Mass flow	662 kg/h
Discharge gas temp. w/o cooling	116,2 °C
optimal high pressure	75,0 bar(a)

Tentative Data.
*according to EN12900 (10K suction gas superheat)

Application Limits 100% 4MTE-10K

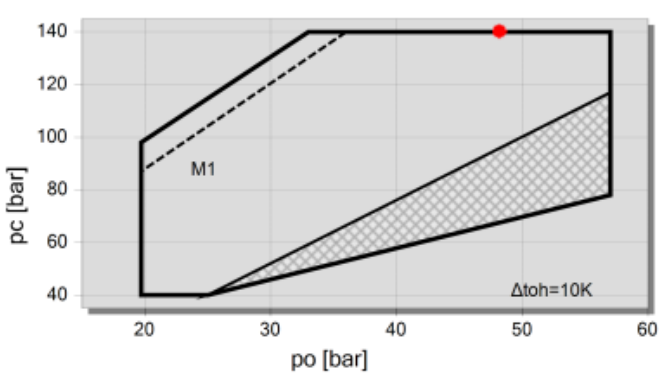

Legend

- mind operating parameters
- M1: motor 1
- Operation above designated line not allowed for following compressor models: 4PTE, 4PTC
- A

Technical Data: 4MTE-10K

Dimensions and Connections

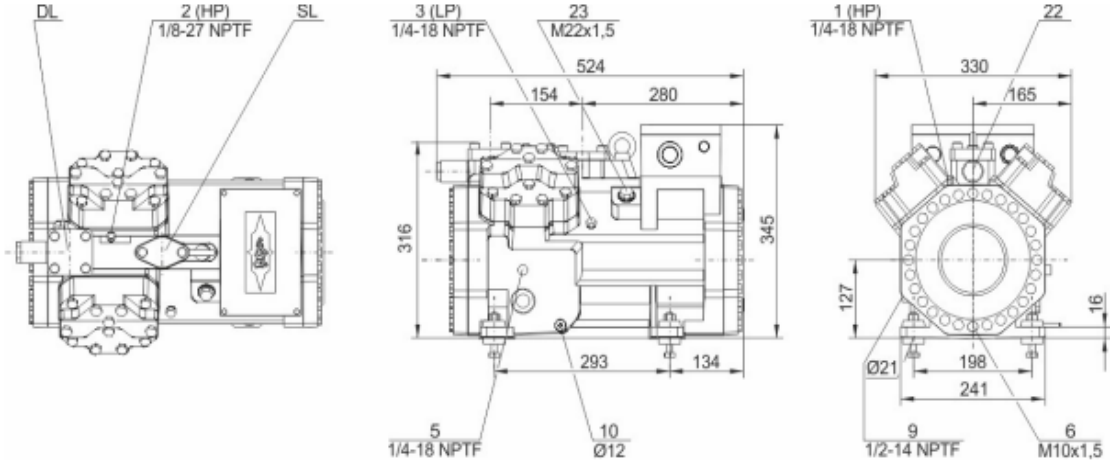

Technical Data

Technical Data	
Displacement (1450 RPM 50Hz)	6,5 m3/h
Displacement (1750 RPM 60Hz)	7,8 m3/h
No. of cylinder x bore x stroke	4 x 30mm x 27mm
Weight	120 kg
Max. pressure (LP/HP)	100/160 bar
Connection suction line	22 mm - 7/8"
Connection discharge line	18 mm - 3/4"
Oil type R744 (CO2)	BSE85K (Standard), BSG68K (Option)
Motor data	
Motor version	1
Motor voltage (more on request)	380-420V Y-3-50Hz
Max operating current	21.9 A
Starting current (Rotor locked)	97.0 A
Max. Power input	12,6 kW
Extent of delivery (Standard)	
Motor protection	SE-B3(Standard), SE-B2(Option)
Enclosure class	IP65
Vibration dampers	Standard
Oil charge	2,00 dm³
Crankcase heater	0..120 W PTC (Standard)
Available Options	
Connection suction line	Option
Discharge shut-off valve	Option
Capacity Control - infinite	100-25% (Option)
Oil level monitoring	OLC-K1 (Option)
Sound measurement	
Sound power level (-10°C / 90bar)	70 dB(A) @ 50Hz
Sound pressure level @ 1m (-10°C / 90bar)	62 dB(A) @ 50Hz

Semi-hermetic Reciprocating Compressors

Motor 1 = e.g. 4TES-12 with 12"HP", primary for air-conditioning (e.g. R22,R407C) and air-conditioning with R134a at high ambient temperatures.
Motor 2 = e.g. 4TES-9 with 8"HP", universal Motor for medium and low temperature application (e.g. R404A, R507A, R407A, R407F) and air-conditioning with R134a
Motor 3 = e.g. 4TES-8, for medium temperature applications and R134a

For more information concerning the application range use the "Limits" button.

Operation modes 4VES-7 to 6FE-44 and 44JE-30 to 66FE-88 with R407F/R407A/R22

CIC = liquid injection with low temperature application, suction gas cooled motor.

ASERCOM certified performance data

The Association of European Refrigeration Component Manufacturers has implemented a procedure of certifying performance data. The high standard of these certifications is assured by:

* plausibility tests of the data performed by experts.
* regular measurements at independent institutes.

These high efforts result in the fact that only a limited number of compressors can be submitted. Due to this not all BITZER compresors are certified until now. Performance data of compressors which fulfil the strict requirements may carry the label "ASERCOM certified". In this software you will find the label at the respective compressors on the right side below the field "result" or in the print out of the performance data. All certified compressors and further information are listed on the homepage of ASERCOM.

Condensing capacity

The condensing capacity can be calculated with or without heat rejection. This option can be set in the menu Program ☐ Options. The heat rejection is constantly 5 % of the power consumption. The condensing capacity is to be found in the line Condensing cap. (with HR) resp. Condensing capacity.

Data for sound emission

Data based on 50 HZ apllication (IP-units 60 Hz) and R404A if not declared.
Sound pressure level: values based on free field area conditions with hemisperhical sound emission in 1 meter distance.

General remarks regarding sound data

Listed sound data were measured under testing conditions in our laboratory. For this purpose the free-standing test sample is mounted on a solid foundation plate and the pipework is connected vibration-free to the largest extend possible. Suction and discharge lines are fixed in a flexible configuration, such that a transmission of vibrations to the environment can be largely excluded. In real installations considerable differences might be observed, compared to the measurements in the laboratory. The airborne sound emitted by the compressor can be reflected from surfaces of the system and this may increase the airborne sound level measured close to the compressor. Vibrations caused by the compressor are also transferred to the system by the compressor feet and piping depending on the damping ratio of the fixings. Thus, the vibrations can induce other components to such an extent that these components contribute to an increase in airborne sound emission. If required, the transfer of vibrations to the system can be minimized by suitable fixing and damping elements.

Legend of connection positions according to "Dimensions":

1 High pressure connection (HP)
2 Connection for discharge gas temperature sensor (HP) (for 4VE(S)-6Y .. 4NE(S)-20(Y) connection for CIC sensor as alternative)
3 Low pressure connection (LP)
4 CIC system: injection nozzle (LP)
4b Connection for CIC sensor
4c Connection for CIC sensor (MP / operation with liquid subcooler)
5 Oil fill plug
6 Oil drain
7 Oil filter (magnetic screw)
8 Oil return (oil separator)
8* Oil return with NH3 and insoluble oil
9 Connection for oil and gas equalization (parallel operation)
9a Connection for gas equalization (parallel operation)

9b Connection for oil equalization (parallel operation)
10 Oil heater connection
11 Oil pressure connection +
12 Oil pressure connection –
13 Cooling water connection
14 Intermediate pressure connection (MP)
15 Liquid injection (operation without liquid subcooler and with thermostatic expansion valve)
16 Connection for oil monitoring (opto-electrical oil monitoring "OLC-K1" or differential oil pressure switch "Delta-PII")
17 Refrigerant inlet at liquid subcooler
18 Referigerant outlet at liquid subcooler
19 Clamp space
20 Terminal plate
21 Maintenance connection for oil valve
22 Pressure relief valve to the atmosphere (discharge side)
23 Pressure relief valve to the atmosphere (suction side)
24 IQ MODULE
SL Suction gas line
DL Discharge gas line
Dimensions can show tolerances according to EN ISO 13920-B.

D-2) Derivation of compressor characteristic equations:

The numerical compressor characterisation method published by Bester (A methodology for the performance characterisation of a variable speed CO2 compressor 2018) will now be applied to derive the equations listed in Table 4-2 that are substituted into Equations (4.1) and (4.2) to predict the R744 discharge temperature and mass flow rate, respectively. Note that only the application of the method will be described in this document and that reference can be made to the study of Bester (A methodology for the performance characterisation of a variable speed CO2 compressor 2018) for more information regarding the method itself.

This method will now be applied to the above-described 4MTE-10K Bitzer compressor and is limited to the compressor's expected operational ranges as discussed in Section 5.1, i.e., a constant operational frequency of 50 Hz, evaporation temperature range of 5.7-16.4°C (suction pressure range of ≈4.04-5.26 MPa), discharge pressure range of 11.0-14.0 MPa, and suction temperature range of ≈11-36°C. As mentioned in Section 5.1, the required operational data of the compressor are obtained from the manufacturer-supplied software.

The first correlation:

The first step in the method will be used to obtain a correlation between one of the varying input values and the two respective output variables. In other words, a correlation between the suction temperature and the discharge temperature will be found, followed by a correlation between the

same mentioned input and the second output, namely the mass flow rate. Whilst obtaining data on the relation between two variables, all other variables are kept constant.

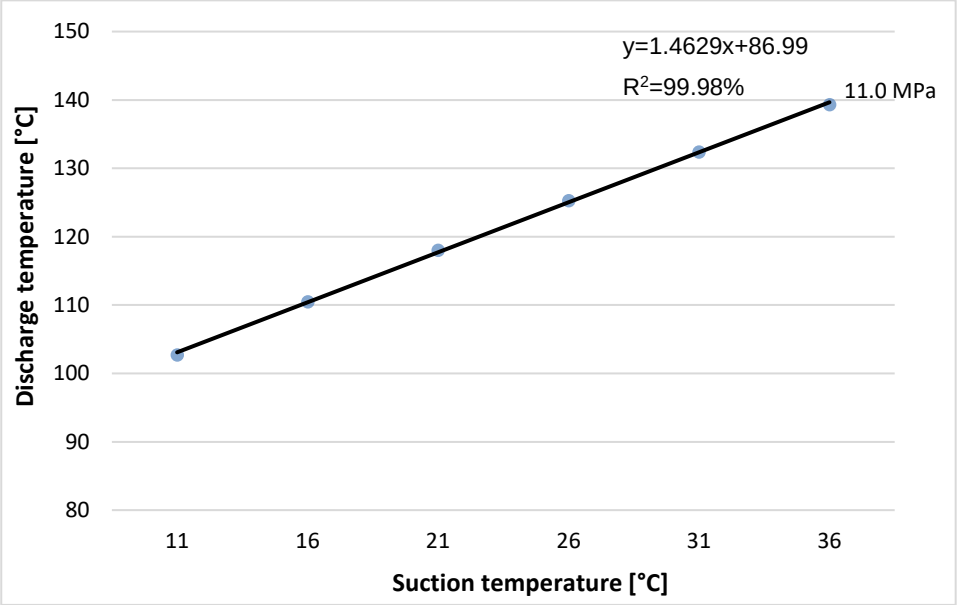

Figure D-1: Plot and correlation of compressor discharge temperature as a function of suction temperature at 11.0 MPa discharge pressure (50 Hz operating frequency and 4.04 MPa suction pressure).

An illustration of the correlation between the suction temperature and discharge temperature is shown in Figure D-1. Note that apart from the constant 50 Hz operating frequency, the data shown in the plot is specific to a 4.04 MPa suction pressure and 11.0 MPa discharge pressure. Whilst the mentioned variables are kept constant, a linear rise in discharge temperature is linked to increased suction temperature. Furthermore, the figure displays the least-squares regression line applied to the data points as well as the correlation coefficient, which yields a 99.98% accuracy between the regression equation and the data points.

At the present stage, the correlation equation from Figure D-1 is in the following form as described by Bester (2018):

$$T_{dis} = \sum_{i=0}^{n} j_i(x_1)\, {T_{suc}}^{i} \tag{D.1}$$

$$j_i(x_1) = j_1(P_{dis}, P_{suc}, Hz) \tag{D.2}$$

With $n = 1$.

The same process is performed to calculate a regression equation between the suction temperature and mass flow rate whilst all other variables are kept constant. At this stage, similar to Equations (D.1) and (D.2), the mass flow rate correlation can be defined as:

$$\dot{m} = \sum_{i=0}^{n} j_i(x_1)\, {T_{suc}}^i \tag{D.3}$$

$$j_i(x_1) = j_1(P_{dis}, P_{suc}, Hz) \tag{D.4}$$

With $n = 1$.

As mentioned before, both the outputs, namely discharge temperature and mass flow rate, are discussed concurrently. Nevertheless, it is important to emphasise that their resulting correlations are developed independently and should not be confused.

In summary of the first correlation, equations have been developed that define the relation between suction temperature and discharge pressure, as well as suction temperature and mass flow rate.

The second correlation:

In the first correlation, the least-square regression equations were applied to relate the two respective outputs to the suction temperature at a constant suction pressure of 4.04 MPa and discharge pressure of 11.0 MPa. This will now be repeated over a range of discharge pressures, although still at the constant suction pressure. Hence, the coefficients of these equations will be known and used to develop the second correlation by establishing their relationship with their corresponding discharge pressures.

At a constant suction pressure of 4.04 MPa, the process described in the first correlation is repeated in increments of 0.5 MPa over the whole range of discharge pressures investigated by the present study, i.e., 11.0 MPa to 14.0 MPa. These data points and accompanying least-squares regression lines are shown in Figure D-2. Consistent with Figure D-1, a linear rise in discharge temperature is notable due to increased suction temperature. Note that these regression lines also have respective regression equations and are listed on the left-hand side of Table D-1.

The equivalent process is performed to calculate regression equations between the suction temperature and mass flow rate over the range of discharge pressures, as shown in Figure D-3.

A linear reduction in mass flow rate can be seen with increased suction temperature. Note that the corresponding regression equations are listed on the right-hand side of Table D-1. From the table, it is evident that the correlation values of the mass flow rate are generally slightly lower than those of the discharge temperature equation.

Nevertheless, the regression equations are deemed accurate, considering that the weakest correlation coefficient value is still 99.25%. Thus, it can be concluded for the first correlation that the generated polynomials are sufficiently accurate within the first degree (thus $n = 1$). As described by Bester (2018), this varies from application and may not always be the case.

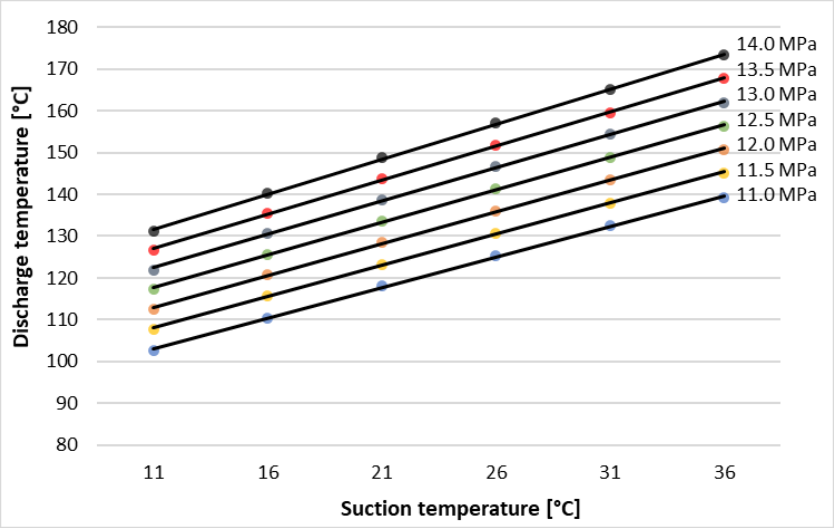

Figure D-2: Plot of compressor discharge temperature as a function of discharge pressure over a range of suction temperatures (50 Hz operating frequency and 4.04 MPa suction pressure).

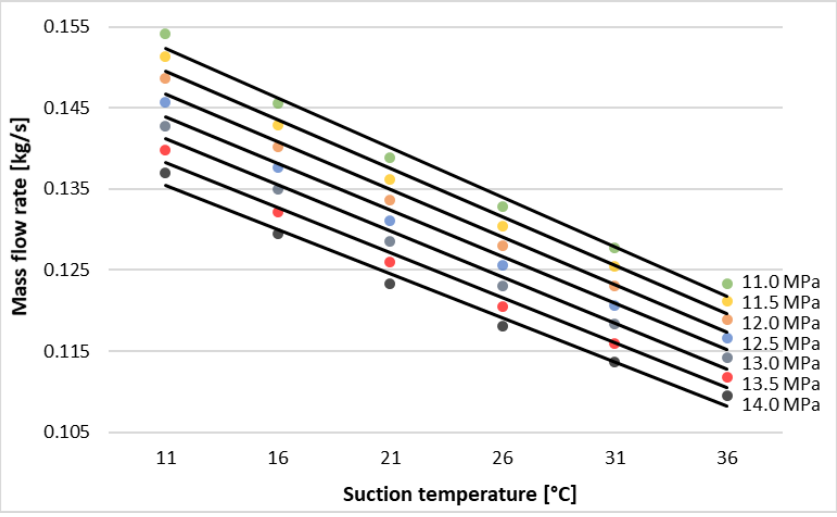

Figure D-3: Plot of compressor mass flow rate as a function of discharge pressure over a range of suction temperatures (50 Hz operating frequency and 4.04 MPa suction pressure).

Table D-1: Discharge temperature and mass flow rate as a function of suction temperature at 10.0 MPa discharge pressure (50 Hz operating frequency and 4.04 MPa suction pressure).

P_{dis} [MPa]	Discharge temperature equation			Mass flow rate equation		
	j_1	j_0	R^2	j_1	j_0	R^2
11.0	1.4629E+00	8.6990E+01	0.99976	-1.2206E-03	1.6577E-01	-0.9930
11.5	1.4940E+00	9.1583E+01	0.99973	-1.1984E-03	1.6275E-01	-0.9928
12.0	1.5251E+00	9.6176E+01	0.99970	-1.1762E-03	1.5972E-01	-0.9925
12.5	1.5594E+00	1.0054E+02	0.99969	-1.1516E-03	1.5662E-01	-0.9926
13.0	1.5966E+00	1.0485E+02	0.99970	-1.2167E-03	1.5511E-01	-0.9935
13.5	1.6354E+00	1.0904E+02	0.99975	-1.1889E-03	1.5188E-01	-0.9936
14.0	1.6786E+00	1.1317E+02	0.99981	-1.2556E-03	1.5017E-01	-0.9936

At this point, the discharge temperature equations listed in Table D-1 can be written as follow:

For $k = 11.0; 14.0$ and since $n = 1$;

$$T_{dis_k} = \sum_{i=0}^{n} j_i(x_1)\, {T_{suc}}^i \tag{D.5}$$

Thus:

$$T_{dis_k} = j_1(x_1) T_{suc} + j_0(x_1)$$

Whereas the mass flow rate equations listed in Table D-1 can be written as:

For $k = 11.0; 14.0$ and since $n = 1$:

$$\dot{m}_k = \sum_{i=0}^{n} j_i(x_1)\, {T_{suc}}^i \tag{D.6}$$

Thus:

$$\dot{m}_k = j_1(x_1) T_{suc} + j_0(x_1)$$

Note from Equations (D.5) and (D.6) that the value k varies from 11.0 to 14.0 and represents the discharge pressure within its operational limits.

At this stage, the coefficients of the equations linking the discharge temperature to the suction temperature are known. The relationship between these coefficients and their corresponding discharge pressures will now be determined using the least-squares method described in the first correlation.

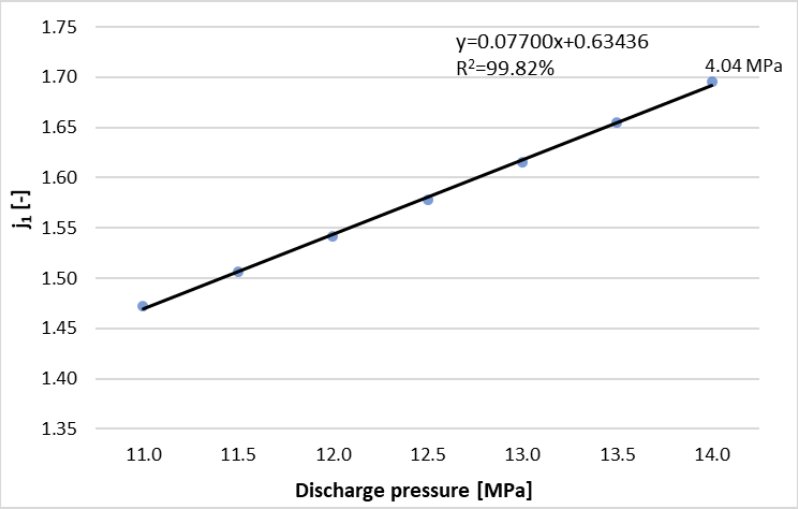

Figure D-4: Plot and correlation of j_1 as a function of discharge pressure for the discharge temperature equations (50 Hz operating frequency and 4.04 MPa suction pressure)

Figure D-4 and Figure D-5 illustrate a plot of j_1 and j_0 at the respective discharge pressures for the discharge temperature equations in Table D-1. Also illustrated are the least-squares regression lines applied to the mentioned data points as well as the corresponding correlation equations and correlation values.

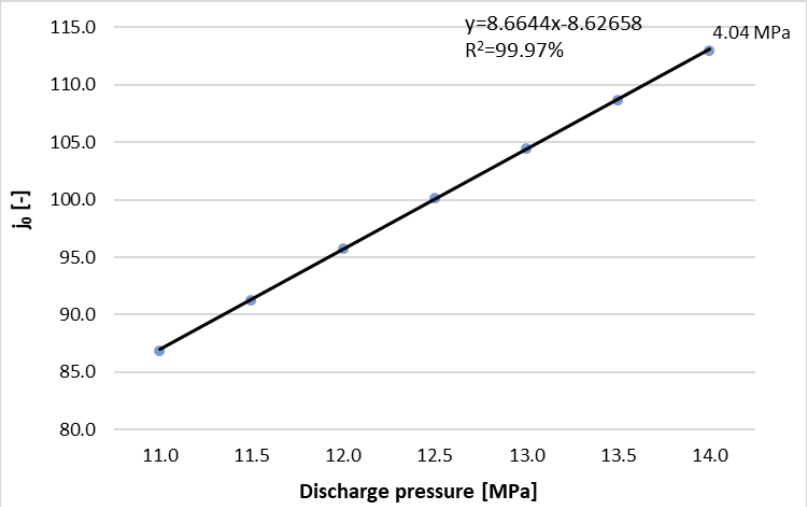

Figure D-5: Plot and correlation of j_0 as a function of discharge pressure for the discharge temperature equations (50 Hz frequency and 4.04 MPa suction pressure).

Similar plots and correlation equations are generated for the mass flow rate equations listed in Table D-1. The coefficients of these resulting equations are listed in Table D-2. Analogous to the first correlation, the least-squares regression method yielded sufficiently accurate correlation values since even the lowest correlation value yielded 99.82% (thus $p = 1$).

At this stage, the equations in Table D-2 (Figure D-4 and Figure D-5) can be written in the form:

With $p = 1\ and\ i = 0{,}1$;

$$j_i(x_1) = \sum_{m=0}^{p} k_{i,m}(x_2)\ {P_{dis}}^m \tag{D.7}$$

Table D-2: Discharge temperature coefficients and mass flow rate coefficients as a function of discharge pressure (50 Hz operating frequency and 4.04 MPa suction pressure).

Discharge temperature equation					
$\boldsymbol{j_1}$			j_0		
$\boldsymbol{k_{1,1}}$	$k_{1,0}$	R^2	$\boldsymbol{k_{0,1}}$	$k_{0,0}$	R^2
0.07700	0.6344	0.9982	8.6644	-8.6258	0.9997
Mass flow rate equation					
$\boldsymbol{j_1}$			j_0		
$\boldsymbol{k_{1,1}}$	$k_{1,0}$	R^2	$\boldsymbol{k_{0,1}}$	$k_{0,0}$	R^2
2.5000e-5	-1.5810e-3	0.9989	-5.9417e-3	2.3308e-1	0.9999

Equation (D.7) can now be combined with the discharge temperature in Equation (D.5) to form:

$$T_{dis} = \sum_{i=0}^{1} j_i(x_1)\ {T_{suc}}^i$$

$$T_{dis} = \sum_{i=0}^{1} \left(\sum_{m=0}^{p} k_{i,m}(x_2)\ {P_{dis}}^m \right) {T_{suc}}^i \tag{D.8}$$

Similarly, Equation (D.7) can be combined with the mass flow rate in Equation (D.6) to form:

$$\dot{m} = \sum_{i=0}^{1} j_i(x_1)\ {T_{suc}}^i$$

$$\dot{m} = \sum_{i=0}^{1} \left(\sum_{m=0}^{p} k_{i,m}(x_2)\ {P_{dis}}^m \right) {T_{suc}}^i \tag{D.9}$$

Since the coefficient values are known, and since $p = 1$ is valid for both Equations (D.8) and (D.9), the following simplifications can be made:

For $l = 4.04$

$$T_{dis_l} = \sum_{i=0}^{1} \left(\sum_{m=0}^{1} k_{i,m}(x_2)\ {P_{dis}}^m \right) {T_{suc}}^i \tag{D.10}$$

$$= \left(k_{1,1}(x_2)P_{dis} + k_{1,0}(x_2)\right)T_{suc} + \left(k_{0,1}(x_2)P_{dis} + k_{0,0}(x_2)\right)$$

And

For $l = 4.04$

$$\dot{m}_l = \sum_{i=0}^{1}\left(\sum_{m=0}^{1} k_{i,m}(x_2)\, {P_{dis}}^{m}\right) {T_{suc}}^{i} \tag{D.11}$$

$$= \left(k_{1,1}(x_2)P_{dis} + k_{1,0}(x_2)\right)T_{suc} + \left(k_{0,1}(x_2)P_{dis} + k_{0,0}(x_2)\right)$$

For an R744 suction pressure of 4.04 MPa, Equations (D.10) and (D.11) should be interpreted as the resulting equations that individually relate the two respective outputs to the inputs, i.e., the discharge pressure and mass flow rate to the suction temperature.

The third correlation:

In the second correlation, the least-square regression equations were used to relate the two induvial outputs, namely discharge temperature and mass flow rate, to two varying inputs, namely the discharge pressure and suction temperature. Whilst doing so, suction pressure was fixed at 4.04 MPa. For the third correlation, this will now be reperformed over a range of suction pressures. Hence, the coefficients of these equations will be known and used to develop the third correlation by determining their relationship with their corresponding suction pressures.

The method described in the second correlation will now be repeated over the full range of suction pressures considered by the present study, i.e., 4.04 MPa to 5.26 MPa. Unlike the first two correlations, for the present correlation, the graphical aid will be given in terms of the mass flow rate.

Figure D-6 and Figure D-7 demonstrate a plot of the mass flow rate's coefficients, namely j_1 and j_0, respectively. These graphs are similar to those depicted in Figure D-4 and Figure D-5, except that they are shown for the mass flow rate and over a range of suction pressures. In other words, the two individual lines in Figure D-6 and Figure D-7 linked to the 4.04 MPa suction pressure are represented by the coefficients listed in Table D-2 for the mass flow rate equation. As is evident in the figures, least-squares regression lines are applied to the plotted data points.

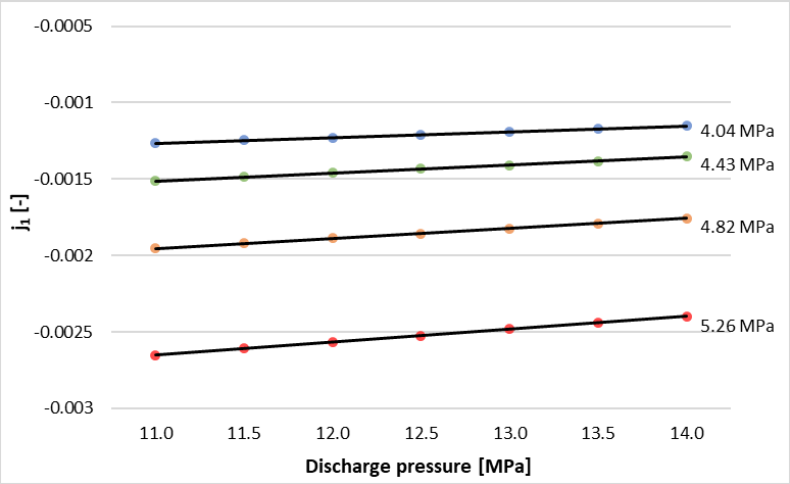

Figure D-6: Plot of the mass flow rate's coefficient j_1 as a function of discharge pressure over the range of suction pressures.

This process involving the range of suction pressures is also repeated for the other output, i.e., the discharge temperature. Table D-3 lists the resulting coefficients of the regression lines used to relate the j_1 and j_0 coefficients of the mass flow rate (Figure D-6 and Figure D-7) and discharge temperature to the discharge pressure over a range of suction pressures. Also included in the table are the correlation coefficients of the regression lines. Consistent with the sufficient accuracy of the correlations at a fixed suction pressure of 4.04 MPa, the correlation coefficients linked to the rest of the suction pressure range are also satisfactory accurate considering that its lowest value was recorded as 99.74%.

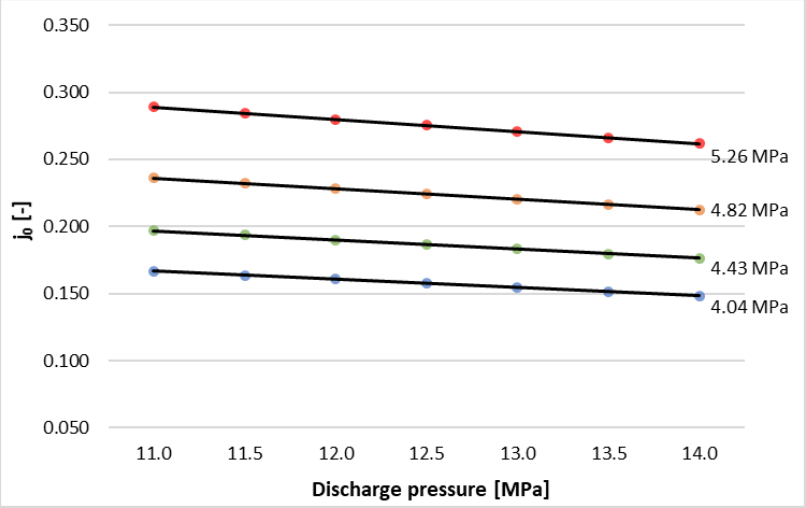

Figure D-7: Plot of the mass flow rate's coefficient j_0 as a function of discharge pressure over the range of suction pressures.

At this point, the discharge temperature and mass flow rate equations listed in Equations (D.10) and (D.11), can be broadened to: For $l = 4.04; 5.26$. Note that the value l represents the suction pressure within its operational limits.

Table D-3: Regression equation coefficients of the discharge temperature and mass flow rate as a function of the discharge pressure over a range of suction pressures.

	Discharge temperature equation					
	j_1			j_0		
$P_{suc}\ [MPa]$	$k_{1,1}$	$k_{1,0}$	R^2	$k_{0,1}$	$k_{0,0}$	R^2
4.04	0.0770	0.6344	0.9982	8.6644	-8.6258	0.9997
4.43	0.0680	0.6876	0.9974	8.2120	-14.3283	0.9998
4.82	0.0709	0.6364	0.9998	7.5663	-17.7900	0.9998
5.26	0.0794	0.5621	0.9989	6.7329	-19.9297	0.9994
	Mass flow rate equation					
	j_1			j_0		
$P_{suc}\ [MPa]$	$k_{1,1}$	$k_{1,0}$	R^2	$k_{0,1}$	$k_{0,0}$	R^2
4.04	2.5000E-05	-1.5810E-03	0.9989	-5.9417E-03	2.3308E-01	0.9999
4.43	5.0000E-05	-2.0552E-03	0.9979	-6.8159E-03	2.7161E-01	0.9998
4.82	6.3492E-05	-2.5837E-03	0.9999	-7.7817E-03	3.1956E-01	0.9999
5.26	8.7320E-05	-3.6168E-03	0.9998	-9.2287E-03	3.9083E-01	0.9999

The coefficients of the least-square equations relating the above correlations to the suction pressure are now known. Once again, the objective is to determine the relationship between these coefficients and the input variable. Thus, these coefficient values will be evaluated relative to the suction pressure.

An illustration hereof is shown for the $k_{1,1}$ coefficient of the discharge temperature equation. The correlation coefficient was found to be the most accurate (99.89%) for a polynomial function of the third order. Note that for all functions before this step, polynomials of the first order were accurate enough. Similar plots are generated and hence evaluations are carried out for the remaining coefficients in Table D-3.

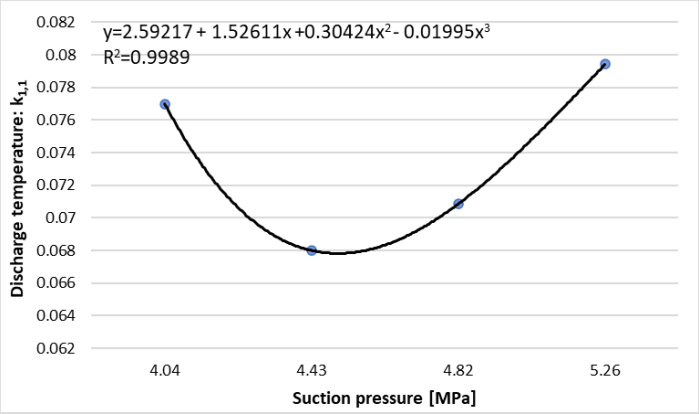

Figure D-8: Plot of the discharge temperature equation's coefficient $k_{1,1}$ over the suction pressure.

The above-mentioned objective has now been satisfied since the relation between the coefficients and suction pressure is integrated from discrete values into a correlational function.

Hence, over the full suction pressure range, Equations (D.10) and (D.11) and can be derived to:

$$T_{dis} = \left(k_{1,1}(P_{suc}) \cdot P_{dis} + k_{1,0}(P_{suc})\right) \cdot T_{suc} + \left(k_{0,1}(P_{suc}) \cdot P_{dis} + k_{0,0}(P_{suc})\right) \quad \text{(D.12)}$$

$$\dot{m} = \left(k_{1,1}(P_{suc}) \cdot P_{dis} + k_{1,0}(P_{suc})\right) \cdot T_{suc} + \left(k_{0,1}(P_{suc}) \cdot P_{dis} + k_{0,0}(P_{suc})\right) \quad \text{(D.13)}$$

With the coefficients that are a function of P_{suc} listed in

Table D-4. Note that the bolded row corresponds to the illustration given in Figure D-8.

Since a fixed operating frequency of 50 Hz is present and all other three input variables of this study's compressor model have been accounted for, the application of Bester (2018)'s method for this study is complete. Note that Equations (D.12) and (D.13) together with

Table D-4 are the ultimate equations from applying this method to the compressor model of the current study.

Table D-4: Internal coefficient functions of suction pressure for Equations (D.12) and (D.13).

Equation	Coefficient	Value
$\boldsymbol{T_{dis}}$	$k_{1,1}(P_{suc})$	$= (\mathbf{-1.9948e^{-2} \cdot P_{suc}^3}) + (\mathbf{3.0424e^{-1} \cdot P_{suc}^2}) + (\mathbf{-1.5261e^{0} \cdot P_{suc}}) + \mathbf{2.5922e^{0}}$
	$k_{1,0}(P_{suc})$	$= (2.3950e^{-1} \cdot P_{suc}^3) + (-3.5242e^{0} \cdot P_{suc}^2) + (1.7092e^{1} \cdot P_{suc}) - 2.6687e^{1}$
	$k_{0,1}(P_{suc})$	$= (1.9083e^{-1} \cdot P_{suc}^3) + (-3.1040e^{0} \cdot P_{suc}^2) + (1.4835e^{1} \cdot P_{suc}) - 1.3189e^{1}$
	$k_{0,0}(P_{suc})$	$= (-2.7107e^{-0} \cdot P_{suc}^3) + (4.3891e^{1} \cdot P_{suc}^2) + (-2.4061e^{2} \cdot P_{suc}) + 4.2585e^{2}$
$\boldsymbol{\dot{m}}$	$k_{1,1}(P_{suc})$	$= (5.2808e^{-5} \cdot P_{suc}^3) + (-7.4167e^{-4} \cdot P_{suc}^2) + (3.5035e^{-3} \cdot P_{suc}) - 5.5059e^{-3}$
	$k_{1,0}(P_{suc})$	$= (-9.1276e^{-4} \cdot P_{suc}^3) + (1.2011e^{-2} \cdot P_{suc}^2) + (-5.3817e^{-2} \cdot P_{suc}) + 7.9997e^{-2}$
	$k_{0,1}(P_{suc})$	$= (-7.0211e^{-4} \cdot P_{suc}^3) + (9.1382e^{-3} \cdot P_{suc}^2) + (-4.1873e^{-2} \cdot P_{suc}) + 6.0374e^{-2}$
	$k_{0,0}(P_{suc})$	$= (2.0301e^{-2} \cdot P_{suc}^3) + (-2.4404e^{-1} \cdot P_{suc}^2) + (1.0744e^{0} \cdot P_{suc}) - 1.4629e^{0}$

APPENDIX E

E-1) Tabular format of verification and validation results

Table E-1: Compressor verification results in table format (Section 5.1)

Condition	Simulation Results			Bitzer-software results			% Relative Error		
	$\dot{m}_r \left[\frac{kg}{s}\right]$	$\Delta T_c\ [°C]$	$W_c\ [kW]$	$\dot{m}_r \left[\frac{kg}{s}\right]$	$\Delta T_c\ [°C]$	$W_c\ [kW]$	$\dot{m}_r$	ΔT_c	W_c
1	0.1466	114.7	11.96	0.1450	114.4	11.92	-0.28%	0.26%	0.34%
2	0.1479	98.4	10.60	0.1472	98.6	10.59	0.46%	-0.20%	0.06%
3	0.1650	86.6	10.22	0.1656	86.5	10.29	-0.34%	0.12%	-0.68%
4	0.1322	120.2	11.64	0.1314	120.4	11.60	0.62%	-0.17%	0.38%
5	0.2199	68.0	9.67	0.2186	68.2	9.71	0.59%	-0.29%	-0.42%
						Average values	0.21%	-0.06%	-0.06%

Table E-2: Gas cooler verification and validation results in table format (Section 5.2)

Condition	Simulation Results			Harris (2014) results			% Relative Error		
	$\Delta T_r\ [°C]$	$\Delta T_w\ [°C]$	$\dot{Q}_H\ [kW]$	$\Delta T_r\ [°C]$	$\Delta T_w\ [°C]$	$\dot{Q}_H\ [kW]$	ΔT_r	ΔT_w	$\dot{Q}_H$
1	64.5	36.6	27.7	63.7	35.6	26.7	1.21%	2.75%	3.71%
2	66.9	42.7	30.1	65.9	41.5	29.0	1.43%	2.87%	3.66%
3	72.6	48.8	32.4	71.4	47.3	31.2	1.61%	3.21%	3.72%
4	70.3	58.4	31.6	69.7	54.7	30.2	0.87%	6.80%	4.50%
5	71.8	65.0	32.3	71.9	62.5	31.8	-0.04%	3.97%	1.70%
						Average values	1.01%	3.92%	3.46%
Condition	**Simulation Results**			**Flownex results**			**% Relative Error**		
	$\Delta T_r\ [°C]$	$\Delta T_w\ [°C]$	$\dot{Q}_H\ [kW]$	$\Delta T_r\ [°C]$	$\Delta T_w\ [°C]$	$\dot{Q}_H\ [kW]$	ΔT_r	ΔT_w	$\dot{Q}_H$
1	64.5	36.6	27.7	64.5	36.7	27.8	-0.05%	-0.25%	-0.22%
2	66.9	42.7	30.1	66.9	42.7	30.1	-0.10%	-0.09%	-0.07%
3	72.6	48.8	32.4	72.6	48.9	32.4	-0.08%	-0.04%	-0.06%
4	70.3	58.4	31.6	70.3	58.4	31.5	-0.06%	0.10%	0.13%
5	71.8	65.0	32.3	71.9	64.9	32.3	-0.01%	0.14%	0.12%
						Average values	-0.06%	-0.03%	-0.02%

Table E-3: Evaporator verification and validation results in table format (Section 5.3)

Condition	Simulation Results			Strydom (2013) results			% Relative Error		
	$T_{r,o}$ [°C]	$T_{a,o}$ [°C]	$\dot{Q}_L$ [kW]	$T_{r,o}$ [°C]	$T_{a,o}$ [°C]	$\dot{Q}_L$ [kW]	$T_{r,o}$	$T_{a,o}$	$\dot{Q}_L$
1	14.6	14.2	9.12	12.8	13.3±0.3	9.03±0.7	13.91%	4.41%	0.00%
2	13.8	14.1	8.80	15.1	14.3±0.4	9.51±0.78	-8.41%	0.00%	0.00%
3	14.3	14.9	5.80	16.4	15.4±0.4	7.15±0.87	-12.62%	-0.67%	-7.64%
4	24.6	25.1	27.98	18.7	24.2±0.5	27.00±0.45	31.50%	1.74%	1.93%
5	22.7	24.7	31.16	16.7	24.4±0.5	29.72±0.37	36.17%	0.00%	3.56%
						Average values	12.11%	1.10%	-0.43%

Condition	Simulation Results			EVAP-COND results			% Relative Error		
	$T_{r,o}$ [°C]	$T_{a,o}$ [°C]	$\dot{Q}_L$ [kW]	$T_{r,o}$ [°C]	$T_{a,o}$ [°C]	$\dot{Q}_L$ [kW]	$T_{r,o}$	$T_{a,o}$	$\dot{Q}_L$
1	14.6	14.2	9.12	14.2	14.5	9.03	2.68%	-2.07%	1.00%
2	13.8	14.1	8.80	13.9	14.6	8.80	-0.50%	-2.82%	0.00%
3	14.3	14.9	5.80	14.4	15.0	5.78	-0.49%	-0.67%	0.35%
4	24.6	25.1	27.98	24.6	25.7	27.98	-0.04%	-2.22%	0.00%
5	22.7	24.7	31.16	22.9	25.6	31.21	-0.70%	-3.17%	-0.16%
						Average values	0.19%	-2.19%	0.24%

E-2) Set ups of commercial software used to gather verification data

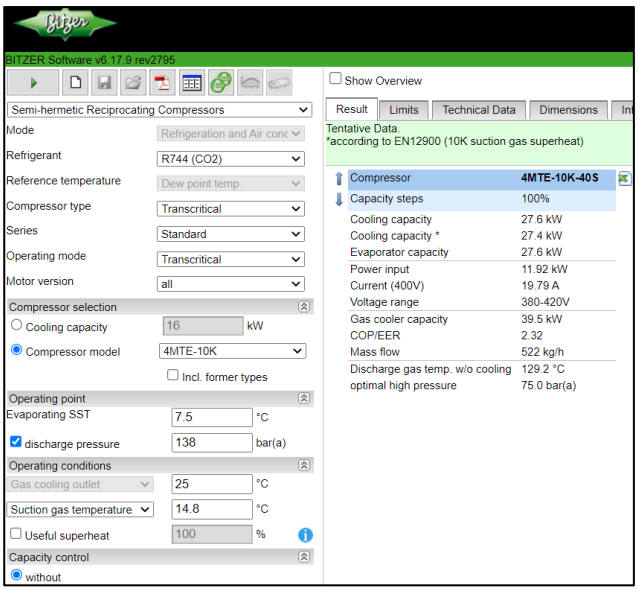

Figure E-1: Set up on Bitzer webpage used to obtain verification data of compressor.

Compressor: In Figure E-1, the set up of the Bitzer software (link in bibliography) are shown in the upper left-hand pane. From thereon, the operating conditions further down the pane can be adjusted as desired.

Gas cooler: In Figure E-2, the set up of the gas cooler model built in Flownex is shown. Note that Flownex does not include a default tube-in-tube heat exchanger and thus the compact heat exchanger was chosen with conduction present on the inner pipe and convection present on both sides of the pipe. The hydraulic diameter and annular flow area were used for the water flow on the annular side and heat losses to the environment was neglected.

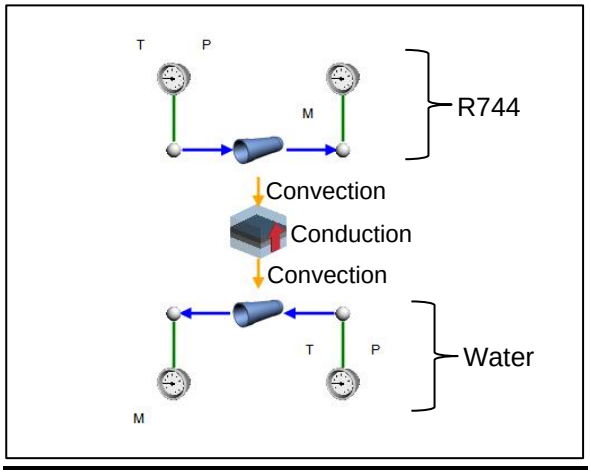

Figure E-2: Set up on Flownex used to obtain verification data of gas cooler.

Evaporator: The model set up and inputs used for the finned tube evaporator in EVAP-COND are shown in Figure E-3. Hence, the operating conditions can be altered under the *Operating Conditions* menu.

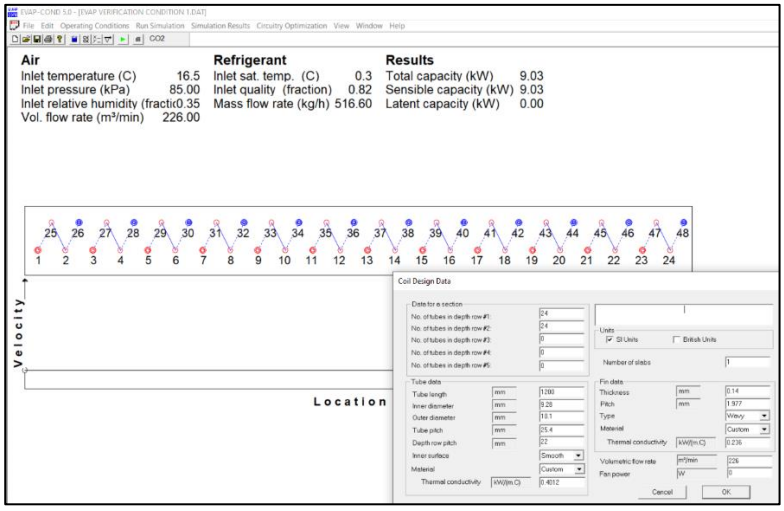

Figure E-3: Set up on EVAP-COND used to obtain verification data of evaporator.

APPENDIX F

EES Code

```
$Load Incompressible

"!_____PROCEDURES_____"

"Compressor: Characteristic polynomial equations developed to calculate refrigerant mass flow rate & discharge temperature"

Procedure comp_polynomials(P_suc_Pa; P_dis_Pa ; T_suc : m_dot ; T_dis)
P_suc=P_suc_Pa*10^(-6)
P_dis=P_dis_Pa*10^(-6)
        t_1_1= 2,59216685056306+(-1,52611022342166)*P_suc+(0,30424307216176)*P_suc^2+(-0,0199482170491549)*P_suc^3
        t_1_0= -26,6874666590547+(17,0915741279337)*P_suc+(-3,52420969949961)*P_suc^2+(0,239497108884264)*P_suc^3
        t_0_1= -13,1894277467706+(14,835069640648)*P_suc+(-3,10400204957371)*P_suc^2+(0,19083253345634)*P_suc^3
        t_0_0= 425,848476263789+(-240,613128921386)*P_suc+(43,890652556457)*P_suc^2+(-2,71073998397157)*P_suc^3
        m_1_1= -0,00550591135894927+(0,00350345437091076)*P_suc+(-0,00074167223116209)*P_suc^2+(5,28082449071634E-05)*P_suc^3
        m_1_0= 0,0799973614349215+(-0,0538170982792595)*P_suc+(0,0120105146806481)*P_suc^2+(-0,00091275797338696 1)*P_suc^3
        m_0_1= 0,0603740293822246+(-0,0418730137538389)*P_suc+(0,00913821457291109)*P_suc^2+(-0,00070210958359174 4)*P_suc^3
        m_0_0= -1,46289837007017+(1,07433815706922)*P_suc+(-0,244037975782327)*P_suc^2+(0,0203011797757573)*P_suc^3
m_dot=(m_1_1*P_dis+m_1_0)*T_suc+(m_0_1*P_dis+m_0_0)
T_dis=(t_1_1*P_dis+t_1_0)*T_suc+(t_0_1*P_dis+t_0_0)
End

"Evaporator: Outlet refrigerant properties"

Function cp_r(x_R744;P_R744;h_R744)
 If (x_R744<=0) or (x_R744>=1) Then
        cp_r=cp(R744;P=P_R744;h=h_R744)
Endif
If (x_R744>0) and (x_R744<1) Then
        Cp_f=cp(R744;P=P_R744;x=0)
        Cp_g=cp(R744;P=P_R744;x=1)
        cp_r=Cp_g*x_R744+Cp_f*(1-x_R744)
Endif
End

Function mu_r(x_R744;P_R744;h_R744)
 If (x_R744<=0) or (x_R744>=1) Then
        mu_r=viscosity(R744;P=P_R744;h=h_R744)
Endif
If (x_R744>0) and (x_R744<1) Then
        mu_f=viscosity(R744;P=P_R744;x=0)
        mu_g=viscosity(R744;P=P_R744;x=1)
        mu_r=mu_g*x_R744+mu_f*(1-x_R744)
Endif
```

```
End

Function k_r(x_R744;P_R744;h_R744)
 If (x_R744<=0) or (x_R744>=1) Then
        k_r=conductivity(R744;P=P_R744;h=h_R744)
Endif
If (x_R744>0) and (x_R744<1) Then
        k_f=conductivity(R744;P=P_R744;x=0)
        k_g=conductivity(R744;P=P_R744;x=1)
        k_r=k_g*x_R744+k_f*(1-x_R744)
Endif
End

Function tempr744(x_R744;P_R744;h_R744)
 If (x_R744<=0) or (x_R744>=1) Then
        tempr744=temperature(R744;P=P_R744;h=h_R744)
Endif
If (x_R744>0) and (x_R744<1) Then
        tempr744=temperature(R744;P=P_R744;x=x_R744)
Endif
End

"Evaporator: Correlation for dry air: Heat transfer coefficient and friction factor"

Procedure chtc_dry&ff(Re_Dc;D_c;Dh_air;F_p;TP_t;theta;N_rows;TP_l;k_a;Pr_a:h_dry;f_a)
If Re_Dc<1000 Then
        J1=0,0045-0,491*Re_Dc^(-0,0316-0,0171*ln(N_rows*tan(theta)))*(TP_l/TP_t)^(-
0,109*ln(N_rows*tan(theta)))*(D_c/Dh_air)^(0,542+0,0471*N_rows)*(F_p/D_c)^0,984*(F_p/TP_t)^(-
0,349)
        J2=-2,72+6,84*tan(theta)
        J3=2,66*tan(theta)

        j_dry=0,882*Re_Dc^J1*(D_c/Dh_air)^J2*(F_p/TP_t)^J3*(F_p/D_c)^(-1,58)*tan(theta)^(-0,2)

        F1=-0,574-0,137*(ln(Re_Dc)-5,26)^0,245*(TP_t/D_c)^(-0,765)*(D_c/Dh_air)^(-
0,243)*(F_p/Dh_air)^(-0,474)*tan(theta)^(-0,217)*N_rows^0,035
        F2=-3,05*tan(theta)
        F3=-0,192*N_rows
        F4=-0,646*tan(theta)

        f_a=4,37*Re_Dc^F1*(F_p/Dh_air)^F2*(TP_l/TP_t)^F3*(D_c/Dh_air)^0,2054*N_rows^F4
Else
        J1=-0,0545-0,0538*tan(theta)-0,302*N_rows^(-0,24)*(F_p/TP_l)^(-
1,3)*(TP_l/TP_t)^0,379*(TP_l/Dh_air)^(-1,35)*(tan(theta))^(-0,256)
        J2=-1,29*(TP_l/TP_t)^(1,77-9,43*tan(theta))*(D_c/Dh_air)^(0,229-1,43*tan(theta))*N_rows^(-
0,166-1,08*tan(theta))*(F_p/TP_t)^(-0,174*ln(0,5*N_rows))
        J3=1

        j_dry=0,0646*Re_Dc^J1*(D_c/Dh_air)^J2*(F_p/TP_t)^(-1,03)*(TP_l/D_c)^0,432*tan(theta)^(-
0,692)*N_rows^(-0,737)

        F1=-0,141*(F_p/TP_l)^0,0512*tan(theta)^(-
0,472)*(TP_l/TP_t)^0,35*(TP_t/Dh_air)^(0,449*tan(theta))*N_rows^(-0,049+0,237*tan(theta))
        F2=-0,562*(ln(Re_Dc))^(-0,0923)*N_rows^0,013
        F3=0,302*Re_Dc^0,03*(TP_t/D_c)^0,026
        F4=-0,306+3,63*tan(theta)

        f_a=0,228*Re_Dc^F1*tan(theta)^F2*(F_p/TP_l)^F3*(TP_l/D_c)^F4*(D_c/Dh_air)^0,383*(TP_l/TP
_t)^(-0,247)
Endif
```

```
Nuss=j_dry*Re_Dc*Pr_a^(1/3)
h_dry=Nuss*k_a/D_c
End

"Evaporator: Correlations for wet air: Heat transfer coefficient and wet pressure drop ratio"

Procedure chtc_wet(Re_Dc;Pr_a;F_p;D_c;N_rows;k_a;A_air_total;A_t_inc;n;Fin_th;TP_l:h_wet)
If (Re_Dc>=300) and (Re_Dc<=10000) Then
        j_wet=0,213262*Re_Dc^(-
0,51507)*N_rows^0,09891*(A_air_total/(A_t_inc*n*12))^0,600543*(Fin_th/TP_l)^0,072448
        Nuss_wet=j_wet*Re_Dc*Pr_a^(1/3)
        h_wet=Nuss_wet*k_a/D_c
Endif
End

"Evaporator: Correlations for fin efficiency"

Procedure eta_fin(TP_t;TP_l;D_c;h_air;k_fin;t_fin;A_f_inc;A_a_inc:eta_f;eta_fo)
        r_o=D_c/2
        X_L=sqrt((TP_t/2)^2+TP_l^2)/2
        X_M=TP_t/2
        R_eq=r_o*(1,27*(X_M/r_o)*(X_L/X_M-0,3)^(1/2))
        PHI=(R_eq/r_o-1)*(1+0,35*ln(R_eq/r_o))
        m=sqrt((2*h_air)/(k_fin*t_fin))
        eta_f=(tanh(m*r_o*PHI))/(m*r_o*PHI)
        eta_fo=1-(A_f_inc/A_a_inc)*(1-eta_f)
End

"Evaporator: Correlations for mass transfer coefficient"

Procedure h_mass(h_c_wet;Cp_a;F_p;D_c;N_rows;A_a_inc;A_t_inc;Re_Dc;TP_l;TP_t:h_m)
        j_m_1=0,2143*(F_p/D_c)^1,3964*(A_a_inc/(A_t_inc))^1,2298*Re_Dc^(-0,224*(F_p/D_c)-
0,1111*(TP_l/D_c)-0,06472*(TP_t/D_c)-0,08751)
        j_m=j_m_1*N_rows^(-0,01884)*(F_p/D_c)^(-0,06725*N_rows-1,4424)*(A_a_inc/(A_t_inc))^(-
0,1664*N_rows-
0,7121)*Re_Dc^(0,04525*N_rows+0,3173*(F_p/D_c)+0,0905*(TP_l/D_c)+0,08353*(TP_t/D_c)-0,5101)
        Le=2,28*N_rows^0,2393*(F_p/D_c)^(0,0239*N_rows+0,4332)*(A_a_inc/(A_t_inc))^(0,0321*N_ro
ws+0,0747)*Re_Dc^(-0,01833*N_rows+0,194*(F_p/D_c)-0,0026*(TP_l/D_c)-
0,03012*(TP_t/D_c)+0,0418)
        h_m=h_c_wet/Cp_a/Le
End

"Evaporator: Cheng et. al (2008) correlation model for R744 two-phase heat transfer coefficient and
pressure drop"
Procedure
r744_tp(G;T_R744;x_R744;D_i;A_ff_r;A_r_inc_E;L_inc;gra;m_dot_r;P_R744;Q_flux;mu_SH;rho_SH:h_tp
;h$;DELTAP_r)

        D_eq=D_i
If x_R744<1 Then
        theta_dry=0
        Pcrit=p_crit(R744)
        pr=P_R744/Pcrit
        M=molarmass(R744)

"Fluid properties"
        rho_l=density(R744;T=T_R744;x=0)
        rho_v=density(R744;T=T_R744;x=1)
        mu_l=viscosity(R744;T=T_R744;x=0)
        mu_v=viscosity(R744;T=T_R744;x=1)
```

k_v=**conductivity**(***R744***;***T***=T_R744;***x***=1)
k_l=**conductivity**(***R744***;***T***=T_R744;***x***=0)
Cp_v=**specheat**(***R744***;***T***=T_R744;***x***=1)
CTP_l=**specheat**(***R744***;***T***=T_R744;***x***=0)
sigma=**surfacetension**(***R744***;***T***=T_R744)
h_vap=**enthalpy**(***R744***;***T***=T_R744;***x***=1)
h_liq=**enthalpy**(***R744***;***T***=T_R744;***x***=0)
h_LV=h_vap-h_liq
We_l=**abs**((G^2*D_eq)/(rho_l*sigma))
We_v=**abs**((G^2*D_eq)/(rho_v*sigma))
Fr_v_mori=**abs**(G^2/(rho_v*(rho_l-rho_v)*gra*D_eq))
qcrit=**abs**(0,131*rho_v^0,5*h_LV*(gra*sigma*(rho_l-rho_v))^0,25)
x_iA=1/(1,8^(1/0,875)*(rho_v/rho_l)^(-1/1,75)*(mu_l/mu_v)^(-1/7)+1)
x_di=0,58***exp**(0,52-0,236*We_v^0,17*Fr_v_mori^0,17*(rho_v/rho_l)^0,25*(Q_flux/qcrit)^0,27)
x_de=0,61***exp**(0,57-0,502*We_v^0,16*Fr_v_mori^0,15*(Q_flux/qcrit)^0,72*(rho_v/rho_l)^(-0,09))
epsilon_x_IA=x_iA/(rho_v*((1+0,12*(1-x_iA))*(x_iA/rho_v+(1-x_iA)/rho_l)+(1,18*(1-x_iA)*((gra*sigma*(rho_l-rho_v))^(1/4)))/(G*rho_l^0,5)))
epsilon=x_R744/(rho_v*((1+0,12*(1-x_R744))*(x_R744/rho_v+(1-x_R744)/rho_l)+(1,18*(1-x_R744)*((gra*sigma*(rho_l-rho_v))^(1/4)))/(G*rho_l^0,5)))
A_l=A_ff_r*(1-epsilon)
A_l_x_IA=A_ff_r*(1-epsilon_x_IA)

"Flow regimes"

"Intermittent flow"
If x_R744<x_iA ***Then***
deltadelta=D_eq/2-**sqrt**(**abs**((D_eq/2)^2-(2*A_l)/(2*3,1415-theta_dry)))
delta=**if**(deltadelta;(D_eq/2);deltadelta;deltadelta;(D_eq/2))
delta_IA=D_eq/2-**sqrt**(((D_eq/2)^2-(2*A_l_x_IA)/(2*3,1415-theta_dry)))
Re_delta=(4*G*(1-x_R744)*delta)/(mu_l*(1-epsilon))
Re_v=**abs**((G*x_R744*D_eq)/(mu_v*epsilon))
Prandl_l=**abs**((CTP_l*mu_l)/k_l)
Prandl_v=**abs**((Cp_v*mu_v)/k_v)
S=1
h_cb=**abs**(0,0133*Re_delta^0,69*Prandl_l^0,4*(k_l/delta))
h_nb=**abs**(131*Q_flux^0,58*pr^(-0,0063)*(-**log10**(pr))^(-0,55)*M^(-0,5))
h_wet=((S*h_nb)^3+h_cb^3)^(1/3)
h_v=0,023***abs**(Re_v)^0,8***abs**(Prandl_v)^0,4*(k_v/D_eq)
h_tp=(theta_dry*h_v+(2*3,1415-theta_dry)*h_wet)/(2*3,1415)
u_v=(G*x_R744)/(rho_v*epsilon)
f_A=3,128*Re_v^(-0,454)*We_l^(-0,0308)
DELTAP_A=4*f_A*(L_inc/D_eq)*((rho_v*u_v^2)/2)
Re_LO=(G*D_eq)/mu_l
f_LO=0,079/Re_LO^0,25
DELTATP_lO=4*f_LO*(L_inc/D_eq)*(G^2/(2*rho_l))
DELTAP_r=DELTATP_lO*(1-epsilon/epsilon_x_IA)*DELTAP_A*(epsilon/epsilon_x_IA)
h$='Intermittent'
Else

"Annular flow"
If (x_R744>x_iA) and (x_R744<x_di) ***Then***
deltadelta=D_eq/2-**sqrt**((D_eq/2)^2-(2*A_l)/(2*3,1415-theta_dry))
delta=**if**(deltadelta;(D_eq/2);deltadelta;deltadelta;(D_eq/2))
delta_IA=D_eq/2-**sqrt**(((D_eq/2)^2-(2*A_l_x_IA)/(2*3,1415-theta_dry)))
Re_delta=(4*G*(1-x_R744)*delta)/(mu_l*(1-epsilon))
Re_v=(G*x_R744*D_eq)/(mu_v*epsilon)
Prandl_l=(CTP_l*mu_l)/k_l
Prandl_v=(Cp_v*mu_v)/k_v
S=1-1,14*(1-delta/delta_IA)^2,2
h_cb=0,0133*Re_delta^0,69*Prandl_l^0,4*(k_l/delta)

```
        h_nb=131*abs(Q_flux)^0,58*abs(pr)^(-0,0063)*abs(-log10(pr))^(-0,55)*abs(M)^(-0,5)
        h_wet=((S*h_nb)^3+h_cb^3)^(1/3)
        h_v=0,023*Re_v^0,8*Prandl_v^0,4*(k_v/D_eq)
        h_tp=(theta_dry*h_v+(2*3,1415-theta_dry)*h_wet)/(2*3,1415)
        u_v=(G*x_R744)/(rho_v*epsilon)
        f_A=3,128*Re_v^(-0,454)*We_l^(-0,0308)
        DELTAP_r=4*f_A*(L_inc/D_eq)*((rho_v*u_v^2)/2)
        h$='Annular'
    Else

    "Dryout flow"
    If (x_R744>x_di) and (x_R744<x_de) Then
        A_l_x_di=A_ff_r*(1-x_di)
        epsilon_x_di=x_di/(rho_v*((1+0,12*(1-x_di))*(x_di/rho_v+(1-x_di)/rho_l)+(1,18*(1-
x_di)*((gra*sigma*(rho_l-rho_v))^(1/4)))/(G*rho_l^0,5)))
        deltadelta=D_eq/2-sqrt((D_eq/2)^2-(2*A_l)/(2*3,1415-theta_dry))
        delta=if(deltadelta;(D_eq/2);deltadelta;deltadelta;(D_eq/2))
        deltadelta_x_di=D_eq/2-sqrt((D_eq/2)^2-(2*A_l_x_di)/(2*3,1415-theta_dry))
        delta_x_di=if(deltadelta_x_di;(D_eq/2);deltadelta_x_di;deltadelta_x_di;(D_eq/2))
        delta_IA=D_eq/2-sqrt(((D_eq/2)^2-(2*A_l_x_IA)/(2*3,1415-theta_dry)))
        Re_delta_x_di=(4*G*(1-x_di)*delta)/(mu_l*(1-epsilon_x_di))
        Re_v_x_di=(G*x_di*D_eq)/(mu_v*epsilon_x_di)
        Re_H_x_de=((G*D_eq)/mu_v)*(x_de+(rho_v/rho_l)*(1-x_de))
        Prandl_l=(CTP_l*mu_l)/k_l
        Prandl_v=(Cp_v*mu_v)/k_v
        Y_x_de=1-0,1*((rho_l/rho_v-1)*abs(1-x_de))^0,4
        SS_x_di=1-1,14*(1-delta_x_di/delta_IA)^2,2
        S_x_di=if(x_di;x_iA;1;SS_x_di;SS_x_di)
        h_cb_x_di=0,0133*Re_delta_x_di^0,69*Prandl_l^0,4*(k_l/delta)
        h_v_x_di=0,023*Re_v_x_di^0,8*Prandl_v^0,4*(k_v/D_eq)
        h_nb=131*abs(Q_flux)^0,58*abs(pr)^(-0,0063)*abs(-log10(pr))^(-0,55)*abs(M)^(-0,5)
        h_wet_x_di=((S_x_di*h_nb)^3+h_cb_x_di^3)^(1/3)
        h_m_x_de=(0,00000002*Re_H_x_de^1,97*Prandl_v^1,06*Y_x_de^(-1,83)*(k_v/D_eq))
        h_tp_x_di=(theta_dry*h_v_x_di+(2*3,1415-theta_dry)*h_wet_x_di)/(2*3,1415)
        h_tp=h_tp_x_di-((x_R744-x_di)/(x_de-x_di))*(h_tp_x_di-h_m_x_de)
        u_v_x_di=(G*x_di)/(rho_v*epsilon_x_di)
        f_A_x_di=3,128*Re_v_x_di^(-0,454)*We_l^(-0,0308)
        DELTATP_tp_x_di=4*f_A_x_di*(L_inc/D_eq)*((rho_v*u_v_x_di^2)/2)
        epsilon_H_x_de=(1+((1-x_de)/x_de)*(rho_v/rho_l))^(-1)
        rho_H_x_de=rho_l*(1-epsilon_H_x_de)+rho_v*epsilon_H_x_de
        mu_H_x_de=mu_l*(1-x_de)+mu_v*x_de
        Re_m_x_de=(G*D_eq)/mu_H_x_de
        f_m_x_de=91,2/(Re_m_x_de^0,832)
        DELTAP_m_x_de=4*f_m_x_de*(L_inc/D_eq)*(G^2/(2*rho_H_x_de))
        DELTAP_r=DELTATP_tp_x_di-((x_R744-x_di)/(x_de-x_di))*(DELTATP_tp_x_di-
DELTAP_m_x_de)
        h$='Dryout'
    Else

    "Mist flow"
    If (x_R744>x_de) Then
        Re_H=((G*D_eq)/mu_v)*(x_R744+(rho_v/rho_l)*(1-x_R744))
        Prandl_v=(Cp_v*mu_v)/k_v
        Y=1-0,1*((rho_l/rho_v-1)*(1-x_R744))^0,4
        h_tp=(0,00000002*Re_H^1,97*Prandl_v^1,06*Y^(-1,83)*(k_v/D_eq))
        mu_H=mu_l*(1-x_R744)+mu_v*x_R744
        Re_m=(G*D_eq)/mu_H
        f_m=91,2/(Re_m^0,832)
        epsilon_H=(1+((1-x_R744)/x_R744)*(rho_v/rho_l))^(-1)
        rho_H=rho_l*(1-epsilon_H)+rho_v*epsilon_H
```

```
            DELTAP_r=4*f_m*(L_inc/D_eq)*(G^2/(2*rho_H))
            h$='Mist'
        Endif
        Endif
        Endif
        Endif

Else
        h_tp=1
        h$='Superheat'
        Re_SH=abs((m_dot_r*D_i)/(mu_SH*A_ff_r))
        V_r=m_dot_r/(rho_SH*A_ff_r)
        f_SH=(1,82*log10(Re_SH)-1,64)^(-2)
        DELTAP_r=f_SH* (L_inc/D_eq)* (V_r^2/(2*gra))*(rho_SH*gra)
Endif
End

"!_____________________________________________INPUTS_____________________________________
_____________"

"Compressor"
        P_dis=12,0*(10^6)       [Pa]
        {DOS=5,0                [°C]}

"Gas cooler"
        P_water_i=250*(10^3)    [Pa]
        T_water_i=15            [°C]
        {m_dot_w=0,1            [kg/s]}
        T_w_o=90                [°C]

"Evap inputs"
        T_amb=25                [°C]
        RH_a=0,30               [-]
        P_amb=85*(10^3)         [Pa]
        V_a=3,0                 [m/s]
        T_amb_wb=wetbulb(AirH2O;T=T_amb;R=RH_a;P=P_amb)
        T_evap=T_amb_wb-8

"General constants"
        Gra=9,81                [m/s^2]

"!_____________________________________________MAIN
CODE_____________________________________________"

"----------------------------------------------------------Main code: Compressor----------------------------------------
------------------"

"Compressor characteristic equations"
        Call comp_polynomials(P_suc; P_dis; T_suc : m_dot_r_total ; T_dis)

"Boundary conditions"
        P_suc=P_r_o_E[N_inc_E]
        T_suc=T_r_o_E[N_inc_E]
        h_suc=enthalpy(R744;T=T_suc;P=P_suc)

"Work rate & DOS"
        W_dot_c=m_dot_r_total*(h_dis-h_suc)
        h_dis=enthalpy(R744;T=T_dis;P=P_dis)
        DOS=T_suc-T_evap
```

"----------Main code: Gas Cooler----------"

"Geometry"

L_GC=30,32 [m]
t_tube_GC=0,00275 [m]
D_ii_GC=0,016 [m]
D_oi_GC=0,026035 [m]
R_f_ii_GC=0,0000
R_f_io_GC=0,0000
N_inc_GC=16
Abs_R_SS=1,5*(10^(-5))
D_io_GC=D_ii_GC+2*t_tube_GC
D_H_r_GC=D_ii_GC
D_H_w=D_oi_GC-D_io_GC
A_ff_r_GC=1/4*pi*D_ii_GC^2
A_ff_w=1/4*pi*D_oi_GC^2-1/4*pi*D_io_GC^2
A_r_GC=pi*D_ii_GC*L_GC
A_w=pi*D_io_GC*L_GC
L_inc_GC=L_GC/N_inc_GC
A_r_inc_GC=A_r_GC/N_inc_GC
A_w_inc=A_w/N_inc_GC
Rel_R_SS=Abs_R_SS / D_H_w

"Boundary conditions"

Inc_GC[0]=0
P_r_o_GC[0]=P_dis
T_r_o_GC[0]=T_dis
h_r_o_GC[0]=**enthalpy**(***R744***;***T***=T_dis;***P***=P_dis)
s_r_o_GC[0]=**entropy**(***R744***;***T***=T_dis;***P***=P_dis)
P_w_i[N_inc_GC+1]=P_water_i
T_w_i[N_inc_GC+1]=T_water_i
h_w_i[N_inc_GC+1]=**enthalpy**(***Water***;***T***=T_water_i;***P***=P_water_i)
s_w_i[N_inc_GC+1]=**entropy**(***Water***;***T***=T_water_i;***P***=P_water_i)

"Discretisation Function"

Duplicate i=1;N_inc_GC

"Links between succeeding increments"

Inc_GC[i]=Inc_GC[i-1]+1

h_r_i_GC[i]=h_r_o_GC[i-1]
P_r_i_GC[i]=P_r_o_GC[i-1]
T_r_i_GC[i]=T_r_o_GC[i-1]
s_r_i_GC[i]=s_r_o_GC[i-1]
h_w_o[i]=h_w_i[i+1]
P_w_o[i]=P_w_i[i+1]
T_w_o[i]=T_w_i[i+1]
s_w_o[i]=s_w_i[i+1]

"Mean increment properties"

P_r_GC[i]=(P_r_o_GC[i]+P_r_i_GC[i])/2
T_r_GC[i]=(T_r_o_GC[i]+T_r_i_GC[i])/2
h_r_GC[i]=(h_r_o_GC[i]+h_r_i_GC[i])/2
s_r_GC[i]=(s_r_o_GC[i]+s_r_i_GC[i])/2
P_w[i]=(P_w_i[i]+P_w_o[i])/2
T_w[i]=(T_w_i[i]+T_w_o[i])/2
h_w[i]=(h_w_i[i]+h_w_o[i])/2
s_w[i]=(s_w_i[i]+s_w_o[i])/2

```
        Delta_Pinch_GC[i]=T_r_GC[i]-T_w[i]

        "Fluid properties at mean increment position"
        mu_r_GC[i]=viscosity(R744;h=h_r_GC[i];P=P_r_GC[i])
        Cp_r_GC[i]=cp(R744;h=h_r_GC[i];P=P_r_GC[i])
        rho_r_GC[i]=density(R744;h=h_r_GC[i];P=P_r_GC[i])
        k_r_GC[i]=conductivity(R744;h=h_r_GC[i];P=P_r_GC[i])
        mu_w[i]=viscosity(Water;h=h_w[i];P=P_w[i])
        Cp_w[i]=cp(Water;h=h_w[i];P=P_w[i])
        rho_w[i]=density(Water;h=h_w[i];P=P_w[i])
        k_w[i]=conductivity(Water;h=h_w[i];P=P_w[i])

        "Convection heat transfer coefficients"
        Pr_r_GC[i]=Cp_r_GC[i]*mu_r_GC[i]/k_r_GC[i]
        Re_r_GC[i]=4*m_dot_r_total/(pi*D_H_r_GC*mu_r_GC[i])
        Nuss_r_GC[i]=if(Re_r_GC[i];2300;4,36;4,36;0,023*abs(Re_r_GC[i])^0,8*abs(Pr_r_GC[i])^0,3)
        h_c_r_GC[i]=Nuss_r_GC[i]*k_r_GC[i]/D_H_r_GC
        Pr_w[i]=Cp_w[i]*mu_w[i]/k_w[i]
        Re_w[i]=rho_w[i]*V_w[i]*D_H_w/mu_w[i]
        Nuss_w[i]=if(Re_w[i];2300;4,36;4,36;0,023*Re_w[i]^0,8*Pr_w[i]^0,4)
        h_c_w[i]=Nuss_w[i]*k_w[i]/D_H_w

        "Overall thermal resistance"
        1/UA_GC[i]=1/(h_c_r_GC[i]*A_r_inc_GC)+1/(h_c_w[i]*A_w_inc)+(ln(D_io_GC/D_ii_GC))/(2*pi*k_
t_GC[i]*L_inc_GC)+R_f_ii_GC/A_r_inc_GC+R_f_io_GC/A_w_inc
        k_t_GC[i]=conductivity(Stainless_AISI304; T=(T_r_GC[i]+T_w[i])/2)

        "Heat balance"
        Q_dot_H[i]=UA_GC[i]*(( (T_r_i_GC[i]-T_w_i[i]) - (T_r_o_GC[i]-T_w_o[i]) )/( ln( (T_r_i_GC[i]-
T_w_i[i]) / (T_r_o_GC[i]-T_w_o[i]) ) ))
        Q_dot_H[i]=m_dot_r_total*(h_r_i_GC[i]-h_r_o_GC[i])
        Q_dot_H[i]=m_dot_w*(h_w_i[i]-h_w_o[i])

        "Pressure drops"
        V_r_GC[i]=m_dot_r_total/(A_ff_r_GC*rho_r_GC[i])
        P_r_o_GC[i]=P_r_i_GC[i]-Delta_P_gc_R744[i]
        Delta_P_gc_R744[i]=(f_D&H[i]*L_inc_GC*rho_r_GC[i]*V_r_GC[i]^2)/(D_H_r_GC*2)
        Delta_P_r_GC[i]=(f_D&H[i]*L_inc_GC*rho_r_GC[i]*V_r_GC[i]^2)/(D_H_r_GC*2)
        f_D&H[i]=(1,82*log10(Re_r_GC[i])-1,64)^(-2)
        V_w[i]=m_dot_w/(A_ff_w*rho_w[i])
        P_w_i[i]=P_w_o[i]-Delta_P_gc_water[i]
        Delta_P_gc_water[i]=(f_DarcyW[i]*L_inc_GC*rho_w[i]*V_w[i]^2)/(D_H_w*2)
        Delta_P_w[i]=(f_DarcyW[i]*L_inc_GC*rho_w[i]*V_w[i]^2)/(D_H_w*2)
        f_DarcyW[i]=moodychart(Re_w[i];Rel_R_SS)

        "Increment outlet properties"
        T_w_i[i]=temperature(Water;h=h_w_i[i];P=P_w_i[i])
        T_r_o_GC[i]=temperature(R744;h=h_r_o_GC[i];P=P_r_o_GC[i])
        s_w_i[i]=entropy(Water;h=h_w_i[i];P=P_w_i[i])
        s_r_o_GC[i]=entropy(R744;h=h_r_o_GC[i];P=P_r_o_GC[i])
        U_GC[i]=UA_GC[i]/A_r_inc_GC
End

"Total heat transfer rate and output values"
        Q_dot_H_total=sum(Q_dot_H[i];i=1;N_inc_GC)
        Delta_P_w_total=sum(Delta_P_w[i];i=1;N_inc_GC)
        Delta_P_r_GC_total=sum(Delta_P_r_GC[i];i=1;N_inc_GC)
        T_r_o_GC=T_r_o_GC[N_inc_GC]
        T_w_o=T_w_i[1]
        P_w_o=P_w_i[1]
```

"----------Main code: Expansion Valve----------"

"Inlet properties"

h_EX_i=h_r_o_GC[N_inc_GC]
T_EX_i=T_r_o_GC[N_inc_GC]
P_EX_i=P_r_o_GC[N_inc_GC]
s_EX_i=s_r_o_GC[N_inc_GC]

"Outlet properties"

0=h_EX_i-h_EX_o
T_EX_o=T_evap
P_EX_o=**p_sat**(***R744***;***T***=T_evap)
s_EX_o=**entropy**(***R744***;***h***=h_EX_o;***P***=P_EX_o)

"----------Main code: Evaporator----------"

"Geometry"

L_evap=4,15
sigma=0,002028/(0,15*H_inc) {0.03245/(4.8/2)/H_inc}
D_o_E=0,0101
t_fin=0,00014
t_tube_E=0,00041
TP_t=0,0254
TP_l=0,022
N_rows=2
N_inc_E=32
N_circuits=12
D_i_E=D_o_E-t_tube_E*2
A_ff_r_E=PI*(D_i_E/2)^2
A_r_inc_E=PI*D_i_E*L_inc_E
D_c=D_o_E+2*t_fin
F_p=0,002116-t_fin
alpha_air=0,074436/(0,15*H_inc*W_inc) {2.38195/(4.8*H_inc*W_inc)}
Dh_air=4*A_ff_a_total*(W_e)/A_a_total
L_inc_E=L_evap/N_inc_E
W_inc=TP_l
W_e=TP_l*N_rows
H_inc=TP_t
Vol_inc=H_inc*L_inc_E*W_inc
A_fin\A=0,069973/0,074436 {2.23914/2.38195}
A_a_inc=alpha_air*Vol_inc
A_f_inc=A_a_inc*A_fin\A
N_f_inc=L_inc_E/F_p
A_t_inc=PI*D_o_E*(L_inc_E)
A_ff_a=L_inc_E*H_inc*sigma
A_ff_a_total=A_ff_a*(N_inc_E/2)*N_circuits
A_a_total=A_a_inc*N_inc_E*N_circuits

"Boundary conditions"

inc_E[0]=0
T_a_i=T_amb
P_a_i=P_amb
h_r_i_E=h_EX_i
T_r_i_E=T_evap

"Inlet air properties"

Cp_a=**cp**(***AirH2O***;***T***=T_a_i;***R***=RH_a;***P***=P_a_i)

rho_a=**density**(***AirH2O***;***T***=T_a_i;***R***=RH_a;***P***=P_a_i)
mu_a=**viscosity**(***AirH2O***;***T***=T_a_i;***R***=RH_a;***P***=P_a_i)
k_a=**conductivity**(***AirH2O***;***T***=T_a_i;***R***=RH_a;***P***=P_a_i)
h_a_i=**enthalpy**(***AirH2O***;***T***=T_a_i;***R***=RH_a;***P***=P_a_i)
omega_i=**humrat**(***AirH2O***;***h***=h_a_i;***R***=RH_a;***P***=P_a_i)
Re_Dc=(rho_a*V_a_max*D_c)/mu_a
Pr_a=(Cp_a*mu_a)/k_a

"Inlet refrigerant properties"
P_r_i_E=**p_sat**(***R744***;***T***=T_r_i_E)
x_i=**quality**(***R744***;***T***=T_r_i_E;***h***=h_r_i_E)
rho_r_i_E=**density**(***R744***;***T***=T_r_i_E;***h***=h_r_i_E)
Cp_r_i_E=**cp_r**(x_i;P_r_i_E;h_r_i_E)
mu_r_i_E=**mu_r**(x_i;P_r_i_E;h_r_i_E)
k_r_i_E=**k_r**(x_i;P_r_i_E;h_r_i_E)
s_r_i_E=**entropy**(***R744***;***T***=T_r_i_E;***x***=x_i)

"Evaporator material properties"
k_fin=k_ ('Aluminum'; T_a_i)
k_t=k_ ('Copper'; T_a_i)

"Air heat transfer coefficient and friction factor - dry air"
Call **chtc_dry&ff**(Re_Dc;D_c;Dh_air;F_p;TP_t;theta;N_rows;TP_l;k_a;Pr_a:h_c_dry;f_a)
theta=(16*PI)/180

"Air heat transfer coefficient and pressure drop ratio - wet air"
Call **chtc_wet**(Re_Dc;Pr_a;F_p;D_c;N_rows;k_a;A_a_total;A_t_inc;N_inc_E;t_fin;TP_l:h_c_wet)

"Fin efficiency - dry & wet air"
Call **eta_fin**(TP_t;TP_l;D_c;h_c_dry;k_fin;t_fin;A_f_inc;A_a_inc:eta;eta_o)
Call **eta_fin**(TP_t;TP_l;D_c;h_c_wet;k_fin;t_fin;A_f_inc;A_a_inc:eta_wet;eta_o_wet)

"Mass transfer coefficient"
Call **h_mass**(h_c_wet;Cp_a;F_p;D_c;N_rows;A_a_inc;A_t_inc;Re_Dc;TP_l;TP_t:h_m)

"Mass flow calculations"
m_dot_r=m_dot_r_total/N_circuits
G_r_E=m_dot_r/A_ff_r_E
V_a_max=V_a/sigma
m_dot_a=V_a*H_inc*L_inc_E*rho_a

"Discretisation function boundary values"
T_r_o_E[0]=T_r_i_E
h_r_o_E[0]=h_r_i_E
P_r_o_E[0]=P_r_i_E
s_r_o_E[0]=s_r_i_E
Cp_r_o_E[0]=Cp_r_i_E
k_r_o_E[0]=k_r_i_E
mu_r_o_E[0]=mu_r_i_E
rho_r_o_E[0]=rho_r_i_E
x_o[0]=x_i

Duplicate i=1;N_inc_E/4
T_a_i[i]=**average**(T_a_o[-i+17];T_a_o[-i+33])
omega_i[i]=**average**(omega_o[-i+17];omega_o[-i+33])
P_a_i[i]=**average**(P_a_o[-i+17];P_a_o[-i+33])
End
Duplicate i=N_inc_E/4+1;N_inc_E/2
T_a_i[i]=T_a_i
omega_i[i]=omega_i

```
        P_a_i[i]=P_a_i
        End
        Duplicate i=N_inc_E/2+1;24
        T_a_i[i]=average(T_a_o[-i+33];T_a_o[-i+49])
        omega_i[i]=average(omega_o[-i+33];omega_o[-i+49])
        P_a_i[i]=average(P_a_o[-i+33];P_a_o[-i+49])
        End
        Duplicate i=25;N_inc_E
        T_a_i[i]=T_a_i
        omega_i[i]=omega_i
        P_a_i[i]=P_a_i
        End

"Discretisation Function"
        Duplicate i=1;N_inc_E

        "Increment refrigerant side links"
        s_r_i_E[i]=s_r_o_E[i-1]
        Cp_r_i_E[i]=Cp_r_o_E[i-1]
        x_i[i]=x_o[i-1]
        k_r_i_E[i]=k_r_o_E[i-1]
        mu_r_i[i]=mu_r_o_E[i-1]
        rho_r_i[i]=rho_r_o_E[i-1]
        P_r_i_E[i]=P_r_o_E[i-1]
        h_r_i_E[i]=h_r_o_E[i-1]
        inc_E[i]=inc_E[i-1]+1

        "Increment inlet properties"
        T_r_i_E[i]=tempr744(x_i[i];P_r_i_E[i];h_r_i_E[i])
        DP_a[i]=dewpoint(AirH2O;T=T_a_i[i];w=omega_i[i];P=P_a_i[i])

        "Refrigerant heat transfer coefficients"
        Re_r_E[i]=abs((m_dot_r*D_i_E)/(mu_r_i[i]*A_ff_r_E))
        Pr_r_E[i]=(Cp_r_i_E[i]*mu_r_i[i])/k_r_i_E[i]
        f_sh[i]=(1,82*log10(Re_r_E[i])-1,64)^(-2)
        Nuss_sh[i]=(f_sh[i]/8)*(Re_r_E[i]-
1000)*Pr_r_E[i]*(1,07+12,7*sqrt(abs((f_sh[i]/8))*abs(abs(Pr_r_E[i])^(2/3)-1)))^(-1)
        h_c_sh[i]=Nuss_sh[i]*k_r_i_E[i]/D_i_E
        Call
r744_tp(G_r_E;T_r_i_E[i];x_i[i];D_i_E;A_ff_r_E;A_r_inc_E;L_inc_E;gra;m_dot_r;P_r_i_E;Q_flux_E[i];mu_
r_o_E[i];rho_r_o_E[i]:h_c_tp[i];h$[i];Delta_P_r_E[i])
        Q_flux_E[i]=Q_dot_L[i]/A_r_inc_E
        h_c_r[i]=if(x_i[i];1;h_c_tp[i];h_c_sh[i];h_c_sh[i])

        "Increment air properties"
        rho_a[i]=density(AirH2O;T=T_a_i[i];w=omega_i[i];P=P_a_i[i])
        Cp_a[i]=cp(AirH2O;T=T_a_i[i];w=omega_i[i];P=P_a_i[i])
        omega_sw[i]=humrat(AirH2O;T=T_t_o[i];R=1;P=P_a_i[i])
        h_g[i]=enthalpy(Water;T=T_a_i[i];x=1)
        h_f[i]=enthalpy(Water;T=T_t_o[i];x=0)
        AirState$[i]=if(T_t_o[i];DP_a[i];'Wet';'Dry';'Dry')
        rho_a_o[i]=density(AirH2O;T=T_a_o[i];w=omega_o[i];P=P_a_o[i])
        rho_a_avg[i]=(rho_a[i]+rho_a_o[i])/2

        "Heat balance"
        Q_dot_L[i]=m_dot_r*(h_r_o_E[i]-h_r_i_E[i])
        Q_dot_sen[i]=m_dot_a*Cp_a[i]*(T_a_i[i]-T_a_o[i])
        Q_dot_lat[i]=m_dot_a*h_g[i]*(omega_i[i]-omega_o[i])
        Q_dot_L[i]=Q_dot_sen[i]+Q_dot_lat[i]
```

"Characteristic heat transfer"
Q_dot_L[i]=h_c_r[i]*A_r_inc_E*(T_t_i[i]-T_r_i_E[i])
Q_dot_sen[i]=**if**(T_t_o[i];DP_a[i];h_c_wet*A_a_inc*eta_o_wet*(T_a_i[i]-T_t_o[i]);h_c_wet*A_a_inc*eta_o_wet*(T_a_i[i]-T_t_o[i]);h_c_dry*A_a_inc*eta_o*(T_a_i[i]-T_t_o[i]))
Q_dot_lat[i]=**if**(T_t_o[i];DP_a[i];h_m*A_a_inc*eta_o_wet*(omega_sw[i]-omega_i[i])*(h_f[i]-h_g[i]);h_m*A_a_inc*eta_o_wet*(omega_sw[i]-omega_i[i])*(h_f[i]-h_g[i]);0)

"Tube wall conduction"
Q_dot_L[i]=(2*PI*K_t*L_inc_E*(T_t_o[i]-T_t_i[i]))/**ln**(D_o_E/D_i_E)

"Increment outlet properties"
T_r_o_E[i]=**temperature**(***R744***;***h***=h_r_o_E[i];***P***=P_r_o_E[i])
s_r_o_E[i]=**entropy**(***R744***;***h***=h_r_o_E[i];***P***=P_r_o_E[i])

Cp_r_o_E[i]=**cp_r**(x_o[i];P_r_o_E[i];h_r_o_E[i])
k_r_o_E[i]=**k_r**(x_o[i];P_r_o_E[i];h_r_o_E[i])
mu_r_o_E[i]=**mu_r**(x_o[i];P_r_o_E[i];h_r_o_E[i])
rho_r_o_E[i]=**density**(***R744***;***P***=P_r_o_E[i];***h***=h_r_o_E[i])
RH_a_o[i]=**relhum**(***AirH2O***;***T***=T_a_o[i];***w***=omega_o[i];***P***=P_a_o[i])

"Pressure drops"
P_a_o[i]-P_a_i[i]+Delta_P_a[i]=0
Delta_P_a[i]=m_dot_a^2/(2*rho_a[i]*A_ff_a^2)*((1-(A_ff_a/(L_inc_E*H_inc))^2)*(rho_a[i]/rho_a_o[i]-1)+2*f_a*(A_a_inc/A_ff_a)*(rho_a[i]/(rho_a[i]+rho_a_o[i])))
P_r_o_E[i]-P_r_i_E[i]+Delta_P_r_E[i]=0
x_o[i]=**quality**(***R744***;***h***=h_r_o_E[i];***P***=P_r_o_E[i])
End

"Circuit outlet properties"
T_a_o=**average**(T_a_o[1..N_inc_E/4];T_a_o[N_inc_E/2+1..24])
omega_o=**average**(omega_o[1..N_inc_E/4];omega_o[N_inc_E/2+1..24])
P_a_o=**average**(P_a_o[1..N_inc_E/4];P_a_o[N_inc_E/2+1..24])
RH_a_o=**relhum**(***AirH2O***;***T***=T_a_o;***w***=omega_o;***P***=P_a_o)
ha_o=**enthalpy**(***AirH2O***;***T***=T_a_o;***w***=omega_o;***P***=P_a_o)
T_r_o_E=**temperature**(***R744***;***h***=h_r_o_E[N_inc_E];***P***=P_r_o_E[N_inc_E])
P_r_o_E=P_r_o_E[N_inc_E]
Delta_P_r_E_total=P_r_i_E-P_r_o_E[N_inc_E]
Delta_P_a_total=P_amb-P_a_o

"Evaporator heat transfer rates"
Q_dot_sen_total=**sum**(Q_dot_sen[i];i=1;N_inc_E)*N_circuits
Q_dot_lat_total=**sum**(Q_dot_lat[i];i=1;N_inc_E)*N_circuits
Q_dot_L_total=Q_dot_sen_total+Q_dot_lat_total

"----------Main code: Cycle COP & plotting points----------"

"Cycle heating COP"
COP_H=Q_dot_H_total/W_dot_c

"Cycle point: Evaporator outlet / Compressor inlet"
T_R744[1]=T_suc
P_R744[1]=P_suc
h_R744[1]=h_suc
s_R744[1]=**entropy**(***R744***;***T***=T_R744[1];***P***=P_R744[1])

"Cycle point: Compressor outlet / Gas cooler inlet"
T_R744[2]=T_dis
P_R744[2]=P_dis

```
        h_R744[2]=h_dis
        s_R744[2]=entropy(R744;T=T_R744[2];P=P_R744[2])

"Cycle points: Gas cooler discretisation"
        Duplicate i=3;N_inc_GC+1
        T_R744[i]=T_r_o_GC[i-2]
        P_R744[i]=P_r_o_GC[i-2]
        h_R744[i]=h_r_o_GC[i-2]
        s_R744[i]=s_r_o_GC[i-2]
        End

"Cycle point: Gas cooler outlet / Expansion valve inlet"
        T_R744[N_inc_GC+2]=T_EX_i
        P_R744[N_inc_GC+2]=P_EX_i
        h_R744[N_inc_GC+2]=h_EX_i
        s_R744[N_inc_GC+2]=s_EX_i

"Cycle point: Expansion valve outlet / Evaporator inlet"
        T_R744[N_inc_GC+3]=T_EX_o
        P_R744[N_inc_GC+3]=P_EX_o
        h_R744[N_inc_GC+3]=h_EX_o
        s_R744[N_inc_GC+3]=s_EX_o

"Cycle points: Evaporator discretisation"
        Duplicate i=1;N_inc_E
        T_R744[i+N_inc_GC+3]=T_r_o_E[i]
        P_R744[i+N_inc_GC+3]=P_r_o_E[i]
        h_R744[i+N_inc_GC+3]=h_r_o_E[i]
        s_R744[i+N_inc_GC+3]=s_r_o_E[i]
        End

"Cycle points: Water"
        Duplicate i=2;N_inc_GC+2
        T_water[i]=T_w_i[i-1]
        End
```